Université du Québec
à Rimouski

MÉTHANE DISSOUS DANS LE SYSTÈME MARIN DU SAINT-LAURENT

Thèse présentée

dans le cadre du programme de doctorat en océanographie

en vue de l'obtention du grade de philosophiae doctor

PAR

© Yijie Li

[Novembre 2021]

Composition du jury :

[Gwénaëlle Chaillou], président du jury, [Université du Québec à Rimouski]

[Huixiang Xie], directeur de recherche, [Université du Québec à Rimouski]

[Michael Scarratt], codirecteur de recherche, [Institut Maurice-Lamontagne]

[Yves Gelinas], examinateur externe, [Concordia University]

[André Pellerin], examinateur interne, [Université du Québec à Rimouski]

Dépôt initial le [06 août 2021] Dépôt final le [23 novembre 2021]

À ma famille

REMERCIEMENTS

Cette thèse est le résultat d'un parcours de recherche de six ans qui a nécessité une exploration expérimentale approfondie et un travail de terrain intéressant mais intensif. Je tiens à exprimer mes sincères remerciements à tous ceux qui m'ont aidée durant cette période.

À mon superviseur, Huixiang Xie, merci beaucoup pour votre patience, vos encouragements et votre mentorat. Cela fait neuf ans que je vous ai rencontré depuis mes études de maîtrise. Merci pour votre soutien et votre aide considérable, tant dans mes études que dans ma vie.

Aux membres de mon comité de thèse, Michael Scarratt (co-superviseur), Guillaume St-Onge et Douglas Wallace, je tiens à vous remercier pour vos commentaires constructifs et vos conseils tout au long de cette recherche. Je tiens également à remercier Michael Scarratt pour son aide dans la coordination et l'organisation du travail de terrain en mer, ainsi que Guillaume St-Onge et Pierre-Arnaud Desiage pour avoir fourni les coordonnées des stations de pockmark.

Aux membres de mon jury, en plus de deux directeurs de thèse, Gwénaëlle Chaillou, André Pellerin et Yves Gelinas, merci d'avoir partagé vos réflexions, commentaires et suggestions pétillantes pour cette thèse. Merci pour votre gentillesse et votre aide dans la réalisation d'une soutenance aussi merveilleuse et intéressante.

À Cédric Fichot, Lantao Geng, Ellen Damm, Peter S. Galbraith, et Daniel Bourgault, merci pour vos précieuses contributions aux publications évaluées par des pairs tirées de cette thèse.

Je remercie les capitaines, les scientifiques et les équipages de toutes les croisières pour leur aide et leur coopération lors de l'échantillonnage. Je remercie particulièrement François Villeneuve, Félix St-Pierre, Rémi Desmarais et Pascal Rioux pour leur aide lors de l'échantillonnage dans le système marin du St. Laurent, Oliver Zafiriou, Rod Johnson, Natalie Cohen, Makoto Saito, et les techniciens de BIOS pour avoir facilité et/ou aidé à

l'échantillonnage dans la mer des Sargasses, Cédric Fichot et Tara Clemente pour avoir facilité la collecte d'échantillons à la station ALOHA, Cédric Fichot pour avoir aidé à la collecte d'échantillons dans la zone côtière du Massachusetts, et Marie-Pier St-Onge pour avoir aidé à l'échantillonnage du pockmark lors de la mission en mer en février 2019.

Un grand merci à Lantao Geng pour avoir partagé les données de photoproduction de méthane collectées dans les mers arctiques canadiennes et les données de [CH_4] collectées dans l'EGSL en 2014, à Rio Tinto Alcan pour avoir fourni les données de débit d'eau douce de la rivière Saguenay, à l'Institut Maurice Lamontagne (IML) et à l'Institut des sciences de la mer (ISMER) pour avoir fourni les données de CTD et de chlorophylle *a*.

Un grand merci à Claude Belzile et à Mélanie Simard pour l'analyse des échantillons de DOC et de bactéries, à Dominique Lavallée pour l'aide à la manipulation des bouteilles de gaz, et à Martine Belzile pour son aide enthousiaste dans les affaires administratives.

À mes amis et collègues, Inês Léal, Mélanie Gaillard, et Atif Waqas, merci pour la camaraderie et le soutien pendant ces années et pour avoir fait de notre bureau un endroit chaleureux et heureux. Des remerciements particuliers à Xinxin Fei pour sa traduction française des résumés et des remerciements de cette thèse et à Feng Wang pour son aide précieuse dans la programmation R.

À ma famille, merci pour vos encouragements et pour m'avoir fourni un port fiable durant toutes ces années. Je dédie cette thèse à vous tous et surtout à ma grand-mère au ciel. Durant la pandémie de COVID-19 de 2020 et 2021, votre soutien a été ma plus grande motivation pour mener à bien cette étude.

Ce travail a été soutenu par les subventions du CRSNG Discovery (2017-05135), ArcticNet (phase 4) et Québec-Océan accordées à Huixiang Xie et la subvention de la NASA Water Quality (80NSSC18K0344) accordée à Cédric Fichot. J'ai bénéficié de bourses du Conseil de bourse de Chine (CSC) et de l'Institut des sciences de la mer de Rimouski (ISMER). Le temps de navier a été fournie par le Programme de monitorage de la zone Atlantique de Pêches et Océans Canada, le programme Odyssée Saint-Laurent du Réseau Québec Maritime, ArcticNet, et la Mission du stage de l'ISMER.

ACKNOWLEDGEMENTS

This thesis reflects a six-year-long research journey that involved extensive experimental exploration and interesting yet intensive fieldwork. I would like to express my sincere gratitude to all those who have helped me during this period.

To my supervisor, Huixiang Xie, many thanks for your patience, encouragement, and mentoring. It has been nine years since I met you during my master's study. Thank you for your tremendous support and help to both my study and life.

To the members of my thesis committee, Michael Scarratt (co-supervisor), Guillaume St-Onge and Douglas Wallace, I would like to thank you all for your constructive comments and advice throughout this research. I would also like to thank Michael Scarratt for help with coordinating and organizing the field work at sea and Guillaume St-Onge and Pierre-Arnaud Desiage for providing the coordinates of the pockmark stations.

To the members of my jury, in addition to two supervisors, Gwénaëlle Chaillou, André Pellerin and Yves Gelinas, thanks for sharing your sparkling thoughts, comments and suggestions for this thesis. Thank you for your kindness and help in making such a wonderful and interesting defence.

To Cédric Fichot, Lantao Geng, Ellen Damm, Peter S. Galbraith, and Daniel Bourgault, thank you for your invaluable contributions to the peer-reviewed publications from this thesis.

To the captains, scientists, and crews of all cruises, thank you all for your assistance and cooperation in sampling. I would particularly thank François Villeneuve, Félix St-Pierre, Rémi Desmarais, and Pascal Rioux for assistance in sampling in the St. Lawrence marine system, Oliver Zafiriou, Rod Johnson, Natalie Cohen, Makoto Saito, and BIOS technicians

for facilitating and/or assistance in the Sargasso Sea sampling, Cédric Fichot and Tara Clemente for facilitating sample collection from Station ALOHA, Cédric Fichot for assistance in sample collection in coastal Massachusetts, and Marie-Pier St-Onge for helping with the pockmark sampling during the February 2019 cruise.

Many thanks to Lantao Geng for sharing the methane photoproduction data collected in the Canadian Arctic seas and the [CH_4] data collected in the EGSL in 2014, to Rio Tinto Alcan for providing the Saguenay River freshwater discharge data, to the Maurice Lamontagne Institute (IML) and the Insititut des sciences de la mer (ISMER) for providing the CTD and chlorophyll a data.

Many thanks to Claude Belzile and Mélanie Simard for analyzing the DOC and bacterial samples, Dominique Lavallée for help with handling the gas cylinders, and Martine Belzile for enthusiastic help with the administrative affairs.

To my friends and colleagues, Inês Léal, Melanie Gaillard, and Atif Waqas, thank you for the companionship and support over these years and for making our office a warm and happy place. Special thanks to Xinxin Fei for her French translation of the abstracts and acknowledgements in this thesis and to Feng Wang for his great help in R programming.

To my family, thank you for your encouragement and for providing me a reliable harbour over all these years. I dedicate this thesis to all of you and especially to my grandmother in heaven. During the 2020 and 2021 COVID-19 pandemic, your support has been my greatest motivation to complete this study.

This work was supported by the NSERC Discovery (2017-05135), ArcticNet (phase 4), and Quebec-Ocean grants awarded to Huixiang Xie and the NASA Water Quality grant (80NSSC18K0344) awarded to Cédric Fichot. I was supported by scholarships from the China Scholarship Council (CSC) and the Institut des sciences de la mer de Rimouski (ISMER). Ship time was provided by the Atlantic Zone Monitoring Program of Fisheries and Oceans Canada, the Odyssée Saint-Laurent Program of Réseau Québec Maritime, ArcticNet, and the Mission stage of ISMER.

RÉSUMÉ

Le méthane est un puissant gaz à effet de serre dont la concentration atmosphérique et l'émission ont augmenté depuis le début de l'ère industrielle. Parmi les différents environnement aquatiques, l'océan, particulièrement ses zones côtières, est la source d'émission de méthane la plus mal résolue. Le système marin du Saint-Laurent (SMSL), composé du Fjord du Saguenay et de l'Estuaire et Golfe du Saint-Laurent (EGSL), est le plus grand système estuarien semi-fermé du monde. Ironiquement, le SMSL a été exclu des compilations de données mondiales sur le méthane océanique en raison du manque de données. Cette étude a recueilli le premier ensemble de données sur le méthane dissous dans le SLMS et a caractérisé les processus contrôlant les distributions et les flux air-mer de méthane dans ce système.

Dans le Fjord du Saguenay, l'eau de surface est fortement sursaturée en méthane, avec un taux d'émission de méthane par unité de surface estimé à un ordre de magnitude supérieur à l'estimation du flux moyenne pour les océans côtiers mondiaux. La décharge fluviale est la source principale de méthane dans le Fjord du Saguenay, suivi par les apports de l'estuaire inférieur du Saint-Laurent et les sédiments du tronçon supérieur du Fjord. Les émissions atmosphériques et l'oxydation microbienne contribuent de façon comparable à la perte de méthane dans le Fjord. La dynamique de la concentration de méthane ($[CH_4]$) dans l'eau de surface du Fjord est principalement contrôlée par la décharge d'eau douce, tandis que dans l'eau profonde, elle est contrôlée par les événements de renouvellement de l'eau. La composition isotopique du carbone du méthane ($\delta^{13}C_{CH4}$) indique que le méthane provenant des sédiments est biogénique et que la majorité du méthane dans la colonne d'eau est le résidu du méthane oxydé par les microbes.

L'eau de surface de l'EGSL est sursaturée en méthane à l'exception de quelques occasions de quasi-saturation dans le golfe. La $[CH_4]$ et le taux d'émission par unité de

surface diminuent rapidement vers la mer de l'Estuaire Supérieur au Golfe en passant par l'Estuaire Inférieur. La turbidité élevée près de la tête de l'Estuaire Supérieur module la dynamique du méthane dans l'eau de surface, dominée sinon par le mélange physique. La colonne d'eau du chenal Laurentien dans l'estuaire maritime et le golfe est caractérisée par l'ubiquité d'un maximum de [CH_4] en sous-surface et d'un minimum de [CH_4] en profondeur, attribuable à la production et à la consommation biologiques de méthane couplées à la stratification de la colonne d'eau ainsi qu'à la composition et à la circulation de la masse d'eau profonde. Les [CH_4]s élevés mais très variables sont présentes autour des pockmarks sur le fond marin du chenal Laurentien dans l'estuaire maritime. Le méthane émis par les pockmarks subit une dilution rapide et une consommation microbienne avant d'atteindre la surface et de s'échapper dans l'atmosphère. Les conditions hypoxiques dans l'eau de fond de l'estuaire maritime ne semblent pas favoriser de façon significative la production de méthane. Les données de $\delta^{13}C_{CH4}$ impliquent la présence de méthane de multiples sources, fortement oxydé par les microbes dans toute la colonne d'eau de l'EGSL.

Cette étude a également quantifié la photoproduction de méthane à partir de la matière organique dissoute chromophore (MODC) dans les eaux de surface de l'EGSL ainsi que d'autres zones océaniques et a évalué les contributions potentielles de cette voie aux budgets de méthane des eaux de surface dans l'EGSL et dans l'océan mondial. Les résultats révèlent que l'efficacité de la MODC pour la photoproduction de méthane augmente vers la mer à travers les zones de transition terre-océan et qu'elle peut jouer un rôle important dans le maintien de la sursaturation et de l'émission de méthane dans les hautes mers, bien que la photoproduction soit un terme mineur dans le cycle biogéochimique du méthane dans les eaux côtières, y compris l'EGSL.

En conclusion, le SMSL, qui occupe ~0,3 % de la superficie mondiale des océans côtiers (0-200 m), fournit ~0,1 % de l'émission de méthane totale à partir des océans côtiers dans le monde entier. Ce taux d'émission bas disproportionné pour l'SMSL est principalement dû aux grandes dimensions de l'estuaire maritime et du golfe dans l'EGSL, qui ressemblent respectivement aux mers de plateau externe et aux mers sur les talus continentaux, en termes

de [CH_4] d'eau de surface et de flux d'émission. Les multiples sources de méthane entrelacées avec l'hydrodynamique complexe mènent à des distributions de [CH_4] et de $\delta^{13}C_{CH4}$ beaucoup plus dynamiques et hétérogènes dans l'estuaire maritime et le golfe dans l'EGSL que dans l'estuaire supérieur dans l'EGSL et le Fjord du Saguenay. La contribution de la photoproduction de méthane aux budgets de méthane d'eaux de surface est marginale dans l'EGSL et les autres zones côtières mais importante dans les hautes mers.

Mots clés : Estuaire et golfe du Saint-Laurent; Fjord du Saguenay; méthane dissous; répartition; flux air-mer; oxydation microbienne; photoproduction du méthane; composition isotopique; paradoxe du méthane océanique; matière organique dissoute chromophorique

ABSTRACT

Methane is a potent greenhouse gas and its atmospheric concentration and emission have been increasing since the start of the industrial era. Among the various aquatic environments, the ocean, particularly its coastal areas, is the most poorly resolved methane emission source. The St. Lawrence marine system (SLMS), composed of the Saguenay Fjord and the estuary and Gulf of St. Lawrence (EGSL), is the world's largest semi-enclosed estuarine system. Ironically, the SLMS has been excluded from global ocean methane data compilations due to lack of data. This study collected the first dataset of dissolved methane in the SLMS and characterized the processes controlling the distributions and air-sea fluxes of methane in this system.

In the Saguenay Fjord, surface water is highly supersaturated with methane, with an areal methane emission rate estimated to be one order of magnitude higher than the mean flux estimate for the global coastal oceans. River discharge is the dominant source of methane to the Saguenay Fjord followed by inputs from the lower St. Lawrence estuary and sediments in the upper reach of the Fjord. Atmospheric emission and microbial oxidation contribute comparably to the loss of methane in the Fjord. The dynamics of methane concentration ($[CH_4]$) in the surface water of the Fjord is primarily controlled by freshwater discharge while in the deep water by water renewal events. Stable carbon isotopic composition of methane ($\delta^{13}C_{CH4}$) points to the sediments-sourced methane being biogenic and the bulk methane in the water column being the remnant of microbially oxidized methane.

The surface water of the EGSL is supersaturated with methane excepting near-saturation occasions in the Gulf. Both the $[CH_4]$ and the areal emission rate decrease rapidly seaward from the Upper Estuary to the Lower Estuary to the Gulf. High turbidity near the head of the Upper Estuary modulates the otherwise physical mixing-dominated methane dynamics in the surface water. The water column of the Laurentian Channel in the Lower Estuary and the

Gulf is featured with the ubiquity of a subsurface [CH_4] maximum and a deep [CH_4] minimum attributable to biological methane production and consumption coupled with water column stratification and deep water mass composition and circulation. Elevated but highly variable [CH_4]s are present around pockmarks on the seabed of the Laurentian Channel in the Lower Estuary. The pockmark-vented methane undergoes rapid dilution and microbial consumption before reaching the sea surface and escaping to the atmosphere. The hypoxic conditions in the bottom water of the Lower Estuary of do not seem to significantly promote methane production. The $\delta^{13}C_{CH4}$ data implies the presence of multi-sourced, highly microbially oxidized methane throughout the water column of the EGSL.

This study also quantified methane photoproduction from chromophoric dissolved organic matter (CDOM) in the surface waters of the EGSL and other ocean areas and evaluated the potential contributions of this pathway to the surface water methane budgets of the EGSL and the global ocean. The results reveal that the efficiency of CDOM for methane photoproduction increases seaward through land-ocean transitional zones and that while photoproduction is a minor term in the methane biogeochemical cycle in coastal waters, including the EGSL, it may play an important role in maintaining methane supersaturation and emission in open oceans.

In conclusion, the SLMS, which occupies ~0.3% of the global coastal ocean area (0-200 m), provides ~0.1% of the total methane emission from the coastal oceans worldwide. This disproportionally lower emission rate for the SLMS is mainly due to the large dimensions of the Lower Estuary and the Gulf of the EGSL which resemble outer shelf seas and continental slopes, respectively, in terms of surface-water [CH_4] and emission flux. The multiple methane sources intertwined with the complex hydrodynamics lead to far more dynamic and heterogeneous [CH_4] and $\delta^{13}C_{CH4}$ distributions in the Lower Estuary and the Gulf of the EGSL than in the Upper Estuary of the EGSL and the Saguenay Fjord. The contribution of methane photoproduction to the surface-water methane budgets is marginal in the EGSL and other coastal areas but consequential in open oceans.

***Keywords*:** Estuary and Gulf of St. Lawrence; Saguenay Fjord; dissolved methane; distribution; air-sea flux; microbial oxidation; methane photoproduction; isotope composition; oceanic methane paradox; chromophoric dissolved organic matter

TABLE OF CONTENTS

REMERCIEMENTS ix

ACKNOWLEDGEMENTS xi

RÉSUMÉ xiii

ABSTRACT xvii

TABLE OF CONTENTS xxi

LIST OF TABLES xxv

LIST OF FIGURES xxvii

LIST OF ABBREVIATIONS xxxiii

LIST OF SYMBOLS xxxvii

CHAPTER 1 GENERAL INTRODUCTION 1

1.1 METHANE IN EARTH'S ATMOSPHERE 1

1.2 SOURCES OF METHANE TO EARTH'S ATMOSPHERE 3

1.2.1 Anthropogenic sources 5

1.2.2 Natural sources 6

1.3 OCEANIC SOURCES OF METHANE TO THE ATMOSPHERE 9

1.3.1 Biological production in anoxic waters 9

1.3.2 Methane supersaturation in surface waters: The oceanic methane paradox 11

1.3.3 External water-column methane inputs 12

1.4 STABLE ISOTOPE AS A TOOL TO DISTINGUISH DIFFERENT SOURCES 14

1.5 BIOGEOCHEMICAL CYCLING OF METHANE IN THE OCEAN 16

1.6 STATUS OF METHANE STUDY IN THE ST. LAWRENCE MARINE SYSTEM 17

1.7 OBJECTIVES 18

1.8 STRUCTURE OF THE THESIS 19

CHAPTER 2 DISSOLVED METHANE IN THE WATER COLUMN OF THE SAGUENAY FJORD 21

2.1 RÉSUMÉ 22
2.2 ABSTRACT 23
2.3 INTRODUCTION 24
2.4 ENVIRONMENTAL SETTING 26
2.5 METHODS 27
2.5.1 Field sampling 27
2.5.2 Methane measurements 28
2.5.3 Ancillary measurements 30
2.5.4 Calculations of saturation ratio and air-sea flux 30
2.6 RESULTS AND DISCUSSION 31
2.6.1 Surface-water concentrations and air-sea fluxes 31
2.6.2 Estuarine mixing behavior 34
2.6.3 Vertical distributions 37
2.6.4 Isotope composition 42
2.6.5 Microbial oxidation rate in the deep layer 44
2.6.6 Fjord-wide methane budgets 46
2.7 CONCLUSIONS 49
2.8 ACKNOWLEDGEMENTS 51
2.9 DATA AVAILABILITY STATEMENT 51
2.10 TABLES 52
2.11 FIGURES 53
2.12 SUPPLEMENTARY INFORMATION 63
2.12.1 Supplementary figures 63

CHAPTER 3 DISSOLVED METHANE IN THE WORLD'S LARGEST SEMI-ENCLOSED ESTUARINE SYSTEM: THE GULF AND ESTUARY OF ST. LAWRENCE (CANADA) 69

3.1 RÉSUMÉ 70
3.2 ABSTRACT 72
3.3 INTRODUCTION 74
3.4 REGIONAL SETTING 76
3.5 METHODS 80
3.5.1 Sampling 80
3.5.2 Incubations 81
3.5.3 Methane measurement 82
3.5.4 Ancillary measurements 82
3.5.5 Calculations of saturation ratio and air-sea flux 83
3.6 RESULTS AND DISCUSSION 85
3.6.1 Surface water concentrations and estuarine mixing behavior 85
3.6.2 Air-sea fluxes 88
3.6.3 Vertical distributions in the Upper Estuary 90
3.6.4 Vertical distributions in the Lower Estuary and the Gulf 91
3.6.5 Pockmarks 98
3.6.6 Incubation-based net cycling rates 102
3.6.7 Distributions of $\delta^{13}C_{CH4}$ and sources of methane 104
3.7 CONCLUSIONS 108
3.8 ACKNOWLEDGMENTS 110
3.9 TABLES 111
3.10 FIGURES 118
3.11 SUPPLEMENTARY INFORMATION 131
3.11.1 Supplementary tables 131
3.11.2 Supplementary figures 132

CHAPTER 4 PHOTOPRODUCTION OF METHANE IN SURFACE WATERS OF THE ST. LAWRENCE MARINE SYSTEM AND OTHER MARINE ENVIRONMENTS: IMPLICATIONS FOR THE OCEANIC METHANE PARADOX 141

4.1 RÉSUMÉ 142
4.2 ABSTRACT 142
4.3 INTRODUCTION 143
4.4 METHODS 145
4.4.1 Sampling 145
4.4.2 Irradiation experiments 145
4.4.3 Analysis 147
4.4.4 Modeling of methane photoproduction rates 147
4.5 RESULTS AND DISCUSSION 149
4.5.1 Physical, chemical, and optical properties of sampled waters 149
4.5.2 Photoproduction of CH_4 149
4.5.3 Global estimates 151
4.5.4 Implications for CH_4 cycling in the Estuary and Gulf of St. Lawrence 153
4.5.5 Implications for the oceanic methane paradox 154
4.6 CONCLUSION 155
4.7 ACKNOWLEDGEMENTS 156
4.8 DATA AVAILABILITY STATEMENT 156
4.9 TABLES 157
4.10 FIGURES 158
4.11 SUPPLEMENTARY INFORMATION 161
4.11.1 Supplementary text 161
4.11.2 Supplementary tables 169
4.11.3 Supplementary figures 170

CHAPTER 5 GENERAL CONCLUSION 181

REFERENCES 185

LIST OF TABLES

Table 2-1. Range (mean; median) of water temperature, water salinity, dissolved methane concentration ($[CH_4]$), methane saturation ratio, wind speed, and methane water-to-air flux density.....52

Table 3-1. Summary of cruises participated. 111

Table 3-2. Means and ranges ([min, max]) of surface-water methane concentration ($[CH_4]_{surf}$). 112

Table 3-3. Means and ranges ([min, max]) of methane saturation ratio (*SR*), wind speed (U_{10}), methane exchange velocity (*k*), and methane flux density (*j*). 113

Table 3-4. Area-integrated methane fluxes in different seasons and sub-regions of the estuary and Gulf of St. Lawrence (EGSL). 114

Table 3-5. In situ depth, potential temperature (θ), salinity, and $[CH_4]$ in water with a potential density (σ_θ) of 27.25 kg m^{-3} at station TDC5 located in Cabot Strait, the Gulf of St. Lawrence, along with the same properties for the endmembers, North Atlantic Central Water (NACW), and Labrador Current Water (LCW), on the potential density surface of 27.10 kg m^{-3}. 115

Table 3-6. Targeted and real sampling coordinates of the pockmark stations, the distance between the targeted and real coordinates (i.e. horizontal distance deviation, HD), the distance between the deepest sampling depth and the seafloor (i.e. vertical distance deviation or VD), and the $[CH_4]$ at the deepest (i.e. near-bottom) sampling depth ($[CH_4]_{nb}$).....116

Table 3-7. Means and ranges of $\delta^{13}C_{CH4}$ for different sub-regions and different depth layers in the estuary and Gulf of St. Lawrence. 117

Table 3-S1. Fractions of ice cover and open-water areas in different sub-regions of the estuary and Gulf of the St. Lawrence (EGSL) during the winter sampling months. 131

Table 4-1. Physical, chemical, and optical properties of initial (unirradiated) water samples. 157

Table 4-S1. Supplementary information on water sampling and sample irradiation. 169

LIST OF FIGURES

Figure 1-1. Schematic describing the temporal evolutions of carbon dioxide, methane, and oxygen in Earth's atmosphere and the major events controlling their evolutions. 3

Figure 1-2. Global methane budget for the 2008–2017 decade. 5

Figure 1-3. Global annual mean $\triangle CH_4$ climatology. 8

Figure 1-4. Carbon and hydrogen isotope plot to isotopically characterize various sources of biotic and abiotic methane. 16

Figure 2-1. Sampling information and bathymetry and topography of the Saguenay Fjord. 53

Figure 2-2. Distribution of surface-water methane properties as a function of distance to the outermost sill. 54

Figure 2-3. Estuarine mixing behavior of surface-water methane concentration. 55

Figure 2-4. Depth profiles of physical, chemical, and biological properties. 56

Figure 2-5. Potential temperature–salinity diagrams at [CH_4] profiling stations. 57

Figure 2-6. Relationship between methane concentration and water temperature during the Oct-2016 cruise. 58

Figure 2-7. Relationship between methane concentration and apparent oxygen utilization for deep water (>25 m). 59

Figure 2-8. $\delta^{13}C_{CH4}$ data presented using the Rayleigh distillation model (A) and Keeling plot (B). 60

Figure 2-9. Schematic representation of the methane budgets in the Saguenay Fjord for an "average" year of 2016 and 2017. 61

Figure 2-10. Schematic representation of the major drivers controlling the dynamics of [CH_4] and $\delta^{13}C_{CH4}$ in the water column of the Saguenay Ford. 62

Figure 2-S1. Along-fjord distributions of physical and meteorological variables. 63

Figure 2-S2. Relationship between the river-endmember methane concentration and the freshwater discharge rate. 64

Figure 2-S3. Saguenay River freshwater discharge rates over 40 days prior to the onset of water sampling. 65

Figure 2-S4. Vertical profiles of methane concentration ([CH_4]), temperature, and salinity at station F21. 66

Figure 2-S5. Saguenay River freshwater discharge rate and the corresponding river end-member methane concentration. 67

Figure 3-1. Sampling area information and stations. 118

Figure 3-2. Scatter plots of [CH_4] *vs.* distance to Quebec City (**a**) and *vs.* salinity (**b**) along the main longitudinal axis of the EGSL (Fig. 3-1b). 119

Figure 3-3. Lateral distributions of surface-water [CH_4] across the Lower St. Lawrence estuary and the Gulf of St. Lawrence. 120

Figure 3-4. Typical vertical profiles of [CH_4] alongside the corresponding profiles of methane solubility at equilibrium with air, potential temperature (θ), salinity, dissolved oxygen, and turbidity in the Upper St. Lawrence estuary (**a**–**o**). 121

Figure 3-5. Vertical distributions of salinity and temperature (**a, d, g**), chlorophyll *a* fluorescence and dissolved oxygen (**b, e, h**), and [CH_4] and saturation ratio (**c, f, i**) along the main longitudinal axis of the Laurentian Channel in the Lower Estuary and the Gulf sampled during the Oct-16 (**a**–**c)** and Jun-17 cruises (**d**–**f**) and along the cross-channel transect in the Gulf visited during the Jun-15 cruise (**g**–**i**). 122

Figure 3-6. Vertical profiles of [CH_4] demonstrating the presence of the subsurface [CH_4] maximum (SMMax) in four seasons at a site in Cabot Strait area (**a**–**d**). 123

Figure 3-7. Vertical profiles of [CH_4] demonstrating the absence of the subsurface [CH_4] maximum (SMMax) at stations IF8 and Mecatina in the Mecatina Trough and stations IF12 and 35 in the Strait of Isle Belle (**a**–**d**). 124

Figure 3-8. Potential density (**a**) and [CH_4] (**b**) at the subsurface [CH_4] maximum (SMMax) in the Laurentian Channel as a function of distance to station T1 near the head of the channel. 125

Figure 3-9. [CH_4] at pockmark stations *vs.* depth (**a**) and potential density (**c**).....126

Figure 3-10. [CH_4] as a function of incubation time for surface water samples (**a**), the cold-intermediate-layer water samples (**b**), non-pockmark bottom water samples (**c**), and pockmark bottom water samples (**d**).....127

Figure 3-11. Comparison of temperatures (**a**) and $\delta^{13}C_{CH4}$ (**b**) between surface, cold-intermediate-cold-layer (CIL), and sub-CIL water samples collected during the Nov-17 cruise.....128

Figure 3-12. $\delta^{13}C_{CH4}$ *vs.* [CH_4] for different sub-regions and different depth layers (**a**) and the relationship between $\delta^{13}C_{CH4}$ and [CH_4] for bottom water samples collected from the Laurentian Channel and its branches (**b**). 129

Figure 3-13. Schematic representation of the major drivers controlling the dynamics of [CH_4] in the water column of the estuary and Gulf of St. Lawrence. 130

Figure 3-S1. Sampling stations labeled with names for each cruise and locations of weather stations (bottom panel on the right) from which wind speeds were obtained for methane flux calculations. 132

Figure 3-S2. Surface-water light transmission *vs.* distance to Quebec City along the main longitudinal axis of the St. Lawrence estuary during the Oct-17 and Feb-19 cruises. 133

Figure 3-S3. Relationships between surface-water [CH_4] and distance to Quebec City for individual cruises. 134

Figure 3-S4. Relationships between surface-water [CH_4] and salinity for individual cruises. 135

Figure 3-S5. Vertical profiles collected at station TDC5 in Cabot Strait in October 2016 (**a**–**c**) and June 2017 (**d**–**f**).....136

Figure 3-S6. Scatter plots of [CH_4] (**a**) and potential temperature (**b**) *vs.* potential density for three stations on a cross-channel transect (**c**) in the northwest Gulf of St. Lawrence.....137

Figure 3-S7. Vertical profiles collected at station T1 near the head of the Laurentian Channel during the Jun-17 cruise. 138

Figure 3-S8. Near-bottom [CH_4] at pockmark station PM5 as a function of $H^{1.4}*L$. 139

Figure 4-1. Methane photoproduction rate as a function of salinity (**a**) and the initial absorption coefficient at 320 nm (**b**). 158

Figure 4-2. The ratio of CH_4 photoproduction to photochemical loss of $a_g(320)$ (**a**) and the molar ratio of CH_4 to CO photoproduction (**b**) as a function of the initial $a_g(320)$. 159

Figure 4-3. Mapped yearly climatologies (2002-2018) for the surface ocean calculated with the remote-sensing based model 160

Figure 4-S1. Map of sampling stations. 170

Figure 4-S2. Effects of variations in the solar zenith angle (SZA) and vertical depth (z) 171

Figure 4-S3. Hypothetical spectral dependencies of the molar ratio of CH_4 to CO photoproduction. 172

Figure 4-S4. Calculated photoproduction rates of CO and CH_4 for the coastal Massachusetts station (42.156ºN, 70.206ºW) at 5 different vertical depths (0, 2, 5, 10, and 20 m). 173

Figure 4-S5. Temporal evolution of heterotrophic bacterial cell abundance during time-course irradiations. 174

Figure 4-S6. Photoproduction of CH_4 as a function of irradiation time. 175

Figure 4-S7. CO photoproduction rate *versus* the initial $a_g(320)$ and salinity. 176

Figure 4-S8. Linear relationship between $a_g(320)$ and salinity for the samples from the Estuary and Gulf of St. Lawrence that were used for determining the ratio of CH_4 to CO photoproduction. 177

Figure 4-S9. Remote sensing-modeled depth profiles of CH_4 photoproduction rate at the BATS, Station ALOHA, and a site (49°N, 67.8°W) in the lower St. Lawrence estuary. 178

Figure 4-S10. Methane photoproduction from acetone (50 μmol L^{-1}) and acetaldehyde (50 μmol L^{-1}) added to filtered Rimouski River water. 179

LIST OF ABBREVIATIONS

AOU	Apparent oxygen utilization
AOM	Anaerobic oxidation of methane
CDOM	Chromophoric dissolved organic matter
CH_3•	Methyl radicals
CH_3COOH	Acetic acid
CH_4	Methane
Chl *a*	Chlorophyll *a*
CIL	Cold intermediate layer
CO	Carbon monoxide
CO_2	Carbon dioxide
CTD	Conductivity-temperature-depth
DMMin	Deep methane concentration minimum
DMDS	Dimethyldisulfide
DMS	Dimethyl sulfide
DMSP	dimethylsulfoniopropionate
DOC	Dissolved organic carbon
EGSL	Estuary and Gulf of St. Lawrence

GCP	Global Carbon Project
GSL	Gulf of St. Lawrence
H_2	Hydrogen
HCl	Hydrochloric acid
HCO_3^-	Bicarbonate
HD	Horizontal distance deviation
HDPE	High-density polyethylene
HPLC	High performance liquid chromatography
LC	Laurentian Channel
LCW	Labrador Current Water
LE	Lower Estuary
LSLE	Lower Estuary of St. Lawrence
MSH	Methane thiol
MO_x	Aerobic methane oxidation
NACW	North Atlantic Central Water
NTU	Nephelometric turbidity units
O_2	Oxygen
O.D.	Outer diameter
OH	Hydroxyl radical
PDB	Pee Dee Belemnite

PE	Polyethylene
PES	Polyethersulfone
POM	Particulate organic matter
PTFE	Polytetrafluoroethylene
PVC	Polyvinyl chloride
Rrs	Remote-sensing reflectances
SLE	St. Lawrence Estuary
SLMS	St. Lawrence marine system
SMMax	Subsurface methane concentration maximum
SMTZ	Sulfate-methane-transition-zone
SR	Saturation ratio
SZA	Solar zenith angles
Tris-EDTA	10 $mmol^{-1}$ tris(hydroxymethyl)aminomethane (pH 8.0) mix with 1 mmol L^{-1} Ethylenediaminetetraacetic acid (pH 8.0)
TMZ	Turbidity maximum zone
UE	Upper Estuary
USLE	Upper Estuary of St. Lawrence
UV	Ultra-violet
VD	Vertical distance deviation

LIST OF SYMBOLS

a_g	Napierian absorption coefficient
$a_g(\lambda)$	Napierian absorption coefficient at wavelength λ
A_{fh}	Surface sediment area in the Saguenay Fjord's head region upstream of station S13
α	Kinetic carbon isotopic fractionation factor
$[CH_4]$	Dissolved methane concentration
$[CH_4]_{end\text{-}LCW}$	LCW's endmember methane concentration
$[CH_4]_{end\text{-}m}$	Marine-endmember methane concentration
$[CH_4]_{end\text{-}NACW}$	NACW's endmember methane concentration
$[CH_4]_{end\text{-}r}$	River-endmember methane concentration
$[CH_4]^*_{end\text{-}r}$	Effective river-endmember methane concentration
$[CH_4]_{eq}$	Methane concentration equilibrated with the atmosphere
$[CH_4]_{fm}$	Methane concentration at the Saguenay Fjord's mouth
$[CH_4]_{in}$	Methane concentrations inside the pockmark plume at the bottommost sampling depth
$[CH_4]_{mea}$	Surface-water methane concentrations
$[CH_4]_{nb}$	methane concentration at near-bottom sampling depth

$\mathbf{[CH_4]_{out}}$	Methane concentrations outside the pockmark plume at the bottommost sampling depth
$\mathbf{[CH_4]_{surf}}$	Marine-endmember methane concentration
[CO]	Dissolved oxygen concentration
$\boldsymbol{d_d}$	Downward diffusion rate of methane
$\mathbf{d[CH_4]/dz}$	Methane concentration gradient with depth
$\mathbf{\delta^{13}C_0}$	Initial isotope composition
$\mathbf{\delta^{13}C}$	Resulting isotope composition
$\mathbf{\delta^{13}C_{CH4}}$	Stable carbon isotope composition of methane
$\mathbf{\delta^{2}H_{CH4}}$	Stable hydrogen isotope composition of methane
$\mathbf{\Delta a_g(320)}$	Loss amount of CDOM absorption at wavelength 320 nm^{-1}
$\mathbf{\Delta CH_4}$	Difference between the measured surface-water methane concentration and the corresponding methane concentration at equilibrium with air (Chapter 1)
$\mathbf{\Delta CH_4}$	Amount of CH_4 produced by photoproduction (Chapter 4)
$\mathbf{\Delta[CH_4]}$	Difference between expected methane concentration and in situ methane concentrations (Chapter 3)
ΔCO	Amount of CO produced by photoproduction (Chapter 4)
$\mathbf{\Delta CH_4/\Delta CO}$	Molar ratio of CH_4 to CO photoproduction (Chapter 4)
$\boldsymbol{E_d(0\text{-}, \lambda)}$	Downwelling plane irradiance spectra just below the surface
$\boldsymbol{E_d(z, \lambda)}$	Downwelling plane irradiance spectra just at depth z

f	Remaining fraction of methane concentration (Chapter 2)
f	Fraction of open water (Chapter 3)
f_{NACW}	Fraction of NACW
f_{LCW}	Fraction of LCW
F_d	Diffusive methane efflux
$F_{R\text{-}IN}$	River runoff input of methane
$F_{SLE\text{-}IN}$	Input methane from the SLE
$F_{SED\text{-}IN}$	Sedimentary input of methane in the fjord's head region
$F_{F\text{-}OUT}$	Output of methane to the SLE
F_υ	Vertical methane transport flux
H	Difference between the depth of the seafloor and the deepest sampling depth
j	Air-sea flux density of methane
k	Gas transfer velocity
k_{CH4}	Net loss rate constant of methane
k_{eff}	Effective transfer velocity
k_{RC}	Gas transfer velocity using the formula of Raymond and Cole (2001)
k_{W14}	Gas transfer velocity using the formula of Wanninkhof (2014)
K_e	Eddy diffusivity
K_b	Vertical eddy diffusivity

K_d	Diffuse attenuation coefficients
λ	Wavelength
l_{net}	Net loss rate of methane
l_{ox}	Microbial oxidation rate of methane
L	Distance between the real and targeted coordinates of the sampling station
L_{OX}	Microbial oxidation of methane
L_R	Loss of methane in the river water
L_{SA}	Sea-to-air methane emission
L_{SLE}	Loss of methane in the SLE
L_T	Total loss due to microbial oxidation and outgassing of methane
$O_2\%$	Percent oxygen saturation
p_{sw}	In situ production rate of methane in the water column
P_{CH4}	CH_4 photoproduction rate
$PP_{CO}(\lambda)$	Corresponding CO photoproduction action spectra
$\phi_{CO}(\lambda)$	Composite apparent quantum for CO photoproduction
q_r	River flow rate
Q_{10}	Temperature coefficient for aerobic microbial methane oxidation
Q_F	Annual water outflow from the Saguenay Fjord to the SLE
Q_R	Annual river water inflow

Q_{SLE}	Annual water inflow from the SLE to the Saguenay Fjord
R_{sample}	Stable isotope ratios of the sample
$R_{standard}$	Stable isotope ratios of the reference standard
Sc	Schmidt number of methane
S	Salinity
S_{LCW}	LCW slinity endmembers
S_{mix}	In situ Salinities at station TDC5 (Chapter 3)
S_{NACW}	NACW salinity endmembers
σ_θ	Potential density
τ_{CH4}	Turn over time of methane decay
T	Temperature
T_{LCW}	LCW temperature endmembers
T_{mix}	In situ temperatures at station TDC5 (Chapter 3)
T_{NACW}	NACW temperature endmembers
θ	Potential temperature
u	Landward bottom water current speed
U	wind speed at 10 m height
$<U^2>$	Average of wind speeds squared
z	vertical depth (Chapter 4)

CHAPTER 1
GENERAL INTRODUCTION

1.1 METHANE IN EARTH'S ATMOSPHERE

Methane (CH_4), the second most important greenhouse gas, has been postulated to have existed in Earth's atmosphere for billions of years and played a pivotal role in Earth's evolution (Fig. 1-1) (Kasting and Siefert, 2002; Kasting, 2004). Based on this theory, methanogens were widespread and generated methane by combining hydrogen (H_2) and carbon dioxide (CO_2) during the Archean era (i.e. 4-2.5 billion years ago) when oxygen was absent (Catling and Claire, 2005). This biogenic methane production led to elevated atmospheric methane concentrations ([CH_4]s) up to 600 times higher than today (Catling and Claire, 2005). As methane absorbs Earth's outgoing radiation and traps heat, known as the greenhouse effect, it played a crucial role in keeping the young planet Earth warm, although the sun was 25–30% fainter than today during this period (Kasting and Catling, 2003). However, the methanogens did not dominate forever. As oxygenic cyanobacteria got their start and brought oxygen (O_2) to the atmosphere ~2.3 billion years ago, the atmospheric methane was oxidized by O_2 and its concentration decreased as oxygen concentration increased (Fig. 1-1). Such a decrease in the atmospheric [CH_4] chilled the planet by a few tens of ℃, which could explain the 0.3-billion year Paleoproterozoic global ice ages that started ~2.4 billion years ago (Pavlov et al., 2000). As the atmosphere evolved to an oxic state, methane would never again exert prominent effect on climate but still has been an important influence at later times. Today, methanogens are confined to restricted, oxygen-free environments, fermenting, for example, formate, acetate or lactate into CH_4 (Kasting, 2001).

If we move our attention back to modern times, the greenhouse effect has made methane a focal topic, scientifically and societally, due to increasing human activities. NOAA

global monitoring network indicates that the atmospheric concentrations and emissions of methane have continuously increased over decades since 1750 (pre-industrial era), with a global anthropogenic emission of ~359 Tg $year^{-1}$ (~60% of the total emission) (IPCC, 2013; Kirschke et al., 2013; Saunois et al., 2020), making methane the second most important anthropogenic greenhouse gas after CO_2 in terms of climate forcing. The surface dry-air mole fraction of methane rose from the pre-industrial level of ~722 ppb to 1650 ppb by the mid-1980s, nearly stabilized over the period from 1999 to 2006 at the level of ~1774 ppb, and thereafter grew rapidly to ~1875 ppb in 2020 (Etheridge et al., 1998; Dlugokencky et al., 2005; *Ed Dlugokencky, NOAA/GML: www.esrl.noaa.gov/gmd/ccgg/trends_ch4/*). The atmospheric methane growth rate was ~5.7 ppb $year^{-1}$ over 2007–2013, reached 12.9 ppb $year^{-1}$ in 2014, averaged 8.5 ppb $year^{-1}$ over 2015–2019, and peaked at 14.8 ppb $year^{-1}$ in 2020 (*Ed Dlugokencky, NOAA/GML*).

About 90% of the atmospheric methane is destroyed by the hydroxyl radical (·OH) in the troposphere (Khalil and Rasmussen, 1985; Cantrell et al., 1990) and the remainder is largely removed by excited atomic oxygen and atomic chlorine in the stratosphere and by oxidation in aerated soils (Saunois et al., 2016), leading to a methane turnover time of less than 10 years in the troposphere (Prather et al., 2012). The global atmospheric [CH_4] trend is driven by the imbalance between the emissions and sinks of methane, resulting in ~23% (~0.62 W m^{-2}) of the global greenhouse gas-induced radiative forcing (Etminan et al., 2016). However, quantifying the global methane budget faces an enormous challenge because of the various geographically overlapping methane sources and the uncertain chemical loss of methane by its reaction with ·OH (Saunois et al., 2020). Thus, to assess the impact of methane on climate change, it is imperative to understand its sources and the processes regulating the source strengths.

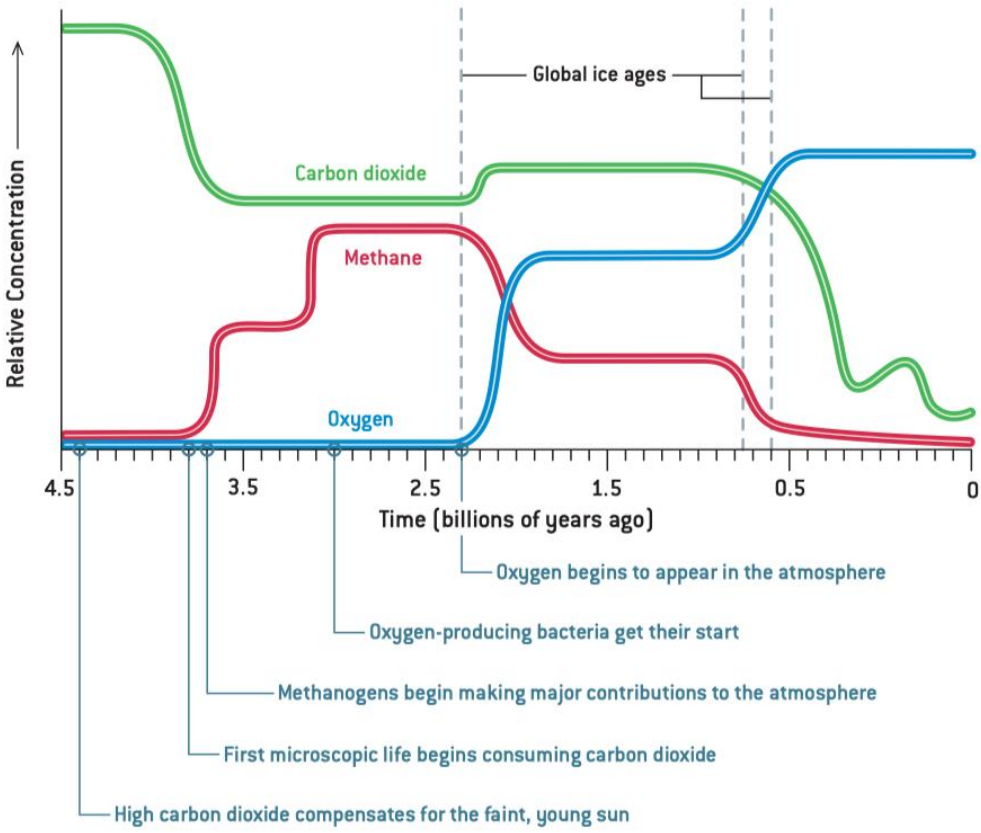

Figure 1-1. Schematic describing the temporal evolutions of carbon dioxide, methane, and oxygen in Earth's atmosphere and the major events controlling their evolutions. (After Kasting, 2004)

1.2 SOURCES OF METHANE TO EARTH'S ATMOSPHERE

The increasing atmospheric [CH_4] can be classified into three main emission processes, biogenic, pyrogenic and thermogenic, depending on the mechanism of its production (Bousquet et al., 2006; Neef et al., 2010; Schaefer et al., 2016). Biogenic methane is produced by methanogens in anaerobic environments, such as wetlands, rice paddies or inside animal intestines (Bauchop and Mountfort, 1981; Whiticar et al., 1986; Whiticar, 2020). As the last member of organic decomposition chain, methanogens can use acetic acid or carbon dioxide produced by other *Archaea* (e.g. hydrogen-producing acetogenic bacteria) to generate methane (Aitken et al., 2004; Whiticar, 2020). Pyrogenic methane, as an important abiotic

source, originates from the incomplete combustion of biomass, like biomass burning and biofuel usage (van der Werf et al., 2006; Worden et al., 2017). Thermogenic methane is formed due to the breakdown of buried organic matter at elevated temperatures and pressures in Earth's crust. Thermogenic methane can reach the atmosphere through natural gas seepages and human activities such as coal mining and oil and gas production (Bernard et al., 1976; Etiope et al., 2008; Zavala-Araiza et al., 2021). Some methanogenesis is a mixture of biological and thermal processes (e.g. Kvenvolden, 1988; Townsend et al., 2016; Moore et al., 2018). For instance, methane hydrates, the ice-like cages of methane, can be formed of biogenic or thermogenic methane (section 1.3). According to the magnitude of impact of human activities, all these emission sources can be characterized as natural and/or anthropogenic. The bottom-up and top-down approaches can be used to analyze the regional and global methane budget but with limitations (Kirschke et al., 2013).

The bottom-up approach is based on estimations for individual processes or on inventories representing different source types. Total methane emissions are derived by multiplying the average emissions by the number of sources (e.g. He et al., 2020; Lamb et al., 2015; Saunois et al., 2020). Top-down global and regional methane emission estimates were obtained directly from measurements on tower- or aircraft-based platforms (Karion et al., 2015; Saunois et al., 2016, 2020). This method of integrating multiple emissions sources makes it difficult to distinguish between the different methane sources (i.e. gridded optimized fluxes per source). At the global scale, the total methane emission estimate for the 2008–2017 decade is 576 (550–594) Tg CH_4 $year^{-1}$ by the top-down approach and 737 (594–880) Tg CH_4 $year^{-1}$ by the bottom-up approach (Saunois et al., 2020). In order to better quantify the global methane emissions per source category, an ensemble of bottom-up and top-down approaches were gathered under the umbrella of Global Carbon Project (GCP) (http://www.globalcarbonproject.Org). Five broad categories of anthropogenic and natural sources are classified: fossil fuel, agriculture and waste, biomass and biofuel burning, natural wetlands and other natural emissions. The source category-based methane emission estimates are summarized in Fig. 1-2 (Saunois et al., 2020).

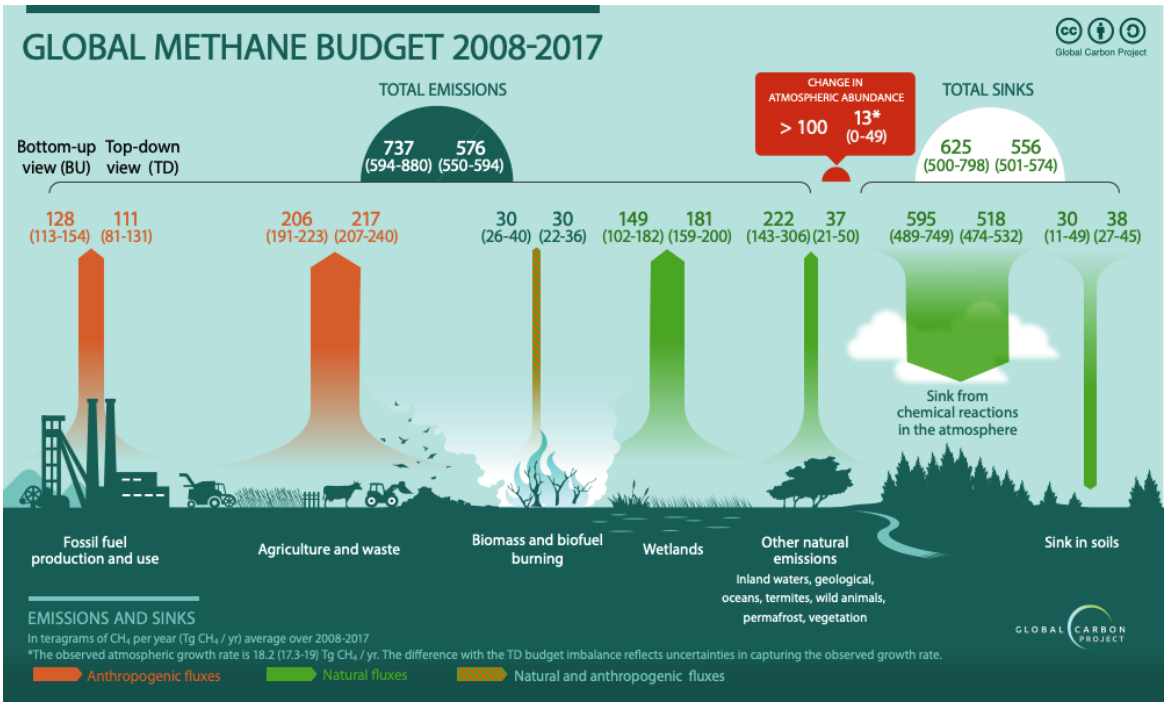

Figure 1-2. Global methane budget for the 2008–2017 decade. (After Saunois et al., 2020).

1.2.1 Anthropogenic sources

For the decade of 2008–2017, total anthropogenic methane emission estimate is 366 (349–393) Tg CH_4 $year^{-1}$ for bottom-up approach and 359 (336–376) Tg CH_4 $year^{-1}$ for top-down (Kirschke et al., 2013; Saunois et al., 2020). Anthropogenic emissions can be divided into three components: fossil fuels, agriculture and waste, and biomass and biofuel burning. Fossil fuels mostly come from exploitation, transportation, and use of coal, oil, and natural gas. Since natural gas is mainly composed of methane, leakage during extraction and transportation and incomplete combustion of gas flares contribute to methane emissions (Lamb et al., 2015). The bottom-up approach yields a global emission estimate of 128 (113–154) Tg CH_4 $year^{-1}$ from fossil fuels and other industries, accounting for 35% (30%–42%) of the total global anthropogenic emission (Saunois et al., 2020). Emission from agriculture and waste, estimated as 206 (range: 191–223) Tg CH_4 $year^{-1}$, occupies the largest share (56%) of the total anthropogenic input (Saunois et al., 2020). This category includes emissions from

domestic livestock, mainly ruminants (111 (106–116) Tg CH_4 $year^{-1}$) (Johnson et al., 2002, Saunois et al., 2020), rice cultivation (30 Tg (35–38) CH_4 $year^{-1}$) (Zhang et al., 2016; Carlson et al., 2017; Saunois et al., 2020), and waste management (65 (60–69) Tg CH_4 $year^{-1}$) (Saunois et al., 2020; Thorneloe et al., 2000). Biomass and biofuel burning takes up the rest (9%) of the anthropogenic emission, with a value of 30 (26–40) Tg CH_4 $year^{-1}$, of which 30%–50% is from biofuel burning (Saunois et al., 2020).

1.2.2 Natural sources

The bottom-up and top-down estimations of total natural emissions are quite different corresponding to values of 371 (245–488) Tg CH_4 $year^{-1}$ and 218 (183–248) Tg CH_4 $year^{-1}$ over the 2008–2017 decade, respectively (Saunois et al., 2020). This discrepancy probably comes from the overestimation in bottom-up approach of some natural sources (e.g. wetlands and other inland water systems) due to poorly documented measurements, the risk of "double counting" of ecosystem types (Armentano and Menges, 1986), and the challenge of partitioning emissions into anthropogenic (e.g. human driven land-use wetlands or aquaculture ponds) and natural sources (Woodward et al., 2012). Moreover, some methane emissions are not available on regional scales. For example, freshwater, permafrost, and marine seepage emission rates are still extensively debated (Thornton et al., 2020). In general, natural methane origination can be classified into three parts: aquatic ecosystems (e.g. inland waters, coastal and open oceans, and offshore geological sources), onshore geological sources, and other natural sources (e.g. termites and wild animals). Remarkably, a recent study revealed that almost half (~37%–49%) of the total global methane emission comes from natural aquatic sources, to which freshwater wetlands contribute approximately ~37–63% (Rosentreter et al., 2021).

1.2.2.1 Aquatic ecosystems

Inland waters are comprised of two main categories: wetlands and other inland water systems (e.g. lakes, reservoir, river, and streams). Wetlands, including peatlands (bogs and

fens), mineral wetlands (swamps and marshes), and seasonal or permanent floodplains, are deemed to be the major natural source of atmospheric methane (Matthew and Fung, 1987). Yet some wetlands that are involved in human-driven land-use purposes, like agriculture and housing, could be considered as anthropogenic sources (Bubier and Moore, 1994; Woodward et al., 2012). Since methanogens degrade organic matter to produce methane in anoxic conditions, wetlands with water-logged soils are the ideal environments for their activities. A warmer and more anaerobic environment with soil rich in organic matter allows for more efficient methanogenesis (Christensen et al., 2003). The global methane emission from wetlands has been estimated to be 148.6 ± 15.2 Tg CH_4 $year^{-1}$ (bottom-up approach), accounting for ~41% of the total natural source for the 2008–2017 period (Saunois et al., 2020). Methane emission from inland water systems other than wetlands (lakes, ponds, reservoirs, streams and rivers) is estimated as 159 (117–212) Tg CH_4 $year^{-1}$ by Saunois et al. (2020), while Rosentreter et al., (2021) reported a higher value of ~206 Tg CH_4 $year^{-1}$.

The amount of methane emitted to the atmosphere from coastal and open oceans, including estuaries, is considered to be small but not negligible, with a range from 1 to 35 Tg CH_4 $year^{-1}$ obtained by earlier studies (Rhee et al., 2009; Etiope 2015) and 9 to 22 (mean: ~13) Tg CH_4 $year^{-1}$ by more recent studies (Weber et al., 2019; Buitenhuis et al., 2020; Saunois et al., 2020), when combining all biogenic, geological, and hydrate sources. The wide range and high uncertainty of the oceanic methane flux estimates is related to sparse sampling and large spatiotemporal variations driven by tidal pumping and thermohaline gradients, especially in coastal areas (Rosentreter et al., 2018). The global surface-water [CH_4] data compiled by Weber et al., (2019) highlights the poor sampling coverage in certain major ocean basins, including both coastal and open-ocean areas (Fig. 1-3). Based on two machine-learning models, Weber et al. (2019) arrived at a total oceanic diffusive methane emission of 4.1 (2.2–6.3) Tg CH_4 $year^{-1}$, of which the near-shore environment (0–50 m, ~3.7% of the ocean area) is the largest but most uncertain contributor (2.0 (0.8–3.8) Tg CH_4 $year^{-1}$), followed sequentially by the open ocean (>2000 m, ~83.9% of the ocean area), the outer shelf (50–200 m, ~3.7% of the ocean area), and the continental slope (200–2000 m,

~8.7% of the ocean area), with emission fluxes of 1.0 (0.6–1.4), 0.74 (0.3–1.0), and 0.36 (0.2–0.6) Tg CH_4 $year^{-1}$, respectively.

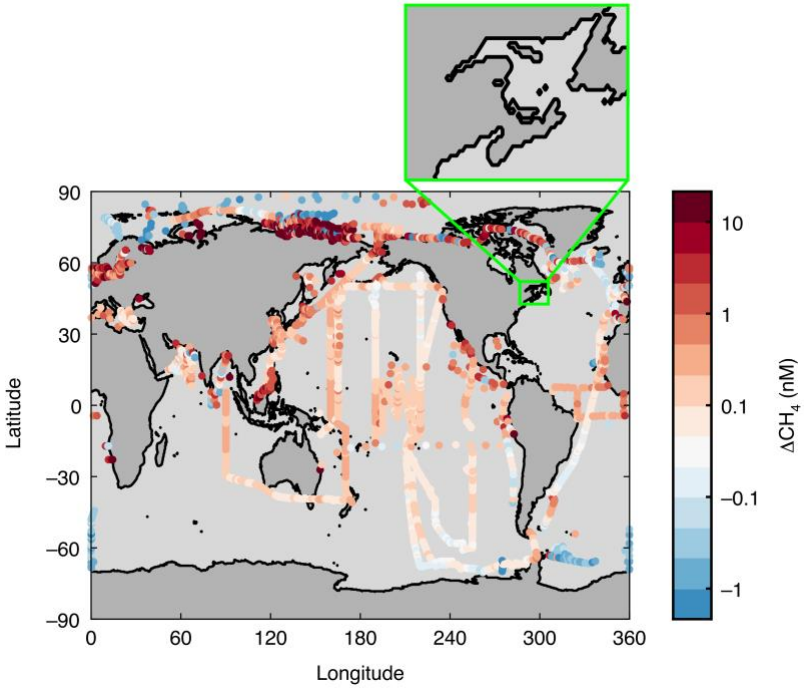

Figure 1-3. Global annual mean △CH_4 climatology. △CH_4 is the difference between the measured surface-water [CH_4] and the corresponding [CH_4] at equilibrium with air. The upper-right panel is a close-up view of the St. Lawrence marine system showing the absence of methane data in this water body. (After Weber et al., 2019)

1.2.2.2 Onshore and offshore geological sources

Geologic seepage is the third largest natural source after wetlands and freshwater systems (Etiope et al., 2019). Methane can be released from hydrocarbon production in sedimentary basins and escape to the atmosphere through tectonic faults and fractured rocks. Such degassing process occurs from five onshore sources (i.e. mud volcanoes, gas and oil seeps, microseepage, geothermal manifestations, and volcanoes) and one offshore source (i.e. submarine seepage). However, technical difficulties, such as their similar isotopic signatures with those of fossil fuel production, or co-located sources (Petrenko et al., 2017), lead to inconsistent estimates of geological methane emissions. The global geological methane

emission has been reported to be ~45 (18–63) Tg CH_4 $year^{-1}$, of which 7 (5–10) Tg CH_4 $year^{-1}$ are emitted offshore and 38 (13–53) Tg CH_4 $year^{-1}$ are emitted onshore (Etiope and Schwietzke, 2019). The largest geological methane emission is deemed to be related to exhalation from microseepages on land, which approximately account for 57% of the continental petroleum field area (Etiope et al., 2019).

1.2.2.3 Other natural sources

Aside from the above sources, termites and wild animals also make contribution to methane emissions. Termites are involved in nutrient cycling and can release methane as they anaerobically decompose plant biomass in their guts (Sanderson, 1996). The termite source has been estimated to release on average 9 (3–15) Tg CH_4 $year^{-1}$ over the decade of 2008–2017 (Saunois et al., 2017). Similar to domestic livestock, wild animals also emit methane from their rumens through microbial fermentation. However, wild animals only contribute ~2 (1–3) Tg CH_4 $year^{-1}$ (Saunois et al., 2017).

1.3 OCEANIC SOURCES OF METHANE TO THE ATMOSPHERE

Although the world ocean is considered to be a methane emitter to the atmosphere, the magnitudes and/or mechanisms of the sources and sinks of methane in the marine system are still under debate and have received far less attention than those in wetlands and soils. Sources of methane in the ocean can be roughly divided into *in situ* (within the water column) and *ex situ* (outside of the water column) sources.

1.3.1 Biological production in anoxic waters

In anoxic systems, remineralization of complex organic matter produces monomers which are fermented to H_2, low-molecular-weight fatty acids, alcohols and methylated compounds (Rogers and Whitman, 1991). Methanogens use simple molecules, primarily H_2 and acetate, as substrates whose supply depends on the activities of other microorganisms (Rudd and Taylor, 1980). H_2 is preferred in marine environments (reaction 1-1) due to the

depletion of acetate by sulfate reducers, while acetate is more favored in freshwater environments (reaction 1-2) due to the absence of sulfate reducers (Whiticar, 1999).

$$CO_2 + 4H_2 \rightarrow CH_4 + 2H_2O \text{ } (CO_2 \text{ reduction}) \quad (1\text{-}1)$$

$$CH_3COOH \rightarrow CO_2 + CH_4 \text{ (acetate fermentation)} \quad (1\text{-}2)$$

The open-ocean water column is not expected to have significant methanogenesis because of the presence of O_2. Even in anoxic basins large-scale methanogenesis in the water column has rarely been observed due to the presence of abundant sulfate and the occurrence of sulfate reduction (Albert et al., 1995). Studies in anoxic marine sediments indicate that methanogenic processes only take place when sulfate is nearly exhausted (Martens and Berner, 1977; Crill and Martens, 1983). Generally, the restriction of microbial methanogenesis arises from two mechanisms. First, the energy yield of organic matter oxidation by various electron acceptors decreases in the order of $O_2 > NO_3^- >$ Mn(IV) > Fe(III) > $SO_4^{2-} > CO_2$ (Thauer et al., 1977). Hence, CO_2, which produces methane through its reaction with H_2, is energetically the least favorable electron acceptor. Second, the effective capture of H_2 and acetate by sulfate reducers makes the concentrations of H_2 and acetate too low for methanogens to function. Therefore, significant microbial methane production in anoxic environments occurs only when the sulfate concentration decreases to a point at which methanogenesis would be possible.

However, Oremland et al. (1982a) reported that methane production could still occur in anoxic saltmarsh sediments involving active sulfate reduction. They revealed that two species of methanogens, *Methanpsarcina barkeri* and *Methanococcus mazei*, could grow on and produce methane from methanol and methylated amines (Weimer and Zeikus, 1978). Methanol can be generated by bacterial degradation of lignins (Donnelly and Dagley, 1980) or pectin (Schink and Zeikus, 1980), while methylated amines can be generated by decomposition of choline, creatine and betaine (Neill et al., 1978; Hippe et al., 1979), or by bacterial reduction of trimethylamine oxide (Strøm et al., 1979). Several laboratory experiments using lake, estuarine, and marine sediments have also demonstrated that

additions of methanol, methionine, methylated amines, dimethyl sulfide (DMS), dimethyldisulfide (DMDS) and methane thiol (MSH) are able to stimulate methane production (Oremland and Polcin, 1982; Oremland et al., 1982b; King, 1984; Kiene et al., 1986). DMS is a degradation product of dimethylsulfoniopropionate (DMSP) which is produced by certain marine phytoplankton species (Stefels et al., 2007; Yoch, 2002). Zindler et al. (2012) concluded that DMSP and its degradation products serve as substrates for methanogenic bacteria in the water column of the western Pacific Ocean. The substrates mentioned above are termed "noncompetitive substrates" for methanogenesis, because sulfate reducers do not use them, thereby obviating the competition between methanogens and sulfate reducers (Oremland and Polcin, 1982).

1.3.2 Methane supersaturation in surface waters: The oceanic methane paradox

In open oceans, the highest [CH_4]s are usually located in the surface layer which abounds with oxygen and sulfate. Moreover, [CH_4]s in surface open oceans are mostly supersaturated relative to the atmosphere (Weber et al., 2019), implying in situ production of methane in the upper ocean. As methanogenesis is traditionally considered to occur only under strict anoxic conditions, this phenomenon is termed the "oceanic methane paradox" (Kiene, 1991; Reeburg, 2007). Methane in surface waters has been shown to be produced through 1) methanogenesis taking place in anoxic microenvironments of organic aggregates (Karl and Tilbrook, 1994; Grossart et al., 2011; Bogard et al., 2014), the guts of zooplankton or fish (de Angelis and Lee, 1994; Oremland, 1979), and inside bacterial cells (Damm et al., 2015a); 2) bacterial degradation of methylphosphate (Karl et al., 2008; Repeta et al., 2016; Ye et al., 2020) and DMSP (Damm et al., 2008; Damm et al., 2010; Damm et al., 2015a) under phosphate- and nitrate-stressed environments, respectively; 3) metabolic activity of certain phytoplankton species (e.g. *Emiliania huxleyi*, *Phaeocystis sp.*, and *Phaeocystis globosa*) (Lenhart et al., 2016; Klintzsch et al., 2019) and various cyanobacteria (Bižić et al., 2020); 4) photodegradation of chromophoric dissolved organic matter (CDOM) (Zhang and Xie, 2015). Despite the demonstration, mostly in laboratory experiments, of the capability of

the aforementioned biotic and abiotic processes to produce methane, the mechanisms of these processes and their contributions to the oceanic methane paradox remain largely unknown.

1.3.3 External water-column methane inputs

1.3.3.1 Particulate organic matter

Particulate organic matter (POM) is formed by phytoplankton through photosynthetic processes in the ocean euphotic zone (Hedges and Keil, 1995; Yamanaka and Tajika, 1996). The debris deposits to the sediment with its sinking flux decreasing exponentially with increasing depth, leading to less than 1% passing a depth of 4000 m (Hedges and Keil, 1995). The POM sinking flux is highly variable and relies on various factors controlling primary productivity, such as nutrient supply, water temperature and depth, and the ecosystem structure. Acetate and other volatile fatty acids formed as degradation products from the buried complex organic matter provide the primary substrates for methanogenesis (Emerson and Hedges, 1988), as the burial rate of organic matter is positively correlated with the sedimentation rate, methanogenesis prevails mostly in sediments with high particle sinking rates (Henrichs and Reeburgh, 1987). It has been estimated that 0.1% of the ocean primary productivity is channeled to methanogenesis (Henrichs and Reeburgh, 1987). Methane produced in sediments can be transferred into the overlying water column via molecular diffusion and sediment resuspension (Henrichs and Reeburgh, 1987).

1.3.3.2 Hydrothermal vents and cold seeps

Hydrothermal vents and cold seeps are commonly found at continental margins and oceanic spreading centers worldwide (Campbell, 2006). Methane from these scarps or fractures disperses into the ambient water column and rises to the surface water as gas bubbles or streams (Luther et al., 2001; Campbell, 2006).

Hydrothermal vents are isolated areas with fissures on the sea floor where geothermally heated water discharges (Lonsdale, 1977; Corliss et al., 1979). H_2 is produced from seawater-

induced serpentinization of iron and manganese minerals contained in ultramafic rocks (reaction 1-3). The H_2 thus produced reacts with CO_2 at temperatures >300 ℃ to abiotically produce methane in the presence of an iron or iron oxide catalyst, i.e. the Fischer-Tropsch reaction (reaction 1-4) (Charlou et al., 1998; Sleep et al., 2004). The CO_2 in reaction 1-4 is converted from bicarbonate (HCO_3^-) as seawater permeates into the mantle and reacts with the molten basalt (Von Damm, 1990). These reactions occur in hydrothermal vents and near spreading centers (Massoth et al., 1989). Methane produced in the hydrothermal vents is injected into the water column often in the form of methane plumes.

$$6[(Mg_{1.5}Fe_{0.5})\,SiO_4] + 7H_2O \rightarrow 3[Mg_3Si_2O_5(OH)_4] + Fe_3O_4 + H_2 \quad (1\text{-}3)$$

olivine serpentine magnetite

$$CO_2 + 4H_2 \rightarrow CH_4 + 2H_2O \quad (1\text{-}4)$$

Unlike hydrothermal vents, the temperature of cold seeps is similar to that of the surrounding waters. These seeps are places on the seafloor with fissures or cracks where hydrogen sulfide, methane and other hydrocarbon-rich fluids seeping out (Campbell, 2006). Thus, methane and oil release into the water column and may contribute to the atmospheric methane burden (MacDonald et al, 2002; Solomon et al., 2009). However, a large part of the methane can be dissolved into seawater and utilized by methane oxidizers before rising to the surface (Valentine et al., 2001). Dimitrov (2002) estimated that only 0.03~0.15 Tg CH_4 enters the atmosphere from the Black Sea where seeps are extensive, while the bulk of the seep-derived methane is oxidized by microbes before reaching the surface water and escaping to the atmosphere.

1.3.3.3 Methane clathrate hydrates

Substantial volumes of methane gas are trapped below the seafloor and in permafrost, in the form of “methane clathrate hydrates” (Kvenvolden, 1993; Buffett, 2000). These hydrates occur along continental margins at depths of 600-3000 m and represent an enormous methane reservoir globally (500-2500 Gt C, Milkov, 2004). Methane hydrates form at

specific temperatures and pressures. Near the seafloor, active methane oxidation leads to an absence of methane hydrates, because it is impossible to maintain the stability of the hydrates at low methane concentrations. The methane concentrations needed for keeping the hydrates stable are estimated to be 100-200 mmol L^{-1} (Davie and Buffet, 2003). Decomposition of methane hydrates releases methane into the water column, which is then utilized by methanotrophs, with the remaining part vented to the atmosphere. Given the vast amount of methane stored in the form of clathrate hydrates, destabilization of the hydrates could potentially lead to catastrophic impacts on Earth's climate (Whiteman et al., 2013). On the other hand, this enormous reservoir constitutes a huge potential fuel source for human beings (Buffet and Archer, 2004).

1.3.3.4 Terrigenous input

Terrestrial inputs such as inflow of rivers, often contain high levels of methane resulting from both natural (De Angelis and Lilley, 1987) and anthropogenic sources (e.g. agricultural, or urban drainages) (Butler et al., 1987). A number of [CH_4] measurements in rivers have been reported, covering large rivers like the Amazon River (~50 nmol L^{-1} in the main stem; Richey et al., 1988), Mississippi River (~107–366 nmol L^{-1}; Swinnerton and Lamontagne, 1974), Orinoco River (~138 nmol L^{-1} near the river mouth; Jones and Amador, 1993), and other rivers in the world (e.g. Lamontagne, 1973; Wilkniss et al., 1978; de Angelis and Lilley, 1987; Scranton and McShane, 1991). These reports indicate that [CH_4]s in rivers are typically on the order of 100 nmol L^{-1} or more. Mixing between high-[CH_4] river waters and low-[CH_4] seawater may play an important role in controlling [CH_4]s in estuaries (de Angelis and Lilley, 1987). However, riverine methane transport to the ocean remains poorly quantified, though they can be significant methane sources to coastal seas.

1.4 STABLE ISOTOPE AS A TOOL TO DISTINGUISH DIFFERENT SOURCES

Stable isotope results are usually expressed with the δ-notation:

$$\delta = \left\{ \frac{R_{\text{sample}}}{R_{\text{standard}}} - 1 \right\} \times 1000 \text{ per mille or ‰} \quad (1\text{-}5)$$

R_{sample} and $R_{standard}$ denote the stable isotope ratios of the sample and the reference standard, respectively. The commonly used reference standards are the PeeDee belemnite (PDB) for ^{13}C (Craig, 1957) and the Standard Mean Ocean Water (SMOW) for ^{2}H.

Combining methane stable carbon ($^{13}C/^{12}C$) ($\delta^{13}C_{CH4}$) and hydrogen ($^{2}H/^{1}H$) ($\delta^{2}H_{CH4}$) isotope ratios from each major source can help produce a bottom-up budget of atmospheric measurements (Whiticar and Schaefer, 2007). A sensitivity analysis of atmospheric [CH_4]s and $\delta^{13}C_{CH4}$ to persistent changes in sources and sinks suggested that $\delta^{13}C_{CH4}$ is a potentially powerful indicator of source and sink changes (Lassey et al., 2000). Moreover, these isotopes are widely used to trace methane production, oxidation and transport, particularly in aquatic and sediment environments (Alperin et al., 1988; Whitcar, 1999; Chanton, 2005). In general, methane derived from biogenic processes reveals a $\delta^{13}C$ value range from -40‰ to -80‰, while thermogenic and abiotic such as pyrogenic methane is isotopically heavier with $\delta^{13}C$ values ranging from -30‰ to -50‰ (Tyler, 1991; Levin, 1993; Whiticar, 1999) (Fig. 1-4). The differences in C and H isotope ratios of methane are associated with the coexistence of H_2O and CO_2 pairs during bacterial methane formation and consumption (Whiticar, 2020). Several processes, such as mixing of different sources, oxidation, outgassing, and migration, can shift the $\delta^{13}C$ and $\delta^{2}H$ signatures of methane in the environment (Whiticar, 2020). Microbial methane oxidation usually depletes the lighter isotopologue faster, leading to an increasingly ^{13}C- and ^{2}H-enriched residual pool (Stevens and Rust, 1982; Whiticar, 1999; Whiticar, 2020). Emission of methane from natural waters to the atmosphere and migration of methane through porous media also cause the residual methane to be isotopically heavier (Happell et al., 1995; Pernaton et al., 1996; Prinzhofer and Pernaton, 1997).

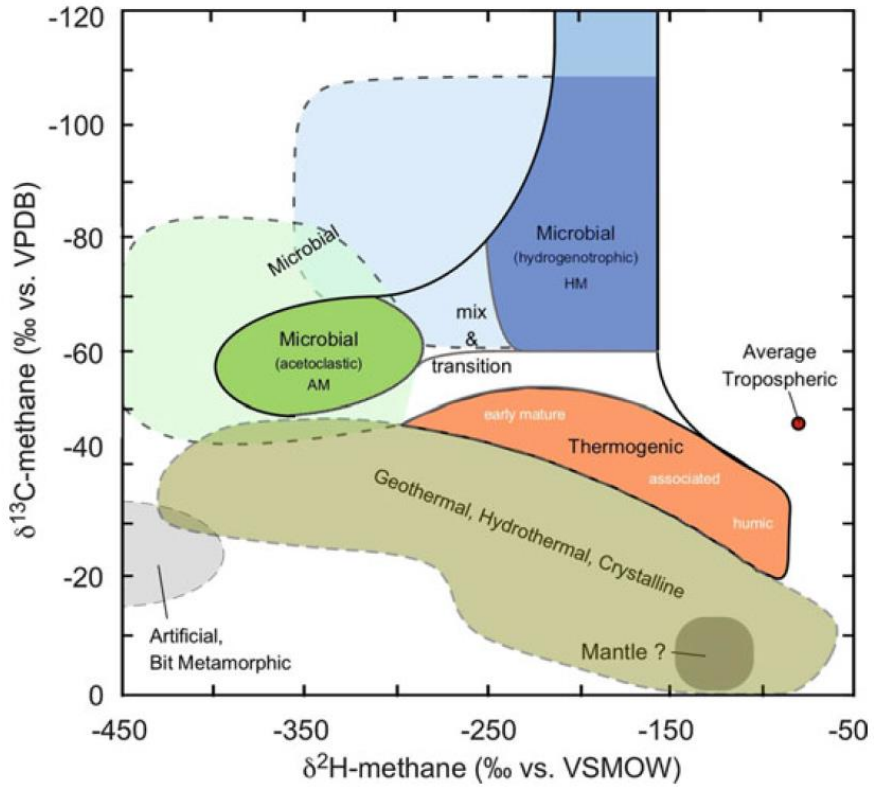

Figure 1-4. Carbon and hydrogen isotope plot to isotopically characterize various sources of biotic and abiotic methane. (After Whiticar, 2020, 1999)

1.5 BIOGEOCHEMICAL CYCLING OF METHANE IN THE OCEAN

The amount of methane transferrable from the ocean to the atmosphere depends on the combination of production, consumption, and physical transport of methane in the ocean. As mentioned earlier, systematic establishment of methane fluxes in the ocean is difficult due to the lack of available observations pertaining to spatiotemporal variability, especially in shelf areas and estuaries (Fig. 1-3, section 1.2.2.1). Furthermore, slight perturbations in the ambient environment can bring potentially large changes in the oceanic methane fluxes, highlighting the importance of understanding the pathways of methane cycling in marine ecosystems. On its way from sediments to the sea surface, in addition to diffusion in the water column regulated by water stratification conditions (Rusanov et al., 2002; Schmale et al., 2010), methane can be effectively removed by microbial oxidation involving methanotrophic

bacteria, which is a very important part of the methane cycle in the ocean (Grant and Whiticar, 2002; Reeburg, 2007). In fact, microbial oxidation consumes ~90% of the gross methane production in the ocean (~85 Tg CH_4 $year^{-1}$), while egress to the atmosphere takes the remaining 10% (Reeburg, 2007).

Methane oxidation takes place under both oxic and anoxic conditions. Aerobic methane oxidation (MOx) occurs in both marine and freshwater systems (Scranton and Brewer 1977; Whiticar and Faber 1986; Valentine et al., 2001), with generally slow rates. In oxic open oceans, the rate ranges from 0.15 nM $year^{-1}$ in waters of <10 years old to 10^{-4} nM $year^{-1}$ in waters having ages of >150 years (Scranton and Brewer, 1977). However, faster oxidation with fractional turnover times of days (de Angelis et al., 1993) and months (Valentine et al., 2001) has been observed in hydrothermal plumes and in waters close to active hydrate dissociation.

Anaerobic oxidation of methane (AOM) is thought to be the major sink for methane in anoxic marine sediments, equivalent to the sulfate-methane-transition-zone (SMTZ), and thus controls the upward flux of methane within the sediments and into the overlying water column (Barnes and Godlberg, 1976; Reeburg, 2007). It is estimated that AOM can consume >70 to 300 Tg CH_4 $year^{-1}$ (Reeburgh 1996; Hinrichs and Boetius 2002), with an estimated 5–25% of methane in sediments entering the water column after consumption (Valentine 2002).

1.6 STATUS OF METHANE STUDY IN THE ST. LAWRENCE MARINE SYSTEM

Here the St. Lawrence marine system (SLMS) refers to the Estuary and Gulf of the St. Lawrence (EGSL) plus its largest tributary, the Saguenay Fjord. The St. Lawrence ranks the second largest river system (after the Mississippi River) in North America in terms of freshwater discharge and the EGSL is the largest semi-enclosed estuarine system in the world characterized by complex hydrodynamics, geology, and chemical and biological processes (El-Sabh and Silverberg, 1990). The Saguenay Fjord, located on the north shore of the St. Lawrence estuary, is a deep, multi-silled, and year-round oxygenated fjord receiving organic-

rich freshwater from Lac Saint-Jean. A more detailed description of the EGSL and Saguenay Fjord is provided in sections 2.4 and 3.4.

To the best of my knowledge, no direct measurements of [CH_4] have been reported to date in either the water column or the sediments of the SLMS despite this system being among the world's most intensively studied estuaries (El-Sabh and Silverberg, 1990). Previous studies indirectly related to methane cycling in the EGSL include 1) acoustic and video observations showing widespread pockmarks on the seafloor of the Lower St. Lawrence estuary and the Gulf of St. Lawrence (Syvitski and Praeg, 1989; Josenhans et al., 1990; Bolduc et al., 2008; Pinet et al., 2008; Lavoie et al., 2010; Sirdeys, 2019); 2) isotopic analyses demonstrating the presence of methane-derived authigenic carbonates in sediments collected in the vicinity of several pockmark sites in the Lower St. Lawrence Estuary (Lavoie et al., 2010; Savard et al., 2021); 3) underground water surveys revealing high [CH_4]s of predominantly biogenic origin in many shallow aquifers in the St. Lawrence Lowlands upstream of the St. Lawrence Estuary (Moritz et al., 2015; Bordeleau et al., 2018; Rivard et al., 2018).

The lack of methane data for the SLMS left it unmentioned in global ocean data compilations for methane concentrations and air-sea fluxes (e.g. Borges and Abril, 2011; Weber et al., 2019) (Fig. 1-3) in spite of the enormous size of the SLMS relative to other estuarine water bodies. It is thus urgent to fill in this data blank on the oceanic methane data map. Moreover, the diverse and complex physical, chemical, biological, and geological processes present in the SLMS render it to be ideal for exploring the pathways that control the distribution of [CH_4] in the water column and thus its emission to the atmosphere.

1.7 OBJECTIVES

This research aims to provide the first dataset of dissolved methane in the water column of the SLMS that allows assessing the contribution of the SLMS to the global estuarine methane emission and elucidating the processes responsible for the production, transport and

cycling of dissolved methane in this estuarine system. The specific objectives are listed as follows:

Objective 1: To determine the spatial and seasonal variabilities of the methane emission flux from the SLMS.

Objective 2: To quasi-quantitatively assess the sources, transport, and consumption of methane in the water column of the SLMS by combining [CH_4] profiling, $\delta^{13}C_{CH4}$ analysis, and lab incubations.

Objective 3: To determine the rates of photoproduction of methane from CDOM in the surface waters of the SLMS and other marine environments and evaluate the implications of this photoprocess for methane cycling at regional and global ocean scales.

1.8 STRUCTURE OF THE THESIS

This thesis is structured according to the "paper-style" defined by UQAR's thesis writing regulations. It starts with a General Introduction (Chapter 1) followed sequentially by three papers: Dissolved methane in the water column of the Saguenay Fjord (Chapter 2, published); dissolved methane in the world's largest semi-enclosed estuarine system: the Estuary and Gulf of St. Lawrence (Canada) (Chapter 3, to be submitted); photoproduction of methane in surface waters of the St. Lawrence marine system and other marine environments: Implications for the oceanic methane paradox (Chapter 4, published). The thesis ends with a General Conclusion (Chapter 5).

CHAPTER 2
DISSOLVED METHANE IN THE WATER COLUMN OF THE SAGUENAY FJORD

Yijie Li [1], Huixiang Xie [1*], Michael Scarratt [2], Ellen Damm [3], Daniel Bourgault [1], Peter S. Galbraith [2], Douglas W. R. Wallace [4]

[1]Institut des sciences de la mer, Université du Québec à Rimouski, Rimouski, Québec, Canada G5L 3A1

[2]Maurice Lamontagne Institute, Fisheries and Oceans Canada, Mont-Joli, Quebec, Canada G5H 3Z4

[3]Alfred Wegener Institute for Polar and Marine Research, P.O. Box 120161 D-27515 Bremerhaven, Germany

[4]Department of Oceanography, Dalhousie University, Halifax, Nova Scotia, Canada B3H 4R2

Published in Marine Chemistry

Cite this article as: Li, Y., Xie, H., Scarratt, M., Damm, E., Bourgault, D., Galbraith, P.S., Wallace, D.W.R., 2021. Dissolved methane in the water column of the Saguenay Fjord. Mar. Chem. 230, 103926. https://doi.org/10.1016/j.marchem.2021.103926

2.1 RÉSUMÉ

Les environnements proches de la côte sont une source importante de méthane atmosphérique mais l'étendue de cette source est mal comprise, surtout pour les fjords et les fjards. Cette étude a examiné les taux d'émission de méthane et les facteurs contrôlant la dynamique du méthane dissous dans le Fjord du Saguenay, un système de fjord subarctique profond, stratifié et bien oxygéné dans l'Est du Canada. Les concentrations de méthane dissous ([CH_4]) dans la colonne d'eau ont été mesurées en octobre 2016 et en juin, octobre et novembre 2017, avec une composition d'isotope stable de carbone du méthane ($\delta^{13}C_{CH4}$) analysée lors de la mission en novembre 2017. La [CH_4] de l'eau de surface variait de 16 à 184 nmol L^{-1} et diminuait avec l'augmentation de la salinité d'une manière linéaire bi-segmentaire, ce qui infère qu'il est une composante marine temporellement constante mais une composante fluviale dépendante de la décharge d'eau douce. L'ensemble de données de multi-missions donne un taux de saturation moyen du [CH_4] de 12,7 (gamme : 4,5-48,7) et un taux d'émission moyen de 53.4 μmol m^{-2} d^{-1} (gamme : 16.4-256.9 μmol m^{-2} d^{-1}). La [CH_4] était généralement plus élevé dans l'eau de surface qu'en profondeur. Cependant, le mélange induit par le seuil pourrait homogénéiser la [CH_4] près de l'embouchure du fjord et l'apport sédimentaire du méthane biogénique ($\delta^{13}C_{CH4}$: -57.660‰) dans la région de la tête du fjord a accru la [CH_4] dans l'eau de fond sus-jacente jusqu'à 459 nmol L^{-1}. La tendance longitudinale de la [CH_4] sous la couche de surface était principalement contrôlé par le renouvellement de l'eau profonde. La [CH_4] de l'eau profonde a diminué avec l'augmentation de l'utilisation apparente de l'oxygène, ce qui suggère une oxydation du méthane microbienne aérobique aux taux estimés de <0.1 nmol L^{-1} d^{-1}. Les données du $\delta^{13}C_{CH4}$ donnent un facteur de fractionnement isotopique du carbone de 1,08 dans les eaux de surface et les eaux profondes qui indique que l'oxydation microbienne contrôle le fractionnement isotopique du carbone du méthane dans le fjord. Le budget basé sur un bilan massique révèle que les apports fluviaux représente 81 % de l'apport total du méthane dans le fjord (12.13×10^6 mol an^{-1}) et que l'oxydation microbienne du méthane (4.45×10^6 mol an^{-1}) est comparable à l'émission du méthane dans l'atmosphère (4.27×10^6 mol an^{-1}). Cette

étude démontre les rôles importants du ruissellement fluvial et du renouvellement d'eau profonde dans le contrôle de la dynamique de la [CH_4], du $\delta^{13}C_{CH4}$ et de l'émission de méthane dans l'air dans les fjords recevant d'importantes décharges d'eau douce terrestre et soumis à de fréquents renouvellements d'eau profonde. Les taux d'émission de méthane par unité de surface pour les fjords profonds obtenus par cette étude et des études antérieures sont d'un à deux ordres de grandeur plus élevés que l'estimation de flux moyen pour les océans côtiers mondiaux, ce qui fait des fjords et des fjards un contributeur potentiellement important à l'émission de méthane dans les zones côtières.

Mots-Clés **:** Fjord du Saguenay ; méthane dissous ; répartition ; flux air-mer ; oxydation microbienne ; composition isotopique

2.2 ABSTRACT

Near-shore environments are a significant source of atmospheric methane but the size of this source is poorly constrained, particularly for fjords and fjards. This study investigated the methane emission rates and the drivers controlling the dynamics of dissolved methane in the Saguenay Fjord, a deep, stratified, and well-oxygenated subarctic fjord system in eastern Canada. Dissolved methane concentrations ([CH_4]) in the water column were measured in October 2016 and June, October, and November 2017, with stable carbon isotope composition of methane ($\delta^{13}C_{CH4}$) analyzed during the November 2017 survey. Surface-water [CH_4] ranged from 16–184 nmol L^{-1} and decreased with increasing salinity in a bi-segment linear manner, inferring a temporally constant marine endmember but a freshwater discharge-dependent river endmember. The multi-cruises dataset yields a mean [CH_4] saturation ratio of 12.7 (range: 4.5–48.7) and a mean emission rate of 53.4 μmol m^{-2} d^{-1} (range: 16.4–256.9 μmol m^{-2} d^{-1}). [CH_4] was generally higher in surface water than in deep water. However, sill-induced mixing could homogenize [CH_4] near the mouth of the fjord and sedimentary input of biogenic methane ($\delta^{13}C_{CH4}$: −57.660‰) in the fjord's head region increased [CH_4] in the overlying bottom water up to 459 nmol L^{-1}. The longitudinal pattern

of [CH_4] below the surface layer was primarily controlled by deep-water renewal events. Deep-water [CH_4] declined with rising apparent oxygen utilization, suggestive of aerobic microbial methane oxidation at rates estimated to be <0.1 nmol L^{-1} d^{-1}. The $\delta^{13}C_{CH4}$ data yields a carbon isotopic fractionation factor of 1.08 in both the surface and deep waters that points to microbial oxidation dictating the carbon isotopic fractionation of methane in the fjord. Mass-balance budgeting reveals that river runoff accounts for 81% of the total methane input to the fjord (12.13×10^6 mol $year^{-1}$) and that microbial oxidation of methane (4.45×10^6 mol $year^{-1}$) is comparable to emission to the atmosphere (4.27×10^6 mol $year^{-1}$). This study demonstrates the important roles of river runoff and deep-water renewal in controlling the dynamics of [CH_4], $\delta^{13}C_{CH4}$, and methane emission to air in fjords receiving large terrestrial freshwater discharges and experiencing frequent deep-water renewals. The areal methane emission rates for deep fjords obtained by this and earlier studies are one to two orders of magnitude higher than the mean flux estimate for global coastal oceans, placing fjords and fjards as a potentially significant contributor to coastal methane emission.

***Keywords*:** Saguenay Fjord; dissolved methane; distribution; air-sea flux; microbial oxidation; isotope composition

2.3 INTRODUCTION

Methane (CH_4) is the second most important greenhouse gas in the atmosphere after carbon dioxide and delivers ~20% of the global greenhouse gas-induced radiative forcing (IPCC, 2013). Methane also reacts with the hydroxyl radical and thus regulates the oxidizing capacity of the atmosphere (Ehhalt, 1974; Lelieveld et al., 2004). The ocean has long been recognized as a natural source of methane to air (Swinnerton and Linnenbom,1967; Lamontagne et al., 1973) but the estimated diffusive fluxes from the global ocean vary by more than an order of magnitude from 0.4 to18 Tg CH_4 $year^{-1}$ (Bange et al, 1994; Bates et al., 1996; Rhee et al., 2009; Kirschke et al., 2013). More recent studies have narrowed the range to 2.2–6.3 Tg CH_4 $year^{-1}$ (Weber et al., 2019) and 4–10 Tg CH_4 $year^{-1}$ (Saunois et al., 2020), with the estimate for the near-shore environment (0.8–3.8 Tg CH_4 $year^{-1}$) being the

greatest but the most uncertain as compared to those for the outer shelf (0.3–1.0 Tg CH_4 $year^{-1}$), the continental slope (0.2–0.6 Tg CH_4 $year^{-1}$), and the open ocean (0.6–1.4 Tg CH_4 $year^{-1}$) (Weber et al., 2019).

The larger uncertainty in the coastal estimation stems principally from severe undersampling, patchy biogeochemical processes responsible for methane production and consumption, and complex physical forcings that regulate methane distribution in coastal waters. Such patchiness and complexity are particularly salient in land-ocean transitional zones, such as estuaries, bays, and fjords, leading to strong spatiotemporal variations in the concentration, distribution, and air-sea flux of methane. For example, unlike in the upper layer of open oceans where methane is primarily produced by in situ biogeochemical processes (Damm et al., 2010; Zhang and Xie, 2015; Lenhart et al., 2016; Repeta et al., 2016; Schmale et al., 2018; Klintzsch et al., 2019; Ye et al., 2020; Chapter 4), coastal waters may have additional methane inputs from underlying sediments and terrestrial runoff (de Angelis and Scranton, 1993; Reeburgh, 2007). The rates of these inputs depend not only on how fast methane is produced within the source materials but also on the hydrological and physical processes impacting the transport of methane from rivers (e.g. precipitation) and sediments (e.g. tidal and wave actions, bottom currents, and coastal upwelling); these processes are either absent or exert little influence on the dynamics of methane in the upper layer of open oceans.

Information on the concentration and distribution of methane in the water column not only is useful for assessing the emission flux to the atmosphere but also provides clues for identifying and/or quantifying the production and consumption processes regulating the methane distribution and emission. This is particularly true when combined with the analysis of the stable carbon isotope composition of methane ($\delta^{13}C_{CH4}$). Methane produced through microbial degradation of organic matter under anoxic conditions is depleted with ^{13}C ($\delta^{13}C_{CH4} < -50‰$) relative to methane produced through thermal cleavage of organic matter in deep sedimentary strata ($\delta^{13}C_{CH4} > -50‰$), while microbial oxidation of methane increases $\delta^{13}C_{CH4}$ (Whiticar, 1999).

Fjords and fjärds occupy ~43% of the total surface area of estuarine environments and 26% of the global exorheic coastline; they are mainly located at latitudes of north of 45°N (Scandinavia, Canada, Alaska) and south of 45°S (southern Chile) (Borges et al., 2011). Despite their extensive presence, these near-shore aquatic systems are particularly data-poor with respect to methane distributions and atmospheric emissions (Borges et al., 2011). Here we report the first measurement of dissolved methane concentration ($[CH_4]$) and $\delta^{13}C_{CH4}$ in the water column of the Saguenay Fjord in eastern Canada, with the objectives of assessing the emission fluxes of methane, identifying its origins, and elucidating the processes controlling its distribution in this coastal environment.

2.4 ENVIRONMENTAL SETTING

Located in the subarctic eastern Canada, the Saguenay Fjord is the second largest tributary to the St. Lawrence estuary (SLE), with a length of 110 km, an average width of 2.0 km, a 1.1-km wide mouth, and three sills dividing the fjord into an outer basin, a middle basin, and an inner basin, the last of which has an average depth of 280 m and extends over two-thirds of the length of the fjord (Fig. 2-1). The first (outermost) sill is 20 m deep and sits at the mouth near Tadoussac, which is followed by the second and third sills situated 18 and 32 km upstream of the first sill and having depths of 60 and 115 m, respectively (Belzile et al., 2016). The upper fjord bifurcates into the north and south arms. The Saguenay River, with an annual mean freshwater discharge rate of ~1200 $m^3\ s^{-1}$, provides ~90% of the total freshwater input to the fjord through the north arm, with the remaining from several local small rivers (Bélanger, 2003). Cold, dense seawater from the lower SLE that has been tidally upwelled at the head of the Laurentian Channel spills over the sills into the deep inner basin of the fjord (Seibert et al., 1979; Lavoie et al., 2000; Bélanger, 2003, Belzile et al., 2016, Galbraith et al., 2018). Consequently, the water column of the fjord is characterized by a thin (5–10 m) brackish (salinity ~10) surface layer and a saltier (salinity ~30) bottom layer that are separated by a sharp halocline (Drainville, 1968; Therriault et al., 1984). The fjord possesses a typical estuarine circulation in the near surface but comprises multiple inflowing and outflowing layers below the main pycnocline (Stacey and Gratton, 2001; Bourgault et

al., 2012a). The deep fjord is well oxygenated due to multiple deep-water renewal events annually (Bélanger, 2003; Belzile et al., 2016, Galbraith et al., 2018).

The surface water in the Saguenay Fjord is organic-rich and highly colored attributable to the input of soil- and vascular plant-derived dissolved organic matter from the Saguenay River; in contrast, the deep water is organic-poor and far less colored (Tremblay and Gagné, 2009; Xie et al., 2012). Light penetration into the water column is thus limited, resulting in low primary productivity (Côté and Lacroix, 1979; Schafer et al., 1990). Consequently, sediments in the Saguenay Fjord are primarily terrigenous and sedimentation rates decrease with distance downstream (St-Onge and Hillaire-Marcel, 2001; Tremblay and Gagné, 2007). Local pulp and paper mill discharges before the late 1980s led to a substantial increase in sedimentary organic carbon content, particularly in the fjord's head region (Louchouarn et al., 1997; St-Onge and Hillaire-Marcel, 2001). Moreover, the frequent occurrences of episodic meteorological and geologic events, such as landslides, earthquakes, and flash floods, in the Saguenay region during the past ~350 years formed multiple rapidly deposited layers that favor organic carbon preservation in the fjord's sediments (St-Onge and Hillaire-Marcel, 2001).

2.5 METHODS

2.5.1 Field sampling

Field sampling was conducted on 19-20 October 2016 aboard the *CCGS Hudson* and on 18 June, 3–4 October and 3–4 November 2017 aboard the *R/V Coriolis II* (Fig. 2-1); for brevity, these four expeditions will hereafter be referred to as the Oct-16, Jun-17, Oct-17, Nov-17 cruises, respectively. Bulk water was taken from the surface (1–2.5 m) or different depths using 12-L Niskin bottles attached to a standard conductivity-temperature-depth (CTD) rosette. During the Oct-16 cruise, the Niskin bottles were subsampled into 50-mL gas-tight glass syringes via a clean silicone tube. The syringes were flushed with the sample water three times before the final filling, with caution taken to avoid trapping air bubbles. The

syringes were closed with a three-way nylon valve and analyzed for [CH_4] aboard the ship immediately after sample collection. During the remaining three cruises, the bulk water in the Niskin bottles was subsampled into 200-mL glass serum vials, pre-cleaned with acid-soaking and combustion at 450°C, via a clean silicone tube, following the water transfer procedure for collecting dissolved oxygen samples (Grasshoff, 2009). Each serum vial was added with 300 µL of supersaturated mercuric chloride before being closed with a PTFE-lined aluminum crimp seal. In addition to collecting [CH_4] samples, the Nov-17 cruise also acquired samples for $\delta^{13}C_{CH4}$ analysis using the same serum vial method. All [CH_4] and $\delta^{13}C_{CH4}$ samples were collected in duplicate. The sample-filled serum vials were stored in the dark at ~4°C and transported to land-based laboratories for [CH_4] measurement in Rimouski, Canada and for $\delta^{13}C_{CH4}$ analysis at the Alfred Wegner Institute in Bremerhaven, Germany.

Because of technique and resource limitations, the Jun-17 cruise only covered the lower section of the fjord (stations S03, S05, S07, and S09), merely one [CH_4] vertical profile was collected in October 2017 (station F21), and only three stations were sampled for methane with reduced depth resolutions in November 2017 (Fig. 2-1). The three stations visited during the Nov-17 cruise were located in the upper (station S13), middle (station S09), and lower (sation S03) fjord, respectively.

2.5.2 Methane measurements

Dissolved [CH_4] was determined using a static headspace method reported previously (Xie et al., 2002; Zhang and Xie, 2015). Briefly, for the syringe samples analyzed aboard the ship, 5 mL of methane-free nitrogen were introduced into the syringe to obtain a 1:8 gas:water ratio. The syringe was vigorously shaken for 4 min to equilibrate the gas and water phases. For the serum vial samples analyzed on the land, the samples were drawn into a 50-mL glass syringe via a 1/8-inch O.D. PTFE tube prior to the headspace preparation described above. During the sample transfer, the tip of the PTFE tube was inserted close to the bottom of the serum vials. The syringe was rinsed with the sample water before sample drawing.

Each serum vial permitted filling two syringes; their difference fell within the uncertainty of the analytical method (see below), confirming negligible water-air exchange of methane during the sample transfer.

The equilibrated headspace gas in the syringe was injected into a Peak Performer 1 FID gas analyzer (Peak Laboratories, USA) for methane quantification. The [CH_4] in the headspace was converted to the concentration in the original water sample using the solubility data of Wiesenburg and Guinasso (1979). The analyzer was calibrated with a methane standard of 4.94 (Oct-16 cruise) and 5.08 (Jun-17, Oct-17, and Nov-17 cruises) parts per million by volume (ppmv) (Air Liquide) traceable to the National Institute of Standards and Technology. In keeping with the 100% relative humidity in the headspace gas samples, the dry methane standard was saturated with water vapor before injection. A single-point calibration was adopted, since pre-study tests confirmed that the instrument consistently responds linearly up to 10.5 ppmv (~80 nmol L^{-1}) with essentially a zero intercept. This linear response range conformed to that specified by the manufacturer of the analyzer. Larger gas:water ratios in the syringe were used for samples with methane concentrations ([CH_4]s) beyond the analyzer's linear response range. Under the factory-optimized conditions for [CH_4] measurement, the analyzer gave a lower detection limit of 0.045 nmol L^{-1} and a precision of ±4% (at ~5 nmol L^{-1}) (Zhang and Xie, 2015). The mean relative deviation for all duplicate measurements (i.e. field and lab analyses combined) was 2.6%. [CH_4]s for each pair were averaged.

The mixing ratios of methane in the marine boundary layer over the SLE were determined in October 2016 and June 2017 and assumed to be applicable to the Saguenay Fjord. Air samples were drawn in duplicate at the bow, facing the wind, into 10-mL all-glass syringes and analyzed within minutes by direct injection into the methane analyzer. Prior to sampling, the internal wall of the syringes was water-wetted to ensure that the air samples had the same relative humidity (100%) as that in the standard gas (see above).

The $\delta^{13}C_{CH4}$ values were determined using a Delta XP plus Finnigan mass spectrometer according to the method described by Damm et al. (2015b). The samples were pre-

concentrated through purging and trapping with a PreCon Trace Gas Pre-Concentrator (Finnigan). A CO_2 reference gas (Air Liquide) is inserted via the reference gas port in each acquisition to correct for effects that appear in the source of the mass spectrometer. The isotope ratios of all peaks are calculated against this CO_2 working standard. The reproducibility derived from duplicates was 1–1.5%. The isotopic ratios are given in conventional delta notation relative to the Pee Dee Belemnite (PDB) standard.

2.5.3 Ancillary measurements

Water depth, temperature, and salinity were recorded with a SeaBird SBE 9plus CTD and dissolved oxygen with a Sea-Bird SBE 43 probe calibrated by the Winkler method (Grasshoff, 2009). Apparent oxygen utilization (AOU) was calculated as the difference between the in situ oxygen solubility (Garcia et al., 1992) and the measured oxygen concentration. Percent oxygen saturation (O_2%) was calculated as the ratio of the measured oxygen concentration to the in situ oxygen solubility multiplied by 100. Chlorophyll *a* concentration was determined as described in Mitchell et al. (2002).

2.5.4 Calculations of saturation ratio and air-sea flux

The saturation ratio (*SR*) of [CH_4] is defined as:

$$SR = {[\mathrm{CH_4}]_{\mathrm{mea}}}\Big/{[\mathrm{CH_4}]_{\mathrm{eq}}} \tag{2-1}$$

where $[CH_4]_{mea}$ (nmol L^{-1}) denotes the measured [CH_4] and $[CH_4]_{eq}$ (nmol L^{-1}) represents the [CH_4] equilibrated with the atmosphere. $[CH_4]_{eq}$ is calculated using the solubility data of Wiesenburg and Guinasso (1979) and an atmospheric methane mixing ratio of 1.92 ± 0.13 ppmv (n = 72) measured in October 2016 and June 2017 over the SLE. The air-sea flux density of methane (*j*, µmol m^{-2} d^{-1}) is calculated according to Liss and Slater (1974):

$$j = k\left([\mathrm{CH_4}]_{\mathrm{mea}} - [\mathrm{CH_4}]_{\mathrm{eq}}\right) \tag{2-2}$$

where k (cm h^{-1}) signifies the gas transfer velocity calculated using the formula of Raymond and Cole (2001):

$$k = 1.91e^{0.35U}\left(Sc/_{600}\right)^{-0.5} \quad (2\text{-}3)$$

where U stands for wind speed (m s^{-1}) at 10 m height and Sc for the Schmidt number of methane (Wanninkhof, 2014). Wind speed data, available online at the St. Lawrence Global Observatory website (https://ogsl.ca/en), were provided by the weather stations at Pointe de l'lslet, Pointe Claveau, La Baie, and Jonquière along the shore of the Saguenay Fjord (Fig. 2-1). Each weather station fed wind speeds to its closest water sampling stations. Hourly wind speeds were averaged over the sampling day (24 h) and sampling month to assess the air-sea fluxes on the corresponding time scales.

Raymond and Cole (2001) reported three formulae for calculating k in estuarine environments based on data from floating dome studies, non-dome (i.e. tracer) studies, and a combination of the two, respectively. The dome data gives substantially higher k values than does the non-dome data, particularly above intermediate wind speeds. In this study, we chose the formula based on the composite data of the dome and non-dome studies.

2.6 RESULTS AND DISCUSSION

2.6.1 Surface-water concentrations and air-sea fluxes

Given the relatively small sample populations with mostly non-normal distributions, medians, in addition to means, are presented and Wilcoxon Rank Sum Test (Matlab version R2013b), rather than *t*-Test, was performed to determine the statistical significance of the medians ($\alpha = 0.05$). Besides, because of limited sampling coverage during the June- and Nov-17 cruises (Section 2.5.1), data from these two cruises are not compared with those from the Oct-16 and Oct-17 cruises.

Ranges, means, and medians of surface-water [CH_4], methane saturation ratio, and methane air-sea flux, alongside other related variables, are summarized in Table 2-1. The

changes of these variables with distance to the outermost sill are shown in Fig. 2-2 and Supplementary Fig. 2-S1. Surface-water [CH_4] increased from the mouth toward the head of the fjord, with the increase faster in the upper section of the fjord (Fig. 2-2a). [CH_4] near the head of the fjord showed large variability, highest during the Nov-17 cruise and lowest during the Oct-17 cruise. The change in [CH_4] during the Jun-17 cruise was much smaller due to the limited sampling area. The Surface water was highly supersaturated in [CH_4] relative to the atmosphere during all cruises (Fig. 2-2b, Table 2-1). The along-fjord distributions of the saturation ratio essentially mimicked those of [CH_4], indicating that concentration prevailed over solubility in controlling the saturation ratio, despite large variations in surface-water temperature and salinity (Table 2-1, Supplementary Figs. 2-S1a, b) which determine the solubility. The Oct-16 and Oct-17 cruises were not significantly different in terms of the median [CH_4] (p = 1.00) and median saturation ratio (p = 0.82).

The supersaturation led to an egress of methane to the atmosphere (Fig. 2-2c, Table 2-1). The daily wind speed-based mean and median flux density for the Oct-16 cruise are ~4 and ~3 times greater than those for the Oct-17 cruise, contrasting with the insignificant differences in the median [CH_4] and saturation ratio between the two surveys (Table 2-1). This can be ascribed to the higher daily wind speeds during the Oct-16 cruise (Table 2-1, Supplementary Fig. 2-S1c). Using monthly wind speeds, which were comparable between the two cruises, essentially eliminated the difference in the flux density (Table 2-1).

The methane concentrations in the Saguenay Fjord surface water are comparable to those in the deep, strongly fluvial-impacted Reloncaví Fjord in Chile ([CH_4]: 7.6–151.4 nmol L^{-1}) (Farías et al., 2017) but higher than those in many polar fjords with lower terrestrial freshwater inputs, such as the Hornsundfjord, the van Mijenfjord, and the Storfjorden in the Svalbard Archipelago of the Arctic ([CH_4]: 10.0–35 nmol L^{-1}) (Damm et al., 2005; Damm et al., 2007; Mau et al., 2013) and the Cumberland Bay fjord system off the sub-Antarctic island of South Georgia ([CH_4]: ~10 nmol L^{-1}) (Römer et al., 2014). Our values are, however, within the lower bounds of those reported for shallow estuarine environments worldwide ([CH_4]: 2–3600 nmol L^{-1}) (Middelburg et al., 2002; Borges and Abril, 2011; Upstill-Goddard and

Barnes, 2016; Borges et al., 2018; Ye et al., 2019). In shallow coastal systems, surface methane is supplied not only by fluvial input but also by upward transport from anoxic sediments where methane is produced anaerobically (Borges and Abril, 2011; Borges et al., 2016). In deep fjords, sedimentary input of methane is either unimportant, e.g. in the Saguenay (Sections 2.6.3 and 2.6.6) and Reloncaví Fjords (Farías et al., 2017), or stronger vertical stratification and greater water depths hinder upward diffusion of methane from the seafloor into surface waters, as in the case of certain polar fjords (Damm et al., 2005; Römer et al., 2014).

The multi-cruises methane flux densities estimated for the Saguenay Fjord, 16.4–256.9 μmol m^{-2} d^{-1} (mean: 53.4 μmol m^{-2} d^{-1}) based on monthly wind speeds, are similar to those reported for the Reloncaví Fjord in Chile (23.9–136.0 μmol m^{-2} d^{-1}) (Farías et al., 2017) and the Storfjorden in the Svalbard Archipelago (26–104 μmol m^{-2} d^{-1}) (Damm et al., 2007), higher than those for the Saanich Inlet in British Columbia, Canada (1.2–57.0 μmol m^{-2} d^{-1}) (Bullister et al., 1982; Lilley et al., 1982; Ward et al., 1989; Capelle et al., 2019), but much lower than those for the Mariager Fjord in Denmark (240–4500 μmol m^{-2} d^{-1}) (Fenchel et al., 1995). The Saguenay, Reloncaví, and Storfjorden are all deep (maximum depths >200 m) and stratified fjords having oxic bottom waters. The Saanich Inlet is a deep fjord with seasonally anoxic bottom water wherein [CH_4]s can reach up to low-millimolar levels; rapid microbial consumption and strong water column stratification, however, inhibit upward transport of methane to the surface and further to the atmosphere (Ward et al., 1989; Capelle et al., 2019). The Mariager Fjord is a stratified water body with anoxic bottom water highly prolific in methane (>30 mmol L^{-1}) (Fenchel et al., 1995). The shallow depths of this fjord (<30 m), nevertheless, may allow significant amounts of methane to be diffused from the bottom water to the surface ([CH_4]: 500-900 nmoL L^{-1}) and thus be partly responsible for the more elevated methane air-sea fluxes observed in this system.

Fjords and fjards, with a worldwide surface area of 0.456×10^6 km^2, are the most extensive estuarine water bodies and take up 43% of the total surface area of the estuarine environments (1.067×10^6 km^2) (Borges et al., 2011). Based on the flux estimates for the

Mariager Fjord and the shallow, anoxic Aby-Tendo Lagoons in Ivory Coast (methane flux density: 800–1500 μmol m^{-2} d^{-1}), Borges et al. (2011) obtained a methane emission rate of 3.96 Tg CH_4 $year^{-1}$ for global fjords and fjards, accounting for 60% of the emission from all estuarine environments combined (6.60 Tg CH_4 $year^{-1}$) and translating to a global mean flux density of 1490 μmol m^{-2} d^{-1}. This value is one to three orders of magnitude higher than those for the deep fjords aforementioned and is likely overestimated. Indeed, a more recent assessment of methane emission from global estuarine environments arrives at <3–3.5 Tg CH_4 $year^{-1}$, equivalent to <480–560 μmol m^{-2} d^{-1} (Saunois et al., 2020), which are in the same order of magnitude as the upper bounds for the Saguenay and Reloncaví Fjords. The flux estimates for the deep fjords are, however, one to two orders of magnitude higher than the mean flux estimate for global coastal oceans with a bottom depth of <200 m (5.3 μmol m^{-2} d^{-1}) (Weber et al., 2019), suggesting that fjords and fjards are a potentially significant oceanic source of methane to the atmosphere. Given the extensive distributions of fjords and fjards at high latitudes in both hemispheres, the methane emission data currently available are very meager. More surveys are needed to expand the flux dataset and improve the global extrapolation.

2.6.2 Estuarine mixing behavior

The surface-water [CH_4] *vs.* salinity plots for the Oct-16 and Oct-17 cruises show bi-segmented linear increases in [CH_4] with decreasing salinity (Fig. 2-3). The slopes of these linear relations broke at salinity ~19 in 2016 and ~10 in 2017 and were correspondingly ~20 times and ~26 times steeper in the less saline water than in the saltier water. The limited data from the Nov-17 cruise also exhibited a similar pattern, with a slope break at salinity ~7. The June 2017 data obtained from the lower section of the fjord generally followed the trend of October 2017. Notably, the data collected from station F21 in the south arm of the fjord during October 2017 fits into the trend established by the rest of the data (Fig. 2-3), suggesting that the surface-water [CH_4] in the south arm was mainly controlled by freshwater discharge from the Saguenay River.

Although the slopes broke at varying salinities among different cruises, $[CH_4]$s converged at higher salinities (Fig. 2-3), suggesting little temporal variability in the marine endmember ($[CH_4]_{end\text{-}m}$). In contrast, $[CH_4]$s diverged toward the freshwater zone, indicating variable river endmembers ($[CH_4]_{end\text{-}r}$). Extrapolation of the regression lines to zero salinity gives $[CH_4]_{end\text{-}r}$ of 193.4 nmol L^{-1}, 142.5 nmol L^{-1}, and 263.3 nmol L^{-1} for the Oct-16, Oct-17, and Nov-17 cruises, respectively. $[CH_4]_{end\text{-}r}$ was found to increase linearly with the freshwater discharge rate averaged over the sampling day at station S13 (Supplementary Fig. 2-S2). As the time gaps between the sampling campaigns ranged from one month (October *vs.* November 2017) to over one year (October 2016 *vs.* November 2017), this linear relationship appears applicable to both short and intermediate time scales. The intercept of the regression line (i.e. 10.1 nmol L^{-1} at zero freshwater discharge) represents the amount of methane added, likely from sediments, to the river runoff during its transit from where the discharge rate was measured to the limit of saltwater intrusion in the Saguenay River. This amount, nonetheless, is only 3–7% of the river endmembers obtained above, demonstrating that $[CH_4]$ in the river source water is the main control on $[CH_4]_{end\text{-}r}$.

The estuarine $[CH_4]$ mixing behavior observed in the Saguenay Fjord is similar to those in the Elbe and Thames estuaries (Middelburg et al., 2002). Rapid loss of methane in low salinity regions has been spotted in many estuaries worldwide and attributed to microbial oxidation, outgassing, and dilution with low-$[CH_4]$ seawater (Middelburg et al., 2002; Zhang et al., 2008; Borges et al., 2011; Ye et al., 2019). In our case, the bi-segment linear pattern also suggests the possibility of a second freshwater methane source with an endmember lower than the effective river endmember defined by the y-intercept of the flatter regression line in Fig. 2-3 ($[CH_4]^*_{end-r}$). To reach the value of $[CH_4]^*_{end-r}$ (25.8 nmol L^{-1}) requires the freshwater discharge rate of the second methane source to be $>\left(\frac{[CH_4]_{end-r}}{[CH_4]^*_{end-r}} - 1\right)$ times the discharge rate of the Saguenay River. Taking $[CH_4]_{end\text{-}r}$ for the Oct-17 cruise (142.5 nmol L^{-1}) as the lower limit gives a factor of 4.5, which is implausible, since the water flow from all secondary tributaries combined is only ~10% of the total freshwater discharged into the Saguenay Fjord (Bélanger, 2003).

Another factor influencing the shape of estuarine mixing curves of dissolved constituents is the period of source variation in the river flow relative to the flushing time of the estuary. When the flushing time and the source variation period are similar, a bent curve can result even for a conservative constituent (Bowers and Brett, 2008). The flushing time of surface water in the Saguenay Fjord is ~1.5 d (Delaigue et al., 2020). Prior to and during the Oct-17 cruise, the river flow rate (q_r) was rather stable over a period of 34 d (1471 ± 29 m^3 s^{-1}; Supplementary Fig. 2-S3b). The stability of the river flow also implies a stable $[CH_4]_{end-r}$ over the same period of time based on the linear relationship between the two variables (Supplementary Fig. 2-S2). The timescale of the $[CH_4]_{end-r}$ variation (34 d) was thus ~23 times longer than the flushing time, thereby eliminating the possibility of a significant effect of temporal $[CH_4]_{end-r}$ variations on the shape of the mixing curve.

During the Oct-16 and Nov-17 cruises, the river flow experienced 36% and 82% increases, respectively, over the 30-d mean flow rates before water sampling (Oct-16: 1593 m^3 s^{-1}; Nov-17: 1724 m^3 s^{-1}, Supplementary Figs. 2-S3a,c). As the durations of the increases in the river flow (2 d) were comparable to the flushing time (1.5 d), the system might not have reached a new steady state during sampling, particularly in the lower section of the fjord. Two lines of evidence, however, suggest that a non-steady state, if true, could not be the principal contributor to the bi-segment mixing behavior of $[CH_4]$ observed. First, the October 2017 case demonstrates that the slope break exists even though the river flow (and hence the source of methane) is constant over a period much longer than the flushing time. Second, if the slope break during the Oct-16 and Nov-17 cruises were mainly caused by the recent increases in the river flow, $[CH_4]^*_{end-r}$ (25.8 nmol L^{-1}, Fig. 2-3) would essentially represent the true endmember of the river water present prior to the flow increases. Based on the relationship between $[CH_4]_{end-r}$ and q_r (i.e. $[CH_4]_{end-r} = 0.0885 \times q_r + 10.09$, Supplementary Fig. 2-S2), this endmember corresponds to a freshwater discharge rate of 178 m^3 s^{-1}. This value is unrealistically low and only 10–11% of the 30-d mean river flow rates preceding the flow increases. Notably, the stations during the Oct-16 cruise were not sampled sequentially (e.g. stations S09 and S10 were sampled after stations S11-13 and stations S02 and S05 were visited last) but the data show consistent trends within the respective linear

segments (Fig. 2-3). The system thus appeared to be stable with respect to the distribution of surface-water [CH_4]. It could be that the increased river discharge substantially reduced the flushing time, thereby decreasing the time required to reach a new steady state. Microbial consumption and outgassing, rather than multiple endmembers and/or $[CH_4]_{end\text{-}r}$ variations, should thus be primarily responsible for the [CH_4] mixing behavior observed in the surface water.

2.6.3 Vertical distributions

The density structures were highly stratified within the top 25 m of the water column on all [CH_4] profiling occasions except for the outer basin (station S03) during the Oct-16 cruise which showed little stratification (Fig. 2-4). For the stratified structures, the surface mixed layer depths (i.e. the depth from the surface to the onset of the main pycnocline) were mostly ≤7 m but reached ~18 m at station S07 located over the innermost sill (Fig. 2-1b) during the Oct-16 cruise. The water column was always oxygenated, with percent saturations of >70% (Fig. 2-4). Chlorophyll *a* (chl *a*) profiles collected during the Oct-16 and Jun-17 cruises often exhibited different vertical distributions among different stations (Figs. 2-4a,b). Surface-water chl *a* generally increased up-fjord, with the concentration in the top 25 m averaging 0.25 mg m^{-3} (range: 0.06-0.87 mg m^{-3}) during the Oct-16 cruise and 0.84 mg m^{-3} (range: 0.06-2.47 mg m^{-3}) during the Jun-17 cruise. Primary productivity in the Saguenay Fjord has long been recognized to be low due to light limitation caused by the highly colored surface water (Côté and Lacroix, 1978; Schafer et al., 1990).

[CH_4]s at station S03 in the outer basin showed little vertical variations in the entire water column during the Oct-16 and Nov-17 cruises, which was in line with the weak density stratification at this locality in October 2016 (Fig. 2-4a) but inconsistent with the well stratified density structure in November 2017 (Fig. 2-4c). It could be that the surface stratification in November 2017 had been established only shortly before water sampling so that microbial methane consumption in deep water (>25 m) was undetectable. To a lesser extent, this also might have happened to station S07 in October 2016 at which [CH_4] in the

surface mixed layer (mean: 20.8 ± 0.2 nmol L^{-1}) was only slightly higher than below the pycnocline (mean: 16.4 ± 1.1 nmol L^{-1}), despite the strong density stratification (Fig. 2-4a). This speculation is supported by the fact that intense vertical mixing in the outer and middle basins occurs frequently due to sill-induced turbulence (Geyer and Cannon, 1982; Stacey and Gratton, 2001). Notably, the deep [CH_4]s at station S07 were almost identical to those at station S03, which can alternatively be explained by a recent intrusion of deep water from the outer basin into the middle basin, as demonstrated by their similar temperature–salinity curves (Figs. 2-5a,a´). In June 2017, [CH_4] profiles in the outer and middle basins (stations S03, S05, and S07) were all characterized by a rapid downward decrease within the top 15 m followed by relatively stable concentrations at greater depths, conforming to the density structures (Fig. 2-4b). Remarkably, all three profiles converged to similar [CH_4]s below 15 m (mean ± SD: 12.3 ± 0.8 nmol L^{-1}), despite the three stations having quite different temperature–salinity signatures (Figs. 2-5b,b´). This feature could result from a combination of 1) the rather constant $[CH_4]_{end\text{-}m}$ in the SLE seawater (Section 2.6.2) intruding into the outer basin, 2) the relatively stable [CH_4] in the lower-reach surface water (Fig. 2-2a) modifying the physical properties of the SLE water that spread into the outer and middle basins, and 3) the timescales of vertical and horizontal mixing within the outer and middle basins being shorter than that of microbial methane consumption due at least partly to the sill-induced turbulence.

Except for station S13, [CH_4] profiles in the inner basin, regardless of the sampling seasons and years, generally resembled those collected from the outer and middle basins in June 2017 but had subtler deep features on certain occasions (Figs. 2-4a–c). For example, [CH_4] at station S11 in October 2016 increased to 4.0-5.2 nmol L^{-1} below 100 m after reaching a minimum (1.8 nmol L^{-1}) at ~50 m. This phenomenon could be linked to different water masses present at shallower and deeper depths, as discussed in more detail below. Deep [CH_4] features were also recorded at station S09 in June 2017, displaying a maximum at 102 m (11.7 nmol L^{-1}), a minimum at ~150 m (2.1 nmol L^{-1}) and an enhancement toward the bottom (9.5 nmol L^{-1}). The minimum at 150 m was located within a cold water mass (lowest temperature: 1.98°C) (Figs. 2-5b,b´) supposedly formed from the previous winter's shallow

water renewal and subsequently warmed by mixing with surrounding waters (Belzile et al., 2016). In contrast, the bottom water at station S09 was warmer and saltier, typical of the Saguenay deep water formed from last winter's deep basin renewal (Belzile et al., 2016), suggesting that the relatively elevated near-bottom [CH_4] at station S09 was more likely associated with a methane-richer water mass than with a sedimentary input. The absence of near-bottom [CH_4] increases in October 2016 and November 2017 (Figs. 2-4a,c) further reinforces this speculation. A significant episodic production of methane in the sediments seems unlikely, given the relative temperature stability in the bottom water (Belzile et al., 2016).

The larger spatial sampling coverage in October 2016 permits a better examination of the relationship between [CH_4] and water mass composition. According to Galbraith et al. (2018), a 2016 summer water renewal event generated a warm tongue at mid-depths (50–150 m; core: 120–150 m) that had reached the fjord's head by late August. At the time of methane sampling in the late mid-October, a hint of this tongue was still discernible despite more extensive mixing with the colder resident water (Fig. 2-6a). This water renewal created an up-fjord decrease in temperature in the deep layer of the inner basin (Galbraith et al., 2018; Fig. 2-6a), with the colder water being older than the intruding warmer water. In the absence of additional sources, [CH_4]s in the colder water should be lower than in the warmer water due to longer microbial consumption in the former. This prediction matches the parallel up-fjord decline in [CH_4], excluding the head region (Fig. 2-6b). Indeed, the deep [CH_4] decreased linearly with decreasing temperature (Fig. 2-6c). It is interesting to note that, at similarly low temperatures (<3.5 °C), shallower water (25–100 m) had lower [CH_4]s (range: 1.8–6.3 nmol L^{-1}; mean: 4.2 nmol L^{-1}) than did deeper water (>150 m, range: 4.0–8.0 nmol L^{-1}; mean: 5.7 nmol L^{-1}) (Fig. 2-6c). The lowest [CH_4] in the shallower water (1.8 nmol L^{-1}, ~50 m at station S11) was located within a pocket of cold water (<2.5 °C) centered at ~70 m near the head of the fjord (Fig. 2-6a), while the relatively higher [CH_4]s in the shallower water (also at station S11) were in the vicinity of the cold pocket. The presence of this cold pocket is a common summertime phenomenon caused by the traping of cold water formed from the shallow renewal event during the past mid- or late winter; the deeper water,

however, carries the trait of the SLE water that renewed the inner basin during the autumn or winter of the preceding year (Belzile et al., 2016). The higher [CH_4]s found in the deeper water could be attributed to the fact that, during the deep-water renewal, the intruding SLE water mixes with the remnant of previous summer's intermediate water containing methane-rich surface water (Bourgault et al., 2012a; Belzile et al., 2016).

The [CH_4] profiles at station S13 near the fjord's head were distinct by having much higher [CH_4]s at the bottom than at the surface: 388.7 *vs.* 143.5 nmol L^{-1} in October 2016 (Fig. 2-4a) and 459.2 *vs.* 184.2 nmol L^{-1} in November 2017 (Fig. 2-4c). There was, however, a striking difference between the two cruises: [CH_4] in October 2016 increased monotonically with increasing depth but in November 2017 exhibited a marked minimum at 10 m (18.2 nmol L^{-1}) which was 9 times lower than the [CH_4] at the same depth in October 2016 (164.8 nmol L^{-1}). This large difference is unexpected per the density structures on the two occasions. The 10 m depth was located within the center of the pycnocline in October 2016 but at the base of the pycnocline in November 2017, favoring upward diffusion of methane toward the 10 m depth in November. One possible reason was a much higher local microbial consumption rate at this depth in November. Notably, the temperature-salinity curves of stations S03 and S13 intersect at the temperature of ~3.1°C and salinity of ~28.32 (Figs. 2-5c,c´), corresponding to the depths of ~19 m at station S03 and ~12 m at station S13, the latter being close to the [CH_4] sampling depth of 10 m. The vertical distribution of [CH_4] at station S03 was rather constant, averaging 19.5 ± 0.4 nmol L^{-1} (Fig. 2-4c) and being only slightly higher than the 10-m [CH_4] of 18.2 nmol L^{-1} at station S13. Hence, the pronounced [CH_4] minimum at station S13 could be alternatively explained by a recent strong shallow subsurface water renewal event (Belzile et al., 2016) that had greatly reduced the subsurface [CH_4] near the head of the fjord.

The [CH_4] profile at station S13 in October 2016 raised a question of whether upward diffusion could be a significant source of methane to the surface water. To assess this possibility, we estimated the diffusive flux from the 10 m depth to the shallowest sampling depth (2.2 m) by multiplying the eddy diffusivity by the [CH_4] gradient within the top 10 m

(2.69 nmol L^{-1} m^{-1} or 2690 nmol m^{-4}). The eddy diffusivity in the top 30 m of the Saguenay Fjord has been determined to be ~10^{-5} m^2 s^{-1} (Belzile et al., 2016), yielding an upward diffusive flux of 2.32 μmol m^{-2} d^{-1}. This value is only 2.4% of the water-to-air flux density of methane at station S13 in October 2016 (Fig. 2-2c), making the diffusion negligible compared with the river input.

The vertical distribution patterns at station S13 imply a significant source of methane in the bottom water or from the underlying sediment. As the entire water column was oxygenated, anaerobic methanogenesis, the dominant methane production pathway in natural environments (Reeburgh, 2007), was not expected in the bottom water. Sedimentary input was thus likely responsible for the highly elevated bottom [CH_4]s at station S13. This argument is supported by the high organic carbon content (>5%) and anoxic conditions in the sediments within the fjord's head region (Smith and Walton, 1980; Lefrançois, 1998; Deflandre et al., 2002). A large component of this organic matter originates from unregulated waste discharges to the head region of the fjord by the local pulp and paper industries before the late 1980s (Louchouarn et al., 1997; Tremblay et al., 2007). A catastrophic flash flood in July 1996 buried the organic-rich sediments with an organic-poor postglacial clay layer of ~7 cm thick in the vicinity of station S13 (Tremblay et al., 2007), which likely slows down but prolongs the organic matter degradation in the older sediments (St-Onge and Hillaire-Marcel, 2001). The organic carbon content in the new surface sediments in the upper fjord (~2%) is similar to or slightly lower than those in the main inner basin (2–3%) (St-Onge and Hillaire-Marcel, 2001; Tremblay et al., 2007) where there is no evidence of significant sedimentary methane release based on the vertical profiles at stations S09 and S11 (Fig. 2-4a). Hence, the high [CH_4] detected in the bottom water of station S13 more likely emitted from the buried organic-rich layer instead of the new surface sediments. It should be noted that the influence of the sedimentary source was rather localized, given the very low deep [CH_4]s at the adjacent station S11 (Figs. 2-4a, 2-6b). This limited influence could be attributed to fast dilution and microbial consumption. The only profile collected from the south arm of the fjord, characterized by rapidly decreasing [CH_4] within the top 30 m and

relatively stable concentrations at deeper depth (Supplementary Fig. 2-S4), also suggests that sediments were not a major source of methane to the water column in that area.

Excluding station S13, [CH_4] in the deep layer was negatively and linearly related to the apparent oxygen utilization (AOU) (Fig. 2-7). These negative correlations demonstrate that aerobic oxidation by methanotrophs was mainly responsible for methane consumption and that release of methane into the water column from sediments, wherein methanogenesis is favored by low-oxygen conditions, was insignificant across the main body of the fjord. The later argument is in line with the absence of elevated [CH_4]s in the bottom water except for the head region (station S13). The slopes of the regression lines for October 2016 and November 2017 are essentially identical but their absolute values are about four times larger than that for June 2017 (Fig. 2-7). The flatter slope in spring suggests that the ratio of oxygen consumption by methane oxidation to that by organic matter oxidation was far lower in spring, which is consistent with the higher chl *a* concentration in spring than in autumn as described earlier. The negative [CH_4]–AOU relations observed in the Saguenay Fjord contrast with those positive relations found in the central Bohai Sea and the East China Sea off the Yangtze River estuary, both of which undergo seasonal oxygen deficiency in the bottom water (Ye et al., 2016; Zhang et al., 2020). Methanogenesis in sediments is considered as the main methane source to the overlying water column in these two areas. As sedimentary methanogenesis is favored by low pelagic oxygen concentrations, increasing [CH_4] in the bottom water with decreasing oxygen concentration (i.e. increasing AOU) is expected (Ye et al., 2016; Zhang et al., 2020). The negative [CH_4]–AOU relations in the Saguenay Fjord thus further corroborate the earlier supposition that sedimentary methane input in the head region (station S13) is a local phenomenon and its influence does not extend to the main body of the inner basin.

2.6.4 Isotope composition

$\delta^{13}C_{CH4}$ in surface water increased from −45.0‰ near the head of the fjord (station S13) to −30.3‰ in the mid-inner basin (station S09) to −28.5‰ in the outer basin (station

S03) (Fig. 2-4d). This downstream enrichment of $^{13}C_{CH4}$ could be attributed to cumulative microbial methane oxidation and outgassing during the down-fjord transit of the surface water; both microbial oxidation and outgassing preferentially remove the isotopically lighter carbon from the resident water (Whiticar and Faber, 1986; Happell et al., 1995). At depths >100 m, which are well below the main pycnoclines, $\delta^{13}C_{CH4}$ at station S09 (−30.7 ± 0.6‰) was higher than that at station S03 (-31.4 ± 0.8‰) (Fig. 2-4c), consistent with the deep water at station S09 being older and thus subjected to longer microbial methane oxidation than at station S03. The difference was, however, marginal (2.1%), which at least can be partly explained by the rather small decrease (21.3%) in deep-water [CH_4] from station S03 (19.2 ± 0.21 nmol L^{-1}) to station S09 (15.1 ± 0.34 nmol L^{-1}) even without accounting for the dilution effect due to water mixing. Note that the difference in deep-water [CH_4] between stations S09 and S03 in November 2017 was far smaller than the 51.4% drop (16.3→7.9 nmol L^{-1}) in October 2016 (Fig. 2-4a).

The vertical distribution of $\delta^{13}C_{CH4}$ at station S13 closely mirrored that of [CH_4], with the lowest $\delta^{13}C_{CH4}$ (−57.7‰) observed at the bottom where [CH_4] reached 459.2 nmol L^{-1} and the highest $\delta^{13}C_{CH4}$ found at 10 m (−30.7‰) having a [CH_4] of only 18.2 nmol L^{-1}. The $\delta^{13}C_{CH4}$ value of −57.7‰ confirms that methane in the bottom water of station S13 originated from microbial degradation of organic matter, which gives $\delta^{13}C_{CH4}$ values of <−50‰ (Whiticar, 1999). Based on the discussion in Section 2.6.3, this microbial methane production took place in the underlying sediments instead of the water column itself. Methane in the surface water was transported down from Lac Saint-Jean, ~71 km upstream of station S13. As in most freshwater systems with organic-rich sediments, methane in Lac Saint-Jean is most likely biogenic as well. The higher $\delta^{13}C_{CH4}$ in the surface water at station S13 (−45.0‰) than expected from a biogenic origin could be due to microbial oxidation and outgassing during water transit from the lake to the head of the fjord.

To ascertain that the $\delta^{13}C_{CH4}$ variability in the Saguenay Fjord resulted from microbial oxidation, we calculated the kinetic carbon isotopic fractionation factor (α) from the Rayleigh distillation model expressed as follows (Coleman et al.,1981):

$$\delta^{13}\mathrm{C} = 1000 \times (1/\alpha - 1) \times ln(f) + \delta^{13}\mathrm{C}_0 \quad (2\text{-}4)$$

where *f* stands for the remaining fraction of [CH_4], $\delta^{13}C_0$ for the initial isotope composition, and $\delta^{13}C$ for the resulting isotope composition. The model was applied to the surface (< 25 m) and deep (>25 m) layers separately because of potential differences in source-water [CH_4] and methane oxidation history between the two layers. Despite limited data available, the data fit the model well (Fig. 2-8a) and give very close α values for the surface (mean ± SE: 1.0075 ± 0.0005) and deep (mean ± SE: 1.0082 ± 0.0003) layers. These values lie within the ranges expected for microbial methane oxidation (1.002-1.017) in sediments (Whiticar and Faber, 1986) and oceanic waters (Damm et al., 2007; Fenwick et al., 2017). Hence, microbial oxidation dominated the kinetic isotopic fractionation in both the surface and deep layers. The essentially identical α values for the surface and deep layers imply that the microbial communities effecting methane oxidation were similar in these two environments with contrasting physical properties (Section 2.6.3). In fact, the Keeling plot (Keeling, 1958), which describes the relationship between $\delta^{13}C_{CH4}$ and the reciprocal of [CH_4] in our case, demonstrates that the data for the surface and deeper layers roughly fall approximately on a single curve (Fig. 2-8b). This implies that the source-water [CH_4]s and the methane oxidation histories in these two water bodies were also similar. The concave Keeling plot reveals that additional processes (i.e. microbial oxidation and outgassing), other than physical mixing of water masses, enhanced $\delta^{13}C_{CH4}$, corroborating the result derived from the Rayleigh distillation model.

2.6.5 Microbial oxidation rate in the deep layer

The data collected during the Oct-16 cruise allows an approximate assessment of the microbial oxidation rate of methane (l_{ox}) in the deep layer (>25 m) of the inner basin, expressed as follows:

$$l_{ox} = l_{net} + d_d + p_{sw} \quad (2\text{-}5)$$

where l_{net} stands for the net loss rate, d_d for the downward diffusion rate, and p_{sw} for the in-situ production rate in the water column. All terms in eq. 2-5 have the units of nmol L^{-1} d^{-1}. l_{net} can be assessed by dividing the up-fjord decrease in [CH_4] in the deep layer (Section 2.6.3) by the time span (~4 months) from the start of water renewal (late June, Galbraith et al., 2018) to the dates of water sampling (October 19–20). The mean deep [CH_4] declined by 12.0 nmol L^{-1} from station S07 to station S11, arriving at a l_{net} of 0.10 nmol L^{-1} d^{-1}. This value should be regarded as an upper limit, since dilution due to mixing of the methane-richer warmer water with the methane-poorer colder water was not considered (Section 2.6.3).

The downward diffusion rate (d_d) is calculated as a product of the vertical eddy diffusivity and the [CH_4] gradient (d[CH_4]/dz) at 25 m divided by the thickness of the deep layer (235 m at station S09 and 155 m at station S11). The eddy diffusivity in the top 30 m of the inner basin is ~10^{-5} m^2 s^{-1} (Belzile et al., 2016). [CH_4] within the top 50 m can be fitted to [CH_4] = 13.6 + 66.1 $e^{-0.170z}$ (R^2 = 0.9999) at station S09 and [CH_4] = 2.2 + 118.4 $e^{-0.138z}$ (R^2 = 0.9999) at station S11, yielding d[CH_4]/dz of 160.3 nmoL m^{-4} and 518.7 nmoL m^{-4}, respectively. The estimated d_d values are 5.9 ×10^{-4} nmol L^{-1} d^{-1} at station S09 and 2.9 ×10^{-3} nmol L^{-1} d^{-1} at station S11, which are insignificant compared with l_{net}.

Potential in situ production of methane in the oxygenated deep layer could arise from microbial degradation of dimethylsulfoniopropionate (DMSP) (Damm et al., 2010) and dissolved organic matter phosphates (Repeta et al., 2016), metabolism of some algal species (Lenhart et al., 2016; Klintzsch et al., 2019). However, the DMSP- and organic phosphorus-derived methane productions are significant only under nitrate- and phosphate-depleted conditions, respectively (Damm et al., 2010; Repeta et al., 2016), neither of which exists in the Saguenay Fjord (Côté and Lacroix, 1978). Moreover, the fjord is low in DMSP due to low abundance of DMSP-producing phytoplankton such as *Emiliania huxleyi*, *Phaeocystis* sp. (Lee et al., 1999); these species are also among the few known major methane producers (Lenhart et al., 2016; Klintzsch et al., 2019). Therefore, the DMSP-, organic phosphorus- and phytoplankton-based methane productions are unlikely significant in the Saguenay Fjord. p_{sw} in eq. 2-5 can thus be ignored as well, making l_{ox} about equal to l_{net}, i.e. <0.10 nmol L^{-1} d^{-1}.

The upper-bound rates for the deep water of the Saguenay Fjord are similar to those found in the Arctic fjord Storfjorden and other methane-poor waters (Mau et al., 2020 and references therein).

2.6.6 Fjord-wide methane budgets

Assuming that the Saguenay Fjord was at a steady state for an "average" year over 2016 and 2017, methane mass balance requires:

$$F_{\text{R-IN}} + F_{\text{SLE-IN}} + F_{\text{SED-IN}} = F_{\text{F-OUT}} + L_{\text{T}} \quad (2\text{-}6)$$

where $F_{\text{R-IN}}$ stands for the river runoff input, $F_{\text{SLE-IN}}$ for the input from the SLE, $F_{\text{SED-IN}}$ for the sedimentary input in the fjord's head region, $F_{\text{F-OUT}}$ for the output to the SLE, and L_{T} for the total loss due to microbial oxidation and outgassing. Smaller rivers, which contribute ~10% of the total freshwater discharge to the fjord (Section 2.5), are also accounted for assessing the river input, assuming that these rivers have similar $[CH_4]$s and temporal variability to those in the Saguenay River. $F_{\text{R-IN}}$, $F_{\text{SLE-IN}}$, and $F_{\text{F-OUT}}$ are calculated as follows:

$$F_{\text{R-IN}} = {\sum_{2016}^{2017}(q_{\text{r}} \times [\text{CH}_4]_{\text{end-r}})}/{2} \quad (2\text{-}7)$$

$$F_{\text{SLE-IN}} = Q_{\text{SLE}} \times [\text{CH}_4]_{\text{end-m}} \quad (2\text{-}8)$$

$$F_{\text{F-OUT}} = Q_{\text{F}} \times [\text{CH}_4]_{\text{fm}} \quad (2\text{-}9)$$

Q_{SLE} stands for the annual water inflow from the SLE to the fjord, Q_{F} for the annual water outflow from the fjord to the SLE, and $[CH_4]_{\text{fm}}$ for $[CH_4]$ at the fjord's mouth represented by the mean $[CH_4]$ at stations S02 and S03 (18.6 nmol L^{-1}). $F_{\text{R-IN}}$ is computed by aggregating the daily input fluxes, $q_{\text{r}} \times [CH_4]_{\text{end-r}}$ (Supplementary Fig. 2-S5), over the 2-year period from January 1, 2016 to December 31, 2017 and then dividing the sum by 2 years. $[CH_4]_{\text{end-r}}$ is derived from its relationship with q_{r} (Supplementary Fig. 2-S2). $[CH_4]_{\text{end-m}}$ (15.3 nmol L^{-1}) is obtained by extrapolating the flatter linear regression line in Fig. 2-3 to salinity 32 which is assigned as the salinity of the fjord's marine source water from the cold intermediate layer

in the lower SLE (Belzile 2016; Galbraith et al., 2018; Delaigue et al., 2019). Q_{SLE} (3900 m^3 s^{-1}) is estimated by dividing the volume of the fjord (41 km^3, Belzile et al., 2016) by the yearly-averaged deep-water renewal time. The number of water renewal events varies interannually, usually 2–4 major deep renewals plus several partial shallow renewals (Belzile et al., 1026). Here we take three full deep renewals per year, leading to a yearly-averaged renewal time of 4 months. Note that the yearly-averaged renewal time differs from the duration of a specific renewal event which can vary from 1–6 months (Belzile et al., 2016; Galbraith et al., 2018). Q_F (5806 m^3 s^{-1}) is the sum of the annual river water inflow (Q_R) and Q_{SLE}, with Q_R (1906 m^3 s^{-1}) taken as the average of 2016 and 2017 (Supplementary Fig. 2-S5a).

$F_{SED\text{-}IN}$ in eq. 2-6 can be estimated as:

$$F_{\mathrm{SED-IN}} = A_{\mathrm{fh}} \times K_{\mathrm{b}} \times \mathrm{d}[\mathrm{CH_4}]/\mathrm{d}z \tag{2-10}$$

where A_{fh} denotes the surface sediment area in the fjord's head region upstream of station S13 (10.5 km^2). K_b is the vertical eddy diffusivity for the deep water of the fjord (~2×10^{-4} m^2 s^{-1}, Belize et al., 2016). $d[CH_4]/dz$ is taken as the slope of the line connecting the two deepest data points on the $[CH_4]$ vertical profile at station S13 in October 2016 (6.3 µmol m^{-4}; Fig. 2-4a). Substituting eqs. 2-7–10 into eq. 2-6 gives L_T.

L_T can be decomposed into the loss in the river water (L_R) and in the SLE water (L_{SLE}), with the latter including the loss of methane released from the sediment to the deep water. L_R can be estimated as:

$$L_{\mathrm{R}} = F_{\mathrm{R-IN}} - F_{\mathrm{R-OUT}} \tag{2-11}$$

and

$$F_{\mathrm{R-OUT}} = Q_{\mathrm{R}} \times [\mathrm{CH_4}]^{*}_{\mathrm{end-r}} \tag{2-12}$$

where $F_{R\text{-}OUT}$ denotes the methane output from the river water to the SLE. $[CH_4]^{*}_{end-r}$ is known (25.8 nmol L^{-1}, Fig. 2-3). Substituting eqs. 2-7 and 2-12 into eq. 2-11 yields L_R and

subtracting L_R from L_T gives L_{SLE}. Alternatively, L_T can be decomposed into sea-to-air emission (L_{SA}) and microbial oxidation (L_{OX}). L_{SA} was obtained by multiplying the area of the fjord (220 km^2) by the mean monthly wind speed-based flux density of all four cruises (53.4 μmol m^{-2} d^{-1}, Fig. 2-2c). Subtracting L_{SA} from L_T gives L_{OX}.

The resulting budgets are given in Fig. 2-9. The budgets indicate that river input (9.83×10^6 mol $year^{-1}$) is the largest source of methane to the Saguenay Fjord, followed by the import from the SLE (1.88×10^6 mol $year^{-1}$), and sedimentary release in the fjord's head region (0.42×10^6 mol $year^{-1}$), giving a total source of 12.13×10^6 mol $year^{-1}$. The fjord exports 3.41×10^6 mol to the SLE annually, to which rivers contribute 1.55×10^6 mol (i.e. 45%), with the remainder (1.86×10^6 mol, 55%) from the re-circulating SLE water and the sediments. Therefore, 84% (8.28×10^6 mol $year^{-1}$) of the river input is lost to microbial oxidation and outgassing, while only 19% (0.44×10^6 mol $year^{-1}$) of the input from the SLE and sediments goes to these two routes. Of the total loss (8.72×10^6 mol $year^{-1}$), microbial oxidation accounts for 51% (4.45×10^6 mol $year^{-1}$) and emission to the air occupies 49% (4.27×10^6 mol $year^{-1}$).

Several elements could contribute to the large difference between the percent loss of methane in the river water (84%) and that in the SLE water (19%) to microbial oxidation and outgassing. First, the river water is highly enriched with methane relative to the SLE water (Section 2.6.3). As both microbial oxidation and outgassing roughly follow first-order kinetics, higher [CH_4]s lead to faster losses. Second, the surface area of the river water in direct contact with the atmosphere relative to its volume is much larger than that for the SLE water, facilitating transfer of methane from the river water to air. Third, except for winter, the surface layer containing the majority of the river water is warmer than the deep layer filled with most of the SLE water, favoring microbial oxidation in the river water. Although [CH_4] near the sediment source in the head region is high, fast dilution by low-[CH_4] surrounding water rapidly reduces the [CH_4] and hence the microbial oxidation rate as well.

The budgets made here could involve potentially large uncertainties due to several unverified extrapolations. The relationship between $[CH_4]_{end\text{-}r}$ and q_r, from which $F_{R\text{-}IN}$ is calculated (eq. 2-7), is built on data from three cruises all undertaken in autumn. Likewise, the relationship between $[CH_4]$ and salinity for deriving $[CH_4]_{end\text{-}m}$ (eq. 2-8) and $[CH_4]^*_{end-r}$ (eq. 2-12) is based on data from four cruises covering only spring and autumn. Similar limitations also apply to $[CH_4]_{fm}$ (eq. 2-9) and the methane emission flux data. The lack of winter data may lead to an overestimation of the methane emission rate since ice cover depresses air-sea gas exchange. Furthermore, merely one vertical profile with adequate depth resolutions is available for evaluating the diffusive methane flux from the sediments (eq. 2-10) in the head region of the fjord. Finally, the number of deep-water renewals in the fjord may deviate from three and some of the events may only lead to partial renewals (Belzile et al., 2016; Galbraith et al., 2018). Several lines of circumstantial evidence, however, do support the rationales underlying some of these extrapolations. For instance, the inferred $[CH_4]_{end\text{-}m}$ (15.3 nmol L^{-1}) is comparable to the $[CH_4]$s observed within or near the cold intermediate layer of the lower SLE in various seasons (mean ± SD: 15.9 ± 4.4 nmol L^{-1}) (Li et al., 2019). Moreover, the convergence of surface $[CH_4]$s at higher salinities and the rather constant surface $[CH_4]$s at the fjord's mouth in different seasons and years (Fig. 2-3) can hardly be interpreted as coincidences. Future investigations covering broader spatiotemporal scales, including long-term time-series observations at both the head and mouth of the fjord, are needed to validate the extrapolations and improve the budgets in this study.

2.7 CONCLUSIONS

Figure 2-10 summarizes the major drivers of methane dynamics in the Saguenay Fjord. The deep bathymetry combined with strong vertical stratification creates two distinct layers with widely different methane drivers. In the surface layer, the spatiotemporal variability of $[CH_4]$ and $\delta^{13}C_{CH4}$ is strongly impacted by the Saguenay River runoff which determines both the residence time of the freshwater in the surface layer and the size of the freshwater endmember of $[CH_4]$. In the deep layer, the frequency and extent of deep-water renewal primarily dictates the space- and time-progression of $[CH_4]$ and $\delta^{13}C_{CH4}$ in the inner basin of

the fjord, with the influence of methane release from sediments confined to the head region. As the river water is highly enriched with methane relative to the deep marine water sourced from the lower SLE, [CH_4] in the Saguenay Fjord generally decreases with depth. However, sill-induced mixing, particularly at high tides, tends to homogenize [CH_4] in the outer and middle basins, and sedimentary input leads to much higher [CH_4] in bottom water than in surface water near the head of the fjord. Microbial methane oxidation mainly controls the carbon isotopic fractionation of methane in both the surface and deep waters.

Freshwater discharge contributes the largest amount of methane to the Saguenay Fjord followed by import from the renewing seawater, while the sedimentary contribution in the head region is marginal. The riverine input is largely lost to microbial oxidation and outgassing before being exported to the SLE. In contrast, the majority of methane imported from water renewals and released from sediments ends in the SLE rather than goes to microbial consumption and air-sea exchange. Emission to the atmosphere is a significant sink of methane in the Saguenay Fjord and its magnitude is comparable to microbial consumption on a yearly basis.

The areal methane emission rates obtained for the Saguenay Fjord, along with those reported for other deep fjords, suggest a potentially large overestimation of the atmospheric methane flux from global fjords and fjards by earlier studies based on only limited data collected from shallow, anoxic fjords and lagoons. The values for the deep fjords are, however, substantially higher than the recent estimates for global coastal oceans. Given their large geographic coverage at high latitudes, fjords and fjards could be a significant contributor to the atmospheric methane efflux from coastal waters. More surveys are needed to expand the scanty data of methane concentrations and air-sea fluxes in fjords and fjards and to better understand the processes controlling the distributions and air-sea exchange of methane in these systems.

2.8 ACKNOWLEDGEMENTS

We thank François Villeneuve, Félix St-Pierre, and Rémi Desmarais for assistance in sampling during the Jun-17 cruise, the Maurice Lamontagne Institute for providing the chlorophyll *a* data, Rio Tinto Alcan for providing the Saguenay River discharge data, and captains, crew, scientists on all cruises, and the DFO Atlantic Zone Monitoring Program for their cooperation. Guillaume St-Onge offered constructive comments during the early stage of data processing. Comments from the Associate Editor and two anonymous reviewers improved the manuscript. This study was supported by H.X.'s NSERC Discovery Grant (2017-05135) and Quebec-Ocean equipment grant. Yijie Li was supported by scholarships from the China Scholarship Council and the Institut des sciences de la mer de Rimouski (ISMER). Ship time was provided by the Fisheries and Oceans Canada and the Mission du stage of ISMER. This is a contribution to ISMER and Quebec-Ocean.

2.9 DATA AVAILABILITY STATEMENT

Data reported in this article are archived at figshare.com and is accessible via https://doi.org/10.6084/m9.figshare.13499655.

2.10 TABLES

Table 2-1. Range (mean; median) of water temperature, water salinity, dissolved methane concentration ([CH_4]), methane saturation ratio, wind speed, and methane water-to-air flux density.

Cruise	**Temperature (°C)**	**Salinity**	**[CH_4] (nmol L^{-1})**	**Saturation ratio**	**Wind speed (m s^{-1})**		**Water-to-air flux density (µmol m^{-2} d^{-1})**	
					Daily	Monthly	Daily wind speed	Monthly wind speed
Oct-16	4.4–10.0 (6.9; 7.3)	5.64–28.71 (18.55; 18.67)	15.7–143.5 (46.6; 20.9)	4.5–40.3 (13.2; 6.0)	1.81–9.94 (5.48; 3.95)	2.66–4.98 (4.08; 4.29)	12.1–290.3 (89.7; 51.8)	19.5–139.0 (46.9; 24.0)
Jun-17	8.5–12.7 (10.9; 11.2)	7.16–15.69 (10.21; 8.99)	22.0–33.4 (28.8; 29.9)	6.3–9.9 (8.5; 8.9)	2.11–4.35 (3.79; 4.35)	4.19–4.23 (4.20; 4.19)	12.3–47.4 (36.0; 42.2)	25.8–44.8 (37.6; 39.9)
Oct-17	6.5–15.0 (11.4; 12.0)	2.97–23.47 (11.09; 9.17)	16.2–102.1 (36.0; 25.6)	4.7–31.6 (10.9; 7.7)	1.22–3.70 (2.10; 1.56)	3.14–4.41 (4.02; 4.29)	9.4–72.4 (23.0; 16.4)	16.4–129.6 (44.1; 36.5)
Nov-17	5.8–8.6 (7.5; 8.0)	2.27–17.38 (8.80; 6.75)	19.3–184.2 (77.2; 28.2)	5.3–48.8 (20.5; 7.6)	4.19–11.99 (7.58; 6.55)	4.29–6.97 (5.95; 6.60)	19.8–567.8 (365.2; 508.1)	52.5–256.9 (128.8; 76.9)

2.11 FIGURES

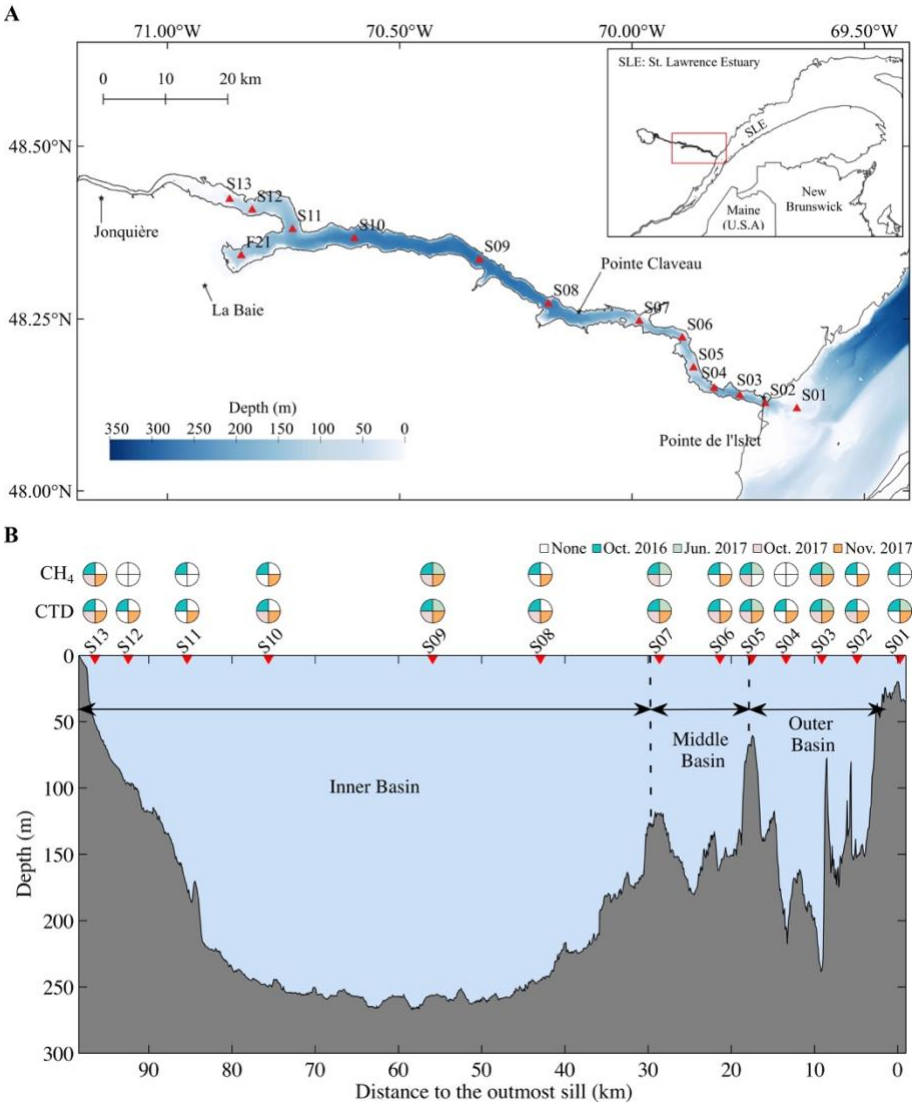

Figure 2-1. Sampling information and bathymetry and topography of the Saguenay Fjord. (A) Map of the study area, sampling stations, and bathymetry. The red rectangle in the inset shows the location of the Saguenay Fjord in eastern Canada. Dark stars denote the locations of weather stations. (B) The longitudinal section showing the topography of the Saguenay Fjord and the distribution of the three basins. Quartered circles indicate the cruises during which methane sampling (upper row) and CTD profiling (lower row) were conducted at a specific station. Different cruises are represented by different colors. Station F21 in the south arm of the fjord is not shown; this station was visited during the Oct-17 cruise only for both methane sampling and CTD profiling.

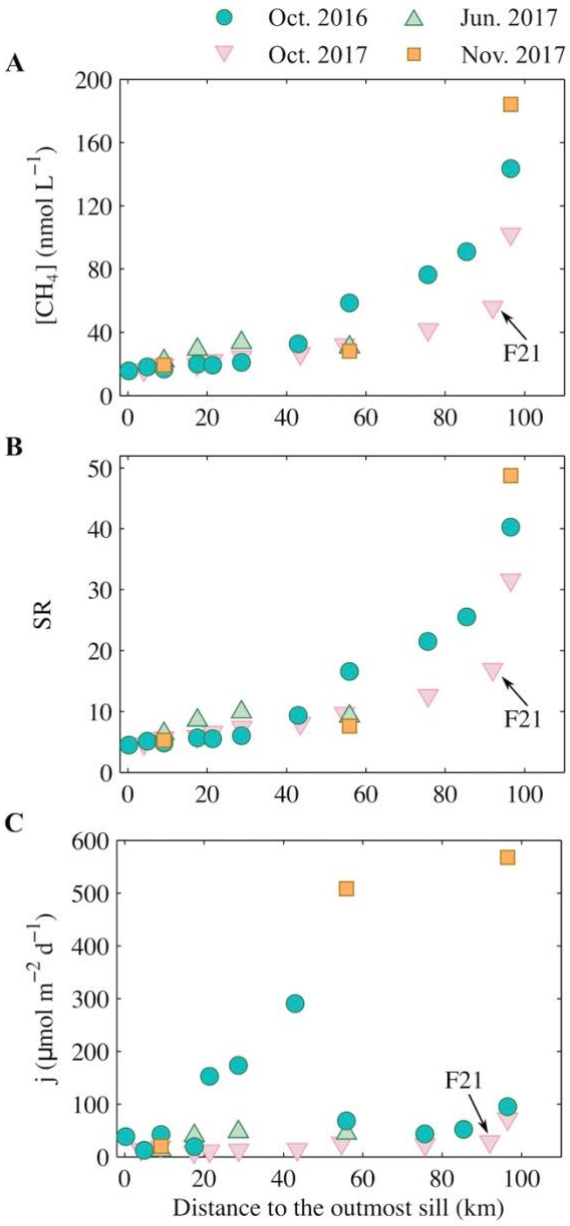

Figure 2-2. Distribution of surface-water methane properties as a function of distance to the outermost sill. (A) Methane concentration. (B) Methane saturation ratio. (C) Daily wind speed-based sea-to-air flux density.

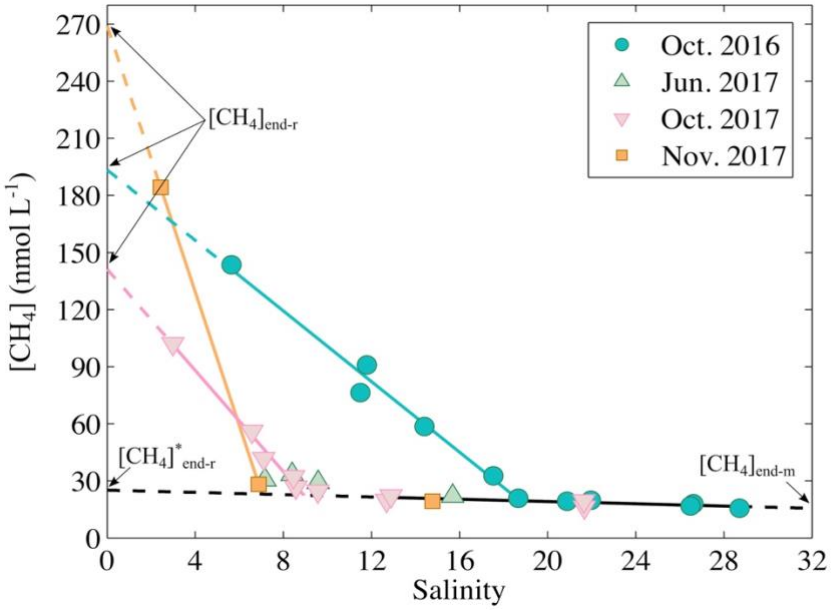

Figure 2-3. Estuarine mixing behavior of surface-water methane concentration. Solid lines are linear least-squares fits of the data. Data fitting is divided into two segments: a steeper slope for lower-salinity samples and a flatter slope for saltier samples. The steeper fitting is performed individually for all three autumn cruises, whereas the flatter fitting used composite data from all four cruises at salinity >10. Dashed lines represent extrapolations of the solid lines. $[CH_4]_{end\text{-}r}$ stands for the river-endmember methane concentration, $[CH_4]^*_{end\text{-}r}$ for the effective river-endmember methane concentration, and $[CH_4]_{end\text{-}m}$ for the marine end member methane concentration. Fitted equations for the steeper lines are: $y = -9.27x + 193.4$ (R^2 =0.983) for October 2016, $y = -13.38x + 142.5$ (R^2 = 0.990) for October 2017, and $y = -34.84x + 263.3$ for November 2017. Fitted equation for the flatter line is $y = -0.33x + 25.8$ (R^2 = 0.725).

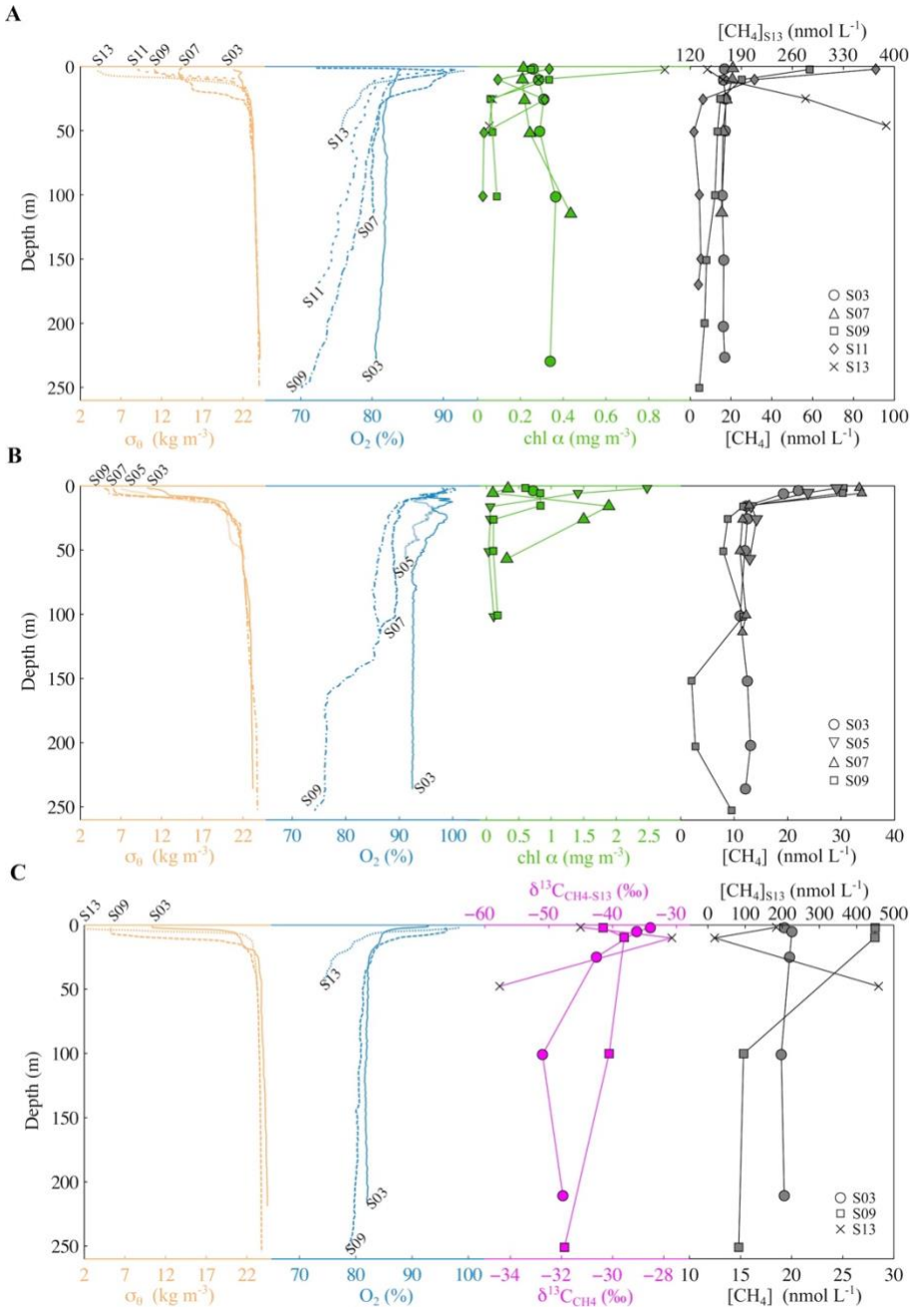

Figure 2-4. Depth profiles of physical, chemical, and biological properties. (A) Oct-16 cruise. (B) Jun-17 cruise. (C) Nov-17 cruise. σ_θ: potential density (σ_θ); O_2%: percent dissolved oxygen saturation; chl *a*: chlorophyll *a* concentration; [CH_4]: methane concentration; $\delta^{13}C_{CH4}$: stable carbon isotope composition of methane. Chl *a* data is not available for November 2017. $\delta^{13}C_{CH4}$ was measured only in November 2017. Different scales are used for [CH_4] at station S13 in panel A and for [CH_4] and $\delta^{13}C_{CH4}$ at station S13 in panel C.

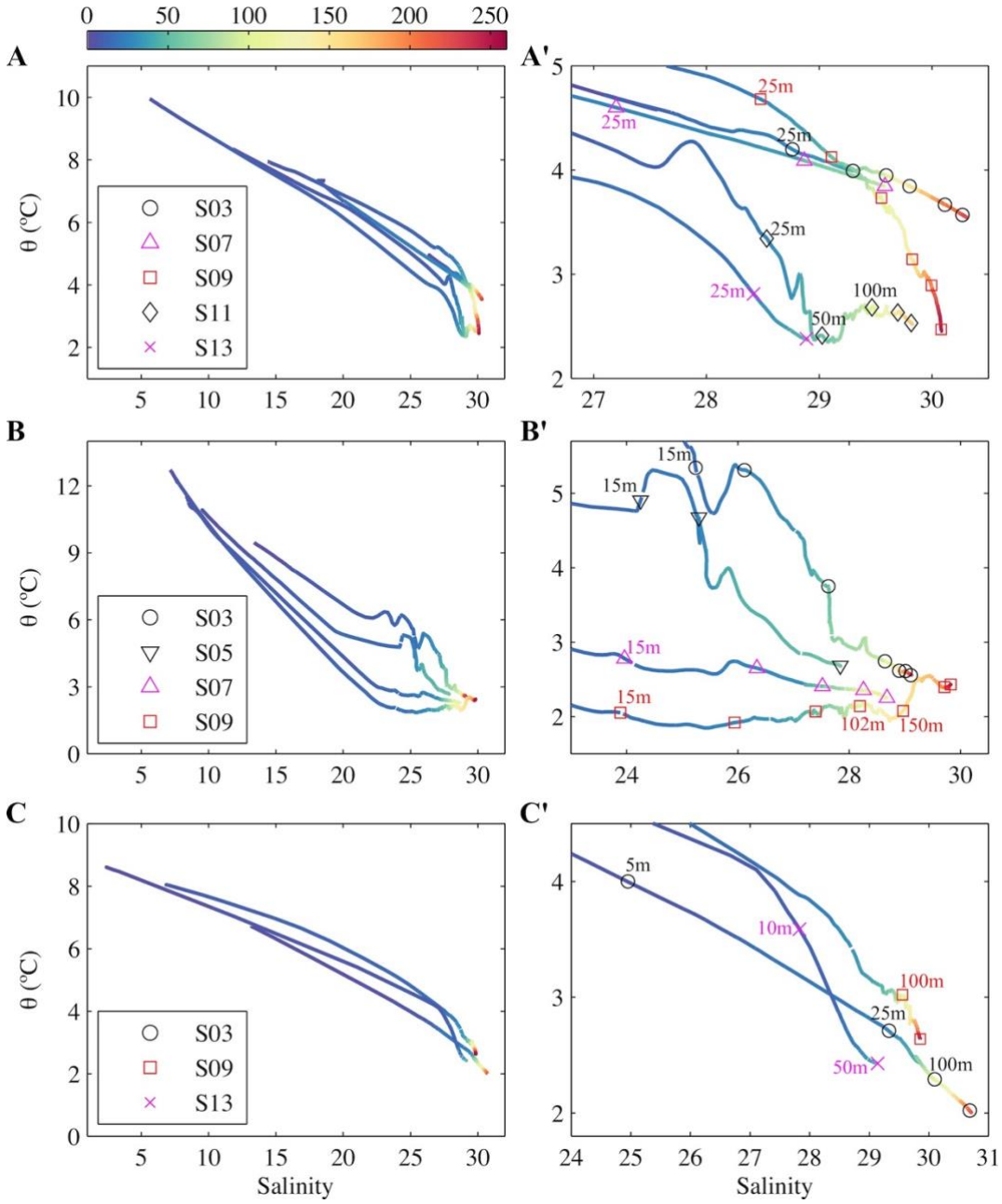

Figure 2-5. Potential temperature–salinity diagrams at [CH_4] profiling stations. (A) Oct-16 cruise. (B) Jun-17 cruise. (C) Nov-17 cruise. Panels A', B', and C' show the enlarged portions of panels A, B, and C, respectively, at deeper depths. Symbols on the curves in panels A', B', and C' denote the [CH_4] sampling points. Numbers next to the symbols are the [CH_4] sampling depths. Color bar represents water depth in meters.

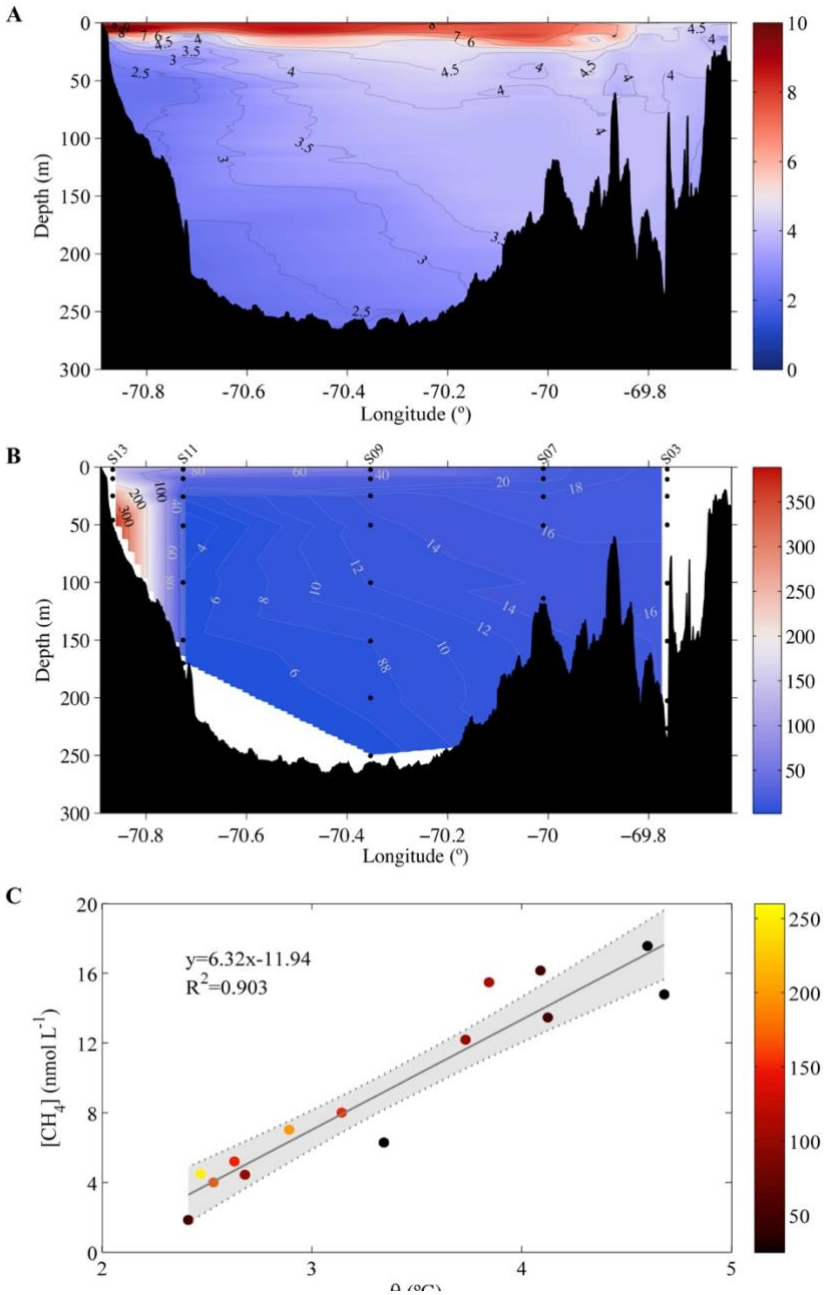

Figure 2-6. Relationship between methane concentration and water temperature during the Oct-2016 cruise. (A) Longitudinal vertical section of water temperature. (B) Longitudinal vertical section of methane concentration. (C) Linear least-squares regression of [CH_4] against temperature for deep water (>25 m) between stations S07 and S11. In panel C: solid line is the fit of the data; dashed lines are 95% confidence intervals; color bar represents water depth in meters.

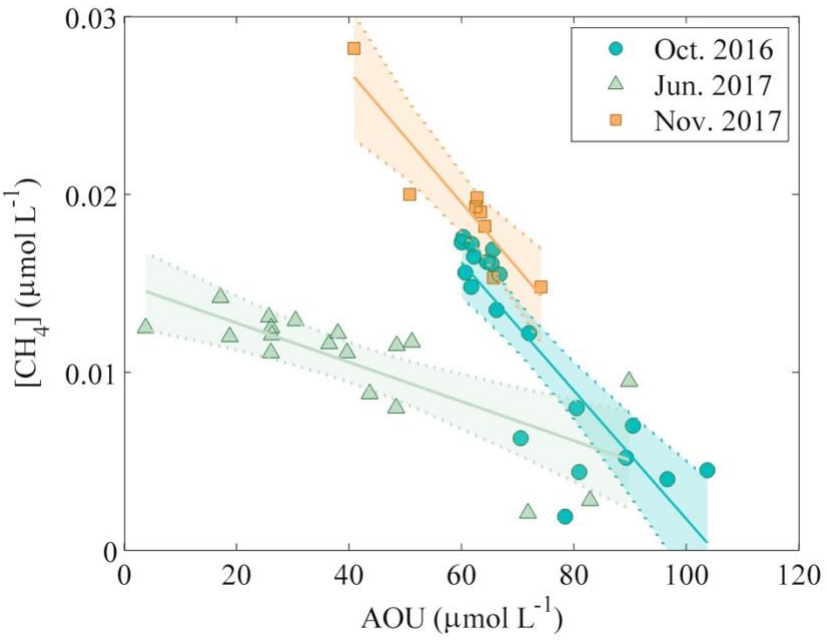

Figure 2-7. Relationship between methane concentration and apparent oxygen utilization for deep water (>25 m). Solid lines are linear least-squares fits. Dashed lines are 95% confidence intervals. Fitted equations are: $y = -0.00036x + 0.0378$ ($R^2 = 0.729$) for October 2016, $y = -0.00011x + 0.0150$ ($R^2 = 0.568$) for June 2017, and $y = 0.00037x + 0.0461$ ($R^2 = 0.843$) for November 2017. Station S13 is excluded.

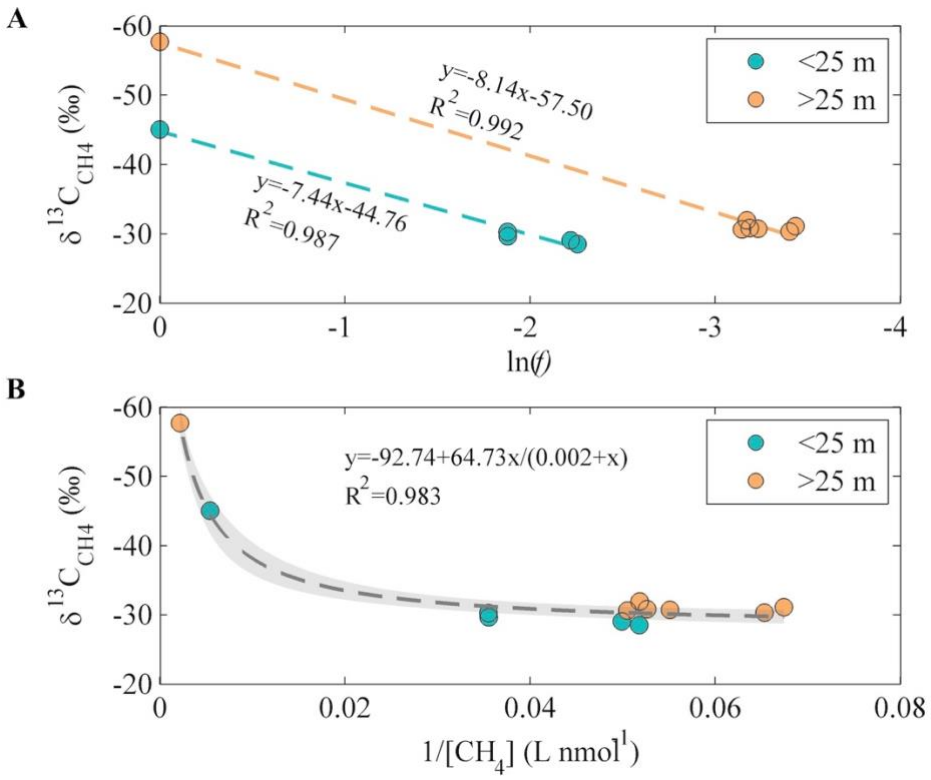

Figure 2-8. $\delta^{13}C_{CH4}$ data presented using the Rayleigh distillation model (A) and Keeling plot (B). *f* in panel A denotes the fraction of the initial methane concentration (184.2 nmol L^{-1} for surface water (<25 m) and 459.2 nmol L^{-1} for deep water (>25 m)). Dashed lines are the least-squares fits of the data. Grey area in panel B represents the 95% confidence intervals. The data were collected from the Nov-17 cruise.

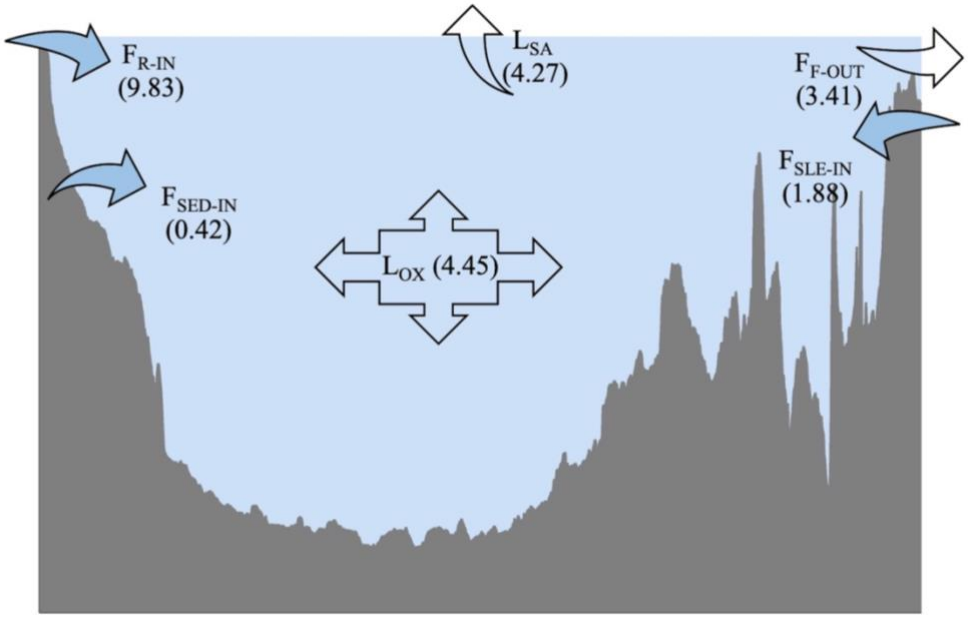

Figure 2-9. Schematic representation of the methane budgets in the Saguenay Fjord for an "average" year of 2016 and 2017. Solid arrow: source; empty arrow: sink. $F_{R\text{-}IN}$: river input; $F_{SLE\text{-}IN}$: input from the St. Lawrence estuary; $F_{SED\text{-}IN}$: input from the sediments in the head region of the fjord; $F_{F\text{-}OUT}$: output to the St. Lawrence estuary; L_{OX}: loss to microbial oxidation; L_{SA}: loss to the atmosphere. Units: 10^6 mol year^{-1}.

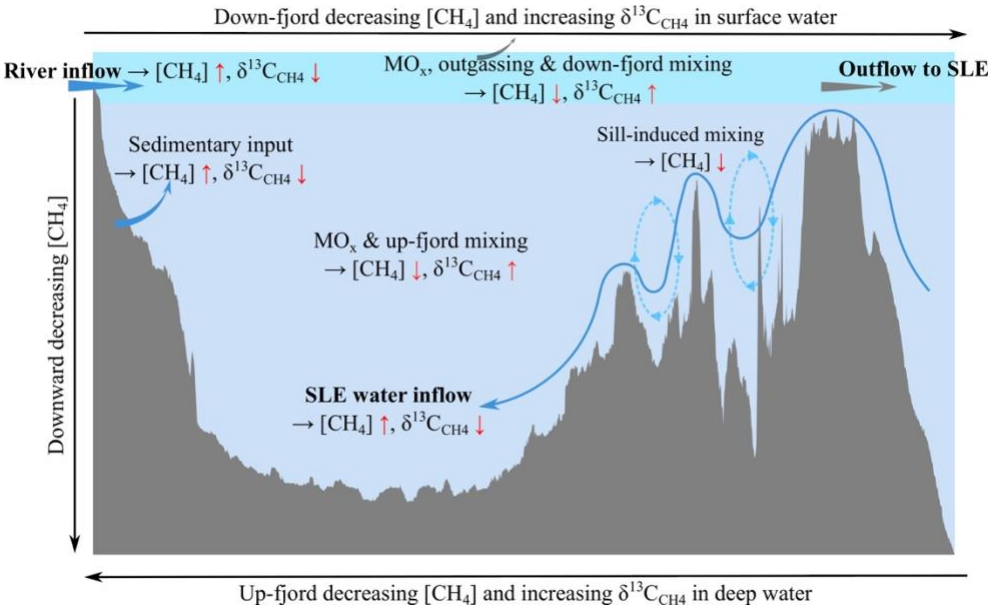

Figure 2-10. Schematic representation of the major drivers controlling the dynamics of $[CH_4]$ and $\delta^{13}C_{CH4}$ in the water column of the Saguenay Ford. Light cyan background color denotes the surface layer and light blue background color signifies the deep layer. Long dark arrows show the overall trends of $[CH_4]$ and/or $\delta^{13}C_{CH4}$; the vertical trend does not apply to the head region where sedimentary input causes $[CH_4]$ in bottom water to be higher than in surface water (see text). MO_x: Microbial methane oxidation. SLE: St. Lawrence estuary. SLE water inflow represents deep-water renewal events.

2.12 SUPPLEMENTARY INFORMATION

2.12.1 Supplementary figures

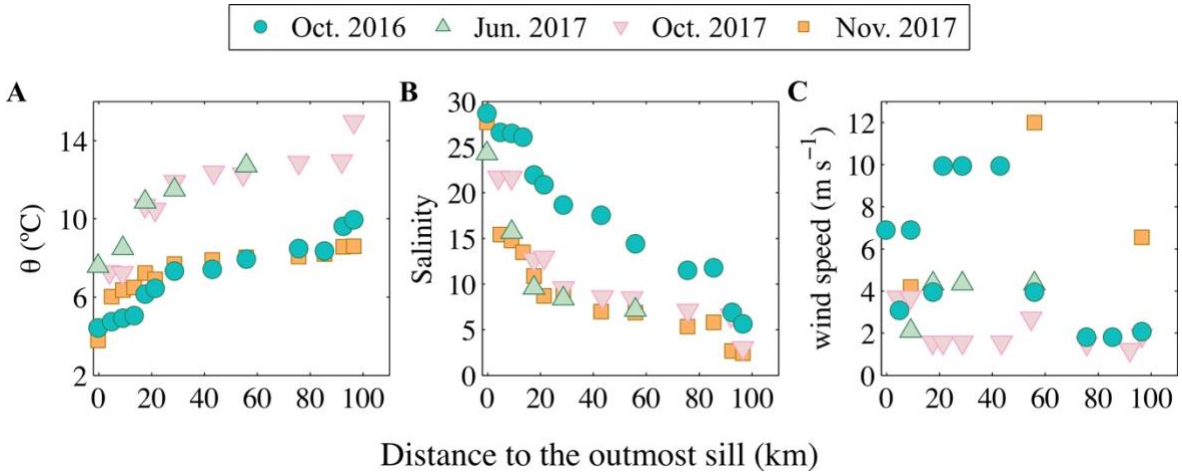

Figure 2-S1. Along-fjord distributions of physical and meteorological variables. (A) Surface-water temperature. (B) Surface-water salinity. (C) Daily mean wind speed.

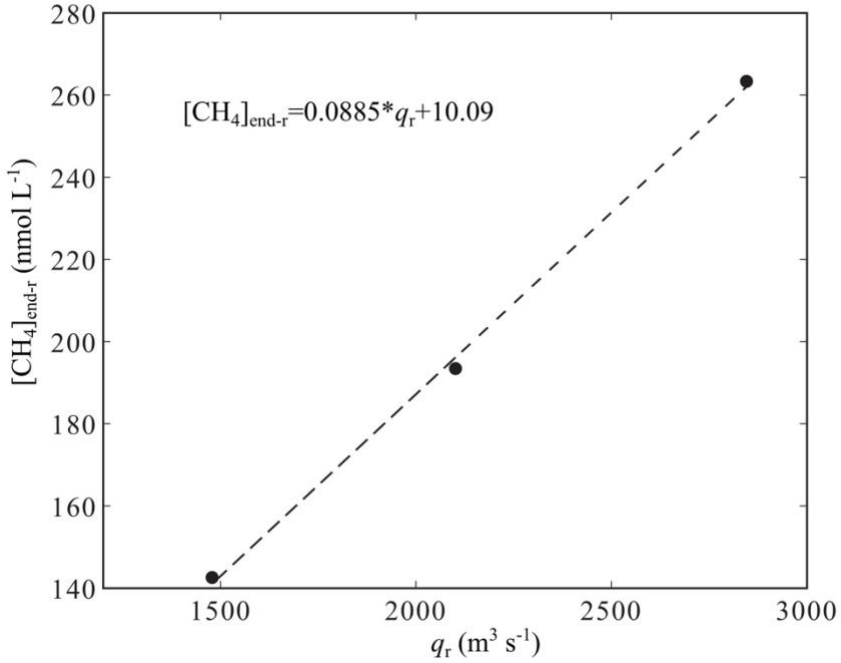

Figure 2-S2. Relationship between the river-endmember methane concentration and the freshwater discharge rate. Freshwater discharge rate is the daily averaged discharge rate of the Saguenay River on the day of water sampling at S13. Line is the linear least-squares fit of the data.

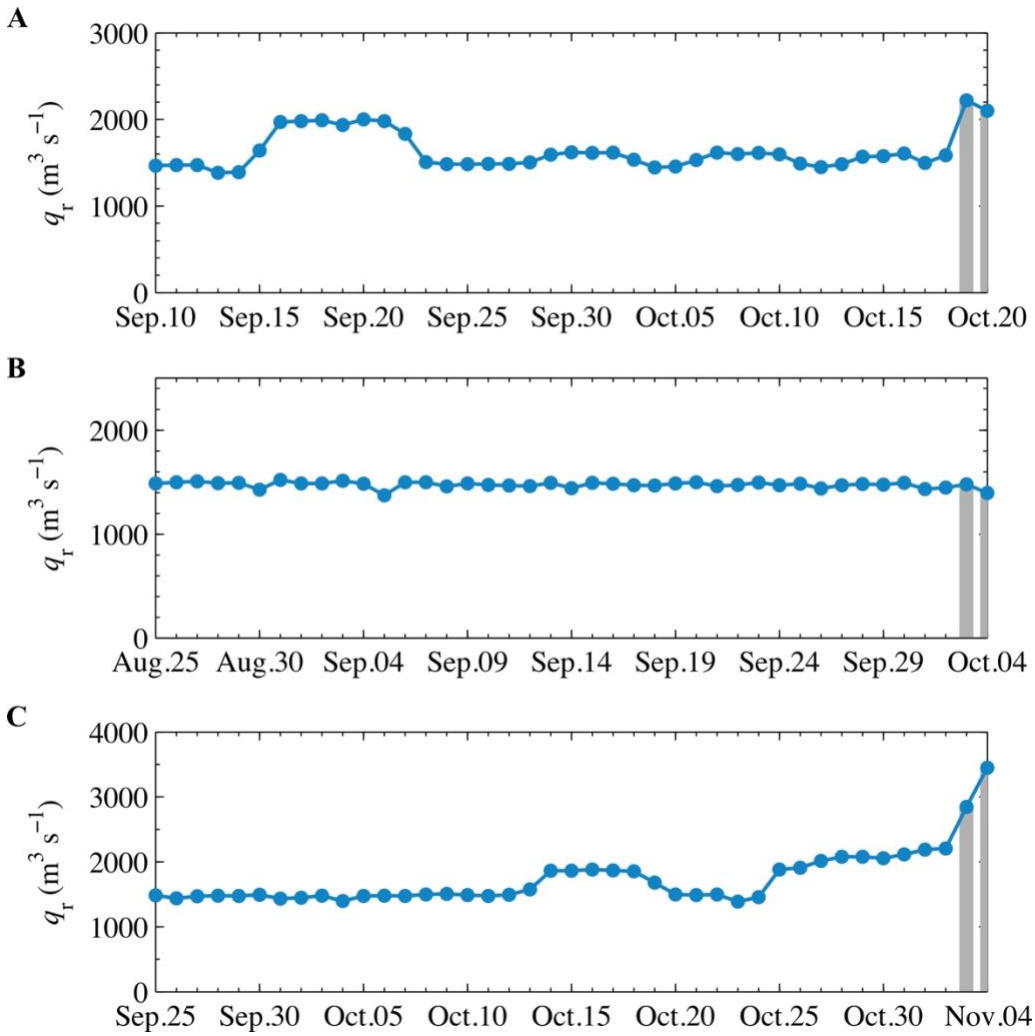

Figure 2-S3. Saguenay River freshwater discharge rates over 40 days prior to the onset of water sampling. (A) Oct-16 cruise. (B) Oct-17 cruise. (C) Nov-17 cruise. Vertical gray bars indicate the sampling dates.

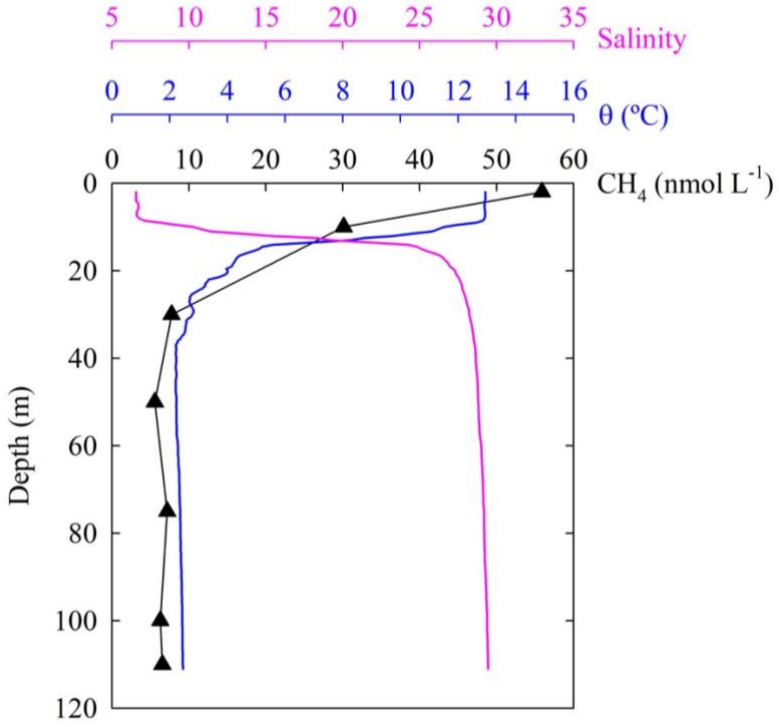

Figure 2-S4. Vertical profiles of methane concentration ([CH_4]), temperature, and salinity at station F21. See Fig. 2-1 in the main text for the location of station F21.

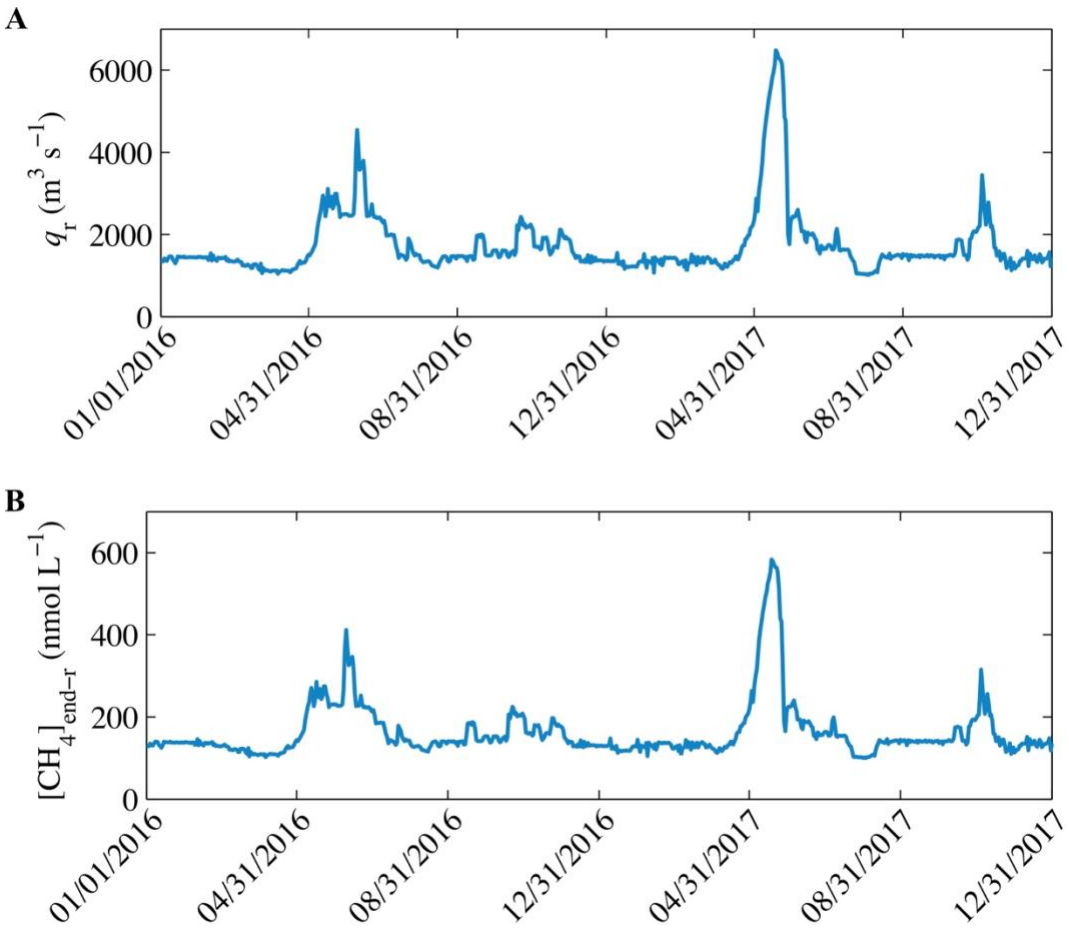

Figure 2-S5. Saguenay River freshwater discharge rate and the corresponding river end-member methane concentration. (A) Freshwater water discharge rate from January 1, 2016 to December 31, 2017. (B) The river end-member methane concentration derived from the relationship between $[CH_4]_{end\text{-}r}$ and q_r shown in Supplementary Figure 2-S2.

CHAPTER 3
DISSOLVED METHANE IN THE WORLD'S LARGEST SEMI-ENCLOSED ESTUARINE SYSTEM: THE GULF AND ESTUARY OF ST. LAWRENCE (CANADA)

Yijie Li [1], Huixiang Xie [1*], Michael Scarratt [2], Ellen Damm [3], Peter S. Galbraith [2], Douglas W. R. Wallace [4]

[1]Institut des sciences de la mer, Université du Québec à Rimouski, Rimouski, Québec, Canada G5L 3A1

[2]Maurice Lamontagne Institute, Fisheries and Oceans Canada, Mont-Joli, Quebec, Canada G5H 3Z4

[3]Alfred Wegener Institute for Polar and Marine Research, P.O. Box 120161 D-27515 Bremerhaven, Germany

[4]Department of Oceanography, Dalhousie University, Halifax, Nova Scotia, Canada B3H 4R2

To be submitted to Progress in Oceanography

3.1 RÉSUMÉ

L'estuaire et le golfe du Saint-Laurent (ESGL) est le plus grand système estuarien semi-fermé du monde, mais il a été jusqu'à présent une zone vide de données sur le méthane. Cette étude a recueilli le premier ensemble de données sur le méthane dissous dans l'EGSL, ce qui a permis d'évaluer les flux air-mer de méthane, de caractériser les répartitions et les sources de méthane dans la colonne d'eau et d'aider à éclairer son cycle biogéochimique. Les concentrations de méthane dans l'eau de surface ($[CH_4]_{surf}$) étaient en moyenne de 57,4 nmol L^{-1} (gamme : 12,5-392,8 nmol L^{-1}) dans l'estuaire supérieur (UE), de 9,8 nmol L^{-1} (gamme : 4,8-21,0 nmol L^{-1}) dans l'estuaire maritime (LE) et de 4,3 nmol L^{-1} dans le golfe (gamme : 2,8-8,9 nmol L^{-1}), avec les concentrations les plus élevées observées dans la zone maximale de turbidité de l'UE. La $[CH_4]_{surf}$ le long de l'axe longitudinal principal a typiquement diminuée de façon exponentielle avec l'augmentation de la salinité et de la distance vers la mer. De manière saisonnière, les moyennes de $[CH_4]_{surf}$ dans les trois sous-régions étaient toutes les plus élevées en hiver. Les $[CH_4]_{surf}$ étaient principalement sursaturées par rapport à l'atmosphère dans l'ensemble de l'EGSL, avec le taux de saturation diminuant de l'UE (moyenne : 15,82 ; gamme : 3,67-126,28) au golfe (moyenne : 1,29 ; gamme : 0,99-2,38) en passant par le LE (moyenne : 2,75 ; gamme : 1,48-5,04). La tendance de distribution régionale de la densité moyenne de flux mer-air était similaire : 31,02 (gamme : 2,11-336,8) µmol m^{-2} d^{-1} dans l'UE, 5,47 (1,14-16,54) µmol m^{-2} d^{-1} dans le LE, 1,63 (-0,03-10,41) µmol m^{-2} d^{-1} dans le golfe. Le taux annuel d'émission de méthane était le plus élevé dans le golfe (117,7 × 10^6 mol), suivi par l'UE (26,0 × 10^6 mol) et le LE (14,8 × 10^6 mol), avec un total de 158,4 × 10^6 mol. La $[CH_4]$ dans la colonne d'eau de l'UE était relativement homogène à la tête de l'estuaire, augmentait avec la profondeur dans la zone maximale de turbidité et reflétait la structure de salinité dans la zone en aval. Les profils verticaux de $[CH_4]$ dans le LE et le golfe étaient caractérisés par un maximum de $[CH_4]$ en sous-surface (SMMax, 4,0-30,4 nmol L^{-1}) et un minimum de $[CH_4]$ en profondeur (DMMin, principalement dans la gamme de 0,17-3,7 nmol L^{-1}) qui étaient omniprésents dans le chenal Laurentien et ses branches. Alors que le SMMax suggère une production biologique de méthane in situ, le DMMin peut être dû au

[CH_4] appauvri dans l'eau de source, largement composée d'Eau centrale de l'Atlantique Nord (NACW). La budgétisation de bilan massique basé sur les données de DMMin et de SMMax a généré un taux de consommation nette de ~0,1 nmol L^{-1} an^{-1} dans la NACW, des taux de production nette de ~40 nmol L^{-1} d^{-1} à la tête du chenal Laurentien et de $2,8 \times 10^{-3}$ nmol L^{-1} d^{-1} près du Détroit de Cabot. Les profils verticaux recueillis aux sites de pockmarks dans le LE ont montré que la [CH_4] près du fond était enrichi mais très variable (10,4-695,3 nmol L^{-1}) et impliquaient un flux diffusif allant jusqu'à ~700 mmol CH_4 m^2 d^{-1} des pockmarks vers l'eau de fond. Peu de méthane libéré par les pockmarks pourrait atteindre la surface de la mer et s'échapper dans l'air avant d'être consommé par les bactéries et/ou dilué par les masses d'eau environnantes à faible teneur en méthane. Aucune influence significative des conditions hypoxiques sur la [CH_4] dans les eaux de fond du LE n'a été observée. Les incubations en laboratoire ont généré une large gamme de taux de cycle du méthane allant d'une production nette de 0,0068 nmol L^{-1} d^{-1} à une consommation nette avec les temps de renouvellement de 33,3-263 jours. Le $\delta^{13}C$ du CH_4 ($\delta^{13}C_{CH4}$ par rapport au PDB) pour l'EGSL allait de -40,91 à -27,42‰ (moyenne : -33,28‰) et n'était pas lié à la [CH_4]. Les valeurs de $\delta^{13}C_{CH4}$ pour la couche intermédiaire froide où se trouvait le SMMax sont constamment plus négatives que celles au-dessus et au-dessous de la couche intermédiaire froide. Cette étude démontre que 1) en termes de [CH_4] et de taux d'émission, l'UE de l'EGSL se comporte comme un typique estuaire macrotidal peu profond, tandis que le LE et le Golfe ressemblent respectivement aux mers de plateau externe et aux mers sur les talus continentaux; 2) les [CH_4] et les taux d'émission dans l'EGSL sont à la limite inférieure des environnements estuariens globaux ; 3) le réservoir de méthane dans l'EGSL est composé de résidus de méthane fortement oxydés d'origine d'eau douce et marine, de méthane thermogénique dérivé du pockmark, et peut-être aussi de méthane biogénique enrichi en ^{13}C ; 4) l'upwelling à la tête du chenal Laurentien est un contributeur potentiellement important au budget de méthane des eaux de surface dans le LE et le Golfe ; 5) les grandes dimensions et les processus physiques et biogéochimiques complexes associés, ainsi que leurs interactions, permettent à l'EGSL, en particulier son LE et golfe, de se distinguer des

environnements estuariens typiques en termes de dynamique du méthane et de cycle biogéochimique.

***Mots-clés* :** Estuaire et golfe du Saint-Laurent ; méthane dissous ; répartition ; flux air-mer ; oxydation microbienne ; composition isotopique.

3.2 ABSTRACT

The Estuary and Gulf of St. Lawrence (EGSL) is the largest semi-enclosed estuarine system in the world but for which there are no previous methane data. This study collected the first dissolved methane dataset from the EGSL, including assessing the methane air-sea fluxes, characterizing the distributions and sources of methane in the water column, and shedding light on its biogeochemical cycling. Surface-water methane concentrations ($[CH_4]_{surf}$) averaged 57.4 nmol L^{-1} (range: 12.5–392.8 nmol L^{-1}) in the Upper Estuary (UE), 9.8 nmol L^{-1} (range: 4.8–21.0 nmol L^{-1}) in the Lower Estuary (LE), and 4.3 nmol L^{-1} in the Gulf (range: 2.8–8.9 nmol L^{-1}), with the highest concentrations observed in the UE's turbidity maximum zone. $[CH_4]_{surf}$ along the main longitudinal axis typically decreased exponentially with increasing salinity and distance seaward. Seasonally, the mean $[CH_4]_{surf}$ in the three subregions were all highest in the winter. $[CH_4]_{surf}$ were mostly supersaturated relative to the atmosphere in the entire EGSL, with the saturation ratio decreasing from the UE (mean: 15.82; range: 3.67–126.28) to the LE (mean: 2.75; range: 1.48–5.04) to the Gulf (mean: 1.29; range: 0.99–2.38). The regional distribution pattern of the mean sea-to-air flux density was similar: 31.02 (range: 2.11–336.8) μmol m^{-2} d^{-1} in the UE, 5.47 (1.14–16.54) μmol m^{-2} d^{-1} in the LE, 1.63 (-0.03–10.41) μmol m^{-2} d^{-1} in the Gulf. The annual methane emission rate was greatest in the Gulf (117.7 × 10^6 mol) followed by the UE (26.0 × 10^6 mol), and the LE (14.8 × 10^6 mol), totalling 158.4 × 10^6 mol. $[CH_4]$ in the UE's water column was relatively homogenous at the head of the estuary, increased with depth in the turbidity maximum zone, and mirrored the salinity structure in the downstream area. The vertical $[CH_4]$ profiles in the LE and the Gulf were characterized by a subsurface $[CH_4]$ maximum (SMMax, 4.0–30.4 nmol L^{-1}) and a deep $[CH_4]$ minimum (DMMin, mostly in the range of 0.17–3.7 nmol L^{-1})

that were omnipresent in the Laurentian Channel and its branches. While the SMMax is suggestive of in situ biological methane production, the DMMin can be attributed to the depleted [CH_4] in the source water largely composed of the North Atlantic Central Water (NACW). Mass-balance budgeting based on the DMMin and SMMax data produced a net consumption rate of ~0.1 nmol L^{-1} $year^{-1}$ in the NACW, net production rates of ~40 nmol L^{-1} d^{-1} at the head of the Laurentian Channel and 2.8 $\times 10^{-3}$ nmol L^{-1} d^{-1} near Cabot Strait. Vertical profiles collected at pockmark sites in the LE displayed enriched but highly variable near-bottom [CH_4] (10.4–695.3 nmol L^{-1}) and implied a diffusive flux of up to ~700 mmol CH_4 m^2 d^{-1} from the pockmarks into the bottom water. Little pockmark-released methane could reach the sea surface and escape to air before being consumed by bacteria and/or diluted by surrounding low-[CH_4] water masses. No significant influence of the hypoxic conditions on [CH_4] in the bottom water of the LE was observed. Lab incubations yielded a large range of methane cycling rates from a net production of 0.0068 nmol L^{-1} d^{-1} to net consumption with turnover times of 33.3–263 days. The $\delta^{13}C$ of CH_4 ($\delta^{13}C_{CH4}$ relative to PDB) for the EGSL ranged from −40.91 to −27.42‰ (mean: −33.28‰) and was not related to the [CH_4]. The $\delta^{13}C_{CH4}$ values for the cold intermediate layer where the SMMax was located are consistently more negative than those above and below the cold intermediate layer. This study demonstrates that 1) in terms of [CH_4] and emission rate, the UE of the EGSL behaves like a typical shallow macrotidal estuary, while the LE and the Gulf resemble outer shelf seas and ocean's slope regions, respectively; 2) the [CH_4] and emission rates in the EGSL are at the lower bound of the global estuarine environments; 3) the methane pool in the EGSL is composed of strongly oxidized methane residues of both freshwater and marine origins, pockmark-derived thermogenic methane, and possibly ^{13}C-enriched biogenic methane as well; 4) upwelling at the head of the Laurentian Channel is a potentially important contributor to the surface water methane budget in the LE and the Gulf; 5) the large dimensions and the associated complex physical and biogeochemical processes and their interactions set the EGSL, particularly its LE and the Gulf, apart from typical estuarine environments in terms of methane dynamics and biogeochemical cycling.

***Keywords*:** Estuary and Gulf of St. Lawrence; dissolved methane; distribution; air-sea flux; microbial oxidation; isotope composition

3.3 INTRODUCTION

As the second most important greenhouse gas with continuously increasing atmospheric concentrations, methane has attracted much attention during the last several decades (IPCC, 2013). Although the ocean has long been recognized as a natural source of atmospheric methane, earlier estimates of the diffusive oceanic methane flux vary by more than an order of magnitude (0.4 to 18 Tg CH_4 $year^{-1}$) (Bange et al, 1994; Bates et al., 1996; Rhee et al., 2009; Kirschke et al., 2013). More recent assessments have substantially reduced the range to 2.2–6.3 Tg CH_4 $year^{-1}$ (mean: 3.84 Tg CH_4 $year^{-1}$) (Weber et al., 2019) and 4–10 Tg CH_4 $year^{-1}$ (Saunois et al., 2020), with coastal oceans (<200 m depth) on average contributing ~70% of the total flux (Weber et al., 2019). The uncertainty in the coastal estimate (1.1–4.8 Tg CH_4 $year^{-1}$) is, however, considerably larger than that in the offshore estimate (0.8–2.0 Tg CH_4 $year^{-1}$) (Weber et al., 2019). The greater uncertainty for coastal waters arises to a large extent from undersampling relative to highly variable dissolved methane concentration ($[CH_4]$) distributions attributable to the complex interactions of production, consumption, and transport of methane in coastal environments. This is particularly true for land-ocean transitional zones, such as estuaries, bays, and fjords, where the effects of freshwater discharge, tidal actions, and gravitational circulations are more pronounced.

Estuaries usually receive large amounts of methane from river runoff (Middelburg et al., 2002; Borges and Abril, 2011). Additional methane may be added to estuarine surface waters through upward transport within the water column; this process, nonetheless, highly depends on the water depth and mixing conditions. In shallow tidal estuaries, upward transport can be an important source of methane to the surface water, leading to methane concentrations ($[CH_4]$s) of up to micromolar levels (Middelburg et al., 2002; Borges and Abril, 2011). In deep, stratified estuarine environments, however, much less deep methane

may reach the surface due to depressed vertical mixing and/or rapid microbial methane consumption in the bottom water (Lidstrim, 1983; Capelle et al., 2019; Chapter 2). Bottom waters in certain estuarine systems can be highly enriched with methane due to input from surface sediments in which biogenic methane accumulates (Fenchel et al., 1995; Capelle et al., 2019; Chapter 2) and/or from sub-seafloor gas/oil reservoirs containing methane of thermogenic and/or biogenic origin (Damm et al., 2005; Pinet et al., 2008; Lavoie et al., 2010). The sub-seafloor methane escapes into the water column often through gas vents, such as pockmarks, which are frequently spotted on continental shelves (Rogers et al., 2006; Forwick et al., 2009; Brothers et al., 2012). Biogenic methane is depleted with the stable isotope of ^{13}C relative to thermogenic methane, which can be used to discriminate the two sources (Whiticar, 1999).

In seasonally ice-covered estuarine systems, the presence of sea ice during winter adds another variable that not only directly hampers air-sea gas exchange (Lovely et al., 2015; Prytherch et al., 2017) but also affects the concentration and distribution of methane in the underlying seawater through brine rejection and drainage (Damm et al., 2015b, 2018; 2021).

Previous methane studies in estuarine environments were mostly conducted in shallow, riverine-dominated systems characterized by high methane concentrations and emission rates (Borges et al., 2011), while much less attention has been paid to large, deep, and stratified (i.e. marine-dominated) estuarine systems. On the eastern seaboard of North America, the surface area of the marine-dominated estuaries is comparable to that of the riverine-dominated estuaries (Cai, 2011), demonstrating the importance of considering both systems in assessing air-sea methane fluxes. Although the east coast of North America hosts some of the largest and most dynamic estuarine systems in the world (e.g. the Delaware estuary/Bay, Chesapeake Bay, and the St. Lawrence estuarine system), lack of data left them unmentioned in recent global compilations of surface water [CH_4]s and methane emission rates (Weber et al., 2019; Saunois et al., 2020). Here we report a multi-season, multi-year dataset on [CH_4] in the water column of the world's largest semi-enclosed estuarine system – the Gulf and Estuary of the St. Lawrence (EGSL) in eastern Canada, with the objectives of assessing the

emission rates of methane, identifying its origins, and elucidating the processes controlling its distribution in this immense estuarine environment.

3.4 REGIONAL SETTING

The EGSL is a seasonally ice-covered water body located at the southern limit of the subarctic zone. It stretches seaward from the landward limit of salt intrusion near Île d'Orléans (~5 km downstream of Quebec City) to the Straits of Cabot and Belle Isle connected to the Atlantic Ocean (Fig. 3-1a). The St. Lawrence estuary, ~400 km long, covers the section upstream of Pointe-des-Monts where it widens into the Gulf of St. Lawrence (GSL). An abrupt landward shoaling from 300 m to 50 m near Tadoussac subdivides the St. Lawrence estuary into the upper and lower estuary (El-Sabh and Silverberg, 1990) (Figs. 3-1a,b). The Upper Estuary (USLE), with a length of ~180 km and an area of 2500 km^2, is narrow (2–24 km wide) and shallow (mostly <30 m deep) (d'Anglejan, 1990). The Upper Estuary is deeper on the north side than on the south side and has a complex bottom topography featured with disconnected channels and troughs separated by ridges and islands (Fig. 3-1b). The Lower Estuary (LSLE) is much larger (area: 8900 km^2; length: ~220 km; width: 30–50 m) and deeper (~300 m) and possesses a relatively smooth topography characterized by the Laurentian Channel (LC), a deep (~300–535 m), wide (average: 50 km; maximum: 80 km), and U-shaped glaciated valley (Figs. 3-1a,b) (Strain, 1988; d'Anglejan, 1990). The LC traverses 1240 km from the eastern Canadian continental margin through the Gulf and the Lower Estuary and terminates at the Lower Estuary's head marked by a shallow (50 m depth), steep sill. The GSL is a semi-enclosed marginal sea covering an area of ~240 000 km^2 (Dufour and Ouellet, 2007). In the northeastern part of the Gulf, two troughs branch from the LC: the Esquiman Channel paralleling the west coast of Newfoundland and the Anticosti Channel which is connected to the Esquiman Channel and parallels the LC north of Anticosti Island. Other topographic features of the Gulf include the shallow (usually <75 m) Magdalen Shelf in the south and the restively isolated, narrow Mecatina Trough aligning with the north coast of the northeastern portion of the Gulf (Fig. 3-1a).

The EGSL receives its freshwater input mainly from the St. Lawrence River draining the Laurentian Great Lakes. With a drainage basin of ~1.32 × 10^6 km^2 and an annual mean freshwater discharge of 11 900 m^3 s^{-1}, the St. Lawrence River is ranked the second largest river system on the North America continent, only after the Mississippi River (El-Sabh, 1988). Additional freshwater delivery to the EGSL mostly comes from the Saguenay Fjord (mean annual discharge: 1 470 m^3 s^{-1}) and several smaller rivers (combined mean annual discharge: 1 440 m^3 s^{-1}) on the north shore of the lower estuary (El-Sabh, 1988).

The input of freshwater creates an estuarine circulation in the St. Lawrence estuary, with a seaward freshwater flow in the surface compensated by a landward seawater motion below. Superimposed on this general circulation are a multitude of local physical features throughout the entire system. In the upper reach of the Upper Estuary, strong tidal actions (mean tidal range: ~5 m) aided by shoaling bottom topography lead to extremely intense mixing and along-estuary salinity gradients. The downstream area of the Upper Estuary often witnesses frontal features partly associated with the complex bathymetry there and the outflow from the Saguenay Fjord (Ingram and El-Sabh, 1990). The abrupt bathymetric change at the head of the LC produces tidally induced upwelling that brings cold nutrient-laden subsurface water to the surface of the Lower Estuary (Therriault et al., 1990; Galbraith, 2006; Cyr et al., 2015). The large dimensions of the Lower Estuary, with its width many times larger than its internal Rossby radius (~10 km) (Lie and El-Sabh, 1983), allow for the development of mesoscale phenomena influenced by Coriolis effects such as cold and warm eddies in the central Lower Estuary and the buoyance-driven coastal jet along the south shore (Lie and El-Sabh, 1983; Mertz et al., 1988), making the St. Lawrence estuary one of the most laterally stratified estuaries worldwide (Larouche et al., 1987). After exiting the mouth of the Lower Estuary, the coastal jet is strengthened by the Anticosti cyclonic gyre in the northwest GSL to form the Gaspe Current, which carries freshwater from the St. Lawrence estuary into the Gulf and flows out through the south side of Cabot Strait. Atlantic surface water enters the Gulf via the north side of Cabot Strait and flows northeast along the west coast of Newfoundland, while Labrador Shelf water comes into the Gulf through the Strait of Belle Isle and moves west along the north shore of the Gulf (Fig. 3-1a).

The water column in the Upper Estuary varies from well mixed in the head region to partially stratified in the downstream area, particularly in the relatively deep northern channels. In contrast, the water column in the Lower Estuary and the Gulf is strongly and permanently stratified. In winter, the water column is characterized by two main layers: the near-freezing surface mixed layer (~75 m thick and salinity ~32 in the Gulf) containing locally formed water and Labrador Shelf water and the warmer (1–7°C) and saltier (salinity: 32–35) lower layer (> 75 m deep) composed of a mixture of North Atlantic Central Water (NACW) and Labrador Current Water (LCW) flowing landward through Cabot Strait (Galbraith, 2006; Bourgault et al., 2017). In spring, warming temperatures and increasing freshwater inputs stratify the surface water, leading to a three-layer structure that persists throughout the summer and fall seasons: the thin (~40 m thick), fresher surface layer (temperature: 3–20°C; salinity: 25–31), the cold intermediate layer (CIL) (temperature: −1.7–3°C; salinity: 31–32.6) located between 40 and 150 m, and the warmer, saltier deep layer (temperature: 3–7°C; salinity: 33–35) (Gilbert and Pettigrew, 1997; Galbraith, 2006; Bourgault et al., 2017). The three-layer structure reverts to the two-layer system during winter due principally to surface cooling and increased wind-driven mixing. In the Gulf, the CIL is a remnant of the preceding winter's cold surface water, whereas in the Lower Estuary it is advected from the Gulf (Ingram, 1979). The residence time of surface water in the Lower Estuary is ~4 months (Silverberg and Sundby, 1990), while it takes 4–7 years for a water parcel in the deep layer to travel from the mouth to the head of the LC (Bugden, 1988; Gilbert, 2004). The 100-m thick bottom layer in the Lower Estuary has been under hypoxic conditions (dissolved oxygen concentration <62.5 μmol L^{-1}) since the mid-1980s due to the permanent water column stratification combined with an increased biological oxygen demand and a reduced inflow of the cold, oxygen-rich LCW relative to the warm, oxygen-poor NACW (Gilbert et al., 2005; Jutras et al., 2020).

The tide in the St. Lawrence Estuary is semidiurnal, with a tidal range reaching nearly 5 m near the head (El-Sabh and Murty, 1990). The estuarine circulation, combined with tide- and wind-forced turbulence and asymmetrical ebb-flood tidal waves, generates a year-round turbidity maximum in the headward region between Île d'Orléans and Île-aux-Coudres where

suspended particle concentrations of 50 to 200 mg L^{-1} are commonly observed (d'Anglejan, 1990). The strong turbulent mixing in the Upper Estuary leads to negligible net deposition of particles and a floor covered mainly with sand and gravels (d'Anglejan and Brisebois, 1978; Silverberg and Sundby, 1979). The particulate matter introduced from the St. Lawrence River (6.5×10^6 tons $year^{-1}$, Rondeau et al., 2000) is mostly transported to the Lower Estuary and the Gulf and settles onto the floor of the LC (d'Anglejan, 1990). Sediments in the LC are typically fine-grained particulates (pelites) composed of, on average, 60% clay, 35% silt and 5% sand (Nota and Loring,1964). The floor and the northwest shoulder of the LC in the Lower Estuary host ~2000 pockmarks, with diameters ranging from a few tens of meters to 700 m (Pinet et al., 2008; Lavoie et al., 2010). The 15-km long Matane pockmark train composed of 109 linear-aligned pockmarks is a prominent geological feature on the floor of the Lower Estuary (Pinet et al., 2010). Authigenic carbonate concretions formed by microbial oxidation of pockmark-released methane have been spotted; video observations and echo-sounder images directly confirmed the presence of actively gas-venting pockmarks (Lavoie et al., 2010). Limited numbers of studies suggest that pockmarks are likely widespread on the seabed of the Gulf as well (Syvitski and Praeg, 1989; Josenhans et al., 1990; Sirdeys, 2019).

Strong mixing and high turbidity limit primary production in the Upper Estuary (Therriault et al., 1990). In the Lower Estuary and the Gulf, the more stable water column, in conjunction with nutrients delivered from the St. Lawrence River and upwelled near the head of the LC, leads to higher primary productivity, with peak values occurring in summer in the Lower Estuary (Therriault and Levasseur, 1986; Mei et al., 2010) and in spring in the Gulf (de Lafontaine et al., 1991; Mei et al., 2010). The Upper Estuary maintains an estuary-adapted, endemic community of zooplankton composed of planktonic and epibenthic copepods and mysids (Runge and Simard, 1990). In the Lower Estuary and the Gulf, the abundance, distribution, and species composition of zooplankton often exhibit substantial regional and seasonal variations, depending on water circulation and water column physical characters, particularly the positions and thermal properties of the CIL (Runge and Simard, 1990; Simard and Lavoie, 1999; Descroix et al., 2005; Harvey et al., 2009). Overall,

copepods of the *Calanus* species dominate mesozooplankton (Roy et al., 2000; Plourde et al., 2002), while *mysids* and *euphausiids* are among the prevailing macrozooplankton in the Lower Estuary and the Gulf (Descroix et al., 2005; Sourisseau et al., 2006). Macrozooplankton contribute a sizable portion (10–20%) of the total zooplankton biomass in the Lower Estuary and the Gulf (Harvey and Devine, 2009).

In summary, the EGSL is composed of three connected regions with widely different oceanographic features. The Upper Estuary resembles a typical macrotidal estuary dominated by physical mixing and abiotic processes, the Lower Estuary is more oceanic in nature and dominated by biological processes (Yeats, 1990), and the Gulf behaves like a shelf sea with larger-scale circulations and stronger biological-physical interactions (Strain, 1988). These features, alongside the large difference in the water renewal times of the surface and deep water in the LC, make the EGSL an ideal natural laboratory for examining the transport and biogeochemical cycling of bioactive elements. The presence of numerous pockmarks and extensive hypoxia make the EGSL even more appealing for methane-oriented research.

3.5 METHODS

3.5.1 Sampling

Table 3-1 lists the cruises undertaken and other relevant sampling information. A total of nine sampling campaigns covered all four seasons, with two in spring, one in summer, three in autumn, and three in winter. As all cruises were opportunistic, the area sampled and stations visited by each cruise were not always the same (Fig. 3-1c, Fig. 3-S1), depending on the primary purpose of the cruise and the resources available. Bulk water was taken from different depths of the water column with 12-L Niskin bottles mounted on standard conductivity-temperature-depth (CTD) rosettes. During the Jun-15, Oct-16, Jun-17, Nov-17, and Feb-19 cruises, the Niskin bottles were subsampled into 50-mL glass syringes (Popper & Sons) via a three-way nylon valve connected to a clean, thick-walled silicone tube (~10 cm long). Care was taken to avoid trapping air bubbles into the syringes during sample

transfer. Prior to sampling, the syringes were thoroughly flushed with the sample water before the final filling. All syringe samples were analyzed for [CH_4] aboard the ship immediately after sample collection. On all other occasions, the Niskin bottles were subsampled into 200-mL glass serum vials again via a clean, thick-walled silicone tube, following the water transfer procedure for collecting dissolved oxygen samples (Grasshoff et al., 2009). Each serum vial was overflowed about twice the volume of the vial to minimize the contact of the sample with air. The vial was then treated with 300 μL of supersaturated mercuric chloride before being closed with a PTFE-lined aluminum crimp seal. All the serum vials were pre-cleaned with acid-soaking and combustion at 450°C for 5 hours. In addition to collecting [CH_4] samples, the Nov-17 cruise also acquired samples for $\delta^{13}C_{CH4}$ using the same serum vial method. Owing to resource limitations, the Nov-17 cruised only sampled 2–4 depths, depending on the total water depth. In the LC and its branches, always four depths were sampled: surface (< 2.5 m), the core of the CIL, sub-CIL (mostly ~200 m), and bottom (3–15 m above the seafloor). All [CH_4] and $\delta^{13}C_{CH4}$ samples were collected in duplicate. The sample-filled serum vials were stored in the dark at ~4°C and transported to land-based laboratories for [CH_4] measurement in Rimouski, Canada and for $\delta^{13}C_{CH4}$ analysis at the Alfred Wegener Institute in Bremerhaven, Germany.

Air samples from the marine boundary layer were collected during the Oct-16 and Jun-17 cruises. Samples were drawn in duplicate at the bow, facing the wind, into 10-mL all-glass syringes and analyzed within minutes by direct injection into the methane analyzer. Prior to sampling, the internal wall of the syringes was water-moistened to ensure that the air samples had the same relative humidity (100%) as that in the standard gas (section 3.5.3).

3.5.2 Incubations

Incubations were conducted during the June-15 and Nov-17 cruises to determine the net cycling rates (i.e. consumption or production) of methane in the water column. Bulk water was collected using Niskin bottles from the surface (<5 m), the subsurface methane maximum (section 3.6.4), and near the bottom (~10 m above the seafloor) at selected stations

in the Lower Estuary and Gulf (stations 10R and 03R in June 2015, PM5, IF35 and IML10 in November 2017, and PM5 in February 2019. Fig 3-S1). The water in the Niskin bottles was subsampled in duplicate into 200-mL all-glass syringes (Jun-15 and Nov-17 cruises) or 200-mL serum vials (Feb-19 cruise) in the manner described in section 3.5.1. The syringes were closed with a three-way nylon valve and serum vials with a PTFE-lined aluminum crimp seal without adding any preservatives. The syringes and serum vials were incubated in the dark at the temperatures close to the *in-situ* temperatures of the incubated samples. [CH_4] in the incubating vessels was monitored at time intervals of days to weeks. Short-term incubations were performed aboard the ships while prolonged incubations were transferred to the land after the cruises.

3.5.3 Methane measurement

The procedures for [CH_4] and $\delta^{13}C_{CH4}$ measurements were exactly the same as those described in Section 2.5.2. Additional information for the EGSL surveys includes: The analyzer was calibrated with methane standards of 4.80 (Jun-15 cruise), 4.94 (Oct-16, Mar-17, Feb-18, and Feb-19 cruises) and 5.08 (Jun-17, Aug-17, Oct-17, and Nov-17 cruises) ppmv (Air Liquide) traceable to the National Institute of Standards and Technology; the mean relative deviation for all duplicate [CH_4] measurements (i.e. field and lab analyses combined) was 3.3%.

3.5.4 Ancillary measurements

Water depth, temperature, and salinity were recorded with a Sea-Bird SBE 9plus CTD, dissolved oxygen ([O_2]) with a Sea-Bird SBE 43 probe calibrated by the Winkler method (Grasshoff, 2009), and chlorophyll *a* fluorescence and turbidity with a Sea-Bird ECO FLNTU sensor (Oct-16, Mar-17, Jun-17, Aug-17, Nov-17, and Feb-18 cruises). During the Oct-17 and Feb-19 cruises, chlorophyll *a* fluorescence was recorded with a Seapoint fluorescence sensor and light transmission with a Wetlabs Cstar transmissometer.

3.5.5 Calculations of saturation ratio and air-sea flux

The saturation ratio (*SR*) of [CH_4] is defined as:

$$SR = {[CH_4]_{mea}}/{[CH_4]_{eq}} \quad (3\text{-}1)$$

Here $[CH_4]_{mea}$ (nmol L^{-1}) denotes the measured [CH_4] and $[CH_4]_{eq}$ (nmol L^{-1}) represents the [CH_4] equilibrated with the atmosphere. $[CH_4]_{eq}$ is calculated using the solubility data of Wiesenburg and Guinasso (1979) and an atmospheric methane mixing ratio of 1.92 ± 0.13 ppmv (n = 78) determined during the Oct-16 and Jun-17 cruises (section 3.1). The air-sea flux density of methane (*j*, µmol m^{-2} d^{-1}) is calculated according to Liss and Slater (1974):

$$j = k([CH_4]_{mea} - [CH_4]_{eq}) \quad (3\text{-}2)$$

Here *k* (cm h^{-1}) signifies the gas transfer velocity calculated using the formula of Raymond and Cole (2001) (k_{RC}, eq. 3-3) and that of Wanninkhof (2014) (k_{W14}, eq. 3-4) for ice-free seasons.

$$k_{RC} = 1.91e^{0.35U}({Sc}/{600})^{-0.5} \quad (3\text{-}3)$$

$$k_{W14} = 0.251\langle U^2\rangle({Sc}/{660})^{-0.5} \quad (3\text{-}4)$$

Here *U* stands for wind speed (m s^{-1}) at the 10-m height, $<U^2>$ for the average of wind speeds squared, and *Sc* for the Schmidt number of methane (Wanninkhof, 2014). Wind speed data, available online at the St. Lawrence Global Observatory website (https://ogsl.ca/en), were provided by the weather stations along the shores of the EGSL (Fig. 3-S1). Weather stations Cap Tourmente and Rivière-du-Loup provided wind speeds for the Upper Estuary, Pointe-au-Père for the Lower Estuary, Longue-Pointe-de-Mingan, Heath Point, Cap Whittle, Daniel's Harbour and Aéroport de Blanc-Sablon for the northern Gulf, and Cap-Chat, Aéroport de Sept-Îles, Cap-d'Espoir, Aéroport des Îles de la Madeleine, Port aux Basques, Heath Point to the southern Gulf (Sampling regions are shown in Fig. 3-1c (inset)). Monthly

wind speeds were averaged over the sampling day (24 h) and sampling month to assess the air-sea fluxes on the corresponding time scales.

Raymond and Cole (2001) reported three formulae for calculating k in estuarine environments based on data from floating dome studies, non-dome (i.e. tracer) studies, and a combination of the two, respectively. The dome data gives substantially higher k values than does the non-dome data, particularly above intermediate wind speeds. In this study, we chose the formula based on the composite data of the dome and non-dome studies to calculate k for the Upper Estuary. The Wanninkhof formula was adopted for the Lower Estuary and the Gulf due to their much larger dimensions relative to the Upper Estuary.

During the winter cruises (Table 3-1), the EGSL was partially covered with ice (Table 3-S1). The effective transfer velocity (k_{eff}, cm h^{-1}) in the presence of sea ice is calculated according to Prytherch et al. (2017):

$$k_{eff} = f \times k \tag{3-5}$$

Here f stands for the fraction of open water and k for the open water gas transfer velocity obtained from eqs. 3-3 and 3-4. Ice cover fractions (i.e. $1-f$) were estimated from weekly Geographic Information System (GIS) charts obtained from the Canadian Ice Service (https://iceweb1.cis.ec.gc.ca/Archive/page1.xhtml?lang=en). All charts were gridded on a 0.01° latitude by 0.015° longitude grid (approximately 1 km resolution). Ice coverage expressed in tenths was then converted to area for each pixel, which was summed for each subregion aforementioned. The total fraction was obtained by dividing the total ice cover area for a specific subregion by the surface area of that region. Note that eq. 3-5 was derived from direct measurements of k_{eff} using the eddy covariance technique (Prytherch et al., 2017). Earlier studies based on indirect measurements suggest that k_{eff} is generally higher than the transfer velocities derived from the wind speed-parameterizations under ice-free conditions, particularly at relatively low ice concentrations (Fanning and Torres, 1991; Loose et al., 2014; Lovely et al., 2015). Therefore, our methane flux estimates for the ice-covered seasons may represent the lower bounds.

3.6 RESULTS AND DISCUSSION

3.6.1 Surface water concentrations and estuarine mixing behavior

Means and ranges of surface-water [CH_4] ([CH_4]$_{surf}$) for different seasons and sub-regions, along with the parallel surface-water temperatures and salinities, are shown in Table 3-2. Based on the composite data combining all cruises, the mean [CH_4]$_{surf}$ decreased from 57.4 nmol L^{-1} (range: 12.5–392.8 nmol L^{-1}) in the Upper Estuary to 9.8 nmol L^{-1} (range: 4.8–21.0 nmol L^{-1}) in the Lower Estuary to 4.3 nmol L^{-1} in the Gulf (range: 2.8–8.9 nmol L^{-1}). [CH_4]$_{surf}$ for the entire EGSL system spanned from 2.8 to 392.8 nmol L^{-1} (mean: 13.3 nmol L^{-1}), which is within the lower end of the range (2–3600 nmol L^{-1}) measured in global estuarine waters (Middelburg et al., 2002; Borges and Abril, 2011; Upstill-Goddard and Barnes, 2016; Borges et al., 2018; Ye et al., 2019). This is consistent with the little accumulation of sediments in the USLE and the much greater depths of the LSLE and the GSL (section 3.4) in comparison with many other organic-rich and shallow estuarine systems, such as the Hudson River Estuary in the United States (De Angelis and Scranton,1993), the Ems Estuary in the Netherlands and Germany (Middelburg et al., 2002), and the Adyar River Estuary in India (Nirmal Rajkumar et al., 2008).

In the Gulf, winter showed the highest mean [CH_4]$_{surf}$ (6.2 nmol L^{-1}) among the four seasons, with the other three seasons exhibiting little variation (3.6–4.4 nmol L^{-1}) (Table 3-2). In the Lower Estuary, only two stations were sampled in summer (Figure 3-S1), making it difficult to assess the full seasonality of [CH_4]$_{surf}$. However, the mean [CH_4]$_{surf}$ in winter (16.5 nmol L^{-1}) was nearly twice those in spring (8.5 nmol L^{-1}) and autumn (8.9 nmol L^{-1}). In the Upper Estuary, the mean [CH_4]$_{surf}$ was again considerably higher in winter (92.9 nmol L^{-1}) than in autumn (51.0 nmol L^{-1}); comparisons with the other two seasons were, nonetheless, not possible due to the absence of summer data and with very limited spring data available (Table 3-2). The higher winter [CH_4]$_{surf}$ throughout the EGSL system could be partly due to a relatively stronger riverine input in winter. The St. Lawrence is a dam-regulated river system and its water flow during winter is higher than under unregulated

conditions. Calculated using the *Qmec* model developed by Bourgault and Matte (2020a, 2020b) and averaged over the relevant cruise periods, the freshwater discharge rate at Quebec City in winter (13883 $m^3 s^{-1}$) was lower than the peak flow during spring (15945 $m^3 s^{-1}$) but higher than those in summer （12690 $m^3 s^{-1}$） and autumn (12774 $m^3 s^{-1}$). Moreover, lower temperatures (Table 3-2) and the presence of sea ice (Table 3-S1) during the winter season could also have contributed to the higher winter $[CH_4]_{surf}$. Low temperatures increase the methane solubility and decrease microbial methane oxidation, while ice cover hinders outgassing from the water column to the atmosphere. Rejection of dissolved gases along with brine during sea ice formation could also increase $[CH_4]$ in the underlying water (Damm et al., 2015b).

The along-estuary distributions of $[CH_4]_{surf}$ in the Upper Estuary showed the highest concentrations in the turbidity maximum zone (TMZ) which was sampled in October 2017 (station ES12: 392.8 nmol L^{-1}) and February 2019 (station P2: 164.2 nmol L^{-1}) but left out or only partially covered during the other cruises due to resource limitations. The light transmissions at stations ES12 (22.4%) and P2 (0.5%) were among the lowest (and hence highest turbidities) observed within the respective cruises (Fig. 3-S2). High $[CH_4]$s have also been measured in the TMZs of the estuaries of the Humber, Forth, and Tay in the UK and have been ascribed to methane release from underlying anoxic sediments during particle resuspension and/or methanogenesis on tidally resuspended particles (Upstill-Goddard et al., 2000; Upstill-Goddard and Barnes, 2016). The TMZ in the USLE may receive additional methane released directly from the nearby Cap Tourmente intertidal marsh on the north shore and indirectly from the sediments eroded away from the marsh during autumn in part due to migratory birds feeding on the marsh plants (Serodes and Troude, 1984; Lucotte and d'Anglejan, 1986). The TMZ in the USLE is also enriched with dissolved and particulate organic matter (Xie et al., 2012), which could lead to enhanced abiotic methanogenesis through photodegradation of the organic matter (Zhang and Xie, 2015; Chapter 4). Note that Middelburg et al. (2002) observed $[CH_4]$ minima, instead of maxima, in the TMZs of certain European tidal estuaries and attributed this phenomenon to intense methane egress and oxidation and lower accumulation of organic matter and methanogenesis in sediments in the

TMZs due to strong currents and turbulent mixing. TMZ-associated processes can thus strengthen both the sources and sinks of methane. In the USLE, the extra methane sources introduced into the TMZ appeared to outweigh the enhanced sinks during the sampling periods.

Excluding the elevated $[CH_4]_{surf}$ data points in the TMZ, $[CH_4]_{surf}$ dropped rapidly with distance to Quebec City in the Upper Estuary (0–190 km) and continued to decrease, but at a much slower pace, further seaward along the main axis of the LC in the Lower Estuary and the Gulf (Fig. 3-2a). The composite data can be fitted to a single equation (inset in Fig. 3-2a), though the patterns for the individual cruises can be best described by different fits (Fig. 3-S3). Similar to the $[CH_4]_{surf}$ *vs*. distance patterns, the distributions of $[CH_4]_{surf}$ *vs.* salinity exhibited faster declining concentrations at relatively low salinities than at higher salinities (Fig. 3-2b). The difference in the decreasing pace between the two salinity zones was, however, substantially smaller than that for the $[CH_4]_{surf}$ *vs*. distance pattern. This was mainly caused by the extremely rapid salinity change within the limited length of the TMZ, which also explains the lack of data between salinity 4 and 13 (Fig. 3-2b). Excluding the Jun-15 cruise which only covered a limited area in the Gulf (Fig. 3-S1), the $[CH_4]_{surf}$ *vs.* salinity relationships for the individual cruises can all be delineated by a simple exponential decay manner save the Nov-17 and Feb-19 expeditions' linear decrease trends (Fig. 3-S4). The exponential decrease in $[CH_4]_{surf}$ with salinity indicates that methane underwent a fast net removal from the surface water during estuarine mixing in the inner Upper Estuary. Similar phenomena have been observed in other tidal estuaries and attributed to intense degassing, microbial oxidation, and dilution with low-$[CH_4]$ seawater in the upper reaches of the estuaries (Middelburg et al., 2002; Zhang et al., 2008; Borges et al., 2011; Ye et al., 2019). The linear relationships for the Nov-17 and Feb-19 cruises suggest that the $[CH_4]_{surf}$ dynamics during these periods was primarily controlled by physical mixing.

Significant lateral variations in $[CH_4]_{surf}$ were observed in the Lower Estuary and the northwest Gulf where cross-shore transects were sampled (Fig. 3-3). Except for transects 3S and 4S, stations near both the north and south shores generally exhibited higher

concentrations relative to those farther away from the shores due presumably to terrestrial freshwater discharge and/or upward diffusion of methane from shallow sediments near the coasts. $[CH_4]_{surf}$ along transects 3S and 4S increased northward, which was particularly evident for transect 4S. The north side of transect 3S could be marginally influenced by the freshwater runoff from the Bersimis River, while the northernmost station on transect 4S was close to the mouths of the Outardes and Manicouagan Rivers (Fig. 3-3). These three rivers combined are a significant source freshwater (9.7%) to the Lower Estuary (El-Sabh, 1988). Riverine inputs could thus be a key factor leading to the higher $[CH_4]_{surf}$ on the north sides of transects 3S and 4S. In the northwest Gulf, the southernmost stations on transects TSI and TASO displayed the highest concentrations on their respective transects, conforming to the fact that these two stations were located within the Gaspe Current carrying the freshwater from the St. Lawrence River (Fig. 3-1a; section 3.4)

3.6.2 Air-sea fluxes

The surface-water saturation ratios (*SR*), transfer velocities, and air-sea flux densities (*j*) of methane are compiled in Table 3-3. $[CH_4]_{surf}$ were always supersaturated (i.e. $SR > 1$) except for 9 occasions when $[CH_4]$s were essentially at equilibrium with the atmosphere (*SR*: 0.99-1.04). These near-saturations occurred exclusively in the Gulf: station 15R, 16R (Jun-15); TBB2, TBB4, TBB5, CH2, IF10 (Oct-16); CH7, CH8 (Jun-17) (Fig. 3-S1). Based on the composite data, the Upper Estuary showed the highest and the most variable saturation ratios (mean: 15.82; range: 3.67–126.28) followed sequentially by the Lower Estuary (mean: 2.75; range: 1.48–5.04), the south Gulf (mean: 1.33; range: 0.99–2.38), and the north Gulf (mean: 1.21; range: 1.03–2.29). The higher variability in the Upper Estuary could be principally attributed to the larger salinity range encountered (0.09–29.33) in comparison with the other subregions (24.03–32.75 save for the value of 16.83 for the nearshore station 11ML of Jun. 2017 near the head of the Lower Estuary). The mean flux density tracked a similar regional variation pattern: 31.02 (range: 2.11–336.8) μmol m^{-2} d^{-1} in the Upper Estuary, 5.47 (1.14–16.54) μmol m^{-2} d^{-1} in the Lower Estuary, 1.78 (−0.03–10.33) μmol m^{-2} d^{-1} in the south Gulf, and 1.30 (0.16–10.41) μmol m^{-2} d^{-1} in the north Gulf. The flux densities

in winter were lower than expected from its relatively higher saturation ratios and wind speeds due to the reduction of the transfer velocities by ice cover (eq. 3-5).

The mean flux density for the USLE (31.02 μmol m^{-2} d^{-1}) is at the lower bound of those reported for the European tidal estuaries (median: 222.6 μmol m^{-2} d^{-1}; range: 3.4-1558.2 μmol m^{-2} d^{-1}, excluding river plumes) (Upstill-Goddard and Barnes, 2016) and well below the mean methane flux density for global estuaries (150.0 μmol m^{-2} d^{-1}) estimated by Rosentreter et al. (2021). The USLE's value is, however, comparable to the mean methane flux density estimated for the global shallow (0–50 m deep) coastal waters (33.0 μmol m^{-2} d^{-1}; range: 12.6-59.8 μmol m^{-2} d^{-1}) (Weber et al., 2019). The mean flux density for the LSLE (5.47 μmol m^{-2} d^{-1}) is within the range reported for the global outer shelf waters (50–200 m; 3.8–12.7 μmol m^{-2} d^{-1}) (Weber et al., 2019), while the mean flux density for the entire GSL (1.63 μmol m^{-2} d^{-1}) is bracketed by the estimates for the global continental slope waters (200–2000 m; 1.1–3.2 μmol m^{-2} d^{-1}) (Weber et al., 2019). Note that the methane fluxes originally reported by Weber et al. (2019) are area-integrated rates. We converted these rates into flux densities using the areas of the above three ocean regions derived from the ETOPO1 Global Relief Model (Eakins and Sharman, 2012).

Area-integrated fluxes were calculated for each season and each subregion to yield annual fluxes for each subregion and the entire EGSL system (Table 3-4). The lack of $[CH_4]$ data for spring and summer in the Upper Estuary and for summer in the Lower Estuary (Table 3-2) prevents a direct assessment of the fluxes for these occasions. A tentative evaluation of these fluxes was made by assuming the average of the autumn and spring mean $[CH_4]_{surf}$ for the summer mean$[CH_4]_{surf}$ in the Lower Estuary and the autumn mean $[CH_4]_{surf}$ for the spring and summer mean $[CH_4]_{surf}$ in the Upper Estuary. The wind speeds for the assumed-$[CH_4]_{surf}$ occasions were used for calculating the transfer velocity. The uncertainty of this approach is unknown but is considered to be relatively smaller for the Lower Estuary case than for the Upper Estuary cases, given the rather small difference in the spring (8.5 ± 2.8 nmol L^{-1}) and autumn (8.9 ± 2.3 nmol L^{-1}) mean $[CH_4]_{surf}$ in the Lower Estuary (Table 3-2). The annual flux estimates indicate that, among the three subregions, the Gulf (117.7 × 10^6 mol $year^{-1}$) is

the largest methane source to the atmosphere, followed by the Upper Estuary (26.0×10^6 mol year^{-1}) and the Lower Estuary (14.8×10^6 mol year^{-1}) (Table 3-4). The flux for the Gulf is greatest due evidently to its much larger area compared to the other two sub-regions. The grand total for the entire EGSL is 158.4×10^6 mol year^{-1}, accounting for 0.28% of the global estuarine methane emission (56.3×10^9 mol year^{-1}, Rosentreter et al., 2021).

3.6.3 Vertical distributions in the Upper Estuary

Typical vertical distributions of [CH_4], along with those of salinity, temperature, [O_2], and turbidity (or light transmission), in the Upper Estuary are shown in Fig. 3-4. A station (MUCCI A) slightly upstream of the head of the estuary was added for comparison. The water column at station MUCCI A was essentially homogeneous based on the structures of salinity, temperature, and turbidity (Figs. 3-4b, c). Accordingly, there was little vertical variation in [CH_4], with only 2% difference between the bottom (41.6 nmol L^{-1}) and surface (40.8 nmol L^{-1}) (Fig. 3-4a). Stations P02 (Figs. 3-4d–f) and ES12 (Figs. 3-4g–i) were located in the TMZ and had partially stratified physical structures. [CH_4]s near the bottom at these two stations (station P02: 180.6 nmol L^{-1}; station ES12: 556.0 nmol L^{-1}) were substantially higher than those at the surface (station P02: 164.2 nmol L^{-1}; station ES12: 392.8 nmol L^{-1}), in line with the increased turbidities near the bottom. Strongly stratified temperature and salinity structures characterized stations ES4 (Figs. 3-4j–l) and P05 (Figs. 3-4m–o) located in the deeper troughs in the lower reach of the Upper Estuary. The [CH_4] profiles essentially mirrored those of salinity and the two variables were highly correlated (*r*: -0.983 for station ES4 and -0.999 for station P02). Downward diffusion, albeit limited by the intense density gradients, thus predominantly controlled the vertical distribution of [CH_4] there. The absence of elevated [CH_4]s near the bottom indicated no significant methane release from resuspended or underlying sediments, consistent with the low turbidities (i.e. high light transmissions) at stations ES4 and P05 (Figs. 3-4i,o) and the negligible deposition of fine sediments in most parts of the Upper Estuary (d'Anglejan and Brisebois, 1978; Silverberg and Sundby, 1979). The [O_2] profiles demonstrate that the water column was oxic throughout the Upper Estuary, precluding anaerobic methanogenesis as a major in situ methane source.

Throughout the water column of the Upper Estuary, [CH_4]s were well above the saturation concentrations at equilibrium with the atmosphere. Downward diffusion from surface water, upward diffusion from underlying sediments, and/or release from resuspended sediments thus exceeded microbial methane oxidation in the water column.

3.6.4 Vertical distributions in the Lower Estuary and the Gulf

Fig. 3-5 shows the vertical distributions of [CH_4], together with those of temperature, salinity, [O_2], and chlorophyll *a* fluorescence, along the main axis of the LC in the Lower Estuary and Gulf surveyed in October 2016 and June 2017 and along a cross-channel transect west of Cabot Strait visited in June 2015. The water column was always highly stratified, with temperature showing a typical 3-layer structure (i.e. warm surface layer, CIL, and warmer deep layer) in the LC (Figs. 3-5a,d,g). The vertical distributions of [CH_4] on both the along- and cross-channel sections were featured with a subsurface maximum (SMMax) often located at the base of the CIL but occasionally at or near the center of the CIL in the non-winter seasons (Figs. 3-5c,f,i). The SMMax was underlain by a [CH_4] minimum at depths of 150-400 m (referred to as deep [CH_4] minimum or DMMin), depending on location. Below the DMMin, [CH_4] gradually increased towards the bottom. Near-bottom [CH_4] maxima were spotted in the boundary area between the Lower Estuary and the Gulf (stations IF37–TSI14, Fig. 3-5c) and in the central Gulf (stations IF32 and TCEN2, Figs. 3-5c,f), suggestive of methane release from the underlying sediments. [CH_4]s were supersaturated by a factor of 1.44–4.66 at the SMMax, undersaturated by a factor of 1.14–20 at the DMMin, and close to saturation below the DMMin excluding the near-bottom maximum spots noted above. The bottom water of the Lower Estuary was hypoxic ([O_2] <62.5 μmol L^{-1}, Figs. 3-5b,e) but no significant correlation between [CH_4] and [O_2] was found (p = 0.17 for Oct-16; p = 0.79 for Jun-17). The hypoxic conditions thus are not a major contributor to the methane stock in the bottom water of the LSLE, consistent with an only modulating role of O_2-deficiency in methane formation seen in O_2-deficient waters worldwide (Naqvi et al., 2010).

Note that the SMMax and DMMin were present not only in the main LC and in spring and autumn (Fig. 3-5) but also in the LC's branches (i.e. the Esquiman and Anticosti Channels, data not shown) and in winter and summer (Fig. 3-6). This phenomenon is thus year-round and ubiquitous in the water column containing warmer deep water. No SMMax and DMMin were observed in areas where the warmer Atlantic water mass was absent, such as the shallow shelves (Fig. 3-5i), the Mecatina Trough in the northeast Gulf (Figs. 3-7a,b,e,f) and the Strait of Belle Isle (Figs. 3-7c,d,g,h).

The depth of the DMMin generally corresponded to the subtle temperature maximum (200–300 m) overlying the more thermally homogenous bottom water (Fig. 3-6). The deep water (>150 m) of the LC (and its branches) is composed of a mixture of cold LCW and warmer NACW, with the proportions of the two water masses changing with depth. The water between 150 and 300 m contains ~75% NACW, while the water below 300 m is fed more with the LCW (50-60%) (Jutras et al., 2020). The DMMin can then be explained by a combination of three factors: 1) the NACW endmember is warmer and thus lower in [CH_4] at its last ventilation; 2) the NACW in the EGSL has a much older ventilation age (>14 years) than does the LCW (a few months to a few years) (Mucci et al., 2011), allowing for longer microbial methane oxidation in the NACW; 3) the warmer temperature further enhances microbial consumption in the NACW. Here we tentatively estimated the net methane loss rate in the NACW using the DMMin observed at station TDC5 located near the center of Cabot Strait (Fig. 3-S1). The vertical profiles of [CH_4] at this station, collected during the Oct-16 and Jun-17 cruises, show the DMMin occurring at depths of 250–350 m with potential density (σ_θ) ranging from 27.079 to 27.442 kg m^{-3} (Fig. 3-S5). This range encompasses σ_θ of 27.25 kg m^{-3} that results from a mixture of the NACW and LCW with respective initial densities of 27.10 kg m^{-3} and temperature and salinity endmembers shown in Table 3-5 (Gilbert et al., 2005; Mucci et al., 2011). The fractions of NACW (f_{NACW}) and LCW (f_{LCW}) in the water with 27.25 kg m^{-3} σ_θ at station TDC5 can be calculated from these endmembers combined with the in situ temperatures (T_{mix}) and salinities (S_{mix}) (Table 3-5) using the following equations:

$$f_{\mathrm{NACW}}\mathrm{T}_{\mathrm{NACW}} + f_{\mathrm{LCW}}\mathrm{T}_{\mathrm{LCW}} = \mathrm{T}_{\mathrm{mix}} \quad (3\text{-}6)$$

$$f_{\mathrm{NACW}}\mathrm{S}_{\mathrm{NACW}} + f_{\mathrm{LCW}}\mathrm{S}_{\mathrm{LCW}} = \mathrm{S}_{\mathrm{mix}} \quad (3\text{-}7)$$

where $\mathrm{T}_{\mathrm{NACW}}$ and $\mathrm{T}_{\mathrm{LCW}}$ denote the NACW and LCW temperature endmembers, respectively, and $\mathrm{S}_{\mathrm{NACW}}$ and $\mathrm{S}_{\mathrm{LCW}}$ represent the two water masses' salinity endmembers. Rearranging eq. 3-6 yields:

$$f_{\mathrm{LCW}} = {}^{(\mathrm{T}_{\mathrm{mix}} - f_{\mathrm{NACW}}\mathrm{T}_{\mathrm{NACW}})}/_{\mathrm{T}_{\mathrm{LCW}}} \quad (3\text{-}8)$$

Substituting eq. 3-8 into eq. 3-7 and rearranging give:

$$f_{\mathrm{NACW}} = {}^{(\mathrm{T}_{\mathrm{LCW}}S_{mix} - T_{\mathrm{mix}}\mathrm{S}_{\mathrm{LCW}})}\Big/_{(\mathrm{T}_{\mathrm{LCW}}\mathrm{S}_{\mathrm{NACW}} - \mathrm{T}_{\mathrm{NACW}}\mathrm{S}_{\mathrm{LCW}})} \quad (3\text{-}9)$$

Substituting eq. 3-9 into eq. 3-8 yields f_{LCW}. The calculated f_{NACW} and f_{LCW} are ~60% and ~40%, respectively, during both the Oct-16 and Jun-17 cruises. The LCW parental water mass along the 27.10 kg m^{-3} isopycnal is outcropped to the east of the Grand Banks of Newfoundland (>200 km from land) (Robbins et al., 2000; Mucci et al., 2011), where the surface-water $[CH_4]$s are unknown. Based on the observation on the nearby Labrador shelf (Geng, 2017), here the LCW's $[CH_4]$ endmember ($[CH_4]_{\mathrm{end\text{-}LCW}}$) is assumed to be approximately equal to the saturation concentration at equilibrium with the atmosphere defined by the LCW's temperature and salinity endmembers (Table 3-5). The NACW parental water mass along the 27.10 kg m^{-3} isopycnal is formed in the northeast part of the subtropical gyre (Da Costa et al., 2005), where surface-water $[CH_4]$s are close to air saturation (Weber et al., 2019). The NACW's $[CH_4]$ endmember ($[CH_4]_{\mathrm{end\text{-}NACW}}$) can then again be calculated from its temperature and salinity endmembers (Table 3-5). The $[CH_4]$ at 27.25 kg m^{-3} σ_θ at station TDC5 expected from only a physical mixing of the NACW and LCW parental water masses is $f_{\mathrm{NACW}} \times [CH_4]_{\mathrm{end\text{-}NACW}} + f_{\mathrm{LCW}} \times [CH_4]_{\mathrm{end\text{-}LCW}}$, giving 3.1 nmol L^{-1} in both October 2016 and June 2017. The difference between this expected $[CH_4]$ and the in situ $[CH_4]$s ($\Delta[CH_4]$: 1.57 nmol L^{-1} for October 2016; 2.16 nmol L^{-1} for June 2017) is attributable to microbial methane oxidation during the travel of the parental water masses

from their ventilation sites to Cabot Strait. As the LCW is cold and only a few months old when it arrives at Cabot Strait (Mucci et al., 2011), microbial methane oxidation is likely minor (section 3.6.6). The loss of methane can thus be entirely attributed to microbial methane oxidation occurring in the NACW, which is warm and has a ventilation time of ~19 years in Cabot Strait (Robbins et al., 2000, Mucci, et al., 2011). Dividing $\Delta[CH_4]$ by the ventilation time yields net loss rates of methane in the NACW, 0.084 nmol L^{-1} $year^{-1}$in October 2016 and 0.11 nmol L^{-1} $year^{-1}$ in June 2017. These rates are comparable to that estimated by Scranton and Brewer (1978) for the North Atlantic Deep Water near its source (0.15 nmol L^{-1} $year^{-1}$, ~10 years old) but 2–3 times that estimated by Rehder et al. (1999) for the northern components of the North Atlantic Deep Water (0.042 nmol L^{-1} $year^{-1}$, 50°–60°N, >600 m deep). Rehder et al. (1999) attributed the relatively higher value of Scranton and Brewer (1978) partly to lateral mixing with "older" water. This might also be the case for our estimation here, since we did not account for the potential mixing of the NACW with "older" water during its passage from the formation site to Cabot Strait. Another factor likely contributing to this discrepancy is the enhanced microbial methane oxidation due to the warmer temperature of the NACW (11.1°C, Table 3-5) compared to the "young" NADW (mostly 2–5°C, Liu and Tanhua, 2019; Puerta et al., 2020), Q_{10} values for aerobic microbial methane oxidation in seawater are unknown but are 3.4–4.4 in waters of two Arctic Alaskan lakes (Lofton et al., 2014), 1.4–2.1 in subarctic peat soils (Dunfield et al., 1993), and ~2.6 in a sandy landfill cover soil (Park et al., 2005). These values roughly fall into the Q_{10} range of 1.8–3.3 for heterotrophic bacterial respiration rates (Genovesi et al., 2011). Applying this Q_{10} range to deep open-ocean waters will increase Rehder et al.'s (1999) methane oxidation rate by 1.4 and 2.9 times (i.e. to 0.060 and 0.12 nmol L^{-1} $year^{-1}$) for increases in temperature of 6 and 9°C, respectively. The temperature effect alone could thus account for the discrepancy between our study and Rehder et al.'s (1999).

The formation of the SMMax is apparently linked to the presence of the DMMin immediately beneath and the lower temperatures of the CIL (and thus higher equilibrium $[CH_4]$s) within which the SMMax were located (Figs. 3-5, 3-6). However, the colder

temperatures could not fully account for the elevated [CH_4]s because 1) most of the SMMax were situated at the base of the CIL instead of its coldest center and 2) the [CH_4]s within the SMMax were highly supersaturated (Figs. 3-5, 3-6). Other processes which could contribute to the formation of the SMMax included an advection of methane through Cabot Strait from shelf waters outside of the EGSL, advection of methane released from local shelf sediments, and/or in situ production. Given that most of the subsurface [CH_4] maxima were distributed within a narrow range of σ_θ (Fig. 3-8a), advection could be significantly implicated from a physical perspective. At an estimated pace of 10 km day^{-1} (Bourgault et al., 2017), it takes ~75 days for a water parcel in the CIL to move from Cabot Strait to the head of the LC. If the advection from the outer shelf were the dominant process responsible for the presence of the SMMax in the EGSL, one would expect the SMMax to progressively diminish or at least stay stable towards the channel's head. The observation, nonetheless, showed an opposite trend, with the SMMax in the head zone being 2.4 times higher than that in Cabot Strait during both the Oct-16 and Jun-17 cruises (Fig. 3-8b). Advection from the outer shelf was thus unlikely the primary driver for maintaining the SMMax. The same argument can be invoked to exclude shelf sediments in the Gulf as the principal source of the SMMax seen in the entire the Lower Estuary and Gulf. In fact, several cross-channel sections in the Gulf (Fig. 3-5i, Fig 3-S6) showed higher [CH_4]s in the central channel than in shelf waters at the depths of the SMMax, making it unlikely for a net transport of shelf sediments-released methane to the central channel. In the Lower Estuary, we do not have sufficient data to prove or disprove a significant role of shelf sediments-released methane in maintaining the supersaturation of [CH_4] within the SMMax. However, given the existence of pockmarks on the northern shoulder (particularly on the northwestern shoulder of the LC) and some of them are located at water depths of as shallow as 60 m (Pinet et al., 2008; Lavoie et al., 2010), it was possible that those shallow and active (if any) pockmarks released methane that was then dissolved in the overlying water column and advected offshore to form or strengthen the SMMax in local areas.

In situ production of methane within anoxic microniches of organic particles, including zooplankton fecal pellets (Karl and Tilbrook, 1994; Holmes et al., 2000), and in

gastrointestinal tracts of zooplankton (de Angelis and Lee, 1994) is another plausible explanation for the SMMax observed. Zooplankton-associated methane production has been frequently proposed to account for supersaturated [CH_4]s in oxic upper oceans, including subsurface methane maxima (Oremland, 1979; de Angelis and Lee, 1994; Karl and Tilbrook, 1994; Holmes et al., 2000; Schmale et al., 2017; Stawiarski et al., 2019). The zooplankton pathway could be relevant in the LSLE and GSL, since this region has particularly high zooplankton biomass compared to other coastal environments (de Lafontaine et al., 1991). In the GSL, fecal pellets-associated downward carbon fluxes at depths of 50–100 m have been estimated to be >50% of the total particulate carbon fluxes (Roy et al., 2000; Genin et al., 2021). Moreover, macrozooplankton occupies a sizable proportion (10–20%) of the total zooplankton biomass in the LSLE and GSL (Harvey and Devine, 2007). It is well known that krill, a major component of the macrozooplankton in this region, form rich aggregations in the northwest Gulf and near the head of the LC (Simard and Lavoie, 1999; Sourisseau et al., 2006). This distribution pattern is similar to the along-channel distribution of the SMMax during the Oct-16 cruise (Fig. 3-8). It remains to be elucidated whether this similarity is coincidental or the krill did play a consequential role in forming the SMMax.

Other in situ methane production processes in the water column include microbial degradation of methylphosphate (Karl et al., 2008; Repeta et al., 2016; Ye et al., 2020) and dimethylsulfoniopropionate (DMSP) (Damm et al., 2008; Damm et al., 2010; Damm et al., 2015a) under phosphate- and nitrate-stressed environments, respectively. The CIL and deep layer of the EGSL are, however, rich in inorganic nutrients (Greisman and Ingram, 1977; Cyr et al., 2015) and thus unfavorable for the organic phosphorus- and DMSP-based methane production. Metabolic activity of certain phytoplankton species (e.g. *Emiliania huxleyi*, *Phaeocystis sp.*, and *Phaeocystis globosa*) (Lenhart et al., 2016; Klintzsch et al., 2019) and cyanobacteria (Bižić et al., 2020) can also produce methane. The SMMax was, nevertheless, located at the depths (14–151 m, mostly >50 m) with little or no light for photosynthesis, consistent with the very low chlorophyll *a* fluorescence values at these depths (Figs. 3-5, 3-6). Although cyanobacteria can produce methane in the dark (Bižić et al., 2020), they are scarce and generally undetectable in the subsurface and deep waters of the LSLE (Cui et al.,

2020). Abiotic methanogenesis through photodegradation of chromophoric dissolved organic matter (CDOM) is another potential mechanism for methane accumulation under oxic conditions (Zhang and Xie, 2015; Chapter 4). Nonetheless, as little solar radiation can reach the depths of the SMMax, the photochemical pathway should be largely irrelevant as well.

An attempt was made to use the [CH_4] profiles to estimate the net methane production rates required to maintain the SMMax at two selected stations visited during the Jun-17 cruise: station T1 at the head of the LC (Fig. 3-S7) and station CH4 slightly to the west of Cabot Strait (Fig. 3-6). Assuming quasi-steady conditions and negligible net lateral fluxes at the depths of the SMMax, the vertical methane transport flux (F_v, μmol m^{-2} s^{-1}) can be calculated as follows:

$$F_v = K_e \left({}^{d[\mathrm{CH_4}]}/_{dz} \right) \tag{3-10}$$

where K_e (m^2 s^{-1}) denotes the eddy diffusivity at the depth of the SMMax (24.9 m at station T1 and 143.9 m at station CH4), d[CH_4]/dz (μmol m^{-4}) for the [CH_4] gradients within the depth range bracketed by the sampling depths immediately above and below the SMMax. The upward and downward [CH_4] gradients were, respectively, 0.15 and 0.11 μmol m^{-4} at station T1 and 0.015 and 0.067 μmol m^{-4} at station CH4. K_e has been estimated to be ~4.5×10^{-2} m^2 s^{-1} for the 25–50 m depth range at the head of the LC (Cyr et al., 2015) and ~2×10^{-5} m^2 s^{-1} for the 100–275 m depth range determined at a station off Rimouski, about 100 km downstream of the head of the LC (Bourgault et al., 2012b). The latter value has also been assumed for the LC in the Gulf (Bourgault et al., 2012b) and is thus used for station CH4 in this study. The much higher K_e at the head of the LC has been attributed to various sill-associated physical processes at this locality, including shear instabilities, internal tides, bottom friction, lee waves, hydraulic jumps, nonlinear internal waves, and vortical structures (Cyr et al., 2015). The net methane production rate (P_{CH4}, μmol m^{-3} s^{-1}) can then be estimated as:

$$P_{CH4} = {}^{dF_v}/_{dz} \tag{3-11}$$

The estimated net production rates are ~40 nmol L^{-1} d^{-1} at station T1 and 2.8 $\times 10^{-3}$ nmol L^{-1} d^{-1} at station CH4. The net production rate is four orders of magnitude larger at station T1. About three quarters of this difference were contributed by the much larger K_e at station T1 and one quarter by the relatively larger [CH_4] gradients at this station.

Eq. 3-10 also derives an upward methane flux of 596.5 µmol m^{-2} d^{-1} from the station T1 SMMax to the surface. Taking an area of ~100 km^2 with a K_e value of ~4.5 $\times$ 10^{-2} m^2 s^{-1} (Cyr et al., 2015) yields 5.96 $\times$ 10^4 mol CH_4 d^{-1} or 5.37 $\times$ 10^6 mol CH_4 over the spring of 2017 being transported into the surface. The time-integrated flux is 28% higher than the atmospheric emission of methane in the Lower Estuary during the same season (4.18 $\times$ 10^6 mol, Table 3-4). Hence, the pumping of methane from the SMMax alone could more than account for the methane emission to the atmosphere and part of the pumped methane may contribute to the methane budget in the Gulf. In addition, the amount of methane pumped into the surface water during the spring is 3.5 times the annual methane input from the Saguenay River into the St. Lawrence estuary (1.55 $\times$ 10^6 mol, Chapter 4).

3.6.5 Pockmarks

Five pockmark sites in total were visited: one (station Bis) was located in the LC off Mont Joli and the rest (stations PM2, PM3, PM5, and PM8) were all on the Matane pockmark train (Fig. 3-9d). Stations Bis and PM3 were sampled one time, whereas the other three stations were sampled multiple times (Table 3-6) The targeted coordinates of these sites were obtained from the database of the Geological Survey of Canada. The real sampling coordinates, however, deviated from the targeted ones often by tens of meters to a few hundred meters but the deviation reached 1390 m at station PM8 during the Jun-17 cruise (Table 3-6).

The [CH_4] vertical profiles collected from the pockmark stations were similar to those at the nearby non-pockmark stations in the LC except that the near-bottom [CH_4]s at the pockmark stations were elevated due supposedly to the discharge of methane from the

pockmarks (Fig. 3-9a). The near-bottom [CH_4]s were highly variable (range: 10.4–695.3 nmol L^{-1}; mean: 214.2 nmol L^{-1}; median: 135.0 nmol L^{-1}) between different stations during a given cruise and between different cruises at a given station (Fig. 3-9a, Table 3-6). The highest concentration (695.3 nmol L^{-1}) is above the levels (<500 nmol L^{-1}) typically found around natural gas seeps (e.g. Valentine et al., 2001; Gant and Whiticar, 2002; Mau et al., 2007; Reeburg, 2007).

Both the highest (695.3 nmol L^{-1}) and lowest (10.4 nmol L^{-1}) near-bottom [CH_4]s were measured at station PM5. This station was sampled five times, with variable distances between the sampling and targeted coordinates (25–489 m) and between the bottommost sampling depths and the seabed (2.6–15 m) (Table 3-6). The lowest [CH_4] was found at 489 m southwest of the targeted coordinates during the Feb-18 cruise, which was the largest deviation among the five samplings. Given that the diameters of the pockmarks in the St. Lawrence estuary are usually <300 m (Pinet et al., 2008), the 489-m deviation was likely outside of the perimeter of the pockmark, thereby at least partly explaining the low [CH_4] observed. In addition to the horizontal distance deviation, the sampling distance above the seabed should also contribute to the variability of the near-bottom [CH_4]. The is confirmed by the near-exponential decrease in the near-bottom [CH_4] as a function of the combined effects of the horizontal and vertical distance deviations at station PM5 (Fig. 3-S8). The dependence of the near-bottom [CH_4] on the vertical distance deviation was stronger than on the horizontal one (the power of 1.4 *vs.* 1), consistent with the notion that diapycnal diffusion is slower than isopycnal diffusion. Extrapolating the horizontal and vertical distance deviations to zeros yields a [CH_4] of 5785 nmol L^{-1} that supposedly represents the [CH_4] at the gas venting center. Note that station PM5 was sampled twice during the Feb-18 cruise only 3 hours apart. The second cast was much closer to the targeted position (horizontal distance deviation: 24 m) and gave a much higher near-bottom [CH_4] (418.5 nmol L^{-1}) relative to the first cast (10.4 nmol L^{-1}). As the bottommost sampling depths of these two casts were on the same isopycnal (27.282 kg m^{-3}) and the first cast was located 464 m downstream of the second one against the landward deep current (section 3.4), the huge difference in the near-bottom [CH_4] between the two casts suggests rapid dilution and/or

microbial oxidation of methane during the downstream transport along the isopycnal. Given that the deep current flows at ~1 km d^{-1} (Bourgault et al., 2017), it takes ~0.5 d for a water parcel to move from the second cast position to the first one, leading to a methane loss rate (dilution plus microbial oxidation) of ~816 nmol L^{-1} d^{-1}.

Stations PM2 and PM8 were each sampled twice, with similar vertical distances from the bottommost sampling depths to the seabed but variable horizontal distance deviations (Table 3-6). The horizontal distance deviation was particularly large for station PM5 during the Jun-17 cruise (1390 m). The near-bottom [CH_4]s at these two stations exhibited an opposite trend found for station PM5 in relation to the horizontal and vertical distances (Table 3-6). This could be due to the migration of the gas discharge center since the last survey in case of station PM2 or to different pockmarks sampled in case of station PM8 based on the very large horizontal distance deviation during the Jun-17 survey. Alternatively, the originally determined coordinates of the PM2 pockmark might somewhat deviate from the fluid venting center. Interference by gas diffusion from adjacent pockmarks could be another possibility (see below) in light of the high density of pockmarks along the linear Matane pockmark train (109 pockmarks across 15 km, Pinet et al., 2010).

Another interesting feature is the "Z-shaped" distribution of [CH_4] observed below 250 m at station PM5 during the Oct-16 and Feb-19 expeditions (Fig. 3-9b). The Feb-19 site was only 26 m east of the Oct-16 site but the maximum and minimum [CH_4]s within the "Z-shaped" structure were 9 and 14 times lower at the Feb-19 site. This large difference could arise from a much lower gas discharge rate of the pockmark during the Feb-19 cruise. It was also plausible that the Feb-19 site was outside of the methane discharge zone but the "Z-shaped" structure was a residue of the parental structure directly located over the discharge zone. The residual structure could be formed through physical transport during which methane underwent fast dilution and/or microbial oxidation. The causes for forming the "Z-shaped" structure are unclear but might be linked to continuous gas discharge at two different depths or sporadic gas eruptions from a single depth combined with rapid dilution and/or microbial oxidation during upward diffusion.

In contrast to the strong near-bottom vertical [CH_4] gradients within the "Z-shaped" structures described above, relatively homogeneous [CH_4]s were observed within the deepest sampling layer of ~20 m at stations PM3, PM5 (Feb-18, first cast), and Bis (Fig. 3-9b). This character could be associated with enhanced vertical eddy diffusion caused by strong boundary mixing near the bottom of these sampling sites (Bourgault et al., 2012b). As elaborated for station PM5 (first cast) earlier, the near-bottom methane at stations PM3 and Bis could also originate from the nearby active pockmarks through advection. Then physical dilution, microbial oxidation, and increasing bottomward eddy diffusion would operate in concert to diminish the near-bottom vertical [CH_4] gradients during the advection. The ease of horizontal diffusion was evidenced by the fact that the most elevated near-bottom [CH_4]s measured at the pockmark stations were located exclusively within a small density interval of 27.1–27.3 (Fig. 3-9c). It is, however, noteworthy that the influence of horizontal diffusion might be limited in distance, as discussed above for the case of station PM5, due to rapid physical dilution and/or microbial oxidation.

The [CH_4] profiles at the pockmark stations also exhibited the DMMin typical of other stations located in the LC and its branches (section 3.6.4). The presence of this DMMin demonstrated that the pockmark-released methane was not diffused into the surface water and then egressed to the atmosphere. For the reasons explained above, it was unlikely for this methane to be advected to the head of the LC and then upwelled to the surface water. Therefore, the pockmark-derived methane in the deep channel floor is lost to dilution and microbial oxidation before reaching the surface and emitting to the atmosphere. This, however, does not exclude the possibility that methane, if any, emanating from the shallower pockmarks (shallowest ~65 m, Pinet et al., 2008) may be transferred to the air. Studies focusing on the shallow pockmarks are needed to resolve this issue.

Assuming a quasi-steady condition, the diffusive methane efflux (F_d, μmol m^{-2} s^{-1}) from pockmark PM5 at the Oct-16 sampling site is estimated as follows:

$$F_d = K_e \left({}^{d[\mathrm{CH_4}]}/_{dz} \right) + u([\mathrm{CH_4}]_{\mathrm{in}} - [\mathrm{CH_4}]_{\mathrm{out}}) \quad (3\text{-}12)$$

where K_e ($m^2\ s^{-1}$) denotes the eddy diffusivity at the bottommost sampling depth (291.4 m), $d[CH_4]/dz$ (82.5 µmol m^{-4}) for the $[CH_4]$ gradient defined by the two deepest sampling depths (286.1 and 291.4 m, Fig. 3-9b), u (0.012 m s^{-1}) represents the landward bottom water current speed (Bourgault et al., 2017), and $[CH_4]_{in}$ and $[CH_4]_{out}$ (µmol m^{-3}) are the $[CH_4]$s inside and outside the pockmark plume at the bottommost sampling depth. K_e at 291.4 m is calculated to be 1.88×10^{-4} $m^2\ s^{-1}$ using the equation of Bourgault et al. (2012b) developed for the water column in the LC off Rimouski, about 89 km upstream of station PM5. $[CH_4]_{in}$ is equal to the $[CH_4]$ at 291.4 m (695.3 µmol m^{-3}, σ_θ = 27.205 kg m^{-3}) and $[CH_4]_{out}$ is taken to be 1.5 µmol m^{-3} measured at a similar σ_θ (27.219 kg m^{-3}, 299.8 m depth) at station IF37 which was the closest non-pockmark station upstream of station PM5 in the sense of against the landward bottom current. The calculated eddy diffusion flux (i.e. the first term in eq. 3-12) is 1.55×10^{-2} µmol $m^2\ s^{-1}$ (or 1.34 mmol $m^2\ d^{-1}$) and the advection flux (i.e. the second term in eq. 3-12) is 8.03 µmol $m^2\ s^{-1}$ (or 694 mmol $m^2\ d^{-1}$). The vertical diffusion is thus negligible compared with the horizontal advection. This flux estimate is likely a lower limit, since the bottommost sampling depth was 2.6 m above the seabed and $[CH_4]$ should further increase towards the floor. This estimate also excludes any ebullition of methane above the bottommost sampling depth. In fact, previous studies documented video images showing gas expulsion from certain pockmarks (Bolduc et al., 2008; Lavoie et al., 2010) but the heights that the bubbles reach before they are completely dissolved in seawater are unknown. It is impossible at this stage to estimate the area-integrated diffusive flux of the pockmark-derived methane based on the collected $[CH_4]$ profiles because the pockmarks' areas over which gases are actively vented are unknown and because the gas venting rates are highly variable among different pockmarks.

3.6.6 Incubation-based net cycling rates

The lab incubations did not show conspicuous or consistent production or consumption of methane in the surface water samples within incubation times of a few days (station 10R) to 85 days (station PM5, Nov-17, referred to as PM5-1 hereinafter) (Fig. 3-10a). The same was true for the 3.5-day incubation of the SMMax sample collected from station 03R (Fig.

3-10b). [CH_4] in the SMMax sample from station IF35, however, increased consistently over the 71-day incubation, albeit slowly (0.0068 nmol L^{-1} d^{-1}). This value is on the same order of magnitude of the net production estimated for the Gulf station CH4 (0.0028 nmol L^{-1} d^{-1}) using the mass budgeting approach (Section 3.6.4). On the other hand, the SMMax sample from station IML10 revealed an exponential decay of [CH_4], with a net loss rate constant (k_{CH4}) of 0.0039 d^{-1} (turnover time, τ_{CH4}: 256 days), demonstrating a net microbial consumption of methane at this locality. The samples from the bottommost sampling depths either exhibited no consistent production or consumption of methane (station IML10) or displayed exponential decay of [CH_4], with k_{CH4} values of 0.025 d^{-1} (τ_{CH4}: 40 days) at station 10R, 0.031 d^{-1} (τ_{CH4}: 33.3 days) at station PM5 (Feb-19, referred to as PM5-2 hereinafter), and 0.012 d^{-1} (τ_{CH4}: 83.3 days) at station PM5-1.

Although the k_{CH4} value for the non-pockmark station 10R is within the range for the two pockmark stations, the translated net consumption rate at the former (0.17 nmol L^{-1} d^{-1}) is much lower than those at the latter (2.30 nmol L^{-1} d^{-1} at station PM5-2; 1.82 nmol L^{-1} d^{-1} at station PM5-1) due to near-bottom in situ [CH_4] at station 10R (6.65 nmol L^{-1}) being much lower than those at stations PM5-2 (74.1 nmol L^{-1}) and PM5-1 (152.0 nmol L^{-1}). Assuming that the k_{CH4} measured at station PM5 during the Feb-19 cruise is also applicable to the Oct-16 sampling at this station when the near-bottom [CH_4] was determined to be 695.3 nmol L^{-1} and the extrapolated seafloor [CH_4] reached 5785 nmol L^{-1} (Section 3.6.5), the consumption rate will increase to 21.6 and 179.3 nmol L^{-1} d^{-1}, respectively. These rates are at the upper bounds of the aerobic methane oxidation rates reported for marine waters worldwide, including those affected by submarine gas seeps and anthropogenic oil spills (Mau et al., 2020 and references therein). These high methane consumption rates are also consistent with the presence of greenish bacterial mats, supposedly composed of methanotrophs, on the seafloor surrounding gas-venting pockmarks in the LSLE (Bolduc et al., 2008; Lavoie et al., 2010) and with the discovery of methane-derived authigenic carbonate cements in sediments at certain pockmark sites in this region (Lavoie et al., 2010; Savard et al., 2021).

3.6.7 Distributions of $\delta^{13}C_{CH4}$ and sources of methane

The ranges and mean values of $\delta^{13}C_{CH4}$ for different sub-regions of the EGSL and different depth layers are summarized in Table 3-7. In spite of the large salinity variation (0.09–29.3) in the surface water of the Upper Estuary, its $\delta^{13}C_{CH4}$ fell in a rather small range (−37.9‰ to −29.5‰) with a mean value of −32.2‰. The mean $\delta^{13}C_{CH4}$ for the deeper waters (−33.4‰) in the Upper Estuary was only marginally lower than its counterpart in the surface water. The surface-water mean $\delta^{13}C_{CH4}$ for the Gulf (−32.6‰) was similar to that in the Upper Estuary but slightly higher than that in the Lower Estuary (−30.2‰). The mean $\delta^{13}C_{CH4}$ for each of the four layers sampled in the Gulf was always somewhat more negative compared with that for the corresponding layer in the Lower Estuary. Among the four layers, the core of the CIL displayed the most negative mean $\delta^{13}C_{CH4}$ in both the Lower Estuary and the Gulf. The mean $\delta^{13}C_{CH4}$ for the core of the CIL (−35.7‰), the Lower Estuary and the Gulf combined, was 14.0% lower than that in the surface (−31.3‰) and 5.9% lower than that in the sub-CIL layer (−33.7‰). These differences, albeit small, are significant ($p < 0.01$) based on *t*-test paired sample for means. An inspection of the depth distributions of $\delta^{13}C_{CH4}$ at the individual stations indicates that $\delta^{13}C_{CH4}$ at the core of the CIL was lower than those in both the surface and the sub-CIL layers for all stations excepting station PM2 (Fig. 3-11b). The $\delta^{13}C_{CH4}$ *vs.* [CH_4] plot does not show clear trends for both the composite data set and the individual data sets for different sub-regions and depth layers (Fig. 3-12a). An exception is the bottom data collected from the LC and its branches, which reveals an exponential rise of $\delta^{13}C_{CH4}$ with increasing [CH_4] excluding station PM5 (Fig. 3-12b).

One striking feature for the entire $\delta^{13}C_{CH4}$ data set is its narrow range (−40.9‰ to −27.4‰) and ^{13}C-enriched values (mean ± s.d.: −34.4‰ ± 3.3‰). All $\delta^{13}C_{CH4}$ values exceed the upper-bound $\delta^{13}C_{CH4}$ for biogenic methane (−50‰) (Whiticar, 1999) and are above the atmospheric equilibrium value of −45‰ (Damm et al., 2015b). Hence, the methane pool in the EGSL is mainly of thermogenic origin or largely composed of highly oxidized biogenic methane or a mixture of the two. In fact, even at the head of the Upper Estuary (salinity: 0.1), the $\delta^{13}C_{CH4}$ values ($\delta^{13}C_{CH4}$: −37.6‰ to −38.4‰) are already far greater than the biogenic

upper bound. At least two factors could contribute to this ^{13}C-enrichment in the St. Lawrence River water. First, waters in the Laurentian Great Lakes, which discharge ~70% of the total freshwater into the St. Lawrence River, have very long residence times (2.6–191 years) (Hudon et al., 2017), allowing for extensive microbial oxidation of methane before the waters outflow to the river. Moreover, microbial oxidation over the long transit from the head of the river to the head of the Upper Estuary (550 km) further enriches the ^{13}C content. Second, large areas of the watersheds draining into the St. Lawrence River are covered by boreal forests (Hudon et al., 2017). It has been posited that methane in rivers with forested watersheds tends to be ^{13}C-enriched compared with methane in rivers with marshy watersheds (Sansone et al., 1999). Similarly enriched $\delta^{13}C_{CH4}$ signatures have been reported for the Oyster and Picassic Rivers in New Hampshire, US that run through forests (Sansone et al., 1999). It is interesting to note that the freshwater near the head of the Saguenay Fjord, which is the largest tributary of the St. Lawrence estuary, also possesses a $\delta^{13}C_{CH4}$ signature of greater than −50‰ (Chapter 2). The Saguenay Fjord receives freshwater via the Saguenay River from Lac Saint-Jean with a boreal forests-covered watershed. However, Lac Saint-Jean (volume: 11.9 km^3) is much smaller than the Great Lakes and the Saguenay River (length: 170 km) is much shorter than the St. Lawrence River, leading to far less time available for methane in Lac Saint-Jean to undergo oxidation before being transported into the fjord. That may partly explain why the $\delta^{13}C_{CH4}$ value near the head of the Saguenay Fjord (−45.018‰), albeit above the upper bound of biogenic methane, is substantially more negative than those at the head of the USLE.

In addition to the surficial runoff, the St. Lawrence River and the EGSL also receive groundwater discharge (Chaillou et al., 2018) but the contribution of groundwater discharge to the total freshwater budget in the EGSL is unknown. $[CH_4]$s ranging from <0.04 to 2869 μmol L^{-1} (mean: 238 μmol L^{-1}) have been reported for shallow aquifers in the St. Lawrence Lowlands west of Quebec City (Moritz et al., 2015). Methane in these aquifers is, however, predominantly biogenic (Moritz et al., 2015; Bordeleau et al., 2018). The enriched $\delta^{13}C_{CH4}$ signatures detected throughout the surface EGSL suggest that the contribution of groundwater methane to the total freshwater methane input into the EGSL is minor or that

methane in the groundwater becomes sufficiently depleted in ^{13}C due to various isotopic fractionation processes (e.g. microbial oxidation, degassing, and migration) before being delivered into the EGSL.

Besides the $\delta^{13}C_{CH4}$-heavy freshwater source, another important process leading to the enriched $\delta^{13}C_{CH4}$ signatures in the surface water of the EGSL could be the upwelling at the head of the LC (Therriault et al., 1990; Galbraith, 2006; Cyr et al., 2015). Part of this $\delta^{13}C_{CH4}$-enriched, upwelled water enters the deep layers of the Upper Estuary and the Saguenay Fjord, mixes into the surface layers, and moves back seaward in the returning estuarine circulations. The other part of the upwelled water is directly transported back to the Lower Estuary and the Gulf. As the volume of the upwelled deep water is much larger than the freshwater discharge, the former likely plays a more important role in maintaining the enriched $\delta^{13}C_{CH4}$ signatures in the surface water.

The more depleted $\delta^{13}C_{CH4}$ signatures in the CIL compared with the other depth layers could be suggestive of a biogenic source of methane, which supports the argument for the zooplankton-associated methane production in the CIL (Section 3.6.4). Note, however, that these CIL $\delta^{13}C_{CH4}$ values (range: −40.9‰–−31.3‰) are considerably less negative than those indicative of biogenic origins. Several explanations can account for this discrepancy. First, the CIL samples for $\delta^{13}C_{CH4}$ analysis were taken from the depths corresponding to the temperature minima, whereas the SMMax were usually located at the base of the CIL (Section 3.6.4). The strongest biogenic signatures thus might have been missed. Second, if methane is produced within anoxic microniches of particulate organic matter (Section 3.6.4), methanogenic substrate limitation may occur (Marty, 1993; Holmes et al., 2000), driving the $\delta^{13}C_{CH4}$ toward heavier values (Whiticar, 1999). This may also partly explain the rather heavy $\delta^{13}C_{CH4}$ value (−31.8‰) at station MUCCI D located in the TMZ and having a high near-bottom [CH_4] (71.4 nmol L^{-1}) (Fig. 3-12a) that could result from methanogenesis in anoxic microniches in suspended particles (Section 3.6.3). Third, as the CIL forms largely from the Gulf surface water of the preceding winter (Galbraith, 2006) when vertical convection and thus air-sea exchange are strong, part of the methane observed in the CIL during the

following autumn could be the oxidized remnant of the last winter's atmospheric methane with a $\delta^{13}C_{CH4}$ value of −45‰ (Damm et al., 2015b). These three explanations could operate individually or collectively to account for the enriched $\delta^{13}C_{CH4}$ signatures in the CIL.

The $\delta^{13}C_{CH4}$ signature in the sub-CIL layer (mean sampling depth ± s.d.: 197 ± 30 m; mean σ_θ ± s.d.: 26.82 ± 0.21 kg m^{-3}) is expected to be controlled to a large extent by the inflowing NACW and LCW. The $\delta^{13}C_{CH4}$ for the NACW has been determined to be ∼−35‰ (Holmes et al., 2000; Keir et al., 2005) and should become progressively heavier due to microbial oxidation during the transit of the water mass from the North Atlantic to the EGSL. The $\delta^{13}C_{CH4}$ for the LCW is unknown and is tentatively assigned the value of −33.1‰ determined in this study near the bottom (95 m depth) of station IF12 in the Belle Isle Strait (Fig. 3-S1), given that the bottom water in the Belle Isle Strait originates from the near-shore component of the Labrador Current. The $\delta^{13}C_{CH4}$ values for the sub-CIL layer (range: −38.3‰–−30.0‰; mean: −33.7‰) are roughly in line with the mixed signatures of the NACW and the LCW. The combination of microbial oxidation during water mass transport, downward diffusion from the SMMax, and potential in situ production could be responsible for the variability of $\delta^{13}C_{CH4}$ and its lack of consistent relationship with $[CH_4]$ in the sub-CIL layer (Fig. 3-12a).

In the bottom waters of the LC and its branches, methane emanation from the hydrocarbon seeps on the seafloor, in addition to the inflowing NACW and LCW, further complicates the $\delta^{13}C_{CH4}$ signature. Seismic signatures and sedimentation characteristics suggest that the pockmark-released methane is likely thermogenic in the deep LC and biogenic on the northwest shoulder of the LC (Pinet et al., 2008; Lavoie et al., 2010). The $\delta^{13}C_{CH4}$ values obtained in the present study for the bottom water samples collected at the three pockmark stations in the deep LC ranged from −36.3 to −27.9‰, which supports the supposition of Pinet et al. (2008) and Lavoie et al. (2010). Nonetheless, caution should be taken to interpret the pockmark $\delta^{13}C_{CH4}$ data, since it is unclear whether the samples were collected at the gas-venting centers or only at their peripheries. In fact, the $[CH_4]$s in some of these samples (Table 3-6) were far lower than expected at the gas-venting centers. Hence,

the $\delta^{13}C_{CH4}$ signatures observed might be biased toward heavier values due to microbial oxidation (Section 3.6.5), which could be particularly true for stations PM2 and PM8 (Fig. 12b) at which the [CH_4]s were 4-6 times lower than at station PM5. This might explain why the $\delta^{13}C_{CH4}$ value at station PM5 is more negative than at stations PM2 and PM8. Moreover, the decrease in $\delta^{13}C_{CH4}$ with declining [CH_4] in the bottom water of the LC and its branches (Fig. 3-12b) is contradictory to the classic paradigm of the modification of $\delta^{13}C_{CH4}$ by microbial methane oxidation (Whiticar, 1999). This, however, conforms to the scenario in which the already ^{13}C-heavy pockmark methane (e.g. station PM5, Fig. 3-12b) is oxidized, becoming further ^{13}C-heavier, and then diluted by the relatively ^{13}C-lighter background methane. The counter-intuitive $\delta^{13}C_{CH4}$-*vs.*-[CH_4] pattern in the bottom water and the lack of consistent trends for the remaining water column thus reflect the complex physical and biogeochemical processes and their interactions that control the $\delta^{13}C_{CH4}$ signatures in the EGSL.

3.7 CONCLUSIONS

Fig. 3-13 schematically summarizes the major processes controlling the input and loss of dissolved methane in the water column of the EGSL. The EGSL is so complex that the concentration, distribution, air-sea flux, source, and biogeochemical behavior of dissolved methane in this vast semi-enclosed water body differ substantially among its three geographical domains. Methane in the Upper Estuary behaves as in a typical shallow macrotidal estuary and is characterized by elevated concentrations, high areal emission rates, river-controlled inputs, mixing-driven spatial distributions, and subordinate turbidity-induced modulations. In the Lower Estuary surface water, the concentration-informed terrestrial signature is dramatically diminished, though still readily noticeable. This signature becomes marginal or undetectable in the Gulf surface water where [CH_4]s are similar to those in the ocean's slope waters. The widespread SMMax and DMMin in the LC and its branches are two salient [CH_4] distribution features in the subsurface and deep waters of the Lower Estuary and the Gulf. While zooplankton-associated methane production could be the primary driver for generating the SMMax, the dominance of the methane-depleted NACW

over the methane-richer LCW in the upper part of the deep layer is likely mainly responsible for producing the DMMin. In spite of the highly elevated [CH_4]s present at certain pockmark sites, the seeped methane appears to be rapidly diluted and/or microbially oxidized before reaching the surface and escaping to the atmosphere. Yet the fast upward transport of methane from the SMMax at the head of the LC may represent an unexpected important contribution to the methane budget in the surface waters of the Lower Estuary and the Gulf. Equally surprising are the universally heavy $\delta^{13}C_{CH4}$ values and the absence of consistent trends of $\delta^{13}C_{CH4}$ against [CH_4] or salinity in an estuarine system that receives large freshwater discharge. This puzzling phenomenon may reflect the complex interactions among different methane endmembers: highly oxidized freshwater and marine methane, in situ-produced, ^{13}C-enriched biogenic methane due to substrate limitation, and thermogenic methane from pockmarks and its oxidized residue.

From a broader perspective, the EGSL is at the lower bound of the global estuarine environments in terms of both methane concentration and emission rate due partly to the low accumulation of sediments in the USLE and the large dimensions of the LSLE and the GSL. The LSLE and the GSL actually more resemble outer shelf seas and ocean slope regions, respectively, per methane concentration and atmospheric emission rate. The large dimensions also set the LSLE and the GSL apart from smaller and shallower estuarine environments by fostering multifaceted mesoscale physical process and oceanic-type biological processes that lead to the formation of the characteristic SMMax and DMMin. Equally noteworthy is that the LSLE sets a stark contrast to the largest tributary of the EGSL—the deep but much narrower Saguenay Fjord where there exist consistent and predictable [CH_4] and $\delta^{13}C_{CH4}$ distribution trends (Chapter 2). The high complexity of the processes governing the distributions of [CH_4] and $\delta^{13}C_{CH4}$ in the LSLE apparently plays a key role in creating this difference.

3.8 ACKNOWLEDGMENTS

We thank François Villeneuve, Félix St-Pierre, Rémi Desmarais, and Pascal Rioux for assistance in sampling during the Mar-17, Jun-17, Aug-17, Oct-17, Nov-17 and Feb-18 cruises, and captains, crew, scientists on all cruises, and the DFO Atlantic Zone Monitoring Program for their cooperation. Pierre-Arnaud Desiage and Guillaume St-Onge provided the coordinates of the pockmark stations. This study was supported by H.X.'s NSERC Discovery Grant (2017-05135) and a Quebec-Ocean equipment grant. Yijie Li was supported by scholarships from the China Scholarship Council and the Institut des sciences de la mer de Rimouski (ISMER). Ship time was provided by the Fisheries and Oceans Canada and the Mission du stage of ISMER. This is a contribution to ISMER and Quebec-Ocean.

3.9 TABLES

Table 3-1. Summary of cruises participated. OHIA: Old Harry Influence Area; EGSL: estuary and Gulf of St. Lawrence; USLE: Upper St. Lawrence estuary; LSLE: Lower St. Lawrence estuary.

Date (DD/MM)	Year	Cruise name designated in main text	Ship name	Cruise number	Area covered	Number of profile stations	Number of surface stations
11/06-18/06	2015	Jun-15	*R/V Coriolis II*	1506_COR1503	OHIA	10	10
16/10-02/11	2016	Oct-16	*CCGS Hudson*	IML-2016-50	EGSL	55	78
03/03-11/03	2017	Mar-17	*CG3029 Earl Grey*	IML-2017-04	LSLE & Gulf	8	8
30/05-19/06	2017	Jun-17	*NGCC Teleost*	IML-2017-08	EGSL	28	56
03/08-31/08	2017	Aug-17	*CGCB Teleost*	IML-2017-27	LSLE & Gulf	15	15
30/09-05/10	2017	Oct-17	*R/V Coriolis II*	1715 MS	LSLE & USLE	8	17
02/11-23/11	2017	Nov-17	*R/V Coriolis II*	IML-2017-48	EGSL	20	20
10/02-23/02	2018	Feb-18	*NGCC Amundsen*	Odyssée_1899	EGSL	2	11
03/02-12/02	2019	Feb-19	*NGCC Amundsen*	Odyssée_1999	EGSL	10	10

Table 3-2. Means and ranges ([min, max]) of surface-water methane concentration ($[CH_4]_{surf}$).

Region	Season	T (°C)	Salinity	$[CH_4]$ (nmol L^{-1})
Upper Estuary	Winter (N = 7)	-0.51 ± 0.40	17.35 ± 11.45	92.9 ± 45.9
		[-1.03, -0.01]	[0.11, 28.36]	[34.4, 164.2]
	Spring (N = 3)	9.54 ± 0.43	17.27 ± 1.74	19.5 ± 6.3
		[9.24, 10.02]	[15.30, 18.61]	[15.0, 26.7]
	Autumn (N = 21)	9.09 ± 4.37	16.98 ± 9.48	51.0 ± 83.0
		[3.84, 20.14]	[0.09, 29.33]	[12.5, 392.8]
	Composite (N = 31)	6.96 ± 5.45	17.09 ± 9.30	57.4 ± 74.0
		[-1.03, 20.14]	[0.09, 29.33]	[12.5, 392.8]
Lower Estuary	Winter (N = 9)	-0.95 ± 0.75	29.31 ± 1.18	16.5 ± 3.3
		[-1.57, 0.21]	[27.98, 31.36]	[11.0, 21.0]
	Spring (N = 10)	6.79 ± 1.44	22.25 ± 2.80	8.5 ± 2.8
		[4.90, 9.87]	[16.83, 26.10]	[4.9, 14.6]
	Summer (N = 2)	10.35 ± 0.13	27.23 ± 0.08	6.1 ± 0.3
		[10.26, 10.44]	[27.17, 27.28]	[5.8, 6.3]
	Autumn (N = 42)	5.80 ± 1.47	27.53 ± 1.62	8.9 ± 2.3
		[1.01, 7.86]	[24.03, 30.73]	[4.8, 15.1]
	Composite (N = 63)	5.14 ± 2.97	26.94 ± 2.77	9.8 ± 3.7
		[-1.57, 10.44]	[16.83, 31.36]	[4.8, 21.0]
Gulf	Winter (N = 13)	-1.47 ± 0.40	31.74 ± 0.43	6.2 ± 1.8
		[-1.78, 0.49]	[31.00, 32.75]	[4.0, 8.9]
	Spring (N = 53)	6.39 ± 1.92	29.68 ± 1.88	4.01 ± 0.8
		[1.10, 10.60]	[25.10, 31.60]	[3.3, 6.6]
	Summer (N = 11)	14.05 ± 3.41	29.52 ± 0.65	3.6 ± 1.0
		[8.59, 18.07]	[28.53, 30.41]	[2.8, 5.9]
	Autumn (N = 52)	6.74 ± 1.98	30.57 ± 0.69	4.4 ± 1.4
		[2.05, 10.64]	(29.03 to 31.42)	[3.1, 8.2]
	Composite (N = 129)	6.39 ± 3.92	30.23 ± 1.45	4.3 ± 1.4
		[-1.78, 18.07]	[25.10, 32.75]	[2.8, 8.9]
Grand composite (N = 223)		6.12 ± 3.97	27.48 ± 5.88	13.3 ± 32.7
		[-1.78, 20.14]	[0.09, 32.75]	[2.8, 392.8]

Table 3-3. Means and ranges ([min, max]) of methane saturation ratio (*SR*), wind speed (U_{10}), methane exchange velocity (*k*), and methane flux density (*j*). *k* for the Upper Estuary was calculated based on eq. 3-3 in the main text and for the other regions on eq. 3-4. Refer to Fig. 3-1c in the main text for the sub-divisions of the estuary and Gulf of St. Lawrence.

Region	Season	*SR*	U_{10} (m s^{-1})	*k* (cm h^{-1})	*j* (µmol m^{-2} d^{-1})
Upper Estuary	Winter (N = 7)	20.57 ± 8.72 [8.55, 33.75]	2.80 ± 0.14 [2.60, 2.88]	0.61 ± 0.29 [0.29, 1.02]	15.57 ± 13.61 [2.11, 39.03]
	Spring (N = 3)	5.84 ± 1.87 [4.47, 7.97]	2.25	2.99 ± 0.04 [2.96, 3.03]	11.65 ± 4.67 [8.29, 16.98]
	Autumn (N = 21)	15.67 ± 26.77 [3.67, 126.28]	2.40 ± 0.07 [2.33, 2.47]	3.11 ± 0.35 [2.68, 4.07]	38.93 ± 72.43 [6.21, 336.81]
	Composite (N = 31)	15.82 ± 22.55 [3.67, 126.28]	2.40 ± 0.20 [2.25, 2.88]	2.53 ± 1.10 [0.29, 4.07]	31.02 ± 60.60 [2.11, 336.81]
Lower Estuary	Winter (N = 9)	4.03 ± 0.80 [2.65, 5.04]	5.15 ± 0.23 [4.96, 5.40]	1.58 ± 0.11 [1.46, 1.75]	4.64 ± 1.06 [2.73, 5.91]
	Spring (N = 10)	2.44 ± 0.84 [1.50, 4.39]	3.50	2.81 ± 0.12 [2.65, 3.07]	3.39 ± 2.05 [1.14, 8.31]
	Summer (N = 2)	1.99 ± 0.10 [1.91, 2.06]	3.73	3.93 ± 0.01 [3.92, 3.94]	2.85 ± 0.29 [2.64, 3.06]
	Autumn (N = 42)	2.59 ± 0.63 [1.48, 4.12]	4.45 ± 0.35 [4.29, 5.28]	4.78 ± 0.54 [4.20, 6.25]	6.27 ± 2.82 [1.75, 16.54]
	Composite (N = 63)	2.75 ± 0.86 [1.48, 5.04]	4.37 ± 0.56 [3.50, 5.40]	3.98 ± 1.30 [1.46, 6.25]	5.47 ± 2.73 [1.14, 16.54]
South Gulf	Winter (N = 11)	1.58 ± 0.44 [1.01, 2.18]	6.44 ± 0.54 [6.03, 7.83]	3.90 ± 2.20 [0.80, 6.55]	1.76 ± 1.61 [0.09, 4.27]
	Spring (N = 39)	1.21 ± 0.23 [0.99, 1.92]	4.75 ± 0.06 [4.71, 4.84]	5.21 ± 0.21 [4.81, 5.63]	0.88 ± 0.93 [−0.03, 3.81]
	Summer (N = 7)	1.36 ± 0.31 [1.10, 1.92]	4.48	5.62 ± 0.62 [4.92, 6.33]	1.36 ± 1.17 [0.40, 3.46]
	Autumn (N = 32)	1.39 ± 0.40 [1.01, 2.38]	5.98 ± 0.26 [5.86, 6.51]	9.26 ± 0.47 [8.30, 10.30]	2.98 ± 3.10 [0.08, 10.33]
	Composite (N= 89)	1.33 ± 0.35 [0.99, 2.38]	5.38 ± 0.76 [4.48, 7.83]	6.54 ± 2.26 [0.80, 10.30]	1.78 ± 2.24 [−0.03, 10.33]
North Gulf	Winter (N = 2)	1.13 ± 0.02 [1.11, 1.14]	6.86	4.07 ± 3.42 [1.65, 6.49]	0.46 ± 0.33 [0.09, 0.70]
	Spring (N = 14)	1.18 ± 0.20 [1.04, 1.84]	4.77	5.29 ± 0.38 [4.72, 6.26]	0.81 ± 0.89 [0.16, 3.63]
	Summer (N = 4)	1.15 ± 0.09 [1.10, 1.29]	4.41	5.95 ± 0.20 [5.72, 6.21]	0.58 ± 0.36 [0.39, 1.12]
	Fall (N = 20)	1.25 ± 0.34 [1.03, 2.29]	5.80 ± 0.30 [5.65, 6.39]	8.77 ± 0.55 [7.90, 10.04]	1.88 ± 2.75 [0.17, 10.41]
	Composite (N = 40)	1.21 ± 0.27 [1.03, 2.29]	5.35 ± 0.69 [4.41, 6.86]	7.04 ± 1.93 [1.65, 10.04]	1.30 ± 2.08 [0.16, 10.41]
Grand composite (N = 223)		3.73 ± 9.65 [0.99, 126.28]		5.18 ± 2.65 [0.36, 10.30]	4.73 ± 12.90 [−0.03, 177.73]

Table 3-4. Area-integrated methane fluxes in different seasons and sub-regions of the estuary and Gulf of St. Lawrence (EGSL). Areas for winter exclude ice-cover. Fluxes for spring and summer in the Upper Estuary and for summer in the Lower Estuary are assumed values (see details in Section 3.6.2 in the main text). Refer to Fig. 3-1c in the main text for the sub-divisions of the EGSL.

Region	**Area (10^3 km^2)**	**Season**	**Flux (10^6 mol)**
Upper Estuary	1.0 (Feb. 2018)	Winter	0.91 ± 0.74
	0.6 (Feb. 2019)		
	2.5	Spring	8.16
	2.5	Summer	7.93
	2.5	Autumn	8.95 ± 16.66
		Subtotal	25.95
Lower Estuary	3.0 (Feb. 2018)	Winter	0.20 ± 0.10
	2.8 (Feb. 2019)		
	8.9	Spring	4.18 ± 2.53
	8.9	Summer	4.17
	8.9	Autumn	6.23 ± 2.76
		Subtotal	14.78
South Gulf	86.9 (Mar. 2017)	Winter	6.07 ± 12.74
	41.5 (Feb. 2018)		
	43.0 (Feb. 2019)		
	163.7	Spring	16.70 ± 17.80
	163.7	Summer	20.44 ± 17.56
	163.7	Autumn	46.93 ± 52.58
		Subtotal	90.14
North Gulf	36.4 (Mar. 2017)	Winter	1.77 ± 1.26
	77.7	Spring	6.78 ± 7.44
	77.7	Summer	4.15 ± 2.58
	77.7	Autumn	14.83 ± 22.37
	77.7	Subtotal	27.53
	Grand total		158.4

Table 3-5. In situ depth, potential temperature (θ), salinity, and [CH_4] in water with a potential density (σ_θ) of 27.25 kg m^{-3} at station TDC5 located in Cabot Strait, the Gulf of St. Lawrence, along with the same properties for the endmembers, North Atlantic Central Water (NACW), and Labrador Current Water (LCW), on the potential density surface of 27.10 kg m^{-3}. The in situ data were interpolated from the measurements made in this study; the depths, potential temperatures, and salinities for the endmembers were obtained from Gilbert et al. (2005) and the [CH_4]s for the endmembers were calculated according to their potential temperatures and salinities (see details in Section 3.6.4 in the main text).

	Depth (m)	**θ (ºC)**	**Salinity**	**[CH_4] (nmol L^{-1})**
	Endmember (σ_θ = 27.10 kg m^{-3})			
NACW	772.7	11.14	35.45	2.77
LCW	170.8	1.05	33.85	3.62
	In situ (σ_θ = 27.25 kg m^{-3})			
Oct-16	267.9	6.75	34.74	1.54
Jun-17	295.2	7.18	34.82	0.96

Table 3-6. Targeted and real sampling coordinates of the pockmark stations, the distance between the targeted and real coordinates (i.e. horizontal distance deviation, HD), the distance between the deepest sampling depth and the seafloor (i.e. vertical distance deviation or VD), and the [CH_4] at the deepest (i.e. near-bottom) sampling depth ($[CH_4]_{nb}$).

Cruise	**Real coordinates (°W, °N)**	**HD (m)**	**VD (m)**	**$[CH_4]_{nb}$ (nmol L^{-1})**
Station Bis (targeted coordinates: 68.498°W, 48.793°N)				
Oct-16	68.498, 48.792	143.8	15	24.6
Station PM2 (targeted coordinates: 67.699°W, 48.977°N)				
Jun-17	67.698, 48.982	546.9	4.4	273.7
Nov-17	67.694, 48.978	363.4	4.1	21.9
Station PM3 (targeted coordinates: 67.648°W, 48.995°N)				
Oct-16	67.650, 48.995	161.6	5.0	89.1
Station PM5 (targeted coordinates: 67.621°W, 49.002°N)				
Oct-16	67.623, 49.003	150.4	2.6	695.3
Nov-17	67.620, 49.003	107.4	5.9	135.0
Feb-18 (cast# 1)	67.628, 49.002	490.0	9.4	10.4
Feb-18 (cast# 2)	67.621, 49.003	67.3	10.9	418.5
Feb-19	67.619, 49.003	171.1	15.0	74.1
Station PM8 (targeted coordinates: 67.759°W, 48.959°N)				
Jun-17	67.752, 48.947	1389.7	5.4	206.8
Nov-17	67.760, 48.958	69.6	6.4	37.2

Table 3-7. Means and ranges of $\delta^{13}C_{CH4}$ for different sub-regions and different depth layers in the estuary and Gulf of St. Lawrence. Data for the below-surface depths at station IF2 in the Belle Isle Strait ($\delta^{13}C_{CH4}$: −40.9‰ at 40.1 m and −33.1‰ at 95.0 m) are excluded from calculation for the Gulf region in this table due to the absence of the cold intermediate layer (CIL) at this locality.

	Depth layer	**$\delta^{13}C_{CH4}$ (‰)**	
		Median	**Mean [min, max]**
Upper Estuary	Surface (<2.5 m) (N = 4)	−30.61	−32.2 [−37.9, −29.5]
	Below surface (>10 m) (N = 7)	−31.77	−33.4 [−38.4, −31.2]
Lower Estuary	Surface (<2.5 m) (N = 6)	−29.94	−30.16 [−32.0, −29.1]
	Core of CIL (N = 6)	−33.41	−33.5 [−36.6, −31.3]
	Sub-CIL (N = 6)	−31.63	−32.87 [−38.9, −30.0]
	Bottom (LC and branches) (N = 6)	−30.48	−31.2 [−36.3, −27.4]
Gulf	Surface (<2.5 m) (N = 10)	−31.73	−32.6 [−36.7, −30.7]
	Core of CIL (N = 9)	−38.17	−37.2 [−40.9, −32.8]
	Sub-CIL (N = 9)	−34.97	−34.79 [−38.3, −30.5]
	Bottom (LC and branches) (N = 9)	−35.31	−34.9 [−38.8, −31.1]

3.10 FIGURES

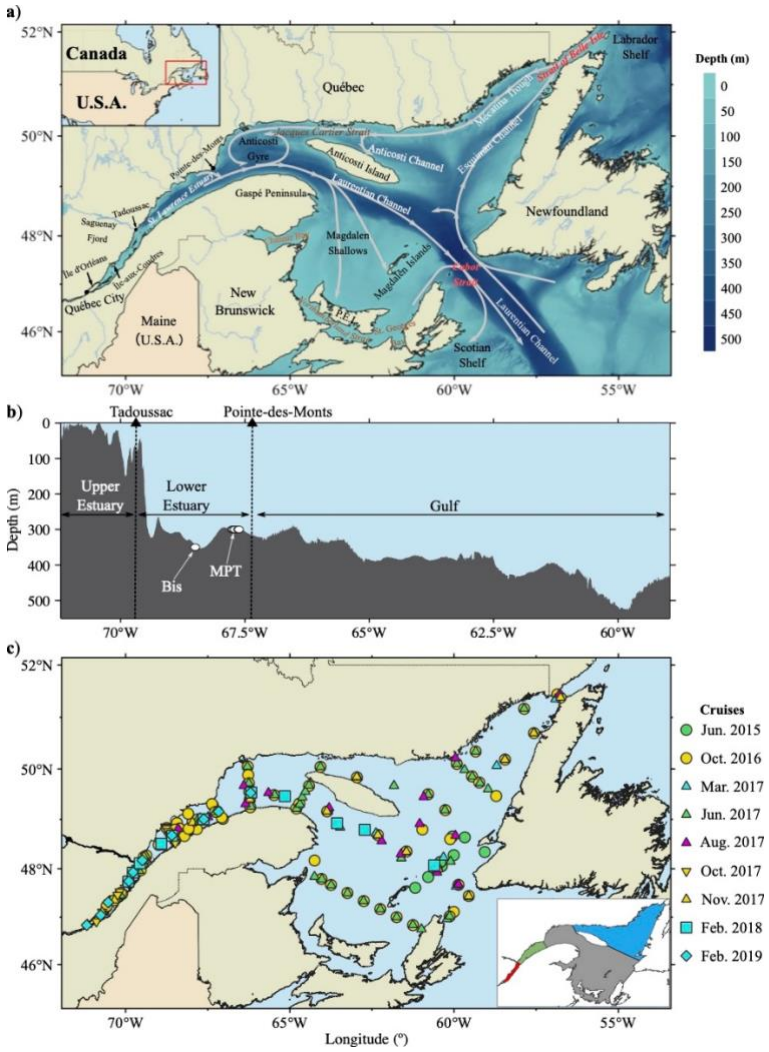

Figure 3-1. Sampling area information and stations. **a**) Bathymetry and surface circulations (after Sheng, 2001) of the estuary and Gulf of St. Lawrence (EGSL). Inset shows the location of the EGSL on the east coast of North America. **b**) Longitudinal vertical section of the EGSL showing the main topographic features of the Upper Estuary and Laurentian Channel in the Lower Estuary and the Gulf. Also shown are the approximate positions of the Bis pockmark site and the Matane Pockmark Train (MPT) sampled in this study. **c**) Map showing all sampling stations from different cruises. Refer to Fig. S1 for station names for each cruise. Inset shows the four sub-regions (red: Upper Estuary; green: Lower Estuary; grey: South Gulf; blue: North Gulf) of the EGSL used to facilitate methane air-sea flux calculation (Section 3.5.5 in the main text).

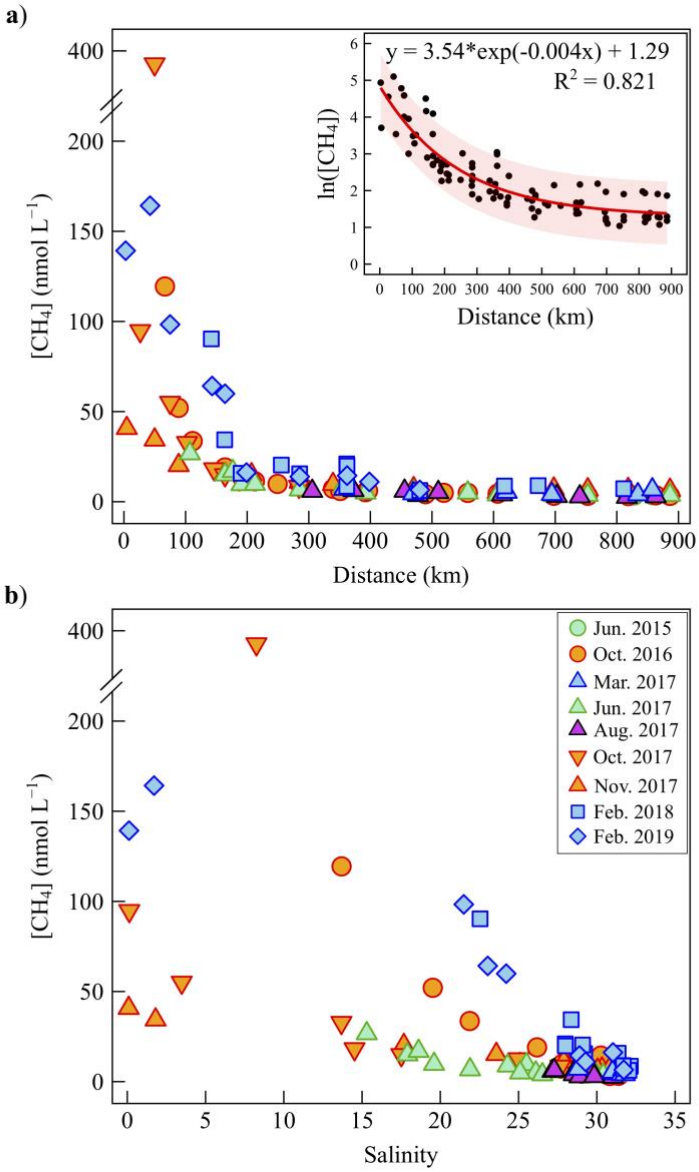

Figure 3-2. Scatter plots of [CH_4] *vs.* distance to Quebec City (**a**) and *vs.* salinity (**b**) along the main longitudinal axis of the EGSL (Fig. 3-1b). Inset in panel **a** shows the relationship between [CH_4] and distance for the composite data of all individual cruises, excluding the elevated [CH_4]s in the turbidity maximum zone during the Oct-17 and Feb-19 cruises. Red area represents the 95% prediction intervals. Note the natural logarithmic scale for [CH_4] in the inset.

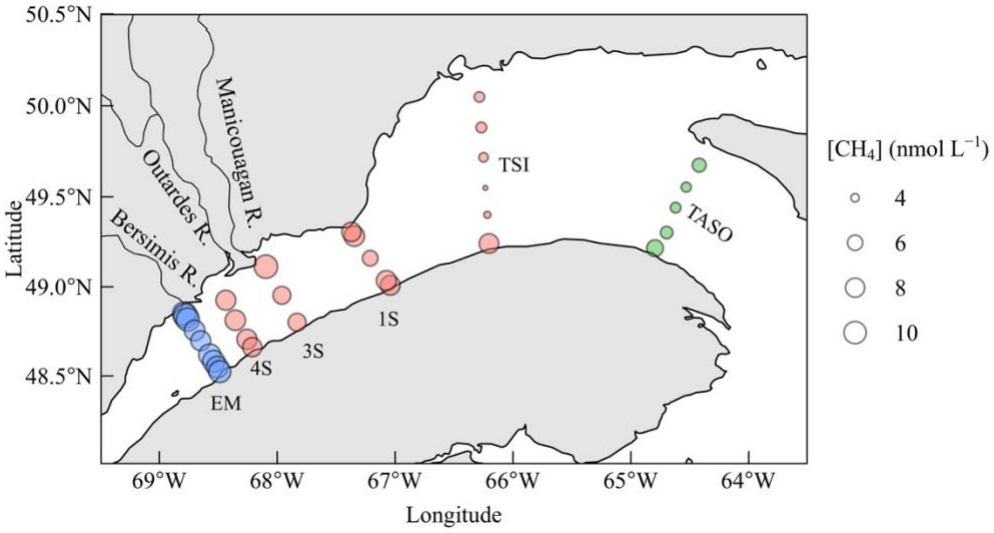

Figure 3-3. Lateral distributions of surface-water [CH_4] across the Lower St. Lawrence estuary and the Gulf of St. Lawrence. Blue: Oct-17; red: Oct-16; green: Jun-17 cruise.

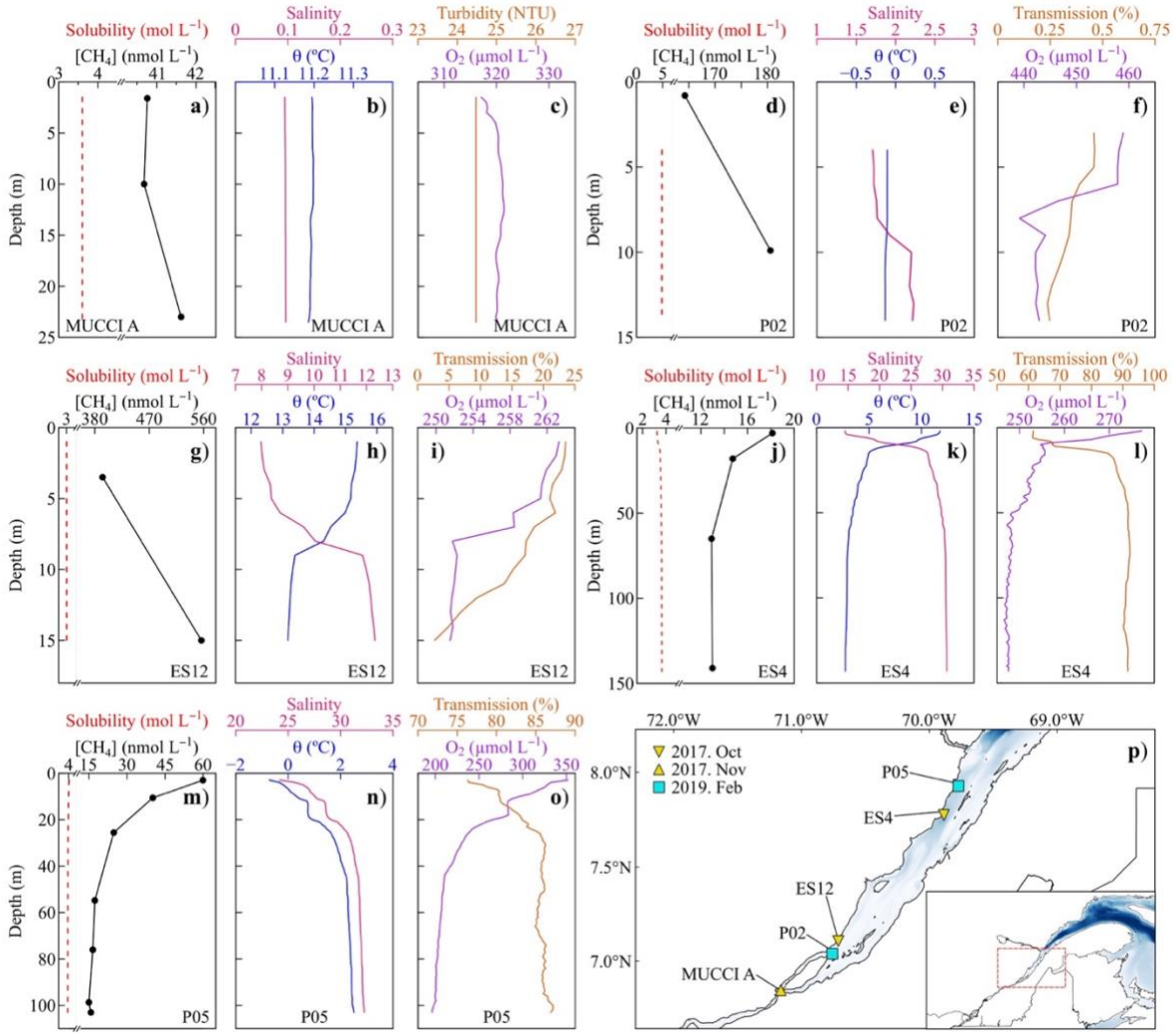

Figure 3-4. Typical vertical profiles of [CH_4] alongside the corresponding profiles of methane solubility at equilibrium with air, potential temperature (θ), salinity, dissolved oxygen, and turbidity in the Upper St. Lawrence estuary (**a**–**o**). Refer to panel **p** for the positions of the sampling stations.

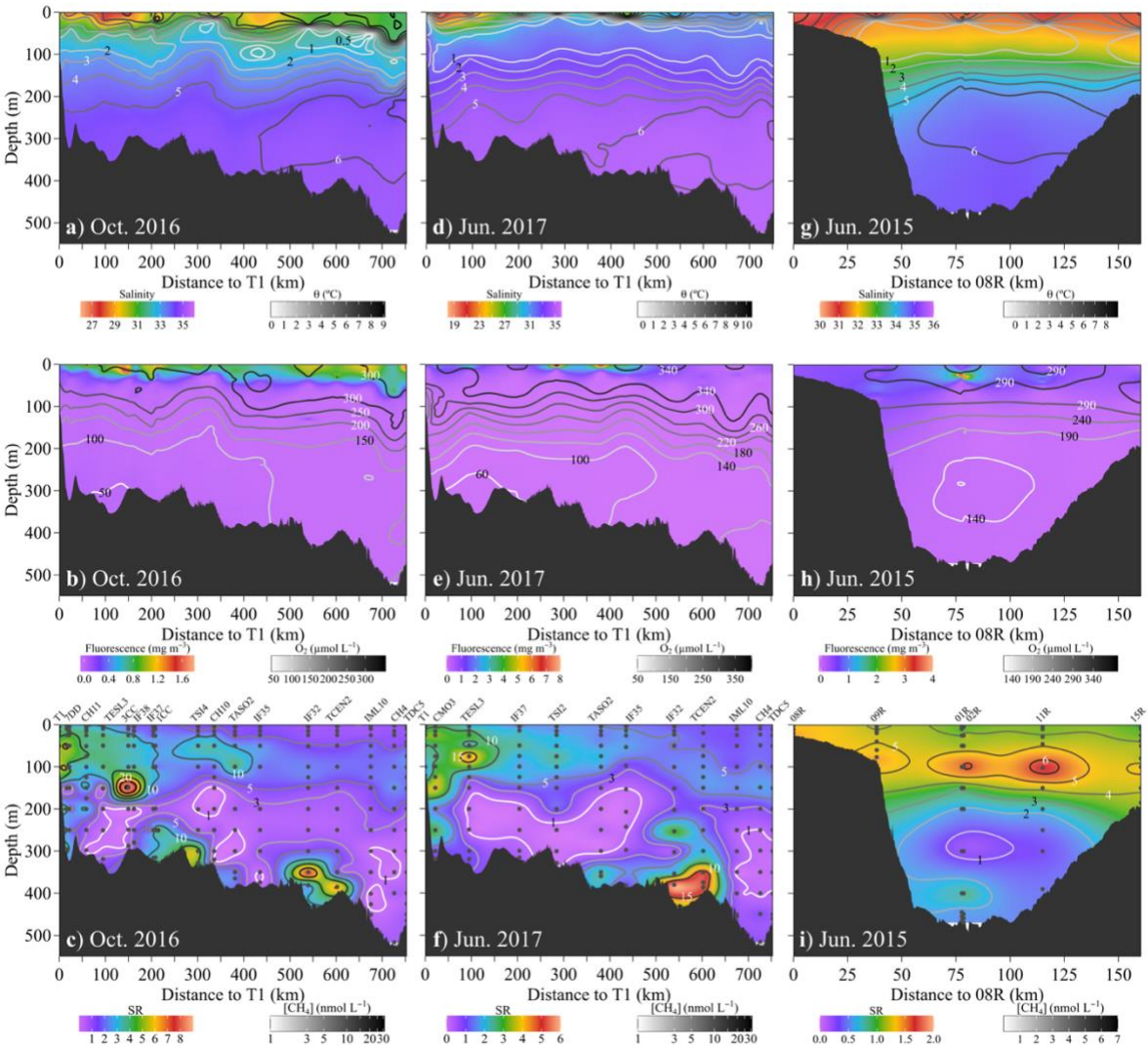

Figure 3-5. Vertical distributions of salinity and temperature (**a, d, g**), chlorophyll *a* fluorescence and dissolved oxygen (**b, e, h**), and [CH_4] and saturation ratio (**c, f, i**) along the main longitudinal axis of the Laurentian Channel in the Lower Estuary and the Gulf sampled during the Oct-16 (**a**–**c)** and Jun-17 cruises (**d**–**f**) and along the cross-channel transect in the Gulf visited during the Jun-15 cruise (**g**–**i**). Black dots in panels **c**, **f**, and **i** represent sampling depths for methane. Labels on the top of these three panels denote the names of the sampling stations. Refer to Fig. 3-S1 (panels Jun. 2015, Oct. 2016, and Jun. 2017) for the positions of the sampling stations.

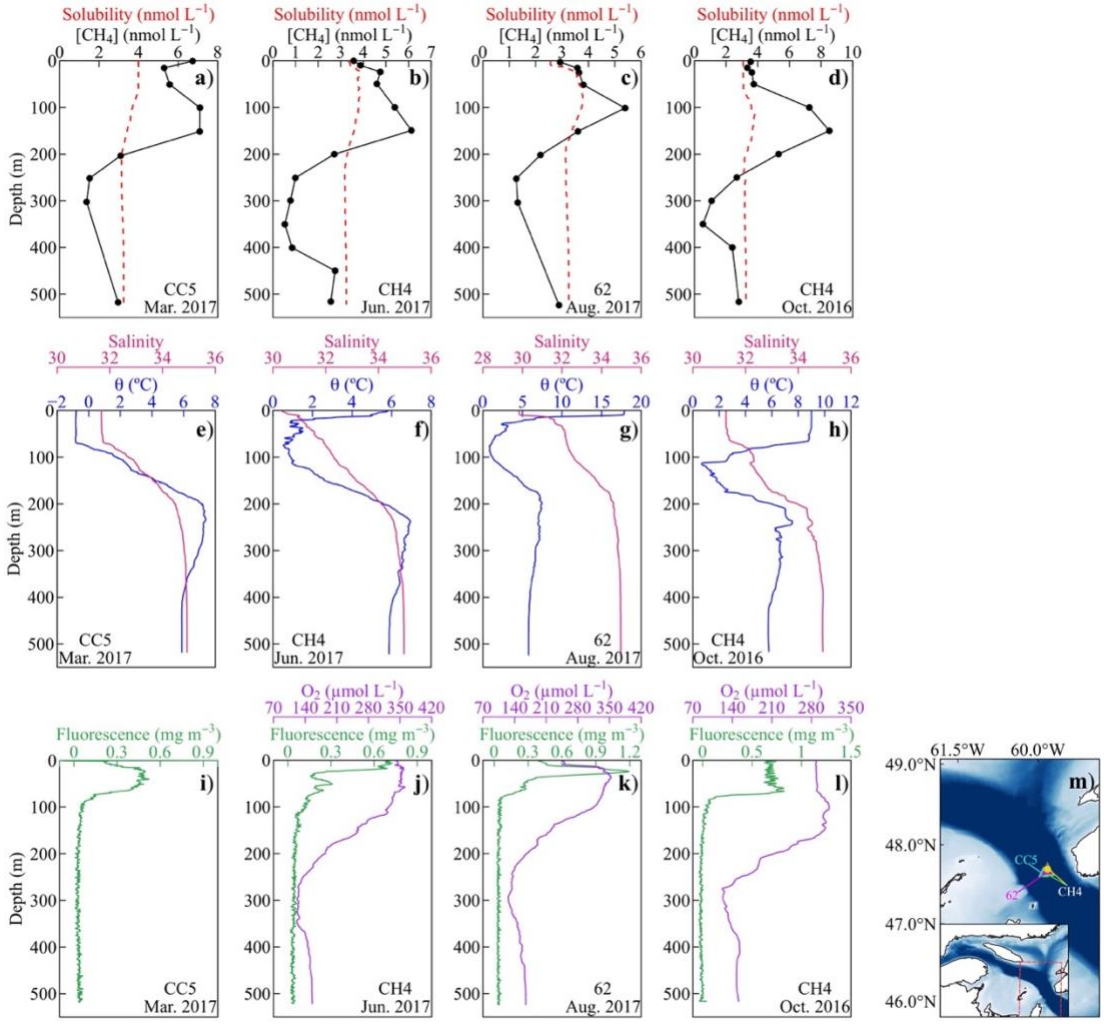

Figure 3-6. Vertical profiles of [CH_4] demonstrating the presence of the subsurface [CH_4] maximum (SMMax) in four seasons at a site in Cabot Strait area (**a**–**d**). Also shown are the corresponding profiles of methane solubility at equilibrium with air (**a**–**d**), potential temperature (θ) and salinity (**e**–**h**), and chlorophyll *a* fluorescence and dissolved oxygen (**i**–**l**). Dissolved oxygen data is unavailable at station CC5 during the Mar-17 cruise. Panel **m** displays the positions of the sampling stations.

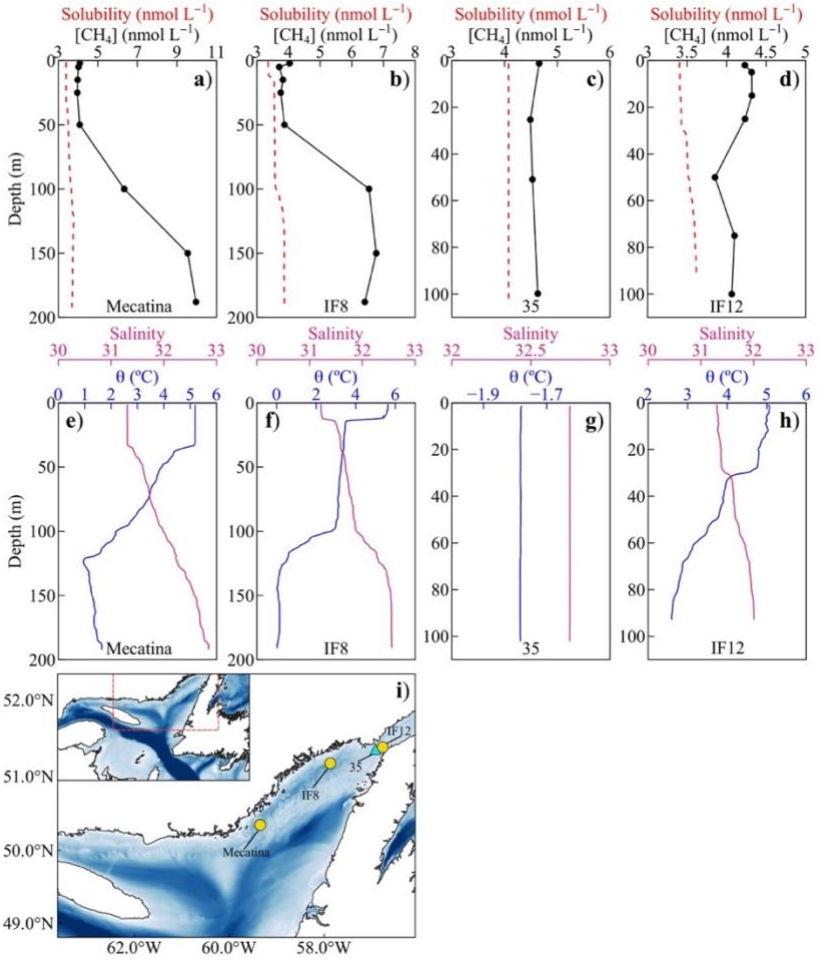

Figure 3-7. Vertical profiles of [CH_4] demonstrating the absence of the subsurface [CH_4] maximum (SMMax) at stations IF8 and Mecatina in the Mecatina Trough and stations IF12 and 35 in the Strait of Isle Belle (**a**–**d**). Also shown are the corresponding profiles of methane solubility with respect to air (**a**–**d**) and potential temperature (θ) and salinity (**e**–**h**). Station 35 was sampled during the Mar-17 cruise and the others were sampled during the Oct-16 cruise. Panel **m** displays the positions of the sampling stations.

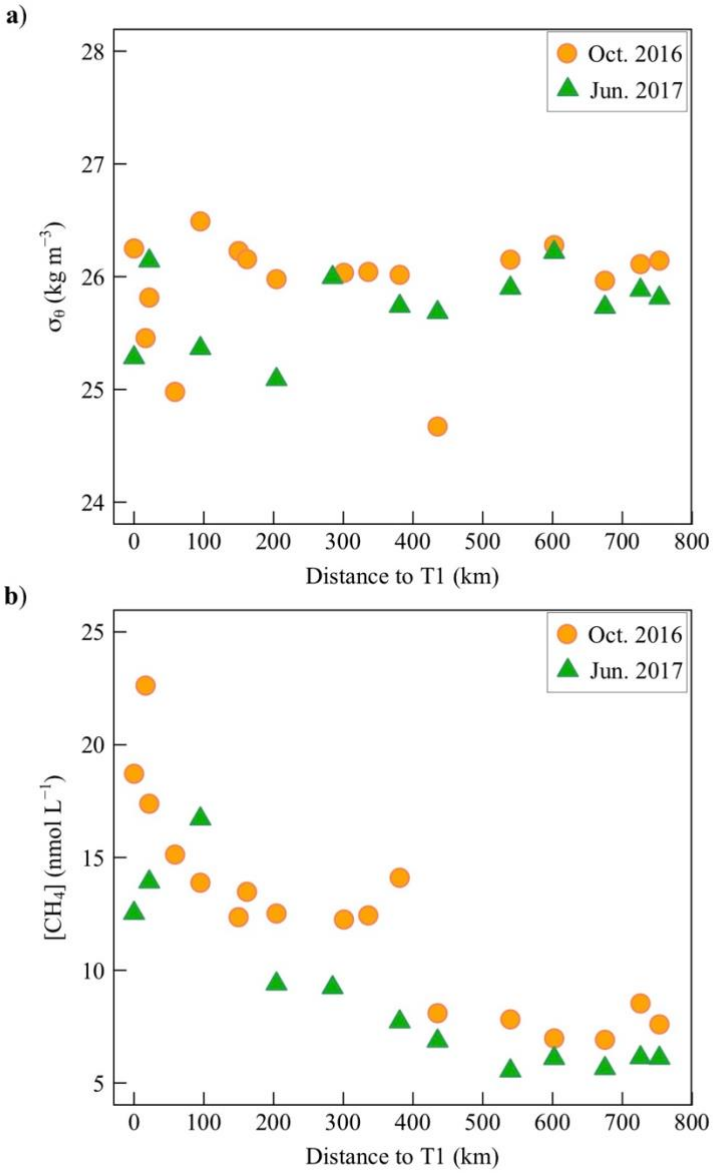

Figure 3-8. Potential density (**a**) and [CH_4] (**b**) at the subsurface [CH_4] maximum (SMMax) in the Laurentian Channel as a function of distance to station T1 near the head of the channel.

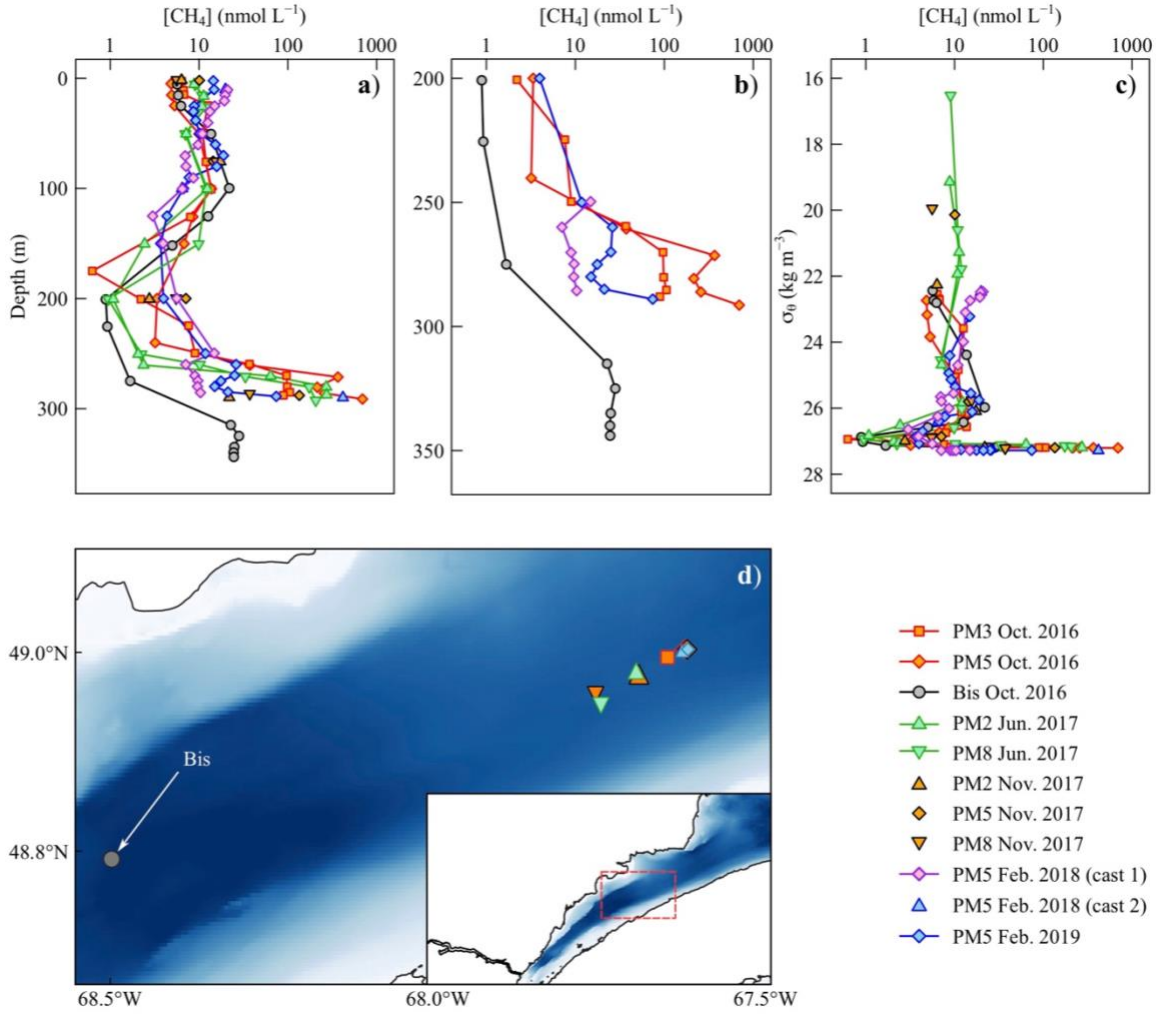

Figure 3-9. [CH_4] at pockmark stations *vs.* depth (**a**) and potential density (**c**). Panel **b** is a close-up view of the lower portions of the concentration-*vs.*-depth profiles for stations PM3, PM5 (Oct-16, Feb-18, and Feb-19), and Bis. Panel **d** shows the locations of the sampling stations. Note that some stations are overlapped on the map due to their proximity.

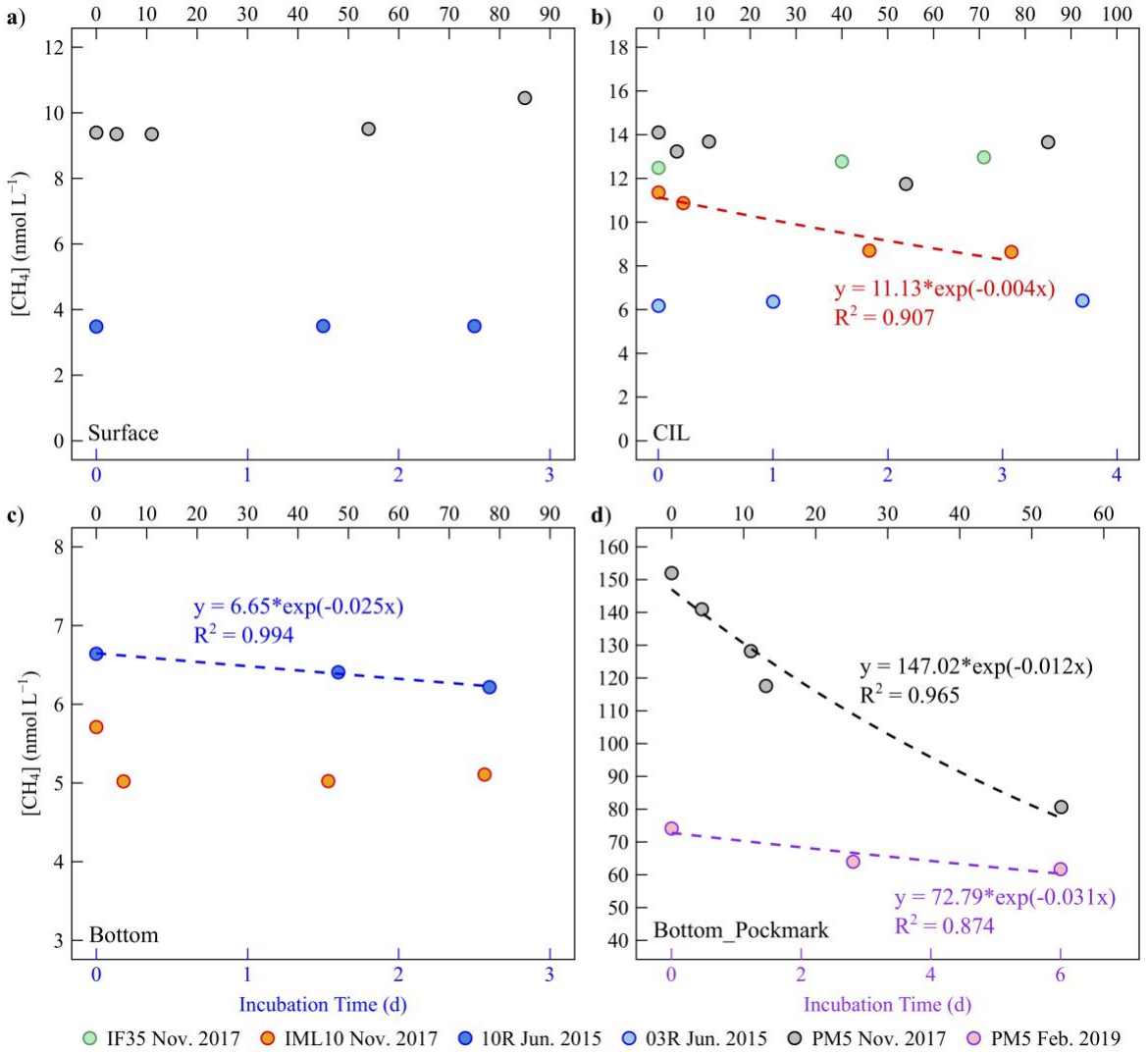

Figure 3-10. [CH_4] as a function of incubation time for surface water samples (**a**), the cold-intermediate-layer water samples (**b**), non-pockmark bottom water samples (**c**), and pockmark bottom water samples (**d**). Refer to Fig. 3-S1 (panels Jun. 2015, Nov. 2017, and Feb. 2019) for the positions of the sampling stations. In panels **a**, **b**, and **c**, the blue dots correspond to the lower x-axis and the rest to the upper x-axis. In panel **d**, the purple dots correspond to the lower x-axis and the rest to the upper x-axis.

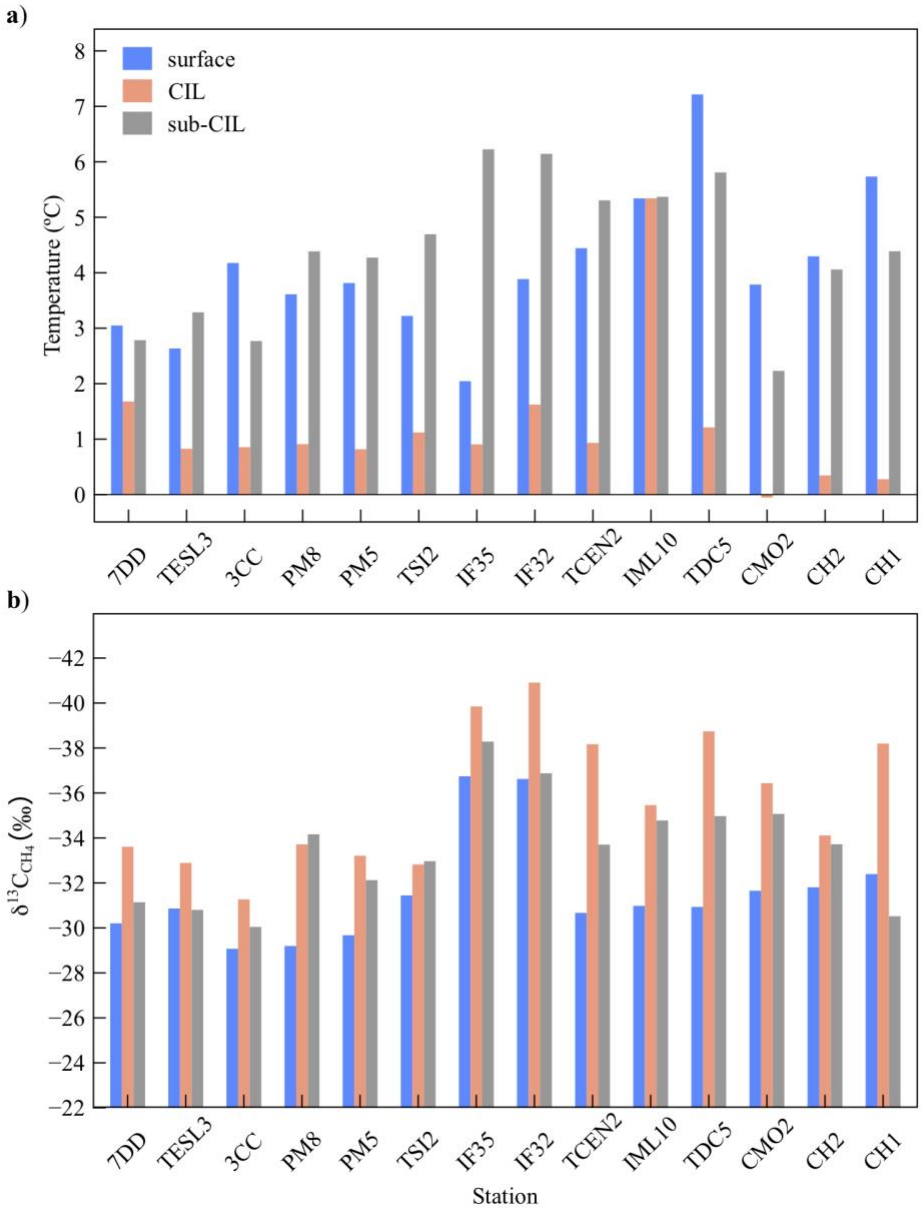

Figure 3-11. Comparison of temperatures (**a**) and $\delta^{13}C_{CH4}$ (**b**) between surface, cold-intermediate-cold-layer (CIL), and sub-CIL water samples collected during the Nov-17 cruise. Refer to Fig. 3-S1 (panel Nov. 2017) for the positions of the sampling stations.

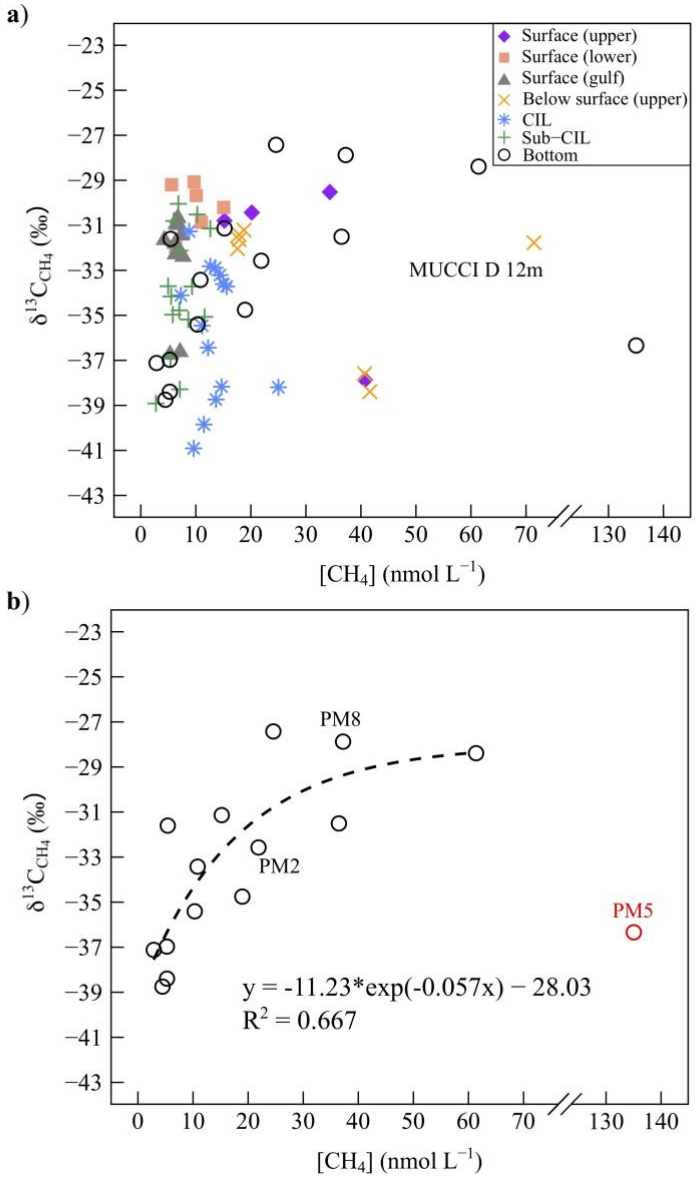

Figure 3-12. $\delta^{13}C_{CH4}$ *vs.* [CH_4] for different sub-regions and different depth layers (**a**) and the relationship between $\delta^{13}C_{CH4}$ and [CH_4] for bottom water samples collected from the Laurentian Channel and its branches (**b**). Upper: Upper Estuary; lower: Lower Estuary; gulf: Gulf of St. Lawrence; CIL: cold intermediate layer.

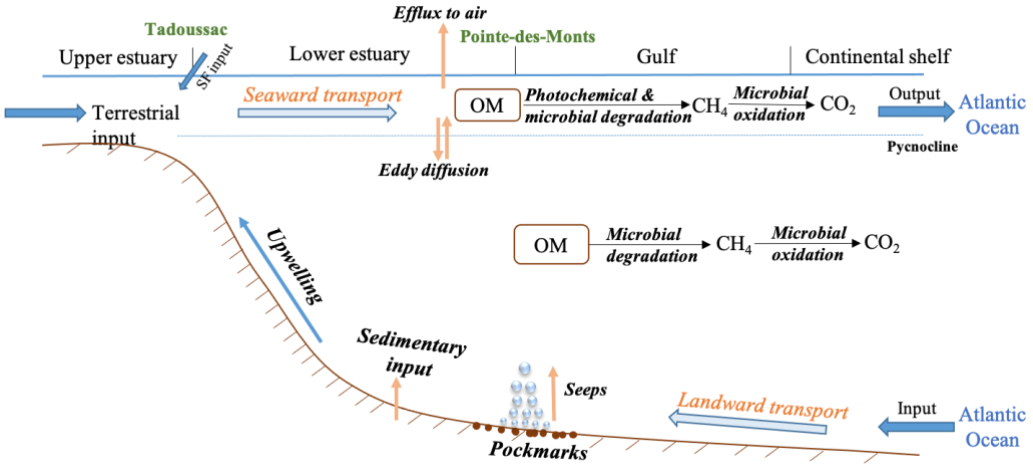

Figure 3-13. Schematic representation of the major drivers controlling the dynamics of [CH_4] in the water column of the estuary and Gulf of St. Lawrence. SF: Saguenay Fjord.

3.11 SUPPLEMENTARY INFORMATION

3.11.1 Supplementary tables

Table 3-S1. Fractions of ice cover and open-water areas in different sub-regions of the estuary and Gulf of the St. Lawrence (EGSL) during the winter sampling months. Refer to Fig. 3-1c in the main text for the sub-divisions of the EGSL.

Cruise	Region	Ice cover fraction	Open water area (10^3 km^2)
Mar. 2017	Upper Estuary	0.67	0.84
	Lower Estuary	0.50	4.43
	North Gulf	0.53	36.38
	South Gulf	0.47	86.90
Feb. 2018	Upper Estuary	0.62	0.95
	Lower Estuary	0.66	2.99
	North Gulf	0.48	40.35
	South Gulf	0.75	41.45
Feb. 2019	Upper Estuary	0.77	0.59
	Lower Estuary	0.69	2.80
	North Gulf	0.69	24.03
	South Gulf	0.74	43.03

3.11.2 Supplementary figures

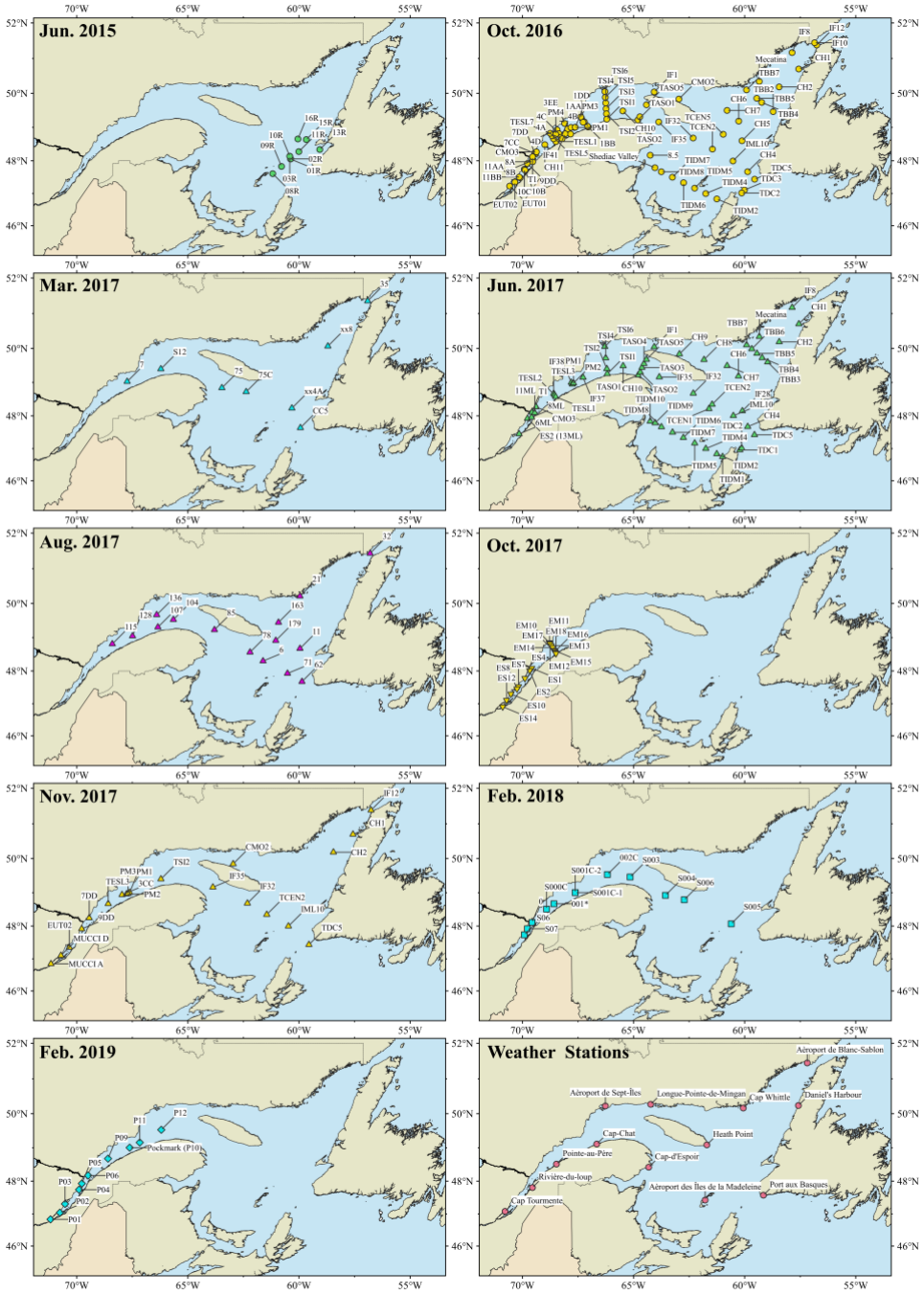

Figure 3-S1. Sampling stations labeled with names for each cruise and locations of weather stations (bottom panel on the right) from which wind speeds were obtained for methane flux calculations.

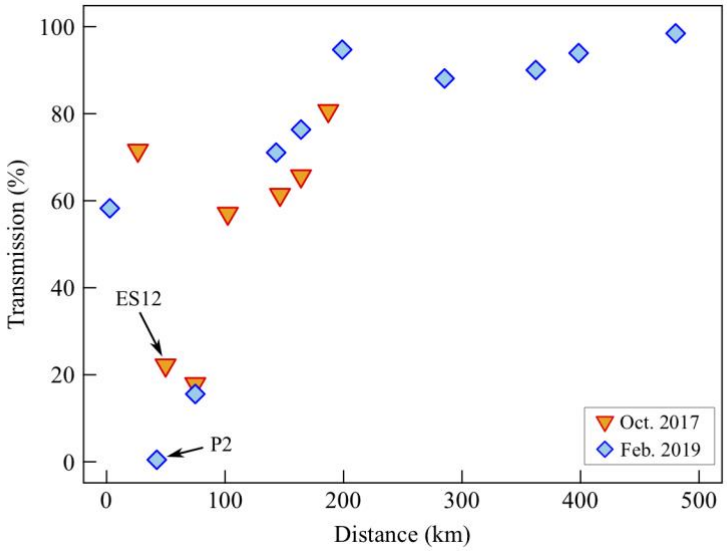

Figure 3-S2. Surface-water light transmission *vs.* distance to Quebec City along the main longitudinal axis of the St. Lawrence estuary during the Oct-17 and Feb-19 cruises.

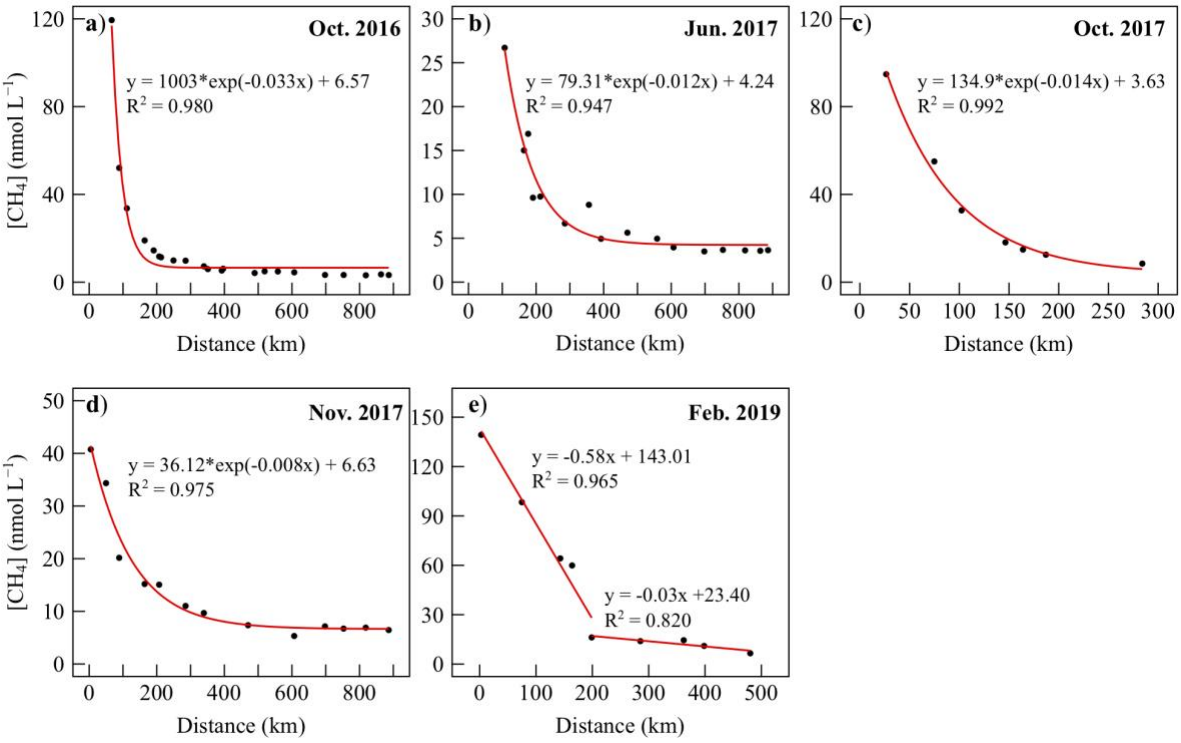

Figure 3-S3. Relationships between surface-water [CH_4] and distance to Quebec City for individual cruises. Elevated [CH_4]s in the turbidity maximum zone during the Oct-17 and Feb-19 cruises are excluded. Lines are best fits of the data.

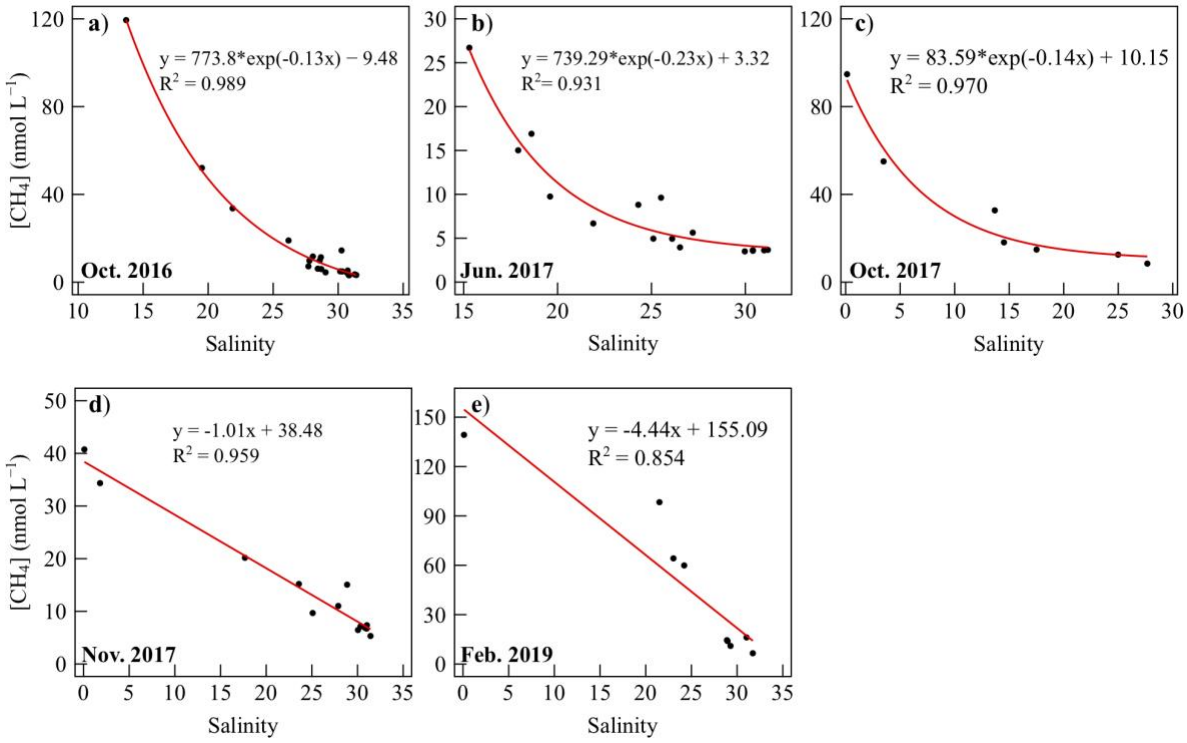

Figure 3-S4. Relationships between surface-water [CH_4] and salinity for individual cruises. Elevated [CH_4]s in the turbidity maximum zone during the Oct-17 and Feb-19 cruises are excluded. Lines are best fits of the data.

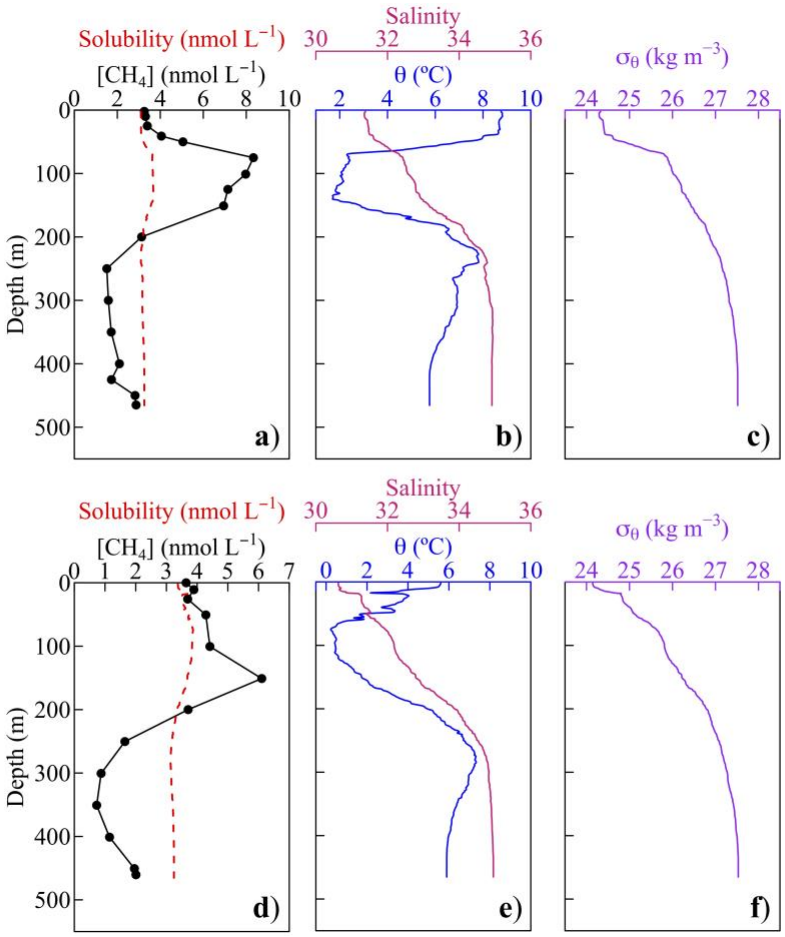

Figure 3-S5. Vertical profiles collected at station TDC5 in Cabot Strait in October 2016 (**a**–**c**) and June 2017 (**d**–**f**). **a**) & **d**): [CH_4] and solubility at equilibrium with air; **b**) & **e**): potential temperature (θ) and salinity; **c**) and **f**): potential density.

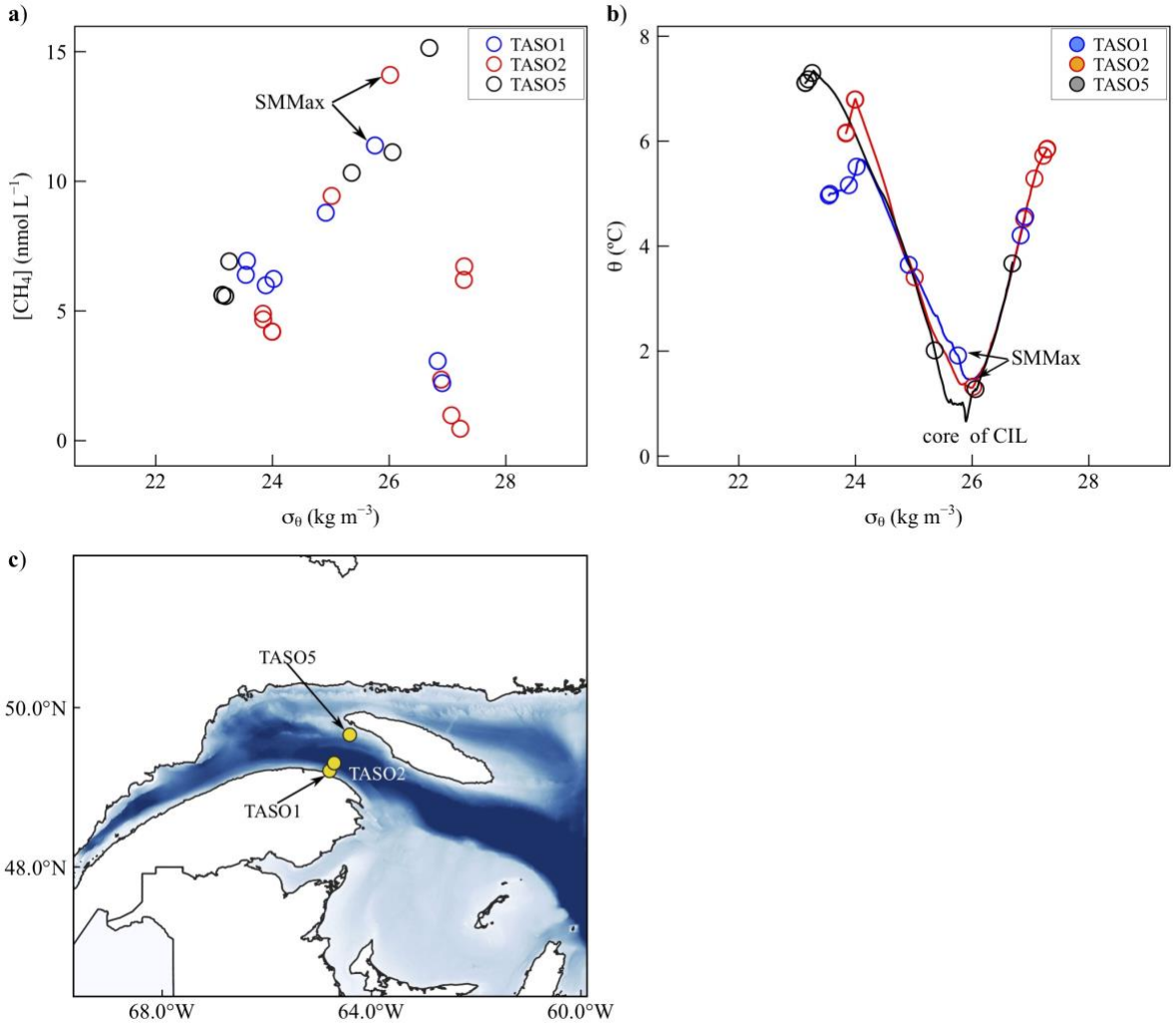

Figure 3-S6. Scatter plots of [CH_4] (**a**) and potential temperature (**b**) *vs.* potential density for three stations on a cross-channel transect (**c**) in the northwest Gulf of St. Lawrence. The data shows that 1) subsurface [CH_4] maxima (SMMax) were present at stations TASO1 and TASO2 (**a**); 2) the SMMax were located at (TASO2) or near (TASO1) the core of the cold intermediate layer (CIL) (**b**); 3) the [CH_4] at the SMMax for station TASO2, which was farther offshore than stations TASO1 and TASO5, was higher than those concentrations at the latter two stations along the same isopycnal (25.94 ± 0.16 kg m^{-3}).

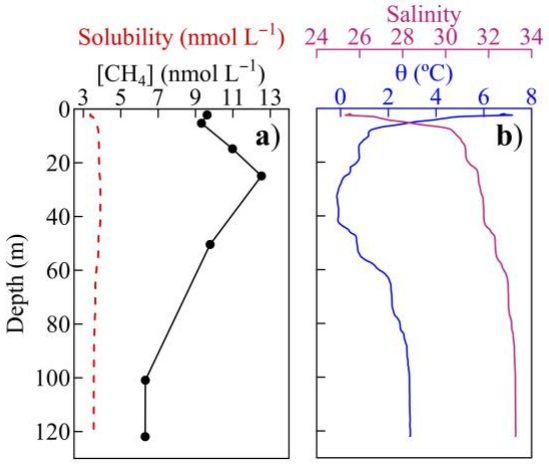

Figure 3-S7. Vertical profiles collected at station T1 near the head of the Laurentian Channel during the Jun-17 cruise. **a**) [CH_4] and solubility at equilibrium with air. **b**) potential temperature (θ) and salinity. Refer to Fig. 3-S1 (panel Jun. 2017) for the position of station T1.

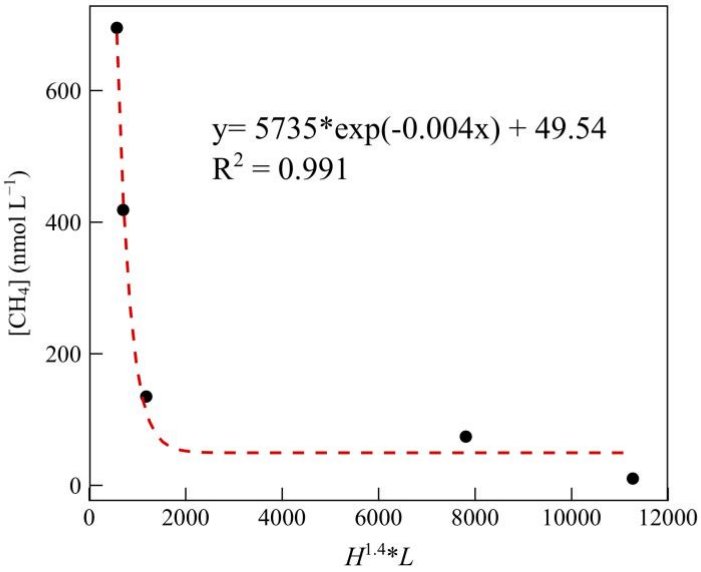

Figure 3-S8. Near-bottom [CH_4] at pockmark station PM5 as a function of $H^{1.4}*L$. *H* (units: m) denotes the difference between the depth of the seafloor and the deepest sampling depth; *L* (units: m) represents the distance between the real and targeted coordinates of the sampling station.

CHAPTER 4

PHOTOPRODUCTION OF METHANE IN SURFACE WATERS OF THE ST. LAWRENCE MARINE SYSTEM AND OTHER MARINE ENVIRONMENTS: IMPLICATIONS FOR THE OCEANIC METHANE PARADOX

Yijie Li [1], Cédric G. Fichot [2], Lantao Geng [3,1,4], Michael Scarratt [5], Huixiang Xie [1*]

[1]Institut des sciences de la mer de Rimouski, Université du Québec à Rimouski, Rimouski, Québec, Canada

[2]Department of Earth and Environment, Boston University, Boston, USA

[3]Guangzhou Marine Geological Survey, China Geological Survey, Guangzhou, China

[4]College of Marine Science and Technology, China University of Geosciences (Wuhan), Wuhan, China

[5]Department of Fisheries and Oceans Canada, Maurice-Lamontagne Institute, Mont-Joli, Quebec, Canada.

Published in Geophysical Research Letters

Cite this article as: Li, Y., Fichot, C.G., Geng, L., Scarratt, M.G., Xie, H., 2020. The contribution of methane photoproduction to the oceanic methane paradox. *Geophys. Res. Lett.* 47, e2020GL088362. https://doi.org/10.1029/2020GL088362

4.1 RÉSUMÉ

Bien que la méthanogénèse soit considérée comme un processus strictement anaérobique, les eaux de surface de la haute mer riches en oxygène sont généralement sursaturées en méthane (CH_4); il s'agit du phénomène de paradoxe du méthane océanique. Nous rapportons ici que la photoproduction du méthane abiotique à partir de la matière organique dissoute chromophorique (CDOM) contribue de manière significative à ce paradoxe. La photoproduction du méthane a été observée lors des irradiations solaires simulées de diverses eaux collectées le long du continuum terre-mer. Les taux de la photoproduction du méthane ont diminué vers la mer, tandis que son efficacité de production relative et le rapport de la photoproduction de méthane à la photoproduction de monoxyde de carbone ($\Delta CH_4/\Delta CO$) ont tous deux suivi une tendance inversée. La modélisation par télédétection incorporant une relation entre $\Delta CH_4/\Delta CO$ et l'absorption de CDOM a donné une photoproduction annuelle de méthane de 118 Gg pour la haute mer mondiale, représentant 20 à 60 % de l'efflux de méthane de haute mer et étant d'une magnitude comparable au puits de l'oxydation-microbienne de méthane de mer supérieure. La photodégradation de la CDOM joue donc un rôle important dans le maintien des concentrations de méthane sursaturé dans la haute mer oxygénée et des émissions de méthane océanique à l'atmosphère. Cependant, la voie photochimique n'est qu'une source mineure de méthane pour les environnements côtiers, y compris l'estuaire et le golfe du Saint-Laurent.

***Mots-clés* :** photoproduction du méthane ; paradoxe du méthane océanique ; matière organique dissoute chromophorique

4.2 ABSTRACT

Although methanogenesis is considered a strictly anaerobic process, oxygen-replete surface open-ocean waters are usually supersaturated with methane (CH_4), a phenomenon termed the oceanic methane paradox. Here we report that abiotic methane photoproduction

from chromophoric dissolved organic matter (CDOM) significantly contributes to this paradox. Methane photoproduction was observed during solar-simulated irradiations of various waters collected along the land-ocean continuum. Methane photoproduction rates decreased seaward, whereas its relative production efficiency and the methane-to-carbon-monoxide (CO) photoproduction ratio ($\Delta CH_4/\Delta CO$) both followed a reversed trend. Remote-sensing modeling incorporating a $\Delta CH_4/\Delta CO$–CDOM absorption relationship yielded an annual methane photoproduction of 118 Gg for the global open ocean, accounting for 20-60% of the open-ocean methane efflux and being of comparable magnitude to the upper-ocean methane microbial-oxidation sink. The photodegradation of CDOM thus plays an important role in maintaining supersaturated methane concentrations in the oxygenated upper open ocean and in sustaining oceanic methane emissions to the atmosphere. However, the photochemical pathway is only a minor source to coastal environments, including the estuary and Gulf of St. Lawrence.

***Keywords*:** methane photoproduction, oceanic methane paradox, chromophoric dissolved organic matter

4.3 INTRODUCTION

Methanogenesis is commonly considered to occur only in strict anaerobes whose activity is inhibited by the presence of oxygen and sulfate (Rheeburg, 2007; Thauer et al., 2008). However, sulfate- and oxygen-rich surface oceans distant from terrestrial and sedimentary influences are usually supersaturated with methane (CH_4) relative to atmospheric equilibrium, a phenomenon referred to as the "oceanic methane paradox" (Kiene, 1991; Rheeburg, 2007). Various biotic explanations have been proposed, including: 1) anaerobic CH_4 production in micro-anoxic niches in sinking particles and in zooplankton and fish guts (Oremland, 1979; Karl & Tilbrook, 1994; Schmale et al., 2018); 2) aerobic CH_4 production by common marine phytoplankton species: *Emiliania huxleyi* (Lenhart et al., 2016), *Phaeocystis globosa*, and *Chrysochromulina sp*. (Klintzsch et al., 2019); 3) aerobic

CH_4 production from microbial decomposition of certain organic phosphorus compounds (Karl et al., 2008; Repeta et al., 2016).

Abiotic CH_4 production under oxic conditions might also explain the oceanic methane paradox. Althoff et al. (2014) discovered CH_4 formation from oxidative reactions of organosulfur compounds and hypothesized that these reactions might occur in living organisms including algae. Bange & Uher (2005) observed CH_4 production from photolysis of acetone added to natural water samples. More recently, Zhang & Xie (2015) observed CH_4 production from photodegradation of chromophoric dissolved organic matter (CDOM) in a highly colored river water sample. Despite evidence that CH_4 can be produced under aerobic conditions by various biotic and abiotic processes, their quantitative relevance to the methane paradox remains weak (Bange & Uher, 2005; Zhang & Xie, 2015), difficult to evaluate (Karl et al., 2008; Althoff et al., 2014; Klintzsch et al., 2019) or has not been assessed on large scales (Repeta et al., 2016).

Photochemical transformations of CDOM play an important role in marine biogeochemical cycles (Mopper et al., 2015; Power et al., 2015) and produce various atmospherically reactive and/or climatically active trace gases (Mopper & Kieber). Carbon monoxide (CO) is arguably the most precisely determined CDOM photoproduct whose global open-ocean photoproduction rate is best known (mean: 40–50 TgC $year^{-1}$, Zafiriou et al., 2003; Stubbins et al., 2006; Fichot & Miller, 2010). The amenability and high sensitivity of the CO measurement has made it a useful proxy for other important but difficult-to-measure photoproducts such as carbon dioxide and biolabile organic carbon (Miller & Moran, 1997; Mopper & Kieber, 2002). Here, we report that the photodegradation of CDOM produces methane in a wide range of waters across the entire land-ocean continuum. By combining lab-determined molar ratios of CH_4 to CO photoproduction into a remote sensing-informed photochemical model, we demonstrate that photoproduction represents a significant source of CH_4 in the surface ocean and is likely an important mechanism behind the methane paradox.

4.4 METHODS

4.4.1 Sampling

Water samples were collected from a range of water types along the land-ocean continuum, including the estuary and Gulf of St. Lawrence (EGSL), the Saguenay Fjord, the Canadian Arctic and Labrador Sea, Coastal Massachusetts, the Sargasso Sea, Station ALOHA in the subtropical North Pacific, and a peatland pond near Rimouski, Quebec (Supplementary Fig. 4-S1). Surface water samples were collected with a clean high-density-polyethylene bucket at the peatland site and elsewhere with Niskin bottles mounted on standard conductivity-temperature-depth (CTD) rosettes. All samples were taken from the surface mixed layer save three from the bottom layer (326 m) at Sta. P9 in the lower St. Lawrence Estuary and from the oxygen minimum zone (775 m) and bottom layer (4001 m) at Station ALOHA. Water samples were gravity-filtered through Pall AcroPak 1000 filtration capsules sequentially containing 0.8-μm microfiber and 0.2-μm polyethersulfone-membrane filters. Filtered samples were transferred into 4-L clear-glass bottles, closed with PTFE-lined screw caps, and stored in darkness at 4 °C until analysis within 3 months of collection. Other relevant sampling information is provided in Supplementary Table 4-S1.

Contamination-controlling measures were taken for sampling, filtration, and sample transfer. Blank tests showed negligible artifacts (Supplementary Text S1 and S2).

4.4.2 Irradiation experiments

The stored water samples were warmed to room temperature, re-filtered (0.2-μm polyethersulfone membrane, Pall) under low vacuum, and bubbled with medical-grade air (Air Liquide) to re-oxygenate the sample and lower the background CH_4 concentrations. Use of medical-grade air minimized pH and carbonate system disturbances. The samples were then siphoned into cylindrical quartz tubes (length: 25.0 cm; i.d.: 2.2 cm) with sufficient overflowing. The tubes were closed free of headspace with ground-glass stoppers, horizontally immersed in a temperature-controlled water bath, and irradiated under a

SUNTEST XLS+ solar simulator equipped with a 1500-W xenon lamp with radiation <290 nm eliminated by a special Suprax ultra-violet (UV) filter. Quartz tubes incubated under opaque conditions served as dark controls. The incident irradiance at the upper surface of the quartz tubes was measured to be ~650 W m^{-2} over the UV and visible spectrum using an OL-756 spectroradiometer fitted with a 2-inch OL IS-270 integrating sphere and calibrated with an OL 756-10E irradiance standard (Gooch & Housego, USA). To facilitate comparison among different samples, the water bath was kept at 8°C, irrespective of the samples' in situ temperatures (Table 4-1).

Irradiations were divided into two groups: 1) time-series to determine the temporal evolution of CH_4 photoproduction, and 2) fixed-duration to determine the molar ratio of CH_4 to CO photoproduction ($\Delta CH_4/\Delta CO$) and/or the CH_4 photoproduction rate (Supplementary Table 4-S1). Separate irradiations were performed for CO and CH_4 due to different irradiation times required. Irradiation lasted from 0.05 to 5 h for CO and from 4 to 8 d for CH_4, depending on the samples' initial Napierian absorption coefficient at wavelength 320 nm ($a_g(320)$). Considering CH_4 photoproduction increased linearly with irradiation time (Section 4.5.2), the difference in irradiation time between the CO and CH_4 experiments should have minimal effects on the calculated $\Delta CH_4/\Delta CO$ ratios. All samples were irradiated in triplicate (time-course) or quadruplicate (fixed-duration), except for the Arctic and Labrador Sea samples (no replicates). Post-irradiation samples were subsampled sequentially for measurements of dissolved CH_4 and CO, CDOM absorbance, and bacterial enumeration (for selected time-course irradiations only). Bacterial samples were fixed with 5% glutaraldehyde (Grade II, Sigma G6257; 20 µL added to 14 mL sample) and stored at –80°C until analysis.

Acetaldehyde and acetone (HPLC grade, Sigma-Aldrich) were tested as potential precursors of CH_4 photochemically produced in natural waters. Samples were prepared by adding each of the compounds to 0.2 µm-filtered, air-equilibrated Rimouski River (48.439 °N, 68.540 °W) water, with a concentration of 50 µmol L^{-1}. The samples were irradiated at

20°C for four days in the same manner as described earlier, along with parallel blanks (i.e. river water only) and dark controls.

4.4.3 Analysis

DOC concentrations of unirradiated samples were determined using a Shimadzu TOC-Vcpn analyzer. UV-visible absorbance spectra of CDOM were recorded with a Perkin-Elmer lambda-35 spectrometer. Absorbances, after baseline corrections per Babin et al. (2003), were converted to the Napierian absorption coefficients, $a_g(\lambda)$ (m^{-1}), where λ is wavelength in nanometers (Fichot and Benner, 2012). Dissolved CH_4 and CO were headspace-extracted and quantified using a Peak Performer 1 Analyzer (Peak Laboratories, USA) and a TA7000 Reduction Gas Analyzer (Trace Analytical, USA), respectively, following the methods of Xie et al. (2002) and Zhang & Xie (2015). Free-living heterotrophic bacterial cell abundance was determined by cytometry (Belzile et al., 2008). See Supplementary Text S3 for detailed analytical methods.

4.4.4 Modeling of methane photoproduction rates

The photochemical model of Fichot & Miller (2010) was used to calculate a global, spatially-explicit, yearly climatology of depth-resolved photoproduction rates of CH_4. The approach involved two steps: 1) calculation of a yearly climatology of depth-integrated photoproduction rates of carbon monoxide (CO) and 2) conversion of the CO photoproduction rates to CH_4 photoproduction rates.

In the first step, the photochemical model of Fichot & Miller (2010) was implemented on a yearly climatology (2002-2018, 9-km × 9-km) of *Aqua* MODIS remote-sensing reflectances (*Rrs*) to derive a corresponding climatology of depth-resolved CO photoproduction rates. Briefly, the Sea*UV* algorithm (Fichot et al. 2008) was implemented on *Rrs* to derive diffuse attenuation coefficients (K_d) of surface waters in the 290-490 nm range. The $a_g(320)/K_d(320)$ ratio of 0.68 and CDOM spectral slope coefficient of 0.0194

from Fichot and Miller (2010) were used to derive a climatology of CDOM absorption coefficient spectra from $K_d(320)$. These climatologies were then combined with a yearly climatology of cloud-corrected modeled irradiance spectra (290–490 nm) and an average apparent quantum yield of CO photoproduction (Fichot & Miller, 2010) to generate depth-resolved CO photoproduction rates. These rates were then integrated over the top 150 m of the water column to produce a globally-mapped yearly climatology of depth-integrated rates of CO photoproduction. This approach assumes a homogenous water column, which is reasonable considering that most of the photoproduction tends to occur in the surface mixed layer (Fichot and Miller, 2010) where CDOM absorption and composition can be considered homogenous.

In the second step, a relationship observed between $\Delta CH_4/\Delta CO$ and the initial $a_g(320)$ in this study was applied to the mapped climatology of $a_g(320)$ to produce a mapped yearly climatology of the $\Delta CH_4/\Delta CO$ ratio. The ratio was then used to derive the mapped yearly climatology of depth-integrated rates of CH_4 photoproduction for the global ocean from the corresponding CO photoproduction climatology. This step assumes that the $\Delta CH_4/\Delta CO$ ratios, which are derived from irradiation experiments in a solar simulator, are generally applicable to the range of solar exposure spectra observed in natural waters. In reality, unconstrained differences between the spectral dependencies of CO and CH_4 photoproduction (stemming from potential differences in the spectral dependencies of their respective apparent quantum yields) represent a potentially important source of uncertainties in the estimated CH_4 photoproduction rates. Here, a careful analysis suggested the uncertainties associated with this assumption are on the order of ±7% and ±21% for surface and depth-resolved CH_4 photoproduction rates, respectively (Supplementary Text S4, and Supplementary Figs. 4-S2–4-S4).

4.5 RESULTS AND DISCUSSION

4.5.1 Physical, chemical, and optical properties of sampled waters

The physical, chemical, and optical data for the initial (unirradiated) samples are shown in Table 4-1. Salinity ranged from zero at the freshwater sites to >36 at the BATS site. Excluding the peatland-pond sample, $a_g(320)$ decreased by more than 2 orders of magnitude from the Charles-River and Saguenay-Fjord stations (24.29 m^{-1} and 25.20 m^{-1}, respectively) to Station ALOHA (0.11 m^{-1}). Absorption in the peatland pond was an order of magnitude higher (173.5 m^{-1}) than at the Charles River and Saguenay Fjord. Surface water DOC concentration spanned from 478 µmol L^{-1} in the Saguenay Fjord (peatland pond DOC data not available) to ~80 µmol L^{-1} in the Gulf of St. Lawrence and open-ocean waters. The CDOM spectral slope coefficient between 275 nm and 295 nm ($S_{275\text{-}295}$) ranged from 12.9 μm^{-1} for the peatland pond to 50.8 μm^{-1} for Station ALOHA. $S_{275\text{-}295}$ is an indicator of CDOM origin and molecular weight, with terrigenous CDOM having lower values than marine CDOM (Helms et al., 2008, Fichot and Benner, 2012). Together, these chemical and optical data indicate that the samples examined represent a broad spectrum of DOM sources and properties in natural waters.

4.5.2 Photoproduction of CH_4

The filtration procedure described in Section 2.1 removed >99% of bacteria. Bacterial growth in the irradiated samples was mostly undetectable but was significant at times in the dark controls (Supplementary Fig. 4-S5). Nonetheless, dark controls showed negligible production or consumption of CH_4 (mean: −1.4%; range: −7.2 to 6.9%). In contrast, CH_4 production was observed in all irradiated samples, increasing approximately linearly with irradiation time (Supplementary Fig. 4-S6). Considering the wide diversity of samples used here, CH_4 photoproduction is likely ubiquitous in natural waters. The rate of CH_4 photoproduction (P_{CH4}) decreased linearly with increasing salinity, except for the highly colored Saguenay-Fjord and peatland-pond samples which fell well above the fitted line (Fig.

4-1a). As revealed by the exponential relationship between ln(P_{CH4}) and ln(a_g(320)), P_{CH4} increased very rapidly with increasing initial a_g(320), ranging from ~24 nmol m^{-3} d^{-1} for the open-ocean samples to 6206 nmol m^{-3} d^{-1} for the extremely colored peatland sample (Fig. 4-1b). The rate of CO photoproduction also increased with a_g(320) (Supplementary Fig. 4-S7), as has been reported previously (Stubbins, 2001).

In contrast, the amount of CH_4 produced per unit loss of CDOM absorption ($\Delta CH_4/\Delta a_g(320)$) decreased rapidly with increasing initial a_g(320), following a power law (Fig. 4-2a). The $\Delta CH_4/\Delta a_g(320)$ of the oligotrophic water samples (salinity >36) was about seven times that of the freshwater samples (salinity <1). This trend indicates that marine CDOM and/or photobleached terrigenous CDOM, which both occur in oligotrophic waters (Andrew et al., 2013), are more efficient at producing CH_4 than is minimally altered terrigenous CDOM. Consequently, the conservative behavior of a_g(320) in the St. Lawrence estuary (Supplementary Fig. 4-S8) suggests an increasing $\Delta CH_4/\Delta a_g(320)$ ratio with an increasing fraction of the marine CDOM endmember. Furthermore, the linear increase of CH_4 with irradiation time during the time-course irradiations implies that the absorbed-photon-based efficiency of CH_4 increases as CDOM is photodegraded. This increase in efficiency during prolonged exposure could be in part responsible for the observed increase in $\Delta CH_4/\Delta a_g(320)$ and $\Delta CH_4/\Delta CO$ (see below) from inland to open-ocean waters.

The $\Delta CH_4/\Delta CO$ ratio exhibited similar behavior to $\Delta CH_4/\Delta a_g(320)$, decreasing rapidly with increasing initial a_g(320) following a power law (Fig. 4-2b). The $\Delta CH_4/\Delta CO$ ratio increased ~30-fold from 6.3×10^{-5} in the Charles River to $>2\times10^{-3}$ in the oligotrophic Atlantic and Pacific waters (Fig. 4-2b), indicating that CDOM from oligotrophic environments is much more efficient at producing CH_4 relative to CO than is terrigenous CDOM. The large range of $\Delta CH_4/\Delta CO$ observed across the land-ocean continuum suggests different primary mechanisms for the photoproduction of these two gases.

Bange and Uher (2005) proposed that CH_4 photoproduction involves the formation of methyl radicals (CH_3•) from CDOM-initiated photoreactions, followed by H-abstraction by

CH_3• from various substrates. Several methylated compounds occurring in natural waters have been identified as precursors of CH_3•, they being acetone (Bange and Uher, 2005) and dimethylsulfide (Zhang and Xie, 2015). Bange and Uher (2005) only observed CH_4 photoproduction from acetone in the absence of O_2, which readily reacts with the CH_3• (Neta et al., 1996), while Zhang and Xie (2015) detected CH_4 photoproduction from DMS under both anoxic and oxic conditions. In this study, acetone, as well as acetaldehyde, was found to be able to produce CH_4 under well-oxygenated conditions (Supplementary Fig. 4-S10). As acetone, acetaldehyde, and DMS are widespread in natural waters (Simó, 2004; Beale et al., 2013; Zhu and Kieber, 2020), they could be among the precursors of CH_4 photochemically produced. Methoxy-substituted phenols, which are photoreactive and enriched in terrigenous CDOM (Sharpless and Blough, 2014), are also considered to be potential CH_4 precursors (Zhang and Xie, 2015). The different CH_4 photoproduction behaviors of river and marine samples could be attributed to 1) methylated compounds and methoxy-substituted phenols having different CH_4-producing efficiencies and 2) different proportions of CH_4-producing methylated compounds and methoxy-substituted phenols in the bulk CDOM pools in the river and marine samples.

4.5.3 Global estimates

The remote-sensing-informed model of Fichot & Miller (2010) facilitated the calculation of mapped yearly climatologies of depth-resolved and depth-integrated photoproduction rates of CH_4 in the global ocean. The model was first used to produce a yearly climatology of CO photoproduction rates (Fig. 4-3a). Depth-integrated CO photoproduction rates are high in the tropics and progressively decrease towards the poles, unlike the global pattern of CDOM absorption (Fig. 4-3b). This mismatch is attributed to CDOM absorption being the primary contributor to the vertical attenuation of UV-blue radiation in natural waters. Thus the magnitude of CDOM absorption mainly controls the vertical distribution of photoproduction in the water-column rather than the magnitude of depth-integrated photoproduction. The latter is more directly influenced by the relative

contribution of CDOM to the total absorption by all water constituents (Bélanger et al. 2008; Fichot & Miller, 2010).

However, CDOM had a major, albeit indirect, influence on the depth-integrated CH_4 photoproduction rates. As was revealed by the inverse power-law relationship between $\Delta CH_4/\Delta CO$ and $a_g(320)$, CDOM from oligotrophic waters is much more efficient at producing CH_4 relative to CO than is terrigenous CDOM. Application of this relationship on the remotely sensed $a_g(320)$ produced a global-ocean pattern of $\Delta CH_4/\Delta CO$ ratios that is the inverse of the $a_g(320)$ pattern (Figs. 4-3b and 4-3c). The highest ratios were thus observed in the subtropical oligotrophic oceans (mean: $\sim 3 \times 10^{-3}$) where $a_g(320)$ values are very low (<0.1 m^{-1}), whereas lower ratios were observed at higher ($>45^o$) latitudes (mean: $\sim 1.4 \times 10^{-3}$) and in coastal waters (mean: $\sim 0.9 \times 10^{-3}$) where $a_g(320)$ is enhanced by inputs from terrestrial environments and/or upwelling of deep CDOM-enriched waters.

This wide range of $\Delta CH_4/\Delta CO$ ratios observed globally greatly influenced the spatial distribution of depth-integrated CH_4 photoproduction rates (Fig. 4-3d). The highest rates were observed in the subtropical gyres where high incident irradiance and high $\Delta CH_4/\Delta CO$ ratios fueled rates typically greater than 80 nmol m^{-2} d^{-1}. The yearly-averaged rates in the subtropical gyres were: 96 nmol m^{-2} d^{-1} in the North Atlantic, 101 nmol m^{-2} d^{-1} in the South Atlantic, 92 nmol m^{-2} d^{-1} in the South Indian, 99 nmol m^{-2} d^{-1} in the North Pacific, and 99 nmol m^{-2} d^{-1} in the South Pacific. In contrast, much lower rates (<40 nmol m^{-2} d^{-1}) were observed in most coastal waters, where low $\Delta CH_4/\Delta CO$ ratios minimized CH_4 photoproduction rates regardless of incident irradiance. The lowest rates (<20 nmol m^{-2} d^{-1}) were observed in the sub-polar and polar regions where low average irradiances are combined with low $\Delta CH_4/\Delta CO$ ratios. The estimated total photoproduction of CH_4 in the global ocean was 121 Gg $year^{-1}$, with the open ocean (water depth >200 m) accounting for 97% of it (i.e. 118 Gg $year^{-1}$).

The vertical distribution of CH_4 photoproduction rates also varied spatially (Supplementary Fig. 4-S9). Rates typically decrease exponentially with depth, but the rate of

decrease can vary dramatically depending on the level of downwelling-irradiance diffuse attenuation caused by the various optically active constituents in the water (Fichot & Miller, 2010). For instance, depth-resolved rates at a St. Lawrence estuary (SLE) site (49°N, 67.8°W) decreased much more rapidly than in oligotrophic waters because of the higher attenuation driven by high CDOM and particle absorption. CH_4 photoproduction is typically concentrated in the top few meters of the water column in estuarine and coastal waters but extends deeper in oligotrophic waters. The photoproduction rate just below the air-water interface at the SLE site (10.4 nmol m^{-3} d^{-1}) is greater than that at BATS (6.6 nmol m^{-3} d^{-1}) or at Station ALOHA (7.5 nmol m^{-3} d^{-1}). However, the depth-integrated (0-150 m) rates displayed an opposite pattern, being far higher at Station ALOHA (102 nmol m^{-2} d^{-1}) and the BATS (72 nmol m^{-2} d^{-1}) than at the SLE site (5 nmol m^{-2} d^{-1}) because of higher solar irradiances and $\Delta CH_4/\Delta CO$ ratios in the open ocean.

4.5.4 Implications for CH_4 cycling in the Estuary and Gulf of St. Lawrence

Zhang and Xie (2012) reported annual mean CO photoproduction rates of 48.3 µmol m^{-2} d^{-1} in the upper SLE, 28.64 µmol m^{-2} d^{-1} in the lower SLE, and 24.21 µmol m^{-2} d^{-1} in the northwest Gulf of St. Lawrence. The mean $\Delta CH_4/\Delta CO$ ratios for the EGSL surface waters measured in this study are 1.23×10^{-4} in the upper SLE, 3.09×10^{-4} in the lower SLE, and 4.02×10^{-4} in the northwest Gulf. Multiplying the CO photoproduction rates by the $\Delta CH_4/\Delta CO$ ratios for the corresponding subregions yields CH_4 photoproduction rates of 0.0060 µmol m^{-2} d^{-1} in the upper SLE, 0.0088 µmol m^{-2} d^{-1} in the lower SLE, and 0.0097 µmol m^{-2} d^{-1} in the northwest Gulf. The annual mean sea-to-air CH_4 flux densities were estimated as 31.02 µmol m^{-2} d^{-1} in the upper SLE, 5.47 µmol m^{-2} d^{-1} in the lower SLE, 2.61 µmol m^{-2} d^{-1} in the northwest Gulf (Chapter 3). CH_4 photoproduction can thus only account for 0.02% of the atmospheric emission in the upper SLE, 0.16% in the lower SLE, and 0.37% in the northwest Gulf. The photochemical pathway is, therefore, a minor source of CH_4 to the EGSL.

4.5.5 Implications for the oceanic methane paradox

To evaluate the role of CH_4 photoproduction in maintaining the supersaturation of CH_4 in open-ocean surface waters, we compared our CH_4 photoproduction rates with ocean-to-atmosphere CH_4 emission rates and microbial CH_4 oxidation rates from the literature. Global open-ocean CH_4 emission rates derived from high-resolution basin-wide observations were estimated at 0.4 (0.2–0.6) Tg $year^{-1}$ based on Pacific data (Bates et al., 1996) and 0.41 (0.29–0.58) Tg $year^{-1}$ based on Atlantic data (Rhee et al., 2009). The open-ocean CH_4 photoproduction rate of 118 Gg $year^{-1}$ (~0.12 Tg yr^{-1}), 95% of which is expected to take place in the mixed layer (Fichot and Miller, 2010), can thus account for 30% (20-60%) of open-ocean CH_4 emissions. Yearly-averaged CH_4 emission rates in the subtropical gyres of the North and South Pacific were estimated at 140 nmol m^{-2} d^{-1} and 285 nmol m^{-2} d^{-1}, respectively, based on the latitude-binned annual flux data of Bates et al. (1996). CH_4 photoproduction rates calculated here are 71% and 35% of these emission rates in the North and South Pacific subtropical gyres, respectively. CH_4 photoproduction can therefore sustain a significant portion of the ocean-to-atmosphere CH_4 emission both on global open-ocean scales and in major oceanic gyres. Photodegradation of CDOM in the surface ocean is therefore a potentially important contributor to the oceanic methane paradox. It appears to be less important in coastal environments, where our global coastal estimate of 3 Gg $year^{-1}$ is small (<1%) compared to the estimated flux of ~0.4 Tg $year^{-1}$ (Rhee et al., 2009).

It should be noted that some estimates of oceanic CH_4 emission have been reported to be an order of magnitude higher than those of Bates et al. (1996) and Rhee et al. (2009). These higher estimates are mostly from literature compilations (e.g. Bange et al., 1994) and/or are speculative (e.g. Lambert & Schmidt, 1993). However, more recent basin-wide measurements in the Atlantic suggest similarly high emission rates on global open-ocean scales (Forster et al., 2009). The exact reasons for this large discrepancy remain unclear but may arise from differences in sampling coverage and wind speed data used for flux calculations, or more plausibly in CH_4 measurement methodology (Forster et al., 2009; Rhee

et al., 2009). Compared to these higher emission rates, our photoproduction rates are relatively small (<10%).

In the open ocean, CH_4 turnover times due to microbial oxidation vary from 14 to 50 years (Scranton & Brewer, 1978; Rehder et al., 1999). When combined with typical surface-water CH_4 concentrations of <3 nmol L^{-1} in major ocean gyres (Bates et al., 1996; Forster et al., 2009; Rhee et al. 2009), these turnover times imply microbial CH_4 oxidation rates of 33-117 nmol m^{-2} d^{-1} in the upper 200 m of the water column. Our average CH_4 photoproduction rate for the open ocean (64 nmol m^{-2} d^{-1}) thus represents 55-182% of these microbial oxidation rates. Holmes et al. (2000) reported a CH_4 oxidation rate of 30 nmol m^{-2} d^{-1} at Station ALOHA, which is ~30% of our yearly-averaged CH_4 photoproduction rate (102 nmol m^{-2} d^{-1}) at this location.

The photochemical source of CH_4 could be significantly larger if photodegradation of particulate organic matter (POM) is also considered. POM photodegradation in open oceans produces CO in an amount that is 20-40% of that from CDOM photodegradation (Xie & Zafiriou, 2009). If the $\Delta CH_4/\Delta CO$ ratio for POM is similar to that for CDOM, our estimate of open-ocean CH_4 photoproduction could increase by 20-40%, to 146-165 Gg $year^{-1}$. The relatively low irradiation temperature (8 °C) maintained during our experiments (Section 4.4.2) might also have led to an underestimate of the global photoproduction of CH_4. The rates of several CDOM photoreactions have been shown to increase with temperature (e.g. Zhang et al., 2006; Zhu et al., 2018), and this could possibly be the case for CH_4 photoproduction. If that were the case, the photochemical source of CH_4 would be even more significant compared to oceanic emission and microbial oxidation.

4.6 CONCLUSION

CH_4 photoproduction is likely ubiquitous in natural waters. While the rate of CH_4 photoproduction increases with the sample's initial CDOM absorption coefficient, the absorption loss-normalized CH_4 photoproduction rate and the molar ratio of CH_4 to CO photoproduction show opposite trends. CH_4 photoproduction in open oceans is significant

compared with outgassing and microbial oxidation. This photochemical pathway, combined with other major surface-ocean methanogenic processes (Repteta et al., 2016; Klintzsch et al., 2019), is likely responsible for the oceanic methane paradox. Future studies should extend sampling coverage, particularly, to the Southern Ocean, determine the contribution from particle photochemistry, and elucidate the mechanisms for CH_4 photoproduction.

4.7 ACKNOWLEDGEMENTS

O. Zafiriou facilitated Sargasso Sea sampling from R/V Atlantic Explorer in 2016 and 2019. Rod Johnson and BIOS technicians collected samples in 2016 and N. Cohen and M. Saito in 2019. T. M. Clemente of the Hawaii Ocean Time-series program facilitated sample collection from Station ALOHA. Y.L. and L.G. were supported by scholarships from the China Scholarship Council and the Institut des sciences de la mer de Rimouski. Comments from the editor and two anonymous reviewers improved the manuscript. Financial support for this study was provided by H.X.'s NSERC Discovery Grant (2017-05135) and ArcticNet (phase 4) grant and C.F.'s NASA Water Quality grant (80NSSC18K0344). Ship time in the Saguenay Fjord and the St. Lawrence estuary and Gulf was provided by Fisheries and Oceans Canada and the Réseau du Québec Maritime.

4.8 DATA AVAILABILITY STATEMENT

Data reported in this study are archived at figshare.com and is accessible via https://doi.org/10.6084/m9.figshare.11935548.

4.9 TABLES

Table 4-1. Physical, chemical, and optical properties of initial (unirradiated) water samples. NA: not available.

Region	Station	Sampling depth (m)	In situ T (°C)	Salinity	DOC (µmol L^{-1})	$a_g(320)$ (m^{-1})	$S_{275-295}$ (μm^{-1})
Canadian Arctic and Labrador Sea	108	10	-1.6	30.372	NA	0.77	25.7
	421	10	0.1	28.473	NA	0.40	32.04
	428	10	2.9	27.495	NA	0.78	26.53
	434	10	4.7	26.921	NA	1.08	24.99
	650	10	1.7	32.324	83.6	0.71	24.54
Estuary and Gulf of St. Lawrence	BSM	0.25	NA	0	305.9	9.85	15.76
	EUT01	3.5	9.64	14.4	158.4	2.88	19.88
	EUT02	4	7.64	19.5	134.4	2.54	19.72
	IML4	2.5	NA	25	139.8	3.70	16.68
	CMO3	2.5	4.99	28.51	99.5	1.87	19.15
	TDC5	2.5	8.75	31.4	83.4	0.862	24.15
	P1	10	-0.01	0.11	327.7	10.68	15.87
	P2	10	-0.14	2.34	317.8	9.89	15.93
	P3	10	-0.71	21.48	162.5	4.07	16.35
	P4	10	-0.73	24.34	137.1	3.19	16.94
	P9	326	5.71	34.49	55.9	0.478	20.55
	P10	10	-1.55	28.9	103.1	1.98	18.50
	P11	10	-1.58	29.3	101.2	1.90	18.60
	P12	10	-1.68	31.72	80.9	0.942	22.10
Saguenay Fjord	SAG13	2.2	9.95	5.88	478.5	25.2	13.83
Sub-tropical N. Pacific Ocean	ALOHA	6.5	24.50	34.72	84.5	0.110	50.82
	ALOHA	775	5.10	34.38	48.6	0.220	21.00
	ALOHA	4001	1.45	34.68	NA	0.225	28.86
Sargasso Sea	BATS	10	NA	34.67	NA	0.210	30.39
Sargasso Sea	Sta. 5	30	25.70	36.48	83.9	0.116	28.94
Coastal Massachusetts	CR	1	21.43	0.31	473.5	24.24	13.92
	RH	1	17.94	22.96	315.8	10.13	15.59
	PIS	1	14.28	27.17	161.7	4.10	17.23
Saint Fabien, Quebec	Peatland pond	0.25	NA	0	NA	173.54	12.88

4.10 FIGURES

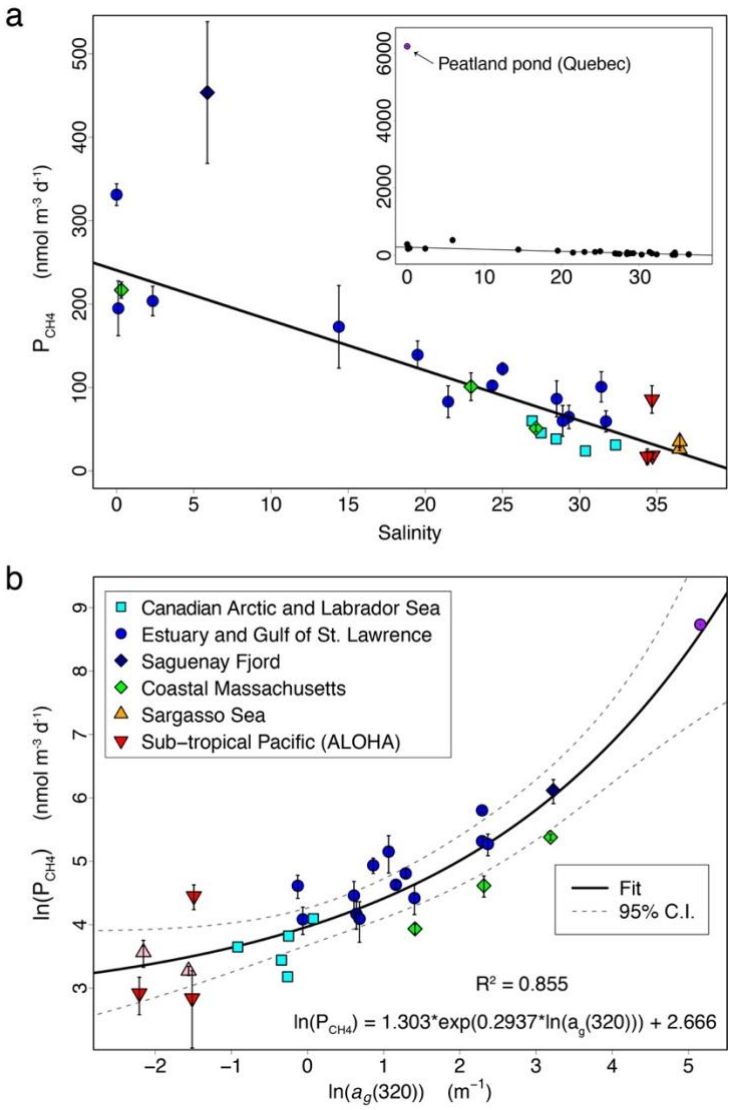

Figure 4-1. Methane photoproduction rate as a function of salinity (**a**) and the initial absorption coefficient at 320 nm (**b**). In panel **a**, line is the linear fit to the data excluding the samples from station SAG13 in the Saguenay Fjord and from the peatland pond in Saint-Fabien, Quebec. The inset shows the plot including the peatland pond sample.

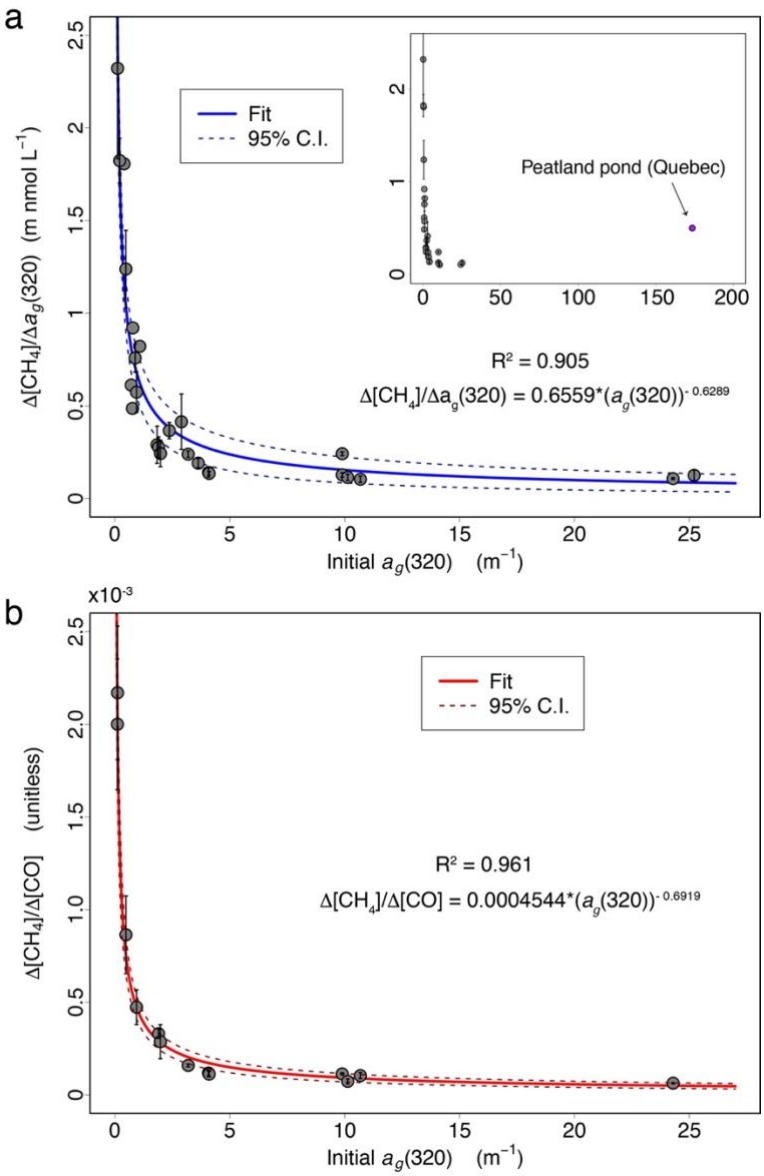

Figure 4-2. The ratio of CH_4 photoproduction to photochemical loss of $a_g(320)$ (**a**) and the molar ratio of CH_4 to CO photoproduction (**b**) as a function of the initial $a_g(320)$. In panel **a**, the fit excludes the peatland pond sample. The inset shows the plot including the peatland pond sample.

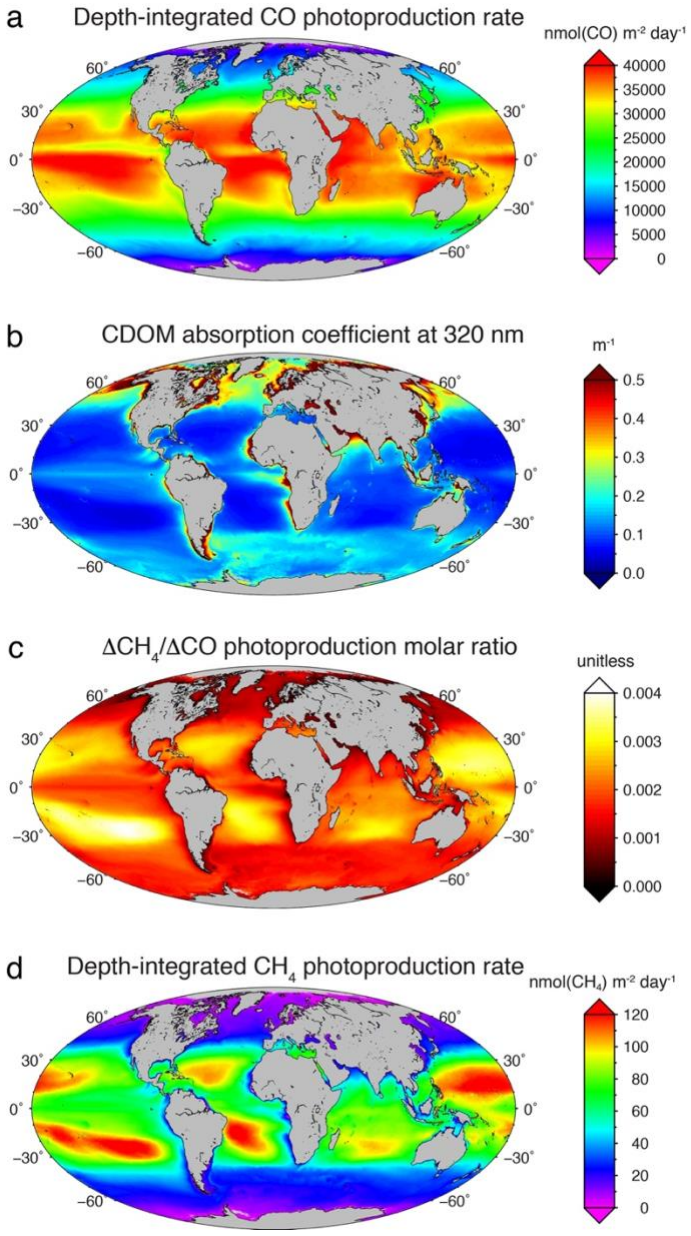

Figure 4-3. Mapped yearly climatologies (2002-2018) for the surface ocean calculated with the remote-sensing based model: Depth-integrated rate of CO photoproduction in the top 150 m (**a**), CDOM absorption coefficient at 320 nm (**b**), molar ratio of CH_4 to CO photoproduction (**c**), and depth-integrated rate of CH_4 photoproduction in the top 150 m (**d**).

4.11 SUPPLEMENTARY INFORMATION

4.11.1 Supplementary text

Text S1. Contamination-controlling measures

Before use, all glassware, including quartz tubes, had been sequentially soaked in 10% reagent-grade HCl overnight, thoroughly rinsed with Nanopure water, air-dried, and combusted at 450 °C. The filtration capsules had been profusely flushed with Nanopure water (~10 L/capsule) and rinsed with sample water (~2 L) before transferring water from the Niskin bottles to the receiving glass bottles. The polyethersulfone (PES) membrane filters used for re-filtering the water samples had been thoroughly flushed with Nanopure water (>0.6 L/filter) under vacuum. Both the filtration capsules and PES membrane filters were confirmed to be free of dissolve organic carbon (DOC) and CDOM contamination after the Nanopure water flushing. The medical-grade air used for re-oxygenating the water samples was passed through a column of silica gel beads (mesh size 30) to remove potential volatile organics present in the air cylinder.

Extra contamination-controlling measures were taken for sampling at Sta. 5 in the Northwest Atlantic. First, the Niskin bottles were pressurized with pure nitrogen during filtration to avoid contacting the bottle water with ambient air. Second, filtered water was transferred into a 19-L clear-glass (Pyrex) carboy sealed with a clean silicone stopper through which two PTFE lines were inserted: one for transferring water into and out of the carboy and the other for venting to ambient air. The venting line was connected to an OMICRON PTFE membrane filter (50 mm in diameter; 0.2 μm in pore size) and a column of silica gel beads (mesh size 30) to minimize potential contamination by atmospheric particles and volatile organics, respectively. The carboy was cleaned sequentially with HPLC-grade methanol (2 × rinsing), Citranox detergent (2-d soaking), 20% reagent-grade HCl (24-h soaking), 1% reagent-grade ammonium (24-h soaking), 5% trace metal-grade HCl (7-d soaking). The carboy was profusely rinsed with Nanopure water between each cleaning step

and with trace metal-grade pure water after the final HCl soaking. Before filtering water into it, the carboy was thoroughly flushed with ambient air flowing through the PTFE filter and the silica gel column. Although 19 L of water was collected from Sta. 5, the majority of this sample was designated for other experiments and only ~3 L was available for the CH_4 experiment in this study.

Text S2. Blank tests

Blank tests were performed to ensure that sample manipulation did not introduce artifacts significantly affecting CH_4 photoproduction. Potential artifacts could come from trace amounts of CH_4-producing substrates added to the samples from the PES filters during filtration and/or from lab air during sample transfer. To verify these potential artifacts, one of the tests compared two Nanopure water samples: one was passed through a PES filter and the other was not. The remaining sample manipulation procedures were identical to those described in section 4.4.2 in the main text. The samples were irradiated, along with parallel dark controls, for 192 h under the same conditions as those for the natural water samples. The resulting change in CH_4 concentration in the filtered sample relative to its dark control (mean ± s.d.: 0.044 ± 0.026 nmol L^{-1}) was not significantly different from that in the unfiltered sample (0.050 ± 0.11 nmol L^{-1}) as determined by two-tailed *t*-test ($\alpha = 0.05$) assuming unequal variance ($p = 0.44$, n = 4). This result demonstrates that filtration-linked artifacts were negligible.

In another test, two subsamples were taken from the 19-L glass carboy containing the water from Sta. 5 (see Supplementary Text S1). Caution was exercised to minimize contact with lab air during each step of sample transfer for one of the subsamples. This was accomplished by flushing all sample-receiving vessels with ultrapure argon (>99.999%, Air Liquide) immediately before sample transfer and maintaining an atmosphere of argon above the water surface in the receiving vessels during the transfer. The sample was 0.2-μm re-filtered with a sterilized PES syringe filter (25 mm in diameter, Whatman) due to difficulty in isolating the sample from lab air under vacuum filtration. The procedure of sample transfer and re-filtration for the second subsample was the same but without argon flushing, thereby

allowing the sample to be in contact with lab air. The two samples were irradiated, alongside parallel dark controls, for 213 h under the conditions described in section 4.4.2 in the main text. The amount of CH_4 photochemically produced was 0.26 ± 0.027 nmol L^{-1} in the sample with minimized contact with lab air and 0.28 ± 0.040 nmol L^{-1} in the sample having routine contact with lab air. These two values are not significantly different based on two-tailed *t*-test ($\alpha = 0.05$) assuming unequal variance ($p = 0.82$, n = 3), indicating negligible artifacts from lab air.

The water samplers employed during this study were made of plastics, i.e. high-density polyethylene (HDPE) for the bucket (used for the peatland pond sampling only) and polyvinyl chloride (PVC) for the Niskin bottles (used on all other occasions). Although blank tests for these samplers were not done due mainly to logistic and technique restrictions, several relevant elements suggest that artifacts, if any, resulting from leaching of organics into water samples should be minor. First, the water-plastic contact times were very short, less than a few minutes in case of the bucket and <0.5 hour for surface waters (the majority of our samples) in case of the Niskin bottles. Second, microplastics of polyethylene (PE) and PVC suspended in artificial seawater (plastics diameter: 200 μm; concentration: 417 mg L^{-1}) did not release significant DOC (<±5%) in the dark or under solar-simulated irradiation (40 h for PE and 7 d for PVC; M. Wu & H. Xie, unpubl. data), indicating that these two types of plastics do not leach out organics even under solar radiation over a period that was much longer than the water-plastic contact times during the field sampling. The fact that the internal walls of the sampling bottles were in the dark further reduces any potential leaching. Lastly and more importantly, a clear decreasing trend of the CH_4 photoproduction rate with increasing salinity (and decreasing CDOM) (Fig. 4-1 in the main manuscript) is inconsistent with a major CH_4 source derived from plastic contamination which is expected to be variable among different bottles and with time.

Text S3. Supplemental information on analytical methods

The DOC Shimadzu TOC-Vcpn carbon analyzer was calibrated with potassium biphthalate. The system was checked at intervals of seven consecutive sample analyses,

against Hansell's low-carbon and deep Florida Strait (700 m) reference waters with DOC concentrations of 1 μmol L^{-1} and 41–44 μmol L^{-1}, respectively. The coefficient of variation on five replicate injections was <1.5 %.

CDOM absorbance spectra were recorded from 800 nm to 200 nm at 1-nm intervals. The spectrometer was fitted with 1- or 10-cm quartz cells and referenced to Nanopure water. The sample cell was rinsed with methanol, pure water, and sample water between individual scans. A baseline correction was applied by subtracting the absorbance value averaged over 683–687 nm from all spectral values (Babin et al., 2003). The Napierian absorption coefficient of CDOM at wavelength λ, $a_g(\lambda)$ (m^{-1}), was calculated as 2.303 times the absorbance divided by the cell's pathlength in meters. The lower detection limit, defined as three times the standard deviation of five replicate analyses of pure water, was 0.02 ± 0.01 m^{-1} over 280–600 nm.

Dissolved CH_4 and CO concentrations were determined using the methods identical to those of Zhang & Xie (2015) and Xie et al. (2002), respectively. Briefly, a syringe-based headspace method (gas:water ratio: ~1:8 for CH_4 and ~1:6 for CO) was used to extract dissolved CH_4 and CO into the gaseous phase. CH_4 in the equilibrated headspace gas was quantified using a Peak Performer 1 gas chromatograph fitted with a flame ionization detector (Peak Laboratories, USA). The analyzer was calibrated using a CH_4 standard of 4.94 parts per million by volume (ppmv) (Air Liquide) traceable to the National Institute of Standards and Technology (NIST). The analyzer was factory-optimized specifically for CH_4 analysis, giving a lower detection limit of 0.045 nmol L^{-1} and a precision of ±4% (Zhang & Xie, 2015). CO in the headspace gas was quantified using a TA7000 Reduction Gas Analyzer (Trace Analytical, USA) calibrated with an NIST-traceable CO standard of 1.05 ppmv. The uncertainty of CO measurement was within ±2% and the lower detection limit was 0.02 nmol L^{-1}. Single-point calibrations were adopted, since pre-study tests showed that the instruments consistently responded linearly up to 10.5 ppmv for CH_4 (~80 nmol L^{-1}) and 1.86 ppmv for CO (~12 nmol L^{-1}) with essentially zero intercepts (Xie et al., 2002; Zhang & Xie, 2015).

Free-living heterotrophic bacterial abundance was determined using an Epics Altra flow cytometer (Beckman Coulter) equipped with a 488 nm argon laser operated at 15 mW (Belzile, 2008). A 0.5 mL subsample was half diluted in 1×Tris-EDTA buffer (pH 8) and the resulting 1 mL solution was incubated with 0.25 µL SYBR Green I (Ci = 10 000×, Invitrogen) for 30 min at room temperature in the dark. We added 10 mL fluorescent beads (1 µm in diameter; Fluoresbrite Plain, YG) to each sample as an internal standard and then analyzed the samples with the cytometer for 3 min. Bacterial cell abundance was calculated from the analysis volume that had been gravimetrically determined and corrected for the dead volume (50 µL, i.e. the volume taken from the sample tube but not accounted for when data acquisition was stopped).

Text S4. Uncertainties associated with the use of a spectrally invariant molar ratio of CH_4 to CO photoproduction

As described in Methods section of the main manuscript, the approach used in this study first calculates depth-integrated CO photoproduction rates using well-established spectral apparent quantum yields of CO photoproduction and then converts these rates to CH_4 photoproduction rates using a molar ratio of CH_4 to CO photoproduction, $\Delta CH_4/\Delta CO$, determined from irradiation experiments carried in a solar simulator. While the value of this ratio has been shown to vary with the initial CDOM absorption coefficient of the sample at 320 nm (see Fig. 4-2b), the potential spectral dependency of this molar ratio is ignored and it is therefore inherently assumed that this ratio is spectrally invariant. As a result, this ratio is assumed to be unaffected by variations in the spectral dependencies of the incident solar irradiances that were typically observed in the sunlit ocean. In reality, one could expect differences in the spectral dependencies of CH_4 and CO photoproduction, which could stem from likely differences in the spectral dependencies of their respective apparent quantum yields. Here, we carried out a simple analysis to assess the sensitivity of CH_4 photoproduction rates calculated with this spectrally invariant $\Delta CH_4/\Delta CO$ ratio to variations in the spectral dependencies of the incident irradiances expected with location, time, and with vertical depth in the water column.

Downwelling plane irradiance spectra and their spectral dependencies were modeled for a range of solar zenith angles (SZA: 0, 20, 40, 60, and 80^{o}) and vertical depths in the water column, and compared to the downwelling plane irradiance incident on the samples during the irradiation experiments in the solar simulator (Supplementary Figs. 4-S2a-d). Irradiance incident on the water surface were modeled using the System for the Transfer of Atmospheric Radiation and converted to below-surface values using a simple ratio of 0.94 (*Ruggaber et al.*, 1997). The SZA combines the effects of latitude, season, or time of day and drives most of the variability of incident surface solar irradiance globally. The effects of atmospheric pressure, ozone concentration, or other atmospheric constituents are more subtler and were ignored here for the purpose of this analysis. The effects of vertical depth were modeled for a station located in coastal Massachusetts (42.156^{o}N, 70.206^{o}W) using a diffuse attenuation coefficient spectrum ($K_d(\lambda)$ for λ = 305–490 nm) measured in situ using a Compact Optical Profiling System [*Morrow et al.*, 2010] and extrapolated to 290 nm using the exponential trend observed between 305 and 340 nm. The modeled surface irradiance spectrum for the SZA=40^{o} was then combined with the measured $K_d(\lambda)$ spectrum to calculate the incident irradiance spectra at different vertical depths (z: 0, 2, 5, 10, and 20 m) using the equation: $E_d(z, \lambda) = E_d(0\text{-},\lambda)*\exp(-K_d(\lambda)*z)$, where $E_d(0\text{-},\lambda)$ and $E_d(z, \lambda)$ represent the downwelling plane irradiance spectra just below the surface and at depth z, respectively. The downwelling irradiance incident on the samples during the experiments was measured using a calibrated UV-Visible spectroradiometer (*Fichot and Benner*, 2014) and was compared to the modeled spectra (Supplementary Figs. 4-S2a-d). Overall, the SZA had subtle effects on the spectral dependencies of the incident irradiances. In contrast, vertical depth had a much more pronounced effects due to the selective attenuation of UV radiation relative to the visible light.

These irradiance spectra were then used to assess the impacts on the modeled spectral dependencies of the CO photoproduction action spectra at the well-mixed coastal Massachusetts station (Supplementary Figs. 4-S2e,f). The CDOM absorption coefficient spectrum (Perkin-Elmer Lambda 650 UV-Visible spectrophotometer, (*Fichot and Benner*,

2011)) measured at the coastal-Massachusetts station, $a_g(\lambda)$, and the composite apparent quantum for CO photoproduction, $\phi_{CO}(\lambda)$, used in this study (*Fichot and Miller*, 2010) were used to calculate the corresponding CO photoproduction action spectra, $PP_{CO}(z,\lambda)$, as in this equation: $PP_{CO}(z,\lambda) = E_d(z, \lambda)*a_g(\lambda)*\phi_{CO}(\lambda)$. Note here that plane irradiance was used instead of scalar irradiance, but this has no implications for the results of the analysis. Like for the incident irradiances, the SZA only has subtle effects on the spectral dependencies of the CO photoproduction action spectra, whereas changes in vertical depth had a major impact, with most of the CO photoproduction being driven by visible light at depth > 20 m. In particular, the action spectra at depths were drastically different from those observed during the irradiation experiments (Supplementary Fig. 4-S2f). These major changes in the spectral dependencies of the CO photoproduction action spectra can, in turn, lead to uncertainties in the CH_4 photoproduction rates calculated using our approach if the molar ratio of CH_4 to CO photoproduction is indeed spectrally variable.

Various plausible hypothetical spectral dependencies of the molar ratio of CH_4 to CO photoproduction were generated and used to assess the sensitivity of the CH_4 photoproduction rates to the variations in the spectral dependencies of the CO photoproduction action spectra (Supplementary Fig. 4-S3). The CDOM absorption coefficient at the coastal-Massachusetts station was measured at $a_g(320)= 0.75\ m^{-1}$, indicating a value of $\Delta CH_4/\Delta CO= 0.555 \times 10^{-3}$ when using the equation of Figure 4-2b. The hypothetical spectral dependencies of the molar ratios generated here (Supplementary Fig. 4-S3) were parameterized using exponential functions and such that it would generate a modeled ratio of $\Delta CH_4/\Delta CO$ that was also equal to 0.555×10^{-3} when applied to the CO photoproduction action spectrum of the samples exposed in the solar simulator. The various curves shown in Supplementary Fig. 4-S3 thus represent several plausible spectral dependencies of the molar ratio of CH_4 to CO photoproduction that could lead to a measured molar ratio $\Delta CH_4/\Delta CO = 0.555 \times 10^{-3}$ during the experiments.

When applied to the modeled CO photoproduction action spectra, these hypothetical spectral dependencies of the molar ratio revealed that variations of the SZA lead to a mere

±7% uncertainty in modeled surface CH_4 photoproduction rates. However, that uncertainty increased dramatically with vertical depth and reaching as high as ±200% at 20 m at this coastal station (Supplementary Fig. 4-S4). However, the overall impact on depth-integrated photoproduction rates remained limited because most photoproduction occurs near the surface, where photoproduction action spectra in natural waters remain spectrally similar to that observed in the solar simulator. Our analysis showed that ~95% of the depth-integrated CO photoproduction occurred within the top 5 m at the coastal-Massachusetts station (Supplementary Fig. 4-S4a), and the uncertainty of depth-integrated CH_4 photoproduction rates remained around ±21% (Supplementary Fig. 4-S4b). Note here that a coastal station was used as an example but similar uncertainties can be expected in open-ocean regions. In these clearer waters, photoproduction reaches a deeper depth but the spectral dependency of the incident irradiance changes more slowly with depth. A simple assessment with simulated data also revealed the uncertainty of depth-integrated CH_4 photoproduction rates can be expected to be around ±20% in the open ocean.

4.11.2 Supplementary tables

Table 4-S1. Supplementary information on water sampling and sample irradiation.

Region	Station*	Month-year	Latitude (°N)	Longitude (°W)	Sampling depth (m)	Irradiation mode	Irradiation purpose**
Canadian	434	10-2015	70.18	133.55	10	Time series	P_{CH4}
Arctic and	428	10-2015	70.79	133.69	10	Time series	P_{CH4}
Labrador Sea	421	10-2015	71.43	134.00	10	Time series	P_{CH4}
	108	10-2015	76.27	74.62	10	Time series	P_{CH4}
	650	10-2015	53.79	55.44	10	Time series	P_{CH4}
Estuary and	BSM	10-2016	46.93	70.74	1	Time series	P_{CH4}
Gulf of St.	EUT01	10-2016	47.23	70.58	3.5	Time series	P_{CH4}
Lawrence	EUT02	10-2016	47.35	70.34	4.0	Time series	P_{CH4}
	IML4	10-2016	48.67	68.58	2.5	Time series	P_{CH4}
	CMO3	10-2016	48.27	69.37	2.5	Time series	P_{CH4}
	TDC5	10-2016	47.44	59.55	2.5	Time series	P_{CH4}
Saguenay Fjord	SAG13	07-2017	48.42	70.87	2.2	Time series	P_{CH4}
Saint Fabien	Peatland	06-2015	48.31	68.87	0.3	Fixed duration	P_{CH4}
Sargasso Sea	BATS	06-2016	31.92	64.34	10	Fixed duration	P_{CH4}
Estuary and	P1	02-2019	46.83	71.18	10	Fixed duration	$\Delta CH_4/\Delta CO$
Gulf of St.	P2	02-2019	47.04	70.75	10	Fixed duration	$\Delta CH_4/\Delta CO$
Lawrence	P3	02-2019	47.31	70.53	10	Fixed duration	$\Delta CH_4/\Delta CO$
	P4	02-2019	47.74	69.90	10	Fixed duration	$\Delta CH_4/\Delta CO$
	P9	02-2019	48.68	58.59	326	Fixed duration	$\Delta CH_4/\Delta CO$
	P10	02-2019	49.00	67.64	10	Fixed duration	$\Delta CH_4/\Delta CO$
	P11	02-2019	49.16	67.17	10	Fixed duration	$\Delta CH_4/\Delta CO$
	P12	02-2019	49.53	66.20	10	Fixed duration	$\Delta CH_4/\Delta CO$
Sub-tropical	ALOHA	04-2019	22.75	158.00	6.5	Fixed duration	$\Delta CH_4/\Delta CO$
North Pacific	ALOHA	04-2019	22.75	158.00	775	Fixed duration	$\Delta CH_4/\Delta CO$
Ocean	ALOHA	04-2019	22.75	158.00	4001	Fixed duration	$\Delta CH_4/\Delta CO$
Sargasso Sea	Sta. 5	06-2019	35.99	69.02	30	Fixed duration	$\Delta CH_4/\Delta CO$
Coastal	CR	06-2019	42.35	71.10	1	Fixed duration	$\Delta CH_4/\Delta CO$
Massachusetts	RH	06-2019	42.73	70.85	1	Fixed duration	$\Delta CH_4/\Delta CO$
	PIS	06-2019	42.71	70.80	1	Fixed duration	$\Delta CH_4/\Delta CO$

*CH: Charles River; RH: Rowley House; PIS: Plum Island Sound. **PCH4: Photoproduction rate of CH4; ΔCH4/ΔCO: the molar ratio of CH4 to CO photoproduction.

4.11.3 Supplementary figures

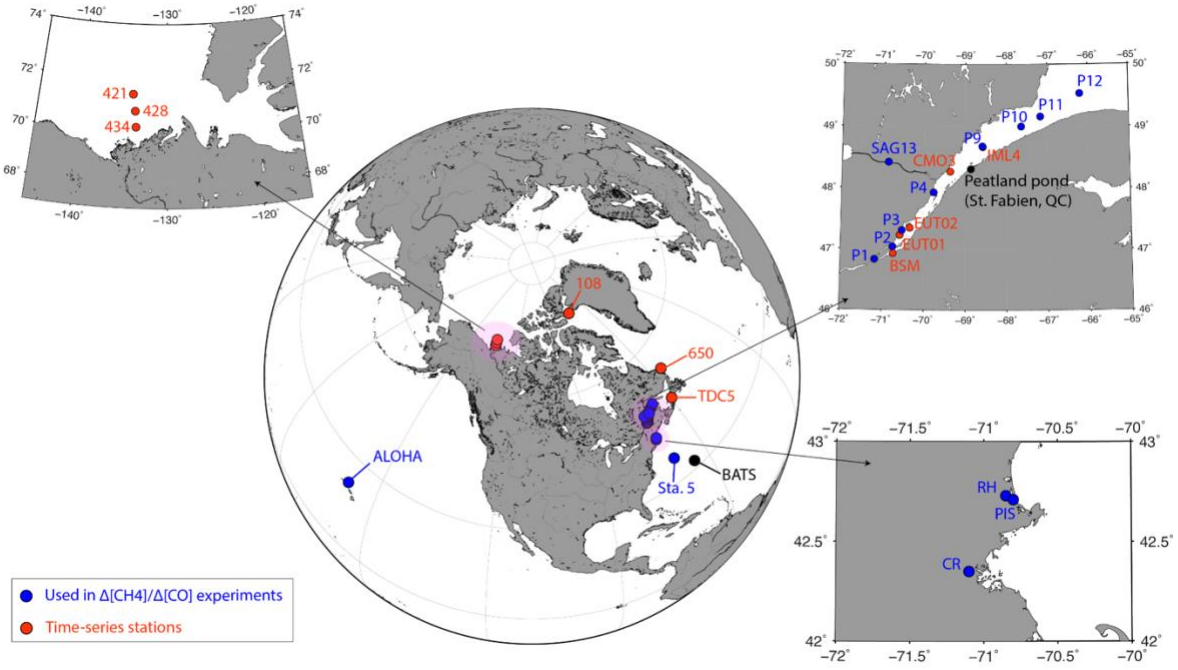

Figure 4-S1. Map of sampling stations. See Table 4-S1 for detailed sampling information at each station. CR: Charles River; RH: Rowley House; PIS: Plum Island Sound.

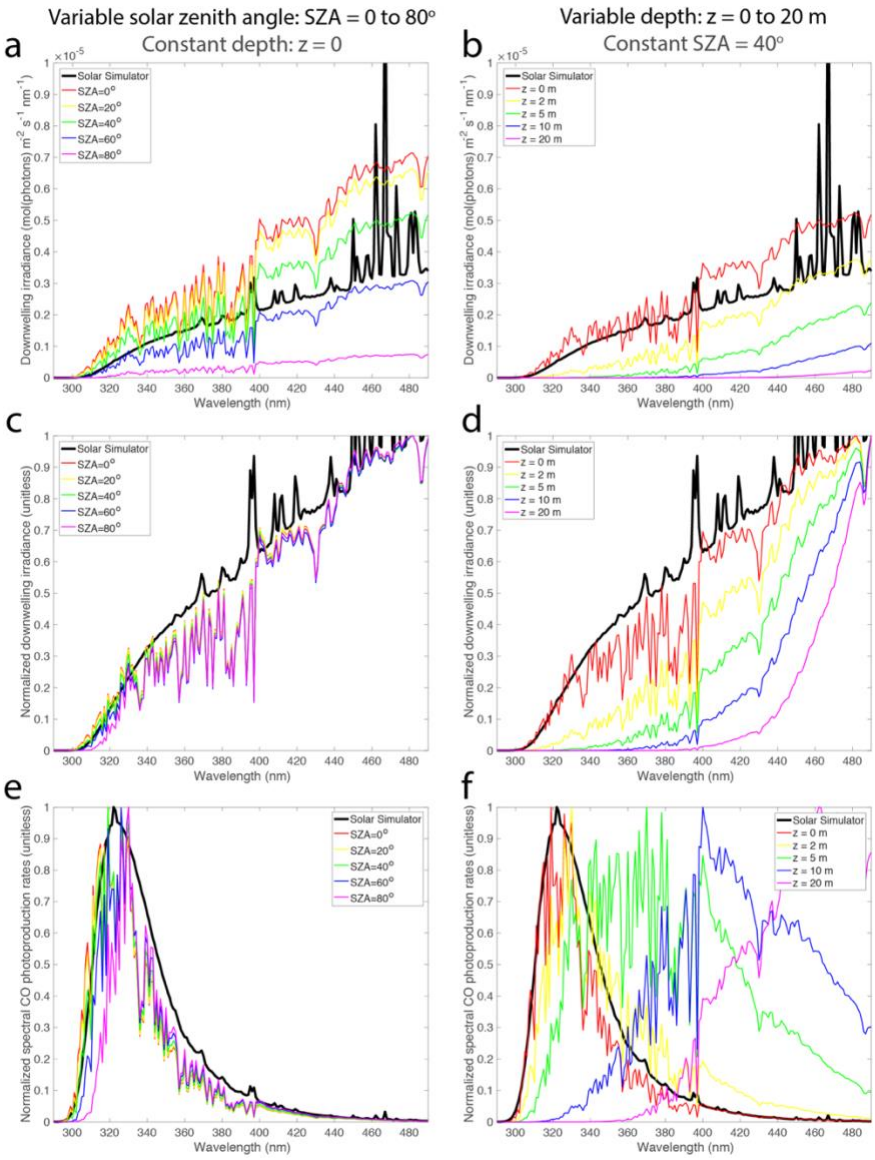

Figure 4-S2. Effects of variations in the solar zenith angle (SZA) and vertical depth (z) on: (**a**, **b**) the spectral incident downwelling plane irradiance, (**c**, **d**) corresponding spectral dependencies of incident spectral downwelling plane irradiance, and (**e**, **f**) corresponding spectral dependencies of CO photoproduction action spectra. Incident surface irradiances were modeled except for the solar simulator spectrum, which was measured. The effects of SZA are shown in the left panels (**a**, **c**, **e**). The SZA combines the effects of latitude, season, or time of day and drives most of the variability of incident solar irradiance globally. The effects of vertical depth are shown in the right panels (**b**, **d**, **f**) for a station located in coastal Massachusetts (42.156ºN, 70.206ºW) using measured vertical diffuse attenuation coefficient spectra (Compact Optical Profiling System) and CDOM absorption coefficient spectra (UV-Visible spectrophotometer).

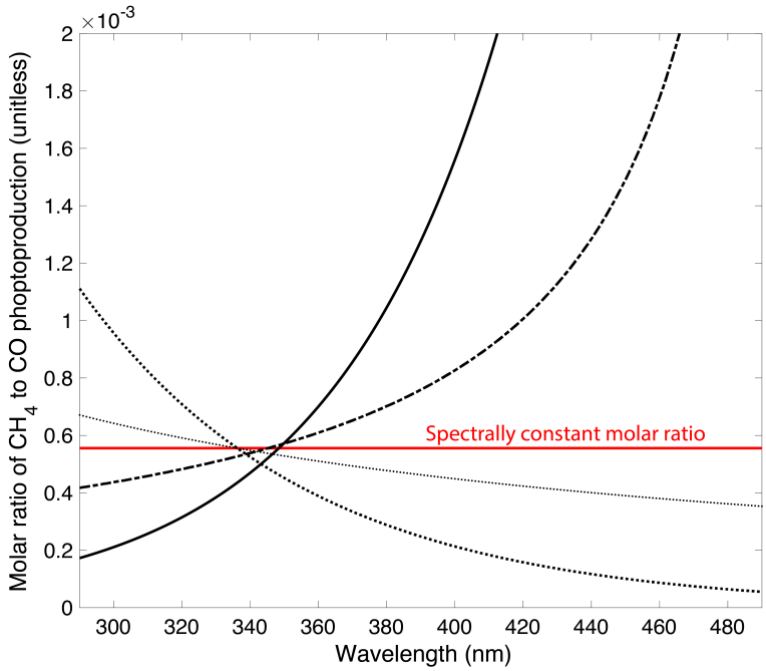

Figure 4-S3. Hypothetical spectral dependencies of the molar ratio of CH_4 to CO photoproduction. The red line represents a spectrally invariant ratio value of ~0.555 x 10^{-3}, corresponding to a value of $a_g(320) = 0.75\ m^{-1}$ (see equation of Fig. 4-2b) measured in a well-mixed water column at a coastal Massachusetts station (42.156ºN, 70.206ºW). All spectral dependencies shown here led to $\Delta CH_4/\Delta CO$ photoproduction ratios of ~0.555 x 10^{-3} when implemented on the solar simulator spectrum.

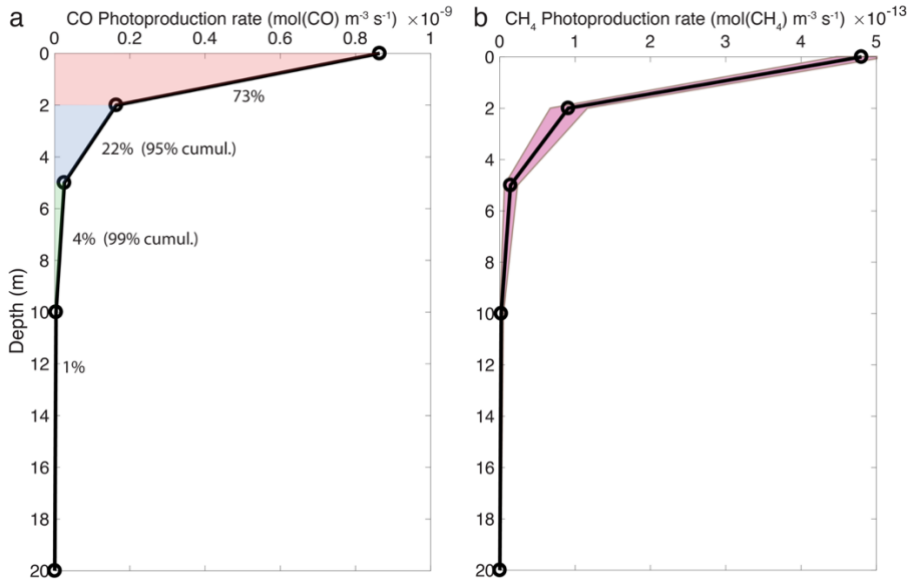

Figure 4-S4. Calculated photoproduction rates of CO and CH_4 for the coastal Massachusetts station (42.156ºN, 70.206ºW) at 5 different vertical depths (0, 2, 5, 10, and 20 m). Panel (**a**) shows that about 95% of the depth-integrated CO photoproduction occurs in the top 5 m of water column at that station. Panel (**b**) shows the corresponding CH_4 rates calculated using the spectrally invariant molar ratio of CH_4 to CO photoproduction of ~0.555 x 10^{-3} (see Fig. 4-S3), along with uncertainty bounds caused by potential variability in the spectral dependency of the molar ratio of CH_4 to CO photoproduction.

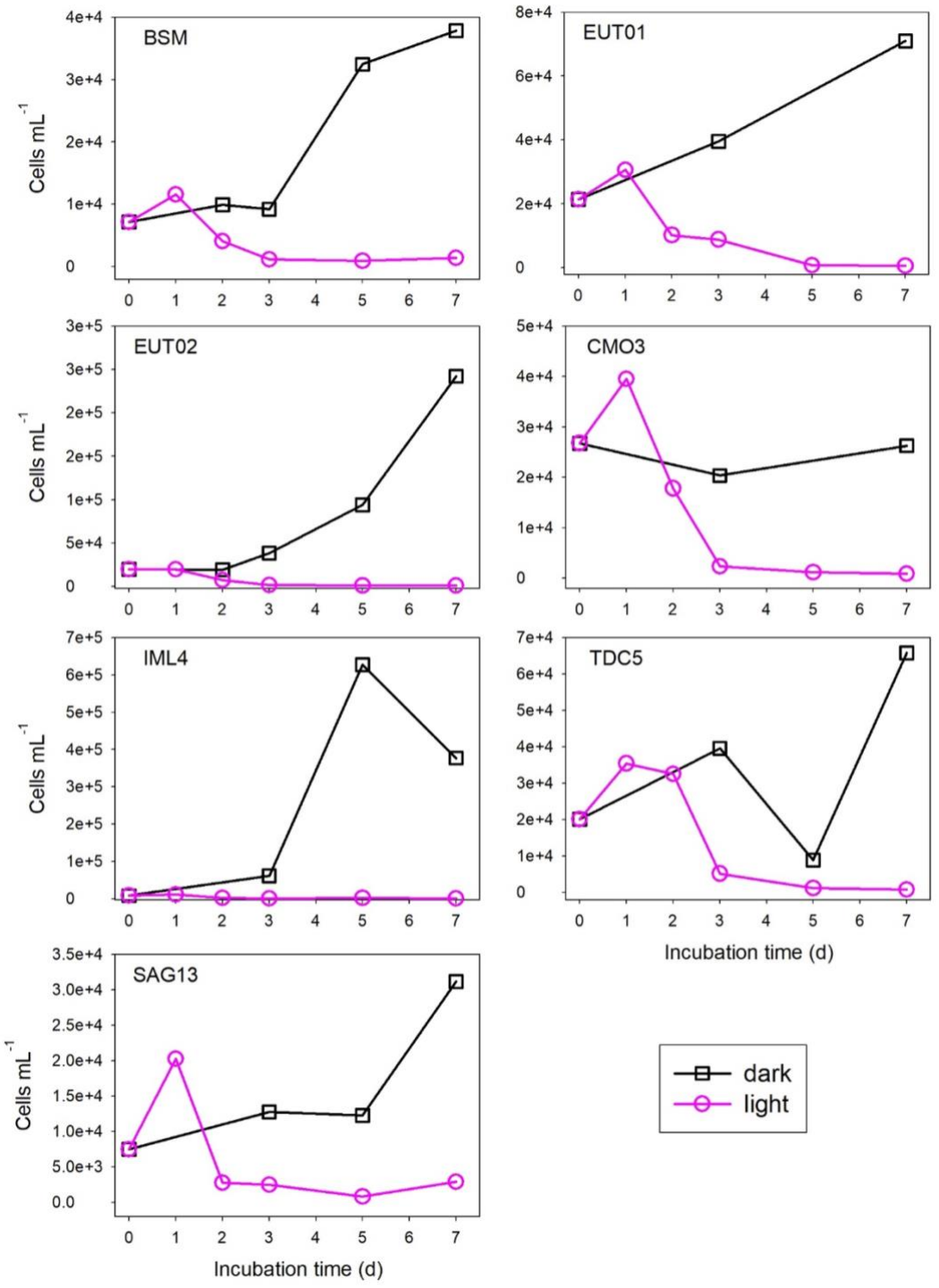

Figure 4-S5. Temporal evolution of heterotrophic bacterial cell abundance during time-course irradiations. Light: irradiated samples; dark: dark controls.

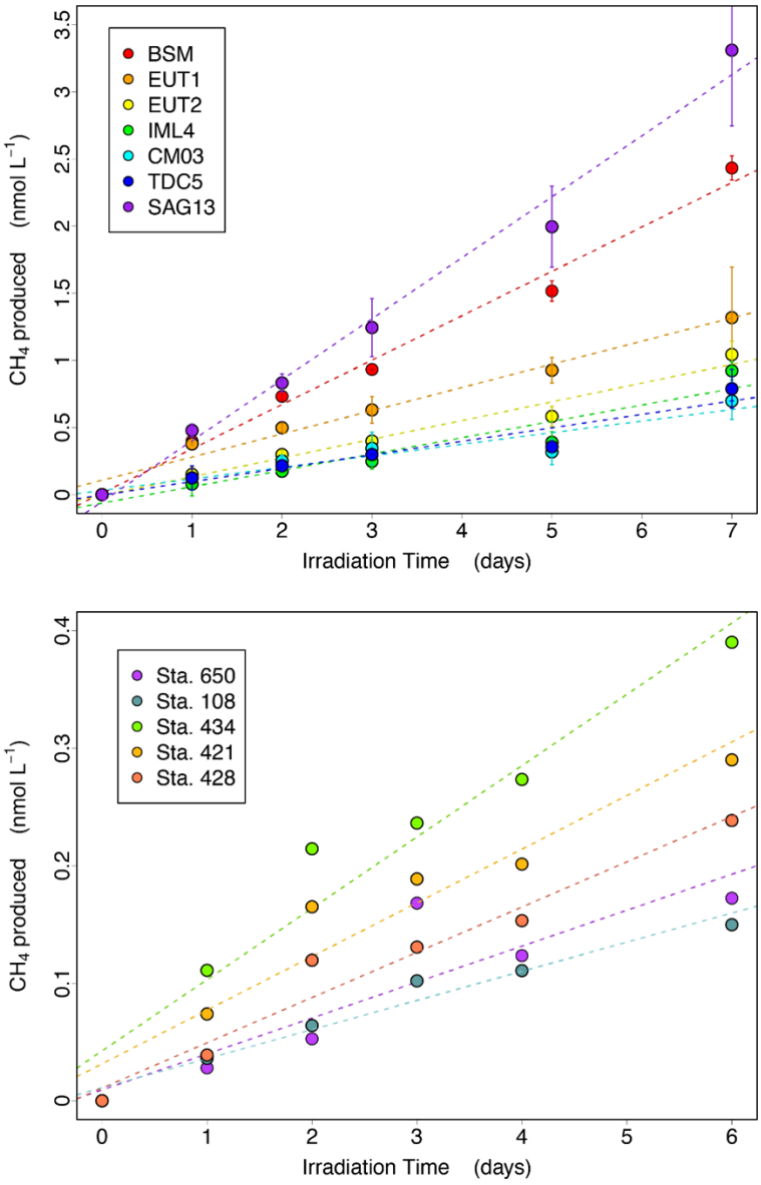

Figure 4-S6. Photoproduction of CH_4 as a function of irradiation time. Dark controls have been subtracted. Error bars in the upper panel are one standard deviation of triplicate irradiations. Lines are linear least-squares regressions of the data. See Fig. 4-S1 and Table 4-S1 for station locations.

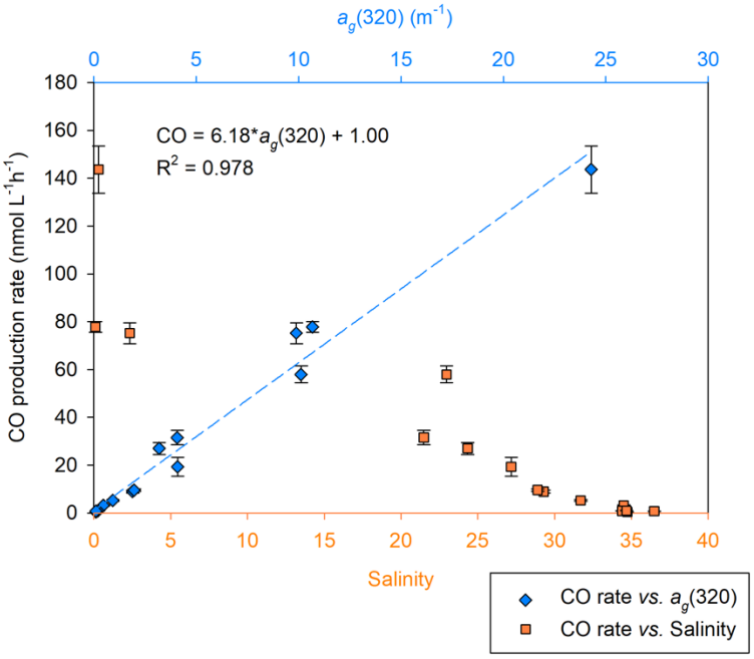

Figure 4-S7. CO photoproduction rate *versus* the initial $a_g(320)$ and salinity. Line is linear least-squares regression of CO *versus* $a_g(320)$.

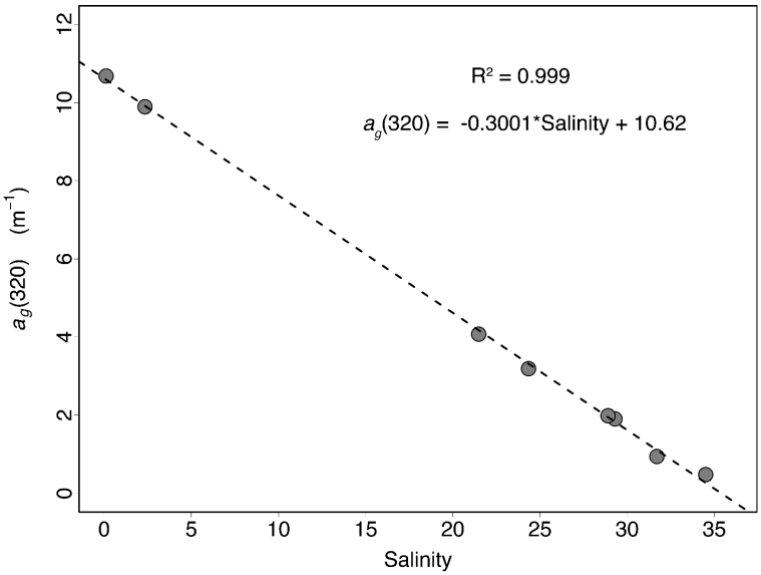

Figure 4-S8. Linear relationship between $a_g(320)$ and salinity for the samples from the Estuary and Gulf of St. Lawrence that were used for determining the ratio of CH_4 to CO photoproduction.

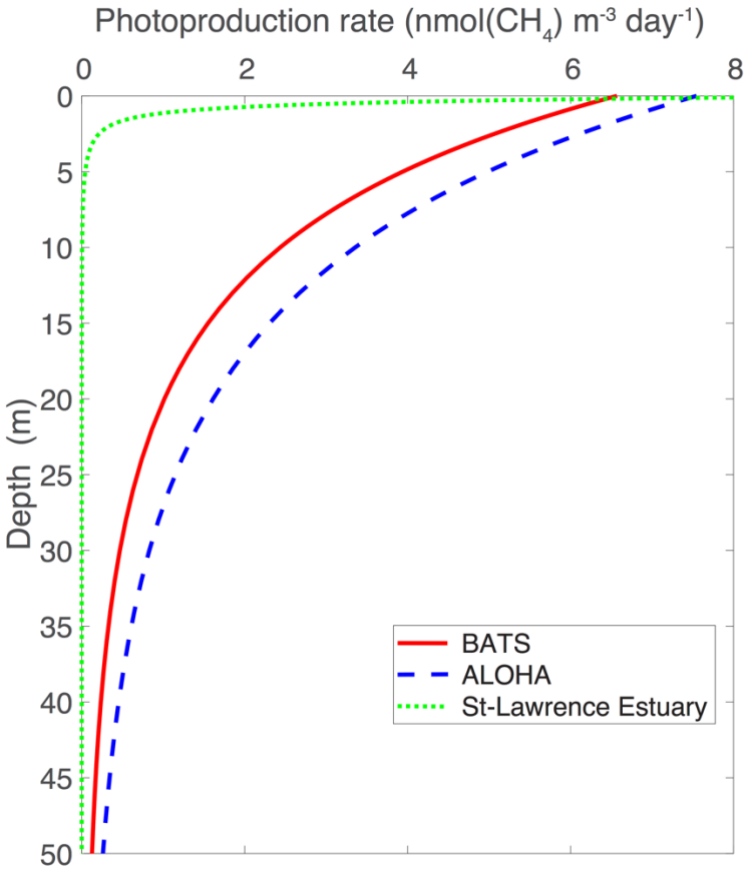

Figure 4-S9. Remote sensing-modeled depth profiles of CH_4 photoproduction rate at the BATS, Station ALOHA, and a site (49°N, 67.8°W) in the lower St. Lawrence estuary.

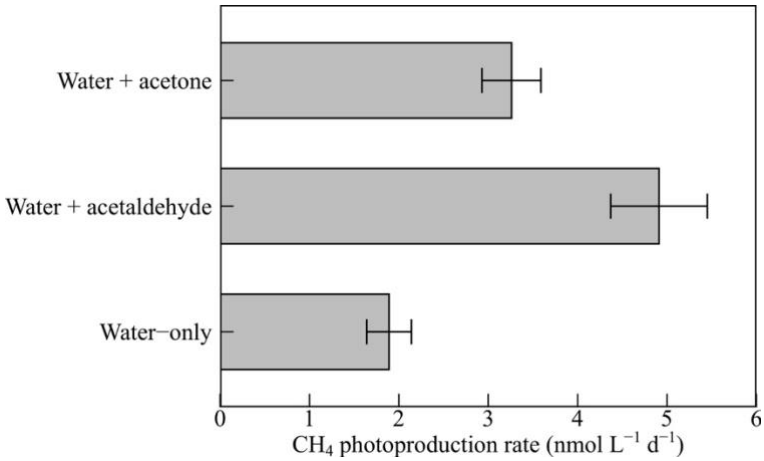

Figure 4-S10. Methane photoproduction from acetone (50 μmol L^{-1}) and acetaldehyde (50 μmol L^{-1}) added to filtered Rimouski River water. Dark controls were subtracted. Error bars are one standard deviation of triplicates.

CHAPTER 5
GENERAL CONCLUSION

The results from this research have broader implications for certain aspects of methane cycling in estuarine environments. First, the age of the freshwater delivered into an estuary appears to play an important role in controlling the $[CH_4]$ and $\delta^{13}C_{CH4}$ in the surface water of the estuary thereby affecting the methane emission rate and the applicability of $\delta^{13}C_{CH4}$ to methane source identification. The older age of the freshwater feeding the St. Lawrence Estuary, due to longer residence times in the Great Lakes and longer transit times through the St. Lawrence River, at least partly accounts for the lower $[CH_4]$ (~125 nmol L^{-1}) and heavier $\delta^{13}C_{CH4}$ signature (~−38‰) in the freshwater endmember of the St. Lawrence Estuary in comparison to the Saguenay Fjord ($[CH_4]$: 142-263 nmol L^{-1}; $\delta^{13}C_{CH4}$: ~−45‰).

Second, the contrast in submarine topography between the USLE and the Saguenay Fjord and LSLE offers a glimpse of how topography could affect the distribution of $[CH_4]$ in the water column and hence its efflux to the atmosphere in estuarine environments. The shallow and rugged seabed of the USLE, in conjunction with large tides, creates strong turbulence in the turbidity maximum zone where methane is produced from underlying or resuspended sediments. This intense mixing facilitates the transfer of methane from bottom water to surface water to air. In contrast, the inner basin of the Saguenay Fjord and the LSLE are featured with deep and stratified water column . Consequently, little methane released from the sediments near the head of the Fjord and from the pockmarks in the LSLE reaches the surface and escapes to the atmosphere. The submarine topography in estuarine environments thus plays a crucial role in partitioning the loss of water-column methane into microbial consumption and outgassing.

Third, the Laurentian Channel in the LSLE and GSL serves as a paradigm illustrating how the interactions of different water masses coupled with biogeochemical processes can produce characteristic [CH_4] distribution patterns in the water column. Although the subsurface methane maximum (SMMax) is not rare in the ocean, the pervasive and simultaneous occurrence of the contiguous SMMax and DMMin (deep methane minimum) observed in the Laurentian Channel is uncommon. This methane fingerprint derives from a near-perfect "collaboration" between various physical and biogeochemical drivers along the vertical axis: cold temperatures (hence high methane solubility) and in situ biological methane production in subsurface water; deep warmer water comprising two parental water masses with contrasting properties (warm and old *vs.* cold and young → low solubility and long microbial oxidation *vs.* the opposite) and depth-dependent volume proportions (cold up and warm down towards the bottom); a seafloor releasing methane into the bottom water from pockmarks and surface sediments. As a stark comparison, the similarly deep and highly stratified inner basin of the Saguenay Fjord is generally devoid of SMMax, DMMin or similar features due to its simpler water mass composition, low biological productivity, and weak sedimentary input.

Finally, this research reveals that large, deep estuarine systems, such as the LSLE and the GSL, tend to have lower or much lower areal methane emission rates than do small, shallow estuaries. In fact, both the surface-water [CH_4]s and areal methane fluxes for the LSLE and the GSL fall in the ranges for outer shelf seas and ocean slopes, respectively. Assigning the large, deep estuaries to the estuarine environment that is conventionally designated for small, shallow estuaries would lower the proportional contribution of the estuarine environment to the global oceanic methane emission flux. In this regard, Weber et al.'s (2019) approach, which divides the marine environment into four water depth-based regions (0-50 m: near-shore environments; 50-200 m: outer shelf seas; 200-2000 m: slopes; >2000 m: open oceans), appears more relevant. This approach will include most shallow estuaries into the near-shore environment category but place the deep, narrow estuarine systems such as the Saguenay Fjord into the outer shelf sea category. These deep, narrow systems, however, may have similar surface-water [CH_4]s and areal methane fluxes to those

in shallow estuaries, particularly if they receive large methane-rich freshwater discharge as in the case of the Saguenay Fjord. Hence, a better classification of estuarine environments is needed for compilation of methane emission data.

In some sense, this exploratory study leads to more questions than answers regarding the biogeochemical cycling of dissolved methane in the EGSL. Particular attention should be paid to addressing the following points in future studies:

1. The current data collected from the landward limit of the USLE only covered two seasons: November 2017 and February 2019. Additional sampling at this interface is needed to elucidate the seasonality and interannual variability of the St. Lawrence River [CH_4] endmember and its potential relationship with the river's freshwater discharge. Such information is essential for assessing the annual river input of methane into the EGSL, which is a key component of the methane budget of this system.

2. The TMZ is highly dynamic with respect to [CH_4] and its distribution but was particularly under-sampled both temporally and spatially. More surveys are imperative to better characterize the spatial and seasonal variations in [CH_4] and to assess the potential influence of the annual cyclic accumulation and destruction of the adjacent marshes on the [CH_4] dynamics in the TMZ.

3. Finer depth-resolved vertical profiles are needed to better locate and quantify the SMMax and DMMin in the LC and its branches, which will help better elucidate the mechanisms for the formation of these two features.

4. Given the high variability of the [CH_4]s observed at the few selected pockmarks in this study, more pockmark surveys are warranted to better resolve the spatiotemporal variations in [CH_4] at different pockmarks and to better appreciate how the [CH_4] changes with increasing distance from the pockmark gas venting centers. Such investigations are preferably conducted concurrently with multibeam bathymetrical and/or video-imaging surveys which deliver morphological information (including surface areas) on the pockmarks, enable real-time pinpointing of the gas venting plumes, and thus facilitate ship

positioning. Moreover, current speed and direction monitoring and turbulent microstructure profiling should also be performed simultaneously so that the diffusion and advection of methane can be calculated from the directly measured current and diffusivity data. Collectively, these multidisciplinary surveys will allow to estimate the input of pockmark-sourced dissolved methane into the bottom water.

5. The lab incubations performed during this study for determing the net methane cycling rates in the water column only covered very limited time (November only) and space (four depths in the Lower estuary and the Gulf only) scales and merely permitted quantifying the net cycling rates. Future studies should use the $^{14}CH_4$-addition technique (Mau et al., 2013) which, combined with bulk water-only incubations, can separate the consumption and production rates. Incubations should be extended to the other seasons and the entire EGSL, with particular attention to the TMZ, the SMMax, and bottom waters surrounding gas-venting pockmarks.

6. To more precisely pinpoint the origins of methane and the processes that may alter it, better spatially (e.g. including the St. Lawrence River and its major tributaries) and seasonally resolved $\delta^{13}C_{CH4}$ data and analyses of additional methane source indicators are needed. These additional source indicators include $\delta^{2}H_{CH4}$ (Whiticar, 1999) and the concentration ratio of methane to the sum of the C2 and C3 hydrocarbons (Schoell, 1980; Whiticar, 1999). Zooplankton culture experiments using ^{14}C-labeled phytoplankton as preys followed by quantification of $^{14}CH_4$ (Stawiarski et al., 2019) are suggested to test the zooplankton-associated methane production hypothesis for explaining the SMMax.

7. More studies are needed to further explore the mechanisms responsible for methane photoproduction from CDOM, including identification of more CH_4-producing precursors, elucidation of the plausible reaction pathways leading to methane formation, and the environmental factors (e.g. temperature, pH, salinity, oxygen, light composition) affecting the methane photoproduction rate. Research is also warranted to explore the potential methane photoproduction from particulate organic matter and its contribution to the oceanic methane paradox.

REFERENCES

Aitken, C.M., Jones, D.M., Larter, S.R., 2004. Anaerobic hydrocarbon biodegradation in deep subsurface oil reservoirs. *Nature* 431, 291–294. https://doi.org/10.1038/nature02922

Albert, D.B., Taylor, C., Martens, C.S., 1995. Sulfate reduction rates and low molecular weight fatty acid concentrations in the water column and surficial sediments of the Black Sea. *Deep Sea Res. Part Oceanogr. Res. Pap.* 42, 1239–1260. https://doi.org/10.1016/0967-0637(95)00042-5

Alperin, M.J., Reeburgh, W.S., Whiticar, M.J., 1988. Carbon and hydrogen isotope fractionation resulting from anaerobic methane oxidation. *Glob. Biogeochem. Cycles* 2, 279–288. https://doi.org/10.1029/GB002i003p00279

Althoff, F., Benzing, K., Comba, P., McRoberts, C., Boyd, D.R., Greiner, S., Keppler, F., 2014. Abiotic methanogenesis from organosulphur compounds under ambient conditions. *Nat. Commun.* 5, 4205. https://doi.org/10.1038/ncomms5205

Armentano, T.V., Menges, E.S., 1986. Patterns of change in the carbon balance of organic soil-wetlands of the temperate zone. *J. Ecol*. 74, 755–774. https://doi.org/10.2307/2260396

Andrew, A.A., Del Vecchio, R., Subramaniam, A., Blough, N.V., 2013. Chromophoric dissolved organic matter (CDOM) in the Equatorial Atlantic Ocean: Optical properties and their relation to CDOM structure and source. *Mar. Chem.*148, 33–43. https://doi.org/10.1016/j.marchem.2012.11.001

Babin, M., Stramski, D., Ferrari, G.M., Claustre, H., Bricaud, A., Obolensky, G., Hoepffner, N., 2003. Variations in the light absorption coefficients of phytoplankton, nonalgal particles, and dissolved organic matter in coastal waters around Europe. *J. Geophys. Res. Oceans* 108, 3211. https://doi:10.1029/2001JC000882

Bange, H.W., Bartell, U.H., Rapsomanikis, S., Andreae, M.O., 1994. Methane in the Baltic and North Seas and a reassessment of the marine emissions of methane. *Glob. Biogeochem. Cycles* 8, 465–480. https://doi.org/10.1029/94GB02181.

Bange, H.W., Uher, G., 2005. Photochemical production of methane in natural waters: implications for its present and past oceanic source. *Chemosphere* 58, 177–183. https://doi.org/10.1016/j.chemosphere.2004.06.022

Barnes, R.O., Goldberg, E.D., 1976. Methane production and consumption in anoxic marine sediments. *Geology* 4, 297–300. https://doi.org/10.1130/0091-7613(1976)4<297:MPACIA>2.0.CO;2

Bates, T.S., Kelly, K.C., Johnson, J.E., Gammon, R.H., 1996. A reevaluation of the open ocean source of methane to the atmosphere. *J. Geophys. Res. Atmospheres* 101, 6953–6961. https://doi.org/10.1029/95JD03348

Bauchop, T., Mountfort, D.O., 1981. Cellulose fermentation by a rumen anaerobic fungus in both the absence and the presence of rumen methanogens. *Appl. Environ. Microbiol.* 42, 1103–1110. https://doi.org/10.1128/aem.42.6.1103-1110.1981

Beale, R., Dixon, J.L., Arnold, S.R., Liss, P.S., Nightingale, P.D., 2013. Methanol, acetaldehyde, and acetone in the surface waters of the Atlantic Ocean. J. Geophys. Res. *Oceans* 118, 5412–5425. https://doi.org/10.1002/jgrc.20322

Bélanger, C., 2003. Observation and Modelling of a Renewal Event in the Saguenay Fjord, Université du Québec à Rimouski: Doctorat en océanographie. Université du Québec à Rimouski.

Bélanger, S., Babin, M., Larouche, P., 2008. An empirical ocean color algorithm for estimating the contribution of chromophoric dissolved organic matter to total light absorption in optically complex waters. *J. Geophy. Res. Oceans* 113, C04027, https://doi.org/10.1029/2007JC004436

Belzile, C., Brugel, S., Nozais, C., Gratton, Y., Demers, S., 2008. Variations of the abundance and nucleic acid content of heterotrophic bacteria in Beaufort Shelf waters during winter and spring. *J. Marine Syst.* 74, 946–956. https://doi.org/10.1016/j.jmarsys.2007.12.010

Belzile, M., Galbraith, P.S., Bourgault, D., 2016. Water renewals in the Saguenay Fjord. *J. Geophys. Res. Oceans* 121, 638–657. https://doi.org/10.1002/2015JC011085

Benner, R., Pakulski, J.D., McCarthy, M., Hedges, J.I., Hatcher, P.G., 1992. Bulk Chemical Characteristics of Dissolved Organic Matter in the Ocean. *Science* 255, 1561–1564. https://doi.org/10.1126/science.255.5051.1561

Bernard, B.B., Brooks, J.M., Sackett, W.M., 1976. Natural gas seepage in the Gulf of Mexico. *Earth Planet. Sci. Lett.* 31, 48–54. https://doi.org/10.1016/0012-821X(76)90095-9

Bižić, M., Klintzsch, T., Ionescu, D., Hindiyeh, M.Y., Günthel, M., Muro-Pastor, A.M., Eckert, W., Urich, T., Keppler, F., Grossart, H.-P., 2020. Aquatic and terrestrial cyanobacteria produce methane. *Sci. Adv.* 6, eaax5343. https://doi.org/10.1126/sciadv.aax5343

Bogard, M.J., del Giorgio, P.A., Boutet, L., Chaves, M.C.G., Prairie, Y.T., Merante, A., Derry, A.M., 2014. Oxic water column methanogenesis as a major component of aquatic CH_4 fluxes. *Nat. Commun.* 5, 5350. https://doi.org/10.1038/ncomms6350

Bolduc, A., Larocque, R., Duchesne, M.J., 2008. Des évents actifs dan l'estuaire maritime du Saint-Laurent, Québec. Comm. Géologique Can. Rech. En Cours 2008–21, 12p.

Bordeleau, G., Rivard, C., Lavoie, D., Lefebvre, R., Ahad, J.M.E., Xu, X., Mort, A., 2018. A multi-isotope approach to determine the origin of methane and higher alkanes in groundwater of the St. Lawrence Platform, Saint-Édouard area, eastern Canada. *Environ. Geosci.* 25, 75–100. https://doi.org/10.1306/eg.04121817020

Borges, A.V., Abril, G., 2011. Carbon dioxide and methane dynamics in estuaries, in: Wolanski, E. and McLusky, D. (Eds), Treatise on Estuarine and Coastal Science, Academic Press, Waltham, pp. 119–161.

Borges, A.V., Champenois, W., Gypens, N., Delille, B., Harlay, J., 2016. Massive marine methane emissions from near-shore shallow coastal areas. *Sci. Rep.* 6, 27908. https://doi:10.1038/srep27908

Borges, A., Abril, G., Bouillon, S., 2018. Carbon dynamics and CO_2 and CH_4 outgassing in the Mekong delta. *Biogeosciences* 15, 1093–1114. https://doi.org/10.5194/bg-15-1093-2018

Bourgault, D., Galbraith, P.S., Winkler, G., 2012a. Exploratory observations of winter oceanographic conditions in the Saguenay Fjord. *Atmos. Ocean* 50, 17–30. https://doi.org/10.1080/07055900.2012.659844.

Bourgault, D., Cyr, F., Galbraith, P.S., Pelletier, E., 2012b. Relative importance of pelagic and sediment respiration in causing hypoxia in a deep estuary. *J. Geophys. Res. Oceans* 117, C08003. https://doi.org/10.1029/2012JC007902

Bourgault, D., Galbraith, P., Dumont, D., 2017. Hydrographie du golfe du Saint-Laurent, in: Archambault, P., Schloss, I.R., Grant, C., Plante, S. (Eds.), Les Hydrocarbures Dans Le Golfe Du Saint-Laurent: Enjeux Sociaux, Économiques et Environnementaux. Notre Golfe, pp. 69–92.

Bourgault, D., Matte, P., 2020a. A physically based method for teal-time monitoring of tidal river discharges from water Level Observations, with an application to the St. Lawrence River. *J. Geophys. Res. Oceans* 125, e2019JC015992. https://doi.org/10.1029/2019JC015992

Bourgault, D., Matte, P., 2020b. Qmec: a Matlab code to compute tidal river discharge from water level. Code Ocean. https://doi.org/10.24433/CO.7299598.V1

Bousquet, P., Ciais, P., Miller, J.B., Dlugokencky, E.J., Hauglustaine, D.A., Prigent, C., Van der Werf, G.R., Peylin, P., Brunke, E.-G., Carouge, C., Langenfelds, R.L., Lathière, J., Papa, F., Ramonet, M., Schmidt, M., Steele, L.P., Tyler, S.C., White, J., 2006. Contribution of anthropogenic and natural sources to atmospheric methane variability. *Nature* 443, 439–443. https://doi.org/10.1038/nature05132

Bowers, D.G., Brett, H.L., 2008. The relationship between CDOM and salinity in estuaries: An analytical and graphical solution. *J. Mar. Syst.* 73, 1–7. https://doi.org/10.1016/j.jmarsys.2007.07.001

Brothers, L.L., Kelley, J.T., Belknap, D.F., Barnhardt, W.A., Andrews, B.D., Legere, C., Hughes Clarke, J.E., 2012. Shallow stratigraphic control on pockmark distribution in north temperate estuaries. *Mar. Geol.* 329–331, 34–45. https://doi.org/10.1016/j.margeo.2012.09.006

Bubier, J.L., Moore, T.R., 1994. An ecological perspective on methane emissions from northern wetlands. *Trends Ecol. Evol.* 9, 460–464. https://doi.org/10.1016/0169-5347(94)90309-3

Buffett, B., Archer, D., 2004. Global inventory of methane clathrate: sensitivity to changes in the deep ocean. *Earth Planet. Sci. Lett.* 227, 185–199. https://doi.org/10.1016/j.epsl.2004.09.005

Buffett, B.A., 2000. Clathrate hydrates. *Annu. Rev. Earth Planet. Sci.* 28, 477–507. https://doi.org/10.1146/annurev.earth.28.1.477

Bugden, G., 1988. Oceanographic conditions in the deeper waters of the Gulf of St. Lawrence in relation to local and oceanic forcing. NAFO SCR Doc. 88, 87.

Buitenhuis, E.T., Suntharalingam, P., Le Quéré, C., 2020. A new estimate of the ocean to atmosphere methane flux, including the first formal uncertainty estimate. *In Prep.*

Bullister, J.L., Guinasso Jr, N.L., Schink, D.R., 1982. Dissolved hydrogen, carbon monoxide, and methane at the CEPEX site. *J. Geophys. Res. Oceans* 87, 2022-2034. https://doi.org/10.1029/JC087iC03p02022

Butler, J.H., Jones, R.D., Garber, J.H., Gordon, L.I., 1987. Seasonal distributions and turnover of reduced trace gases and hydroxylamine in Yaquina Bay, Oregon. *Geochim. Cosmochim. Acta* 51, 697–706. https://doi.org/10.1016/0016-7037(87)90080-9

Cai, W., 2011. Estuarine and Coastal Ocean Carbon Paradox: CO_2 Sinks or Sites of Terrestrial Carbon Incineration? *Annu. Rev. Mar. Sci.* 3, 123–145. https://doi.org/10.1146/annurev-marine-120709-142723

Campbell, K.A., 2006. Hydrocarbon seep and hydrothermal vent paleoenvironments and paleontology: Past developments and future research directions. *Palaeogeogr. Palaeoclimatol. Palaeoecol.* 232, 362–407. https://doi.org/10.1016/j.palaeo.2005.06.018

Cantrell, C.A., Shetter, R.E., McDaniel, A.H., Calvert, J.G., Davidson, J.A., Lowe, D.C., Tyler, S.C., Cicerone, R.J., Greenberg, J.P., 1990. Carbon kinetic isotope effect in the oxidation of methane by the hydroxyl radical. *J. Geophys. Res. Atmospheres* 95, 22455–22462. https://doi.org/10.1029/JD095iD13p22455

Capelle, D.W., Hallam, S.J., Tortell, P.D., 2019. Time-series CH_4 measurements from Saanich Inlet, BC, a seasonally anoxic fjord. *Mar. Chem.* 215, 103664

Carlson, K.M., Gerber, J.S., Mueller, N.D., Herrero, M., MacDonald, G.K., Brauman, K.A., Havlik, P., O'Connell, C.S., Johnson, J.A., Saatchi, S., West, P.C., 2017. Greenhouse gas emissions intensity of global croplands. *Nat. Clim. Change* 7, 63–68. https://doi.org/10.1038/nclimate3158

Catling, D.C., Claire, M.W., 2005. How Earth's atmosphere evolved to an oxic state: A status report. *Earth Planet. Sci. Lett.* 237, 1–20. https://doi.org/10.1016/j.epsl.2005.06.013

Chaillou, G., Lemay-Borduas, F., Larocque, M., Couturier, M., Biehler, A., Tommi-Morin, G., 2018. Flow and discharge of groundwater from a snowmelt-affected sandy beach. *J. Hydrol.* 557, 4–15. https://doi.org/10.1016/j.jhydrol.2017.12.010

Chanton, J.P., 2005. The effect of gas transport on the isotope signature of methane in wetlands. *Org. Geochem.* 36, 753–768. https://doi.org/10.1016/j.orggeochem.2004.10.007

Charlou, J.L., Fouquet, Y., Bougault, H., Donval, J.P., Etoubleau, J., Jean-Baptiste, P., Dapoigny, A., Appriou, P., Rona, P.A., 1998. Intense CH4 plumes generated by serpentinization of ultramafic rocks at the intersection of the 15°20′N fracture zone and the Mid-Atlantic Ridge. *Geochim. Cosmochim. Acta* 62, 2323–2333. https://doi.org/10.1016/S0016-7037(98)00138-0

Christensen, T.R., Ekberg, A., Ström, L., Mastepanov, M., Panikov, N., Öquist, M., Svensson, B.H., Nykänen, H., Martikainen, P.J., Oskarsson, H., 2003. Factors controlling large scale variations in methane emissions from wetlands. *Geophys. Res. Lett.* 30. https://doi.org/10.1029/2002GL016848

Coleman, D.D., Risatti, J.B., Schoell, M., 1981. Fractionation of carbon and hydrogen isotopes by methane-oxidizing bacteria. *Geochim. Cosmochim. Acta* 45, 1033–1037. https://doi.org/10.1016/0016-7037(81)90129-0

Corliss, J.B., Dymond, J., Gordon, L.I., Edmond, J.M., von Herzen, R.P., Ballard, R.D., Green, K., Williams, D., Bainbridge, A., Crane, K., van Andel, T.H., 1979. Submarine Thermal Springs on the Galápagos Rift. *Science* 203, 1073–1083. https://doi.org/10.1126/science.203.4385.1073

Côté, R., Lacroix, G., 1979. Variabilité journalière de la chlorophylle a et des taux de production primaire dans le fjord du Saguenay. *Nat. Can.* 106, 189–198.

Craig, H., 1957. Isotopic standards for carbon and oxygen and correction factors for mass-spectrometric analysis of carbon dioxide. *Geochim. Cosmochim. Acta* 12, 133–149. https://doi.org/10.1016/0016-7037(57)90024-8

Crill, P.M., Martens, C.S., 1983. Spatial and temporal fluctuations of methane production in anoxic coastal marine sediments. *Limnol. Oceanogr.* 28, 1117–1130. https://doi.org/10.4319/lo.1983.28.6.1117

Cui, T., Dawson Travis J., McLatchie Susan, Dunn Katherine, Bielawski Joseph, Walsh David A., McMahon Katherine, 2020. Modelling free-living and particle-associated bacterial assemblages across the deep and hypoxic Lower St. Lawrence Estuary. *mSphere* 5, e00364-20. https://doi.org/10.1128/mSphere.00364-20

Cyr, F., Bourgault, D., Galbraith, P.S., Gosselin, M., 2015. Turbulent nitrate fluxes in the Lower St. Lawrence Estuary, Canada. *J. Geophys. Res. Oceans* 120, 2308–2330. https://doi.org/10.1002/2014JC010272

d'Anglejan, B., 1990. Recent sediments and sediment transport processes in the St. Lawrence Estuary, in: El-Sabh, M.I., Silverberg, N. (Eds.), Oceanography of a Large-Scale Estuarine System: The St. Lawrence. Springer New York, New York, NY, pp. 109–129. https://doi.org/10.1007/978-1-4615-7534-4_6

d'Anglejan, B., Brisebois, M., 1978. Recent sediments of the St. Lawrence middle estuary. *J. Sediment. Res.* 48, 951–964. https://doi.org/10.1306/212F75B3-2B24-11D7-8648000102C1865D

Da Costa, M.V., Mercier, H., Treguier, A.M., 2005. Effects of the mixed layer time variability on kinematic subduction rate diagnostics. *J. Phys. Oceanogr.* 35, 427–443. https://doi.org/10.1175/JPO2693.1

Damm, E., Mackensen, A., Budéus, G., Faber, E., Hanfland, C., 2005. Pathways of methane in seawater: Plume spreading in an Arctic shelf environment (SW-Spitsbergen). *Cont. Shelf Res.* 25, 1453–1472. https://doi.org/10.1016/j.csr.2005.03.003

Damm, E., Schauer, U., Rudels, B., Haas, C., 2007. Excess of bottom-released methane in an Arctic shelf sea polynya in winter. *Cont. Shelf Res.* 27, 1692–1701. https://doi.org/10.1016/j.csr.2007.02.003

Damm, E., Helmke, E., Thoms, S., Schauer, U., Nöthig, E., Bakker, K., Kiene, R.P., 2010. Methane production in aerobic oligotrophic surface water in the central Arctic Ocean. *Biogeosciences* 7, 1099–1108. https://doi.org/10.5194/bg-7-1099-2010

Damm, E., Thoms, S., Beszczynska-Möller, A., Nöthig, E.M., Kattner, G., 2015a. Methane excess production in oxygen-rich polar water and a model of cellular conditions for this paradox. *Polar Sci.* 9, 327–334. https://doi.org/10.1016/j.polar.2015.05.001

Damm, E., Rudels, B., Schauer, U., Mau, S., Dieckmann, G., 2015b. Methane excess in Arctic surface water-triggered by sea ice formation and melting. *Sci. Rep.* 5, 16179. https://doi.org/10.1038/srep16179

Damm, E., Bauch, D., Krumpen, T., Rabe, B., Korhonen, M., Vinogradova, E., Uhlig, C., 2018. The transpolar drift conveys methane from the Siberian Shelf to the central Arctic Ocean. *Sci. Rep.* 8, 4515. https://doi.org/10.1038/s41598-018-22801-z

Damm, E., Ericson, Y., Falck, E., 2021. Waterside convection and stratification control methane spreading in supersaturated Arctic fjords (Spitsbergen). *Cont. Shelf Res.* 224, 104473. https://doi.org/10.1016/j.csr.2021.104473

Davie, M.K., Buffett, B.A., 2003. A steady state model for marine hydrate formation: Constraints on methane supply from pore water sulfate profiles. *J. Geophys. Res. Solid Earth* 108. https://doi.org/10.1029/2002JB002300

de Angelis, M.A., Lilley, M.D., 1987. Methane in surface waters of Oregon estuaries and rivers. *Limnol. Oceanogr.* 32, 716–722. https://doi.org/10.4319/lo.1987.32.3.0716

de Angelis, M.A., Scranton, M.I., 1993. Fate of methane in the Hudson River and Estuary. *Glob. Biogeochem. Cycles* 7, 509–523. https://doi.org/10.1029/93GB01636

de Angelis, M.A., Lilley, M.D., Baross, J.A., 1993. Methane oxidation in deep-sea hydrothermal plumes of the endeavour segment of the Juan de Fuca Ridge. *Deep Sea Res. Part Oceanogr. Res. Pap.* 40, 1169–1186. https://doi.org/10.1016/0967-0637(93)90132-M

de Angelis, M.A., Lee, C., 1994. Methane production during zooplankton grazing on marine phytoplankton. *Limnol. Oceanogr.* 39, 1298–1308. https://doi.org/10.4319/lo.1994.39.6.1298

Deflandre, B., Mucci, A., Gagné, J.-P., Guignard, C., Sundby, B. jørn, 2002. Early diagenetic processes in coastal marine sediments disturbed by a catastrophic sedimentation event. *Geochim. Cosmochim. Acta* 66, 2547–2558. https://doi.org/10.1016/S0016-7037(02)00861-X

de Lafontaine, Y., Demers, S., Runge, J., 1991. Pelagic food web interactions and productivity in the Gulf of St. Lawrence: a perspective, in: Therriault, J.-C. (Ed.), The Gulf of St. Lawrence: Small Ocean or Big Estuary? *Can. Spec. Publ. Fish. Aquat. Sci.*, pp. 99–123.

Delaigue, L., Thomas, H., Mucci, A., 2020. Spatial variations in CO_2 fluxes in the Saguenay Fjord (Quebec, Canada) and results of a water mixing model. *Biogeosciences* 17, 547–566. https://doi.org/10.5194/bg-17-547-2020

Descroix, A., Harvey, M., Roy, S., Galbraith, P.S., 2005. Macrozooplankton community patterns driven by water circulation in the St. Lawrence marine system, Canada. *Mar. Ecol. Prog. Ser.* 302, 103–119.

Dimitrov, L., 2002. Contribution to atmospheric methane by natural seepages on the Bulgarian continental shelf. *Cont. Shelf Res.* 22, 2429–2442. https://doi.org/10.1016/S0278-4343(02)00055-9

Dlugokencky, E.J., Myers, R.C., Lang, P.M., Masarie, K.A., Crotwell, A.M., Thoning, K.W., Hall, B.D., Elkins, J.W., Steele, L.P., 2005. Conversion of NOAA atmospheric dry air CH4 mole fractions to a gravimetrically prepared standard scale. *J. Geophys. Res. Atmospheres* 110. https://doi.org/10.1029/2005JD006035

Donnelly, M.I., Dagley, S., 1980. Production of methanol from aromatic acids by *Pseudomonas putida*. *J. Bacteriol.* 142, 916–924. https://doi.org/10.1128/jb.142.3.916-924.1980

Drainville, G., 1968. Le Fjord du Saguenay. I, Contribution à l'océanographie. *Nat. Can.* 95, 809–855.

Dufour, R., Ouellet, P., 2007. Estuary and Gulf of St. Lawrence marine ecosystem overview and assessment report. *Can. Tech. Rep. Fish. Aquat. Sci.* 2744E, vii+112p.

Dunfield, P., knowles, R., Dumont, R., Moore, T.R., 1993. Methane production and consumption in temperate and subarctic peat soils: Response to temperature and pH. *Soil Biol. Biochem.* 25, 321–326. https://doi.org/10.1016/0038-0717(93)90130-4

Eakins, B.W., Sharman, G.F., 2012. Hypsographic curve of Earth's surface from ETOPO1. NOAA Natl. Geophys. Data Cent. Boulder CO.

Ehhalt, D.H., 1974. The atmospheric cycle of methane. *Tellus* 26, 58–70. https://doi.org/10.3402/tellusa.v26i1-2.9737

El-Sabh, M.I., Murty, Tad.S., 1990. Mathematical Modelling of Tides in the St. Lawrence Estuary, in: El-Sabh, M.I., Silverberg, N. (Eds.), Oceanography of a Large-Scale Estuarine System: The St. Lawrence. Springer New York, New York, NY, pp. 10–50. https://doi.org/10.1007/978-1-4615-7534-4_2

El-Sabh, M.I., 1988. Physical oceanography of the St. Lawrence estuary, in: Kjerfve, B. (Ed.), Hydrodynamics of Estuaries, Vol. II, Estuarine Case Studies. CRC Press Boca Raton, Florida, pp. 61–78.

El-Sabh, M.I., Silverberg, N., 1990. The St. Lawrence Estuary: Introduction, in: El-Sabh, M.I., Silverberg, N. (Eds.), Oceanography of a Large-Scale Estuarine System: The St. Lawrence. Springer New York, New York, NY, pp. 1–9. https://doi.org/10.1007/978-1-4615-7534-4_1

Emerson, S., Hedges, J.I., 1988. Processes controlling the organic carbon content of open ocean sediments. *Paleoceanography* 3, 621–634. https://doi.org/10.1029/PA003i005p00621

Etheridge, D.M., Steele, L.P., Francey, R.J., Langenfelds, R.L., 1998. Atmospheric methane between 1000 A.D. and present: Evidence of anthropogenic emissions and climatic variability. *J. Geophys. Res. Atmospheres* 103, 15979–15993. https://doi.org/10.1029/98JD00923

Etiope, G., Lassey, K.R., Klusman, R.W., Boschi, E., 2008. Reappraisal of the fossil methane budget and related emission from geologic sources. *Geophys. Res. Lett.* 35. https://doi.org/10.1029/2008GL033623

Etiope, G., 2015. Natural gas seepage. Springer International Publishing, Cham. https://doi.org/10.1007/978-3-319-14601-0

Etiope, G., Ciotoli, G., Schwietzke, S., Schoell, M., 2019. Gridded maps of geological methane emissions and their isotopic signature. *Earth Syst. Sci. Data* 11, 1–22. https://doi.org/10.5194/essd-11-1-2019

Etiope, G., Schwietzke, S., 2019. Global geological methane emissions: An update of top-down and bottom-up estimates. *Elem. Sci. Anthr.* 7. https://doi.org/10.1525/elementa.383

Etminan, M., Myhre, G., Highwood, E.J., Shine, K.P., 2016. Radiative forcing of carbon dioxide, methane, and nitrous oxide: A significant revision of the methane radiative forcing. *Geophys. Res. Lett.* 43, 12,614-12,623. https://doi.org/10.1002/2016GL071930

Fanning, K.A., Torres, L.M., 1991. 222Rn and 226Ra: indicators of sea-ice effects on air-sea gas exchange. *Polar Res.* 10, 51–58. https://doi.org/10.3402/polar.v10i1.6727

Farías, L., Sanzana, K., Sanhueza-Guevara, S., Yevenes, M.A., 2017. Dissolved methane distribution in the Reloncaví Fjord and adjacent marine system during Austral winter (41°–43°S). *Estuaries Coasts* 40, 1592–1606. https://doi.org/10.1007/s12237-017-0241-2

Fenchel, T., Bernard, C., Esteban, G., Findlay, B.J., Hansen, P.J., Iversen, N., 1995. Microbial diversity and activity in a Danish fjord with anoxic deep water. *Ophelia* 43, 45–100. https://doi.org/10.1080/00785326.1995.10430576

Fenwick, L., Capelle, D., Damm, E., Zimmermann, S., Williams, W.J., Vagle, S., Tortell, P.D., 2017. Methane and nitrous oxide distributions across the North American Arctic Ocean during summer, 2015. *J. Geophys. Res. Oceans* 122, 390–412. https://doi.org/10.1002/2016JC012493

Fichot, C.G., Benner, R., 2014. The fate of terrigenous dissolved organic carbon in a river-influenced ocean margin, *Global Biogeochem. Cycles* 28, 300–318. https://doi:10.1002/2013GB004670

Fichot, C.G., Benner, R., 2012. The spectral slope coefficient of chromophoric dissolved organic matter ($S_{275–295}$) as a tracer of terrigenous dissolved organic carbon in river-influenced ocean margins. *Limnol. Oceanogr*. 57, 1453–1466. https://doi.org/10.4319/lo.2012.57.5.1453

Fichot, C.G., and Benner, R., 2011. A novel method to estimate DOC concentrations from CDOM absorption coefficients in coastal waters, *Geophys. Res. Lett.* 38, L03610. https://doi:10.1029/2010GL046152

Fichot, C.G., Miller, W.L., 2010. An approach to quantify depth-resolved marine photochemical fluxes using remote sensing: Application to carbon monoxide (CO) photoproduction. *Remote Sens. Environ.* 114, 1363–1377. https://doi.org/10.1016/j.rse.2010.01.019

Fichot, C.G., Sathyendranath, S., Miller, W. L., 2008. SeaUV and SeaUVC: Algorithms for the retrieval of UV/Visible diffuse attenuation coefficients from ocean color. *Remote Sensing Data Assimilation Special Issue* 112, 1584–1602. https://doi.org/10.1016/j.rse.2007.08.009

Forster, G., Upstill-Goddard, R.C., Gist, N., Robinson, C., Uher, G., Woodward, E.M.S., 2009. Nitrous oxide and methane in the Atlantic Ocean between 50°N and 52°S: Latitudinal distribution and sea-to-air flux. *Deep Sea Res*. Part II 56, 964–976. https://doi.org/10.1016/j.dsr2.2008.12.002

Forwick, M., Baeten, N.J., Vorren, T.O., 2009. Pockmarks in Spitsbergen fjords. *Nor. J. Geol. Geol. Foren.* 89, 65–77.

Galbraith, P.S., 2006. Winter water masses in the Gulf of St. Lawrence. *J. Geophys. Res. Oceans* 111. https://doi.org/10.1029/2005JC003159

Galbraith, P., Bourgault, D., Belzile, M., 2018. Circulation et renouvellement des masses d'eau du fjord du *Saguenay. Nat. Can.* 142, 36–46. https://doi.org/10.7202/1047147ar

Garcia, H.E., Gordon, L.I., 1992. Oxygen solubility in seawater: Better fitting equations. *Limnol. Oceanogr.* 37, 1307–1312. https://doi.org/10.4319/lo.1992.37.6.1307

Geng, L., 2017. Studies on the distribution of dissolved methane and its biogeochemistry in Canadian Arctic and Sub-Arctic seas. China University of Geosciences. (in Chinese with English abstract)

Genin, F., Lalande, C., Galbraith, P.S., Larouche, P., Ferreyra, G.A., Gosselin, M., 2021. Annual cycle of biogenic carbon export in the Gulf of St. Lawrence. *Cont. Shelf Res.* 221, 104418. https://doi.org/10.1016/j.csr.2021.104418

Genovesi, L., de Vernal, A., Thibodeau, B., Hillaire-Marcel, C., Mucci, A., Gilbert, D., 2011. Recent changes in bottom water oxygenation and temperature in the Gulf of St. Lawrence: Micropaleontological and geochemical evidence. *Limnol. Oceanogr.* 56, 1319–1329. https://doi.org/10.4319/lo.2011.56.4.1319

Geyer, W.R., Cannon, G.A., 1982. Sill processes related to deep water renewal in a fjord. *J. Geophys. Res. Oceans* 87, 7985–7996. https://doi.org/10.1029/JC087iC10p07985

Gilbert, D., 2004. Propagation of temperature signals from the northwest Atlantic continental shelf edge into the Laurentian Channel. ICES CM 2004, N-7.

Gilbert, D., Pettigrew, B., 1997. Interannual variability (1948–1994) of the CIL core temperature in the Gulf of St. Lawrence. *Can. J. Fish. Aquat. Sci.* 54, 57–67. https://doi.org/10.1139/f96-160

Gilbert, D., Sundby, B., Gobeil, C., Mucci, A., Tremblay, G.-H., 2005. A seventy-two-year record of diminishing deep-water oxygen in the St. Lawrence estuary: The northwest Atlantic connection. *Limnol. Oceanogr.* 50, 1654–1666. https://doi.org/10.4319/lo.2005.50.5.1654

Grant, N.J., Whiticar, M.J., 2002. Stable carbon isotopic evidence for methane oxidation in plumes above Hydrate Ridge, Cascadia Oregon Margin. *Glob. Biogeochem. Cycles* 16, 71–1. https://doi.org/10.1029/2001GB001851

Grasshoff, K., Kremling, K., Ehrhardt, M., 2009. Methods of seawater analysis. John Wiley & Sons.

Greisman, P., Ingram, G., 1977. Nutrient Distribution in the St. Lawrence Estuary. *J. Fish. Res. Board Can.* 34, 2104–2116. https://doi.org/10.1139/f77-278

Grossart, H.-P., Frindte, K., Dziallas, C., Eckert, W., Tang, K.W., 2011. Microbial methane production in oxygenated water column of an oligotrophic lake. *Proc. Natl. Acad. Sci.* 108, 19657. https://doi.org/10.1073/pnas.1110716108

Happell, J.D., Chanton, J.P., Showers, W.J., 1995. Methane transfer across the water–air interface in stagnant wooded swamps of Florida: Evaluation of mass-transfer coefficients and isotropic fractionation. *Limnol. Oceanogr.* 40, 290–298. https://doi.org/10.4319/lo.1995.40.2.0290

Harvey, M., Devine, L., 2009. Oceanographic conditions in the Estuary and the Gulf of St. Lawrence during 2008: zooplankton. Can. Sci. Advis. Secr. Res. Doc. vi + 54 p.

Harvey, M., Galbraith, P.S., Descroix, A., 2009. Vertical distribution and diel migration of macrozooplankton in the St. Lawrence marine system (Canada) in relation with the cold intermediate layer thermal properties. *Prog. Oceanogr.* 80, 1–21. https://doi.org/10.1016/j.pocean.2008.09.001

He, J., Naik, V., Horowitz, L.W., Dlugokencky, E., Thoning, K., 2020. Investigation of the global methane budget over 1980–2017 using GFDL-AM4.1. *Atmospheric Chem. Phys.* 20, 805–827. https://doi.org/10.5194/acp-20-805-2020

Hedges, J.I., Keil, R.G., 1995. Sedimentary organic matter preservation: an assessment and speculative synthesis. *Mar. Chem.* 49, 81–115. https://doi.org/10.1016/0304-4203(95)00008-F

Helms, J.R., Stubbins, A., Ritchie, J.D., Minor, E.C., Kieber, D.J., Mopper, K., 2008. Absorption spectral slopes and slope ratios as indicators of molecular weight, source, and photobleaching of chromophoric dissolved organic matter. *Limnol. Oceanogr.* 53, 955–969. https://doi.org/10.4319/lo.2008.53.3.0955

Holmes, M.E., Sansone, F.J., Rust, T.M., Popp, B.N., 2000. Methane production, consumption, and air-sea exchange in the open ocean: An Evaluation based on carbon isotopic ratios. *Global Biogeochem. Cycles* 14, 1–10. https://doi.org/10.1029/1999GB001209

Henrichs, S.M., Reeburgh, W.S., 1987. Anaerobic mineralization of marine sediment organic matter: Rates and the role of anaerobic processes in the oceanic carbon economy. *Geomicrobiol. J.* 5, 191–237. https://doi.org/10.1080/01490458709385971

Hinrichs, K.-U., Boetius, A., 2002. The anaerobic oxidation of methane: New insights in microbial ecology and biogeochemistry, in: Wefer, G., Billett, D., Hebbeln, D., Jørgensen, B.B., Schlüter, M., van Weering, T.C.E. (Eds.), Ocean Margin Systems. Springer Berlin Heidelberg, Berlin, Heidelberg, pp. 457–477. https://doi.org/10.1007/978-3-662-05127-6_28

Hippe, H., Caspari, D., Fiebig, K., Gottschalk, G., 1979. Utilization of trimethylamine and other N-methyl compounds for growth and methane formation by *Methanosarcina barkeri*. *Proc. Natl. Acad. Sci.* 76, 494. https://doi.org/10.1073/pnas.76.1.494

Hudon, C., Gagnon, P., Rondeau, M., Hébert, S., Gilbert, D., Hill, B., Patoine, M., Starr, M., 2017. Hydrological and biological processes modulate carbon, nitrogen and phosphorus flux from the St. Lawrence River to its estuary (Quebec, Canada). *Biogeochemistry* 135, 251–276. https://doi.org/10.1007/s10533-017-0371-4

Ingram, R.G., 1979. Water mass modification in the St-Lawrence Estuary. *Nat. Can.* 106, 45–54.

Ingram, R.G., El-Sabh, M.I., 1990. Fronts and Mesoscale Features in the St. Lawrence Estuary, in: El-Sabh, M.I., Silverberg, N. (Eds.), Oceanography of a Large-Scale Estuarine System: The St. Lawrence. Springer, New York, NY, pp. 71–93. https://doi.org/10.1007/978-1-4615-7534-4_4

IPCC, 2013. Climate change 2013: The physical science basis. Cambridge University Press, New York.

Johnson, K.A., Kincaid, R.L., Westberg, H.H., Gaskins, C.T., Lamb, B.K., Cronrath, J.D., 2002. The effect of oilseeds in diets of lactating cows on milk production and methane emissions. *J. Dairy Sci.* 85, 1509–1515. https://doi.org/10.3168/jds.S0022-0302(02)74220-3

Jones, R.D., Amador, J.A., 1993. Methane and carbon monoxide production, oxidation, and turnover times in the Caribbean Sea as influenced by the Orinoco River. *J. Geophys. Res. Oceans* 98, 2353–2359. https://doi.org/10.1029/92JC02769

Josenhans, H., Zevenhuizen, J., Maclean, B., 1990. Preliminary seismostratigraphic interpretations from the Gulf of St. Lawrence, Current research, part B, eastern and Atlantic Canada. Geological Survey of Canada, Paper 90-1B.

Jutras, M., Dufour, C.O., Mucci, A., Cyr, F., Gilbert, D., 2020. Temporal changes in the causes of the observed oxygen Decline in the St. Lawrence Estuary. *J. Geophys. Res. Oceans* 125, e2020JC016577. https://doi.org/10.1029/2020JC016577

Karion, A., Sweeney, C., Kort, E.A., Shepson, P.B., Brewer, A., Cambaliza, M., Conley, S.A., Davis, K., Deng, A., Hardesty, M., Herndon, S.C., Lauvaux, T., Lavoie, T., Lyon, D., Newberger, T., Pétron, G., Rella, C., Smith, M., Wolter, S., Yacovitch, T.I., Tans, P., 2015. Aircraft-based estimate of total methane emissions from the Barnett shale region. *Environ. Sci. Technol.* 49, 8124–8131. https://doi.org/10.1021/acs.est.5b00217

Karl, D.M., Tilbrook, B.D., 1994. Production and transport of methane in oceanic particulate organic matter. *Nature 368*, 732–734. https://doi.org/10.1038/368732a0

Karl, D.M., Beversdorf, L., Björkman, K.M., Church, M.J., Martinez, A., Delong, E.F., 2008. Aerobic production of methane in the sea. *Nat. Geosci.* 1, 473–478. https://doi.org/10.1038/ngeo234

Kasting, J.F., 2001. The rise of atmospheric oxygen. *Science* 293, 819. https://doi.org/10.1126/science.1063811

Kasting, J.F., Siefert, J.L., 2002. Life and the evolution of Earth's atmosphere. *Science* 296, 1066. https://doi.org/10.1126/science.1071184

Kasting, J.F., Catling, D., 2003. Evolution of a habitable planet. *Annu. Rev. Astron. Astrophys.* 41, 429–463. https://doi.org/10.1146/annurev.astro.41.071601.170049

Kasting, J.F., 2004. When methane made climate. *Sci. Am.* 291, 78–85.

Keeling, C.D., 1958. The concentration and isotopic abundances of atmospheric carbon dioxide in rural areas. *Geochim. Cosmochim. Acta* 13, 322–334.

Keir, R.S., Greinert, J., Rhein, M., Petrick, G., Sültenfuß, J., Fürhaupter, K., 2005. Methane and methane carbon isotope ratios in the Northeast Atlantic including the Mid-Atlantic Ridge (50°N). *Deep Sea Res. Part Oceanogr. Res. Pap.* 52, 1043–1070. https://doi.org/10.1016/j.dsr.2004.12.006

Khalil, M.A.K., Rasmussen, R.A., 1985. Causes of increasing atmospheric methane: Depletion of hydroxyl radicals and the rise of emissions. *Atmospheric Environ.* 19, 397–407. https://doi.org/10.1016/0004-6981(85)90161-1

Kiene, R.P., Oremland, R.S., Catena, A., Miller, L.G., Capone, D.G., 1986. Metabolism of reduced methylated sulfur compounds in anaerobic sediments and by a pure culture of an estuarine methanogen. *Appl. Environ. Microbiol.* 52, 1037–1045. https://doi.org/10.1128/aem.52.5.1037-1045.1986

Kiene, R.P., 1991. Production and consumption of methane in aquatic systems. In Rogers, J E & Whitman, W B, Microbial Production and Consumption of Greenhouse Gases: Methane, Nitrogen Oxides, and Halomethanes (pp. 307). Washington, DC (USA): American Society for Microbiology

King, G.M., 1984. Metabolism of trimethylamine, choline, and glycine betaine by sulfate-teducing and methanogenic bacteria in marine sediments. *Appl. Environ. Microbiol.* 48, 719–725. https://doi.org/10.1128/aem.48.4.719-725.1984

Kirschke, S., Bousquet, P., Ciais, P., Saunois, M., Canadell, J.G., Dlugokencky, E.J., Bergamaschi, P., Bergmann, D., Blake, D.R., Bruhwiler, L., Cameron-Smith, P., Castaldi, S., Chevallier, F., Feng, L., Fraser, A., Heimann, M., Hodson, E.L., Houweling, S., Josse, B., Fraser, P.J., Krummel, P.B., Lamarque, J.-F., Langenfelds, R.L., Le Quéré, C., Naik, V., O'Doherty, S., Palmer, P.I., Pison, I., Plummer, D., Poulter, B., Prinn, R.G., Rigby, M., Ringeval, B., Santini, M., Schmidt, M., Shindell, D.T., Simpson, I.J., Spahni, R., Steele, L.P., Strode, S.A., Sudo, K., Szopa, S., van der Werf, G.R., Voulgarakis, A., van Weele, M., Weiss, R.F., Williams, J.E., Zeng, G., 2013. Three decades of global methane sources and sinks. *Nat. Geosci.* 6, 813–823. https://doi.org/10.1038/ngeo1955

Klintzsch, T., Langer, G., Nehrke, G., Wieland, A., Lenhart, K., Keppler, F., 2019. Methane production by three widespread marine phytoplankton species: release rates, precursor compounds, and potential relevance for the environment. *Biogeosciences* 16, 4129–4144. https://doi.org/10.5194/bg-16-4129-2019

Kvenvolden, K.A., 1988. Methane hydrates and global climate. *Glob. Biogeochem. Cycles* 2, 221–229. https://doi.org/10.1029/GB002i003p00221

Kvenvolden, K.A., 1993. Gas hydrates-geological perspective and global change. *Rev. Geophys.* 31, 173–187. https://doi.org/10.1029/93RG00268

Lamb, B.K., Edburg, S.L., Ferrara, T.W., Howard, T., Harrison, M.R., Kolb, C.E., Townsend-Small, A., Dyck, W., Possolo, A., Whetstone, J.R., 2015. Direct measurements show decreasing methane emissions from natural gas local distribution systems in the United States. *Environ. Sci. Technol.* 49, 5161–5169. https://doi.org/10.1021/es505116p

Lambert, G., Schmidt, S., 1993. Reevaluation of the oceanic flux of methane: Uncertainties and long term variations. *Chemosphere*, 26, 579–589. https://doi.org/10.1016/0045-6535(93)90443-9

Lamontagne, R.A., Swinnerton, J.W., Linnenbom, V.J., Smith, W.D., 1973. Methane concentrations in various marine environments. *J. Geophys. Res.* 78, 5317–5324. https://doi.org/10.1029/JC078i024p05317

Larouche, P., Koutitonsky, V.G., Chanut, J.-P., El-Sabh, M.I., 1987. Lateral stratification and dynamic balance at the Matane transect in the lower Saint Lawrence estuary. Estuar. *Coast. Shelf Sci.* 24, 859–871. https://doi.org/10.1016/0272-7714(87)90157-0

Lassey, K.R., Lowe, D.C., Manning, M.R., 2000. The trend in atmospheric methane δ13C and implications for isotopic constraints on the global methane budget. *Glob. Biogeochem. Cycles* 14, 41–49. https://doi.org/10.1029/1999GB900094

Lavoie, D., Y. Simard et F.J. Saucier, 2000. Aggregation and dispersion of krill at channel heads and shelf edges: the dynamics in the Saguenay-St. Lawrence Marine Park. *Can. J. Fish. Aquat. Sci.* 57, 1853–1869. https://doi.org/10.1139/f00-138

Lavoie, D., Pinet, N., Duchesne, M., Bolduc, A., Larocque, R., 2010. Methane-derived authigenic carbonates from active hydrocarbon seeps of the St. Lawrence Estuary, Canada. *Mar. Pet. Geol.* 27, 1262–1272. https://doi.org/10.1016/j.marpetgeo.2010.02.014

Lee, P.A., Haase, R., de Mora, S.J., Chanut, J.-P., Gosselin, M., 1999. Dimethylsulfoxide (DMSO) and related sulfur compounds in the Saguenay Fjord, Quebec. *Can. J. Fish. Aquat. Sci.* 56, 1631–1638. https://doi.org/10.1139/f99-094

LeFrançois, L., 1998. Distribution à haute résolution de l'oxigène, du manganèse, du fer, des sulfures et de l'iodure dans l'eau interstitielle des sédiments marins et lacustres. M.S. thesis, Université du Québec à Rimouski.

Lelieveld, J., Dentener, F.J., Peters, W., Krol, M.C., 2004. On the role of hydroxyl radicals in the self-cleansing capacity of the troposphere. *Atmos. Chem. Phys.* 4, 2337–2344. https://doi.org/10.5194/acp-4-2337-2004

Lenhart, K., Klintzsch, T., Langer, G., Nehrke, G., Bunge, M., Schnell, S., Keppler, F., 2016. Evidence for methane production by the marine algae *Emiliania huxleyi*. *Biogeosciences* 13, 3163–3174. https://doi.org/10.5194/bg-13-3163-2016

Levin, I., Bergamaschi, P., Dörr, H., Trapp, D., 1993. Stable isotopic signature of methane from major sources in Germany. *Chemosphere* 26, 161–177. https://doi.org/10.1016/0045-6535(93)90419-6

Lilley, M.D., Baross, J.A., Gordon, L.I., 1982. Dissolved hydrogen and methane in Saanieh Inlet, British Columbia. *Deep. Res.* 29, 1471–1484. https://doi.org/10.1016/0198-0149(82)90037-1

Li, Y., Xie, H., Scarrat, M., Damm, E., 2019. Dissolved methane in the St. Lawrence estuarine system. Geophysical Research Abstracts 21, EGU2019-3395

Lidstrom, M.E., 1983. Methane consumption in Framvaren, an anoxic marine fjord1. *Limnol. Oceanogr.* 28, 1247–1251. https://doi.org/10.4319/lo.1983.28.6.1247

Lie, H.-J., El-Sabh, M.I., 1983. Formation of eddies and transverse currents in a two-layer channel of variable bottom with application to the lower St. Lawrence Estuary. *J. Phys. Oceanogr.* 13, 1063–1076. https://doi.org/10.1175/1520-0485(1983)013<1063:FOEATC>2.0.CO;2

Liss, P.S., Slater, P.G., 1974. Flux of gases across the air-sea interface. *Nature* 247, 181–184. https://doi.org/10.1038/247181a0

Lofton, D.D., Whalen, S.C., Hershey, A.E., 2014. Effect of temperature on methane dynamics and evaluation of methane oxidation kinetics in shallow Arctic Alaskan lakes. *Hydrobiologia* 721, 209–222. https://doi.org/10.1007/s10750-013-1663-x

Lonsdale, P., 1977. Clustering of suspension-feeding macrobenthos near abyssal hydrothermal vents at oceanic spreading centers. *Deep Sea Res.* 24, 857–863. https://doi.org/10.1016/0146-6291(77)90478-7

Loose, B., McGillis, W.R., Perovich, D., Zappa, C.J., Schlosser, P., 2014. A parameter model of gas exchange for the seasonal sea ice zone. *Ocean Sci.* 10, 17–28. https://doi.org/10.5194/os-10-17-2014

Louchouarn, P., Lucotte, M., Canuel, R., Gagné, J.-P., Richard, L.-F., 1997. Sources and early diagenesis of lignin and bulk organic matter in the sediments of the Lower St. Lawrence Estuary and the Saguenay Fjord. 4th Int. Symp. Biogeochem. *Model Estuaries* 58, 3–26. https://doi.org/10.1016/S0304-4203(97)00022-4

Lovely, A., Loose, B., Schlosser, P., McGillis, W., Zappa, C., Perovich, D., Brown, S., Morell, T., Hsueh, D., Friedrich, R., 2015. The Gas Transfer through Polar Sea ice experiment: Insights into the rates and pathways that determine geochemical fluxes. *J. Geophys. Res. Oceans* 120, 8177–8194. https://doi.org/10.1002/2014JC010607

Lucotte, M., d'Anglejan, B., 1986. Seasonal control of the Saint-Lawrence maximum turbidity zone by tidal-flat sedimentation. *Estuaries* 9, 84–94. https://doi.org/10.2307/1351940

Luther, G.W., Rozan, T.F., Taillefert, M., Nuzzio, D.B., Di Meo, C., Shank, T.M., Lutz, R.A., Cary, S.C., 2001. Chemical speciation drives hydrothermal vent ecology. *Nature* 410, 813–816. https://doi.org/10.1038/35071069

MacDonald, I.R., Leifer, I., Sassen, R., Stine, P., Mitchell, R., Guinasso, N., 2002. Transfer of hydrocarbons from natural seeps to the water column and atmosphere. *Geofluids* 2, 95–107. https://doi.org/10.1046/j.1468-8123.2002.00023.x

Martens, C.S., Berner, R.A., 1977. Interstitial water chemistry of anoxic Long Island Sound sediments. 1. Dissolved gases. *Limnol. Oceanogr.* 22, 10–25. https://doi.org/10.4319/lo.1977.22.1.0010

Marty, D.G., 1993. Methanogenic bacteria in seawater. *Limnol. Oceanogr.* 38, 452–456. https://doi.org/10.4319/lo.1993.38.2.0452

Massoth, G.J., Milburn, H.B., Hammond, S.R., Butterfield, D.A., McDuff, R.E., Lupton, J.E., 1988. The geochemistry of submarine venting fluids at Axial Volcano, Juan de Fuca Ridge: New sampling methods and a VENTS program rationale, in: de Luca, M.P., Babb, I. (Eds.), Global Venting, Midwater, and Benthic Ecological Processes. NOAA Rockville, MD, pp. 29–59.

Matthews, E., Fung, I., 1987. Methane emission from natural wetlands: Global distribution, area, and environmental characteristics of sources. *Glob. Biogeochem. Cycles* 1, 61–86. https://doi.org/10.1029/GB001i001p00061

Mau, S., Blees, J., Helmke, E., Niemann, H., Damm, E., 2013. Vertical distribution of methane oxidation and methanotrophic response to elevated methane concentrations in stratified waters of the Arctic fjord Storfjorden (Svalbard, Norway). *Biogeosciences* 10, 6267–6278. https://doi.org/10.5194/bg-10-6267-2013

Mau, S., Tu, T., Becker, M., dos Santos Ferreira, C., Chen, J., Lin, L., Wang, P., Lin, S., Bohrmann, G., 2020. Methane seeps and independent methane plumes in the South China Sea offshore Taiwan. *Front. Mar. Sci.* 7, 543. https://doi.org/10.3389/fmars.2020.00543

Mau, S., Valentine, D.L., Clark, J.F., Reed, J., Camilli, R., Washburn, L., 2007. Dissolved methane distributions and air-sea flux in the plume of a massive seep field, Coal Oil Point, California. *Geophys. Res. Lett.* 34. https://doi.org/10.1029/2007GL031344

Mei, Z., Saucier, F.J., Le Fouest, V., Zakardjian, B., Sennville, S., Xie, H., Starr, M., 2010. Modeling the timing of spring phytoplankton bloom and biological production of the Gulf of St. Lawrence (Canada): Effects of colored dissolved organic matter and temperature. *Cont. Shelf Res.* 30, 2027–2042. https://doi.org/10.1016/j.csr.2010.10.003

Mertz, G., El-Sabh, M.I., Proulx, D., Condal, A.R., 1988. Instability of a buoyancy-driven coastal jet: The Gaspé Current and its St. Lawrence precursor. *J. Geophys. Res. Oceans* 93, 6885–6893. https://doi.org/10.1029/JC093iC06p06885

Middelburg, J.J., Nieuwenhuize, J., Iversen, N., Høgh, N., de Wilde, H., Helder, W., Seifert, R., Christof, O., 2002. Methane distribution in European tidal estuaries. *Biogeochemistry* 59, 95–119. https://doi.org/10.1023/A:1015515130419

Milkov, A.V., 2004. Global estimates of hydrate-bound gas in marine sediments: how much is really out there? *Earth Sci. Rev.* 66, 183–197. https://doi.org/10.1016/j.earscirev.2003.11.002

Miller, W.L., Moran, M.A., 1997. Interaction of photochemical and microbial processes in the degradation of refractory dissolved organic matter from a coastal marine environment. *Limnol. Oceanogr.* 42, 1317–1324. https://doi.org/10.4319/lo.1997.42.6.1317

Mitchell, M. R., Harrison, G., Pauley, K., Gagné, A., Maillet, G., and Strain, P. 2002. Atlantic Zonal Monitoring Program sampling protocol. *Can. Tech. Rep. Hydrogr. Ocean Sci.* 223: iv + 23 pp.

Moore, M.T., Vinson, D.S., Whyte, C.J., Eymold, W.K., Walsh, T.B., Darrah, T.H., 2018. Differentiating between biogenic and thermogenic sources of natural gas in coalbed methane reservoirs from the Illinois Basin using noble gas and hydrocarbon geochemistry. *Geol. Soc. Lond. Spec. Publ.* 468, 151–188. https://doi.org/10.1144/SP468.8

Mopper, K., Kieber, D.J., 2002. Photochemistry and the cycling of carbon, sulfur, nitrogen and phosphorus. In D. A. Hansell & C. A. Carlson (Eds.), *Biogeochemistry of Marine Dissolved Organic Matter* (pp. 455–507). San Diego: Academic Press. https://doi.org/10.1016/B978-012323841-2/50011-7

Mopper, K., Kieber, D. J., Stubbins, A., 2015. Marine photochemistry of organic matter: processes and impacts. In D. A. Hansell & C. A. Carlson (Eds.), *Biogeochemistry of Marine Dissolved Organic Matter (Second Edition)* (pp. 389–450). Boston: Academic Press. https://doi.org/10.1016/B978-0-12-405940-5.00008-X

Moritz, A., Hélie, J.-F., Pinti, D.L., Larocque, M., Barnetche, D., Retailleau, S., Lefebvre, R., Gélinas, Y., 2015. Methane baseline concentrations and sources in shallow aquifers from the shale gas-prone region of the St. Lawrence Lowlands (Quebec, Canada). *Environ. Sci. Technol.* 49, 4765–4771. https://doi.org/10.1021/acs.est.5b00443

Morrow, J.H., Hooker, S.B., Booth, C.R., Bernhard, G., Lind R.N., Brown, J.W., 2010. *Advances in Measuring the Apparent Optical Properties (AOPs) of Optically Complex Waters*, Greenbelt, MD.

Mucci, A., Starr, M., Gilbert, D., Sundby, B., 2011. Acidification of Lower St. Lawrence Estuary bottom waters. *Atmosphere-Ocean* 49, 206–218. https://doi.org/10.1080/07055900.2011.599265

Naqvi, S.W.A., Bange, H.W., Farías, L., Monteiro, P.M.S., Scranton, M.I., Zhang, J., 2010. Marine hypoxia/anoxia as a source of CH_4 and N_2O. *Biogeosciences* 7, 2159–2190. https://doi.org/10.5194/bg-7-2159-2010

Neef, L., van Weele, M., van Velthoven, P., 2010. Optimal estimation of the present-day global methane budget. Glob. Biogeochem. Cycles 24, GB4024. https://doi.org/10.1029/2009GB003661

Neill, A.R., Grime, D.W., Dawson, R.M.C., 1978. Conversion of choline methyl groups through trimethylamine into methane in the rumen. *Biochem. J.* 170, 529–535. https://doi.org/10.1042/bj1700529

Neta, P., Grodkowski, J., Ross, A.B., 1996. Rate constants for reactions of aliphatic carbon-centered radicals in aqueous solution. J. Phys. Chem. Ref. Data 25, 709–1050. https://doi.org/10.1063/1.555978

Nirmal Rajkumar, A., Barnes, J., Ramesh, R., Purvaja, R., Upstill-Goddard, R.C., 2008. Methane and nitrous oxide fluxes in the polluted Adyar River and estuary, SE India. *Mar. Pollut. Bull.* 56, 2043–2051. https://doi.org/10.1016/j.marpolbul.2008.08.005

Nota, D.J.G., Loring, D.H., 1964. Recent depositional conditions in the St. Lawrence River and Gulf — A reconnaissance survey. *Mar. Geol.* 2, 198–235. https://doi.org/10.1016/0025-3227(64)90040-4

Oremland, R.S., 1979. Methanogenic activity in plankton samples and fish intestines: A mechanism for in situ methanogenesis in oceanic surface waters. *Limnol. Oceanogr.* 24, 1136–1141. https://doi.org/10.4319/lo.1979.24.6.1136

Oremland, R.S., Marsh, L., DesMarais, D.J., 1982a. Methanogenesis in Big Soda Lake, Nevada: An alkaline, moderately hypersaline desert lake. *Appl. Environ. Microbiol.* 43, 462–468. https://doi.org/10.1128/aem.43.2.462-468.1982

Oremland, R.S., Marsh, L.M., Polcin, S., 1982b. Methane production and simultaneous sulphate reduction in anoxic, salt marsh sediments. *Nature* 296, 143–145. https://doi.org/10.1038/296143a0

Oremland, R.S., Polcin, S., 1982. Methanogenesis and sulfate reduction: competitive and noncompetitive substrates in estuarine sediments. *Appl. Environ. Microbiol.* 44, 1270–1276. https://doi.org/10.1128/aem.44.6.1270-1276.1982

Park, J.-R., Moon, S., Ahn, Y.M., Kim, J.Y., Nam, K., 2005. Determination of environmental factors influencing methane oxidation in a sandy landfill cover soil. *Environ. Technol.* 26, 93–102. https://doi.org/10.1080/09593332608618586

Pavlov, A.A., Kasting, J.F., Brown, L.L., Rages, K.A., Freedman, R., 2000. Greenhouse warming by CH_4 in the atmosphere of early Earth. *J. Geophys. Res. Planets* 105, 11981–11990. https://doi.org/10.1029/1999JE001134

Pernaton, E., Prinzhofer, A., Schneider, F., 1996. Reconsideration of methane isotope signature as a criterion for the genesis of natural gas: influence of migration on isotopic signatures. *Rev. Inst. Fr. Pétrole* 51, 635–651. https://doi.org/10.2516/ogst:1996042

Petrenko, V.V., Smith, A.M., Schaefer, H., Riedel, K., Brook, E., Baggenstos, D., Harth, C., Hua, Q., Buizert, C., Schilt, A., Fain, X., Mitchell, L., Bauska, T., Orsi, A., Weiss, R.F., Severinghaus, J.P., 2017. Minimal geological methane emissions during the Younger Dryas–Preboreal abrupt warming event. *Nature* 548, 443–446. https://doi.org/10.1038/nature23316

Pinet, N., Duchesne, M., Lavoie, D., Bolduc, A., Long, B., 2008. Surface and subsurface signatures of gas seepage in the St. Lawrence Estuary (Canada): Significance to hydrocarbon exploration. *Mar. Pet. Geol.* 25, 271–288. https://doi.org/10.1016/j.marpetgeo.2007.07.011

Pinet, N., Duchesne, M., Lavoie, D., 2010. Linking a linear pockmark train with a buried Palaeozoic structure: a case study from the St. Lawrence Estuary. *Geo-Mar. Lett.* 30, 517–522. https://doi.org/10.1007/s00367-009-0179-x

Plourde, S., Dodson, J.J., Runge, J.A., Therriault, J.-C., 2002. Spatial and temporal variations in copepod community structure in the lower St. Lawrence Estuary, Canada. *Mar. Ecol. Prog. Ser.* 230, 211–224.

Prather, M.J., Holmes, C.D., Hsu, J., 2012. Reactive greenhouse gas scenarios: Systematic exploration of uncertainties and the role of atmospheric chemistry. *Geophys. Res. Lett.* 39. https://doi.org/10.1029/2012GL051440

Powers, L.C., Babcock-Adams, L.C., Enright, J.K., Miller, W.L., 2015. Probing the photochemical reactivity of deep ocean refractory carbon (DORC): Lessons from hydrogen peroxide and superoxide kinetics. *Mar. Chem.* 177, 306–317.

Prinzhofer, A., Pernaton, É., 1997. Isotopically light methane in natural gas: bacterial imprint or diffusive fractionation? *Chem. Geol.* 142, 193–200. https://doi.org/10.1016/S0009-2541(97)00082-X

Prytherch, J., Brooks, I.M., Crill, P.M., Thornton, B.F., Salisbury, D.J., Tjernström, M., Anderson, L.G., Geibel, M.C., Humborg, C., 2017. Direct determination of the air-sea CO2 gas transfer velocity in Arctic sea ice regions. *Geophys. Res. Lett.* 44, 3770–3778. https://doi.org/10.1002/2017GL073593

Raymond, P.A., Cole, J.J., 2001. Gas exchange in rivers and estuaries: Choosing a gas transfer velocity. *Estuaries* 24, 312–317. https://doi.org/10.2307/1352954

Reeburgh, W.S., 1996. "Soft Spots" in the Global Methane Budget, in: Lidstrom, M.E., Tabita, F.R. (Eds.), Microbial Growth on C1 Compounds. Springer Netherlands, Dordrecht, pp. 334–342. https://doi.org/10.1007/978-94-009-0213-8_44

Reeburgh, W.S., 2007. Oceanic methane biogeochemistry. *Chem. Rev.* 107, 486–513. https://doi.org/10.1021/cr050362v

Rehder, G., Keir, R.S., Suess, E., Rhein, M., 1999. Methane in the northern Atlantic controlled by microbial oxidation and atmospheric history. *Geophys. Res. Lett.* 26, 587–590. https://doi.org/10.1029/1999GL900049

Repeta, D.J., Ferrón, S., Sosa, O.A., Johnson, C.G., Repeta, L.D., Acker, M., DeLong, E.F., Karl, D.M., 2016. Marine methane paradox explained by bacterial degradation of dissolved organic matter. *Nat. Geosci.* 9, 884–887. https://doi.org/10.1038/ngeo2837

Rhee, T.S., Kettle, A.J., Andreae, M.O., 2009. Methane and nitrous oxide emissions from the ocean: A reassessment using basin-wide observations in the Atlantic. *J. Geophys. Res. Atmospheres* 114, D12304. https://doi.org/10.1029/2008JD011662

Richey, J.E., Devol, A.H., Wofsy, S.C., Victoria, R., Riberio, M.N.G., 1988. Biogenic gases and the oxidation and reduction of carbon in Amazon River and floodplain waters: Amazon dissolved gases. *Limnol. Oceanogr.* 33, 551–561. https://doi.org/10.4319/lo.1988.33.4.0551

Rivard, C., Bordeleau, G., Lavoie, D., Lefebvre, R., Malet, X., 2018. Temporal variations of methane concentration and isotopic composition in groundwater of the St. Lawrence Lowlands, eastern Canada. *Hydrogeol. J.* 26, 533–551. https://doi.org/10.1007/s10040-017-1677-y

Robbins, P.E., Price, J.F., Owens, W.B., Jenkins, W.J., 2000. The importance of lateral diffusion for the ventilation of the lower thermocline in the Subtropical North Atlantic. *J. Phys. Oceanogr.* 30, 67–89. https://doi.org/10.1175/1520-0485(2000)030<0067:TIOLDF>2.0.CO;2

Rogers, J.E., Whitman, W.B., 1991. Microbial production and consumption of greenhouse gases: methane, nitrogen oxides, and halomethanes. Washington, DC (USA); American Society for Microbiology.

Rogers, J.N., Kelley, J.T., Belknap, D.F., Gontz, A., Barnhardt, W.A., 2006. Shallow-water pockmark formation in temperate estuaries: A consideration of origins in the western gulf of Maine with special focus on Belfast Bay. *Mar. Geol.* 225, 45–62. https://doi.org/10.1016/j.margeo.2005.07.011

Römer, M., Torres, M., Kasten, S., Kuhn, G., Graham, A.G.C., Mau, S., Little, C.T.S., Linse, K., Pape, T., Geprägs, P., Fischer, D., Wintersteller, P., Marcon, Y., Rethemeyer, J., Bohrmann, G., 2014. First evidence of widespread active methane seepage in the Southern Ocean, off the sub-Antarctic island of South Georgia. *Earth Planet. Sci. Lett.* 403, 166–177. https://doi.org/10.1016/j.epsl.2014.06.036

Rondeau, B., Cossa, D., Gagnon, P., Bilodeau, L., 2000. Budget and sources of suspended sediment transported in the St. Lawrence River, Canada. *Hydrol. Process.* 14, 21–36. https://doi.org/10.1002/(SICI)1099-1085(200001)14:1<21::AID-HYP907>3.0.CO;2-7

Rosentreter, J.A., Maher, D.T., Erler, D.V., Murray, R.H., Eyre, B.D., 2018. Methane emissions partially offset "blue carbon" burial in mangroves. *Sci. Adv.* 4, eaao4985. https://doi.org/10.1126/sciadv.aao4985

Rosentreter, J.A., Borges, A.V., Deemer, B.R., Holgerson, M.A., Liu, S., Song, C., Melack, J., Raymond, P.A., Duarte, C.M., Allen, G.H., Olefeldt, D., Poulter, B., Battin, T.I., Eyre, B.D., 2021. Half of global methane emissions come from highly variable aquatic ecosystem sources. *Nat. Geosci.* 14, 225–230. https://doi.org/10.1038/s41561-021-00715-2

Roy, S., Silverberg, N., Romero, N., Deibel, D., Klein, B., Savenkoff, C., Vézina, A., Tremblay, J.-É., Legendre, L., Rivkin, R.B., 2000. Importance of mesozooplankton feeding for the downward flux of biogenic carbon in the Gulf of St. Lawrence (Canada). *Deep Sea Res. Part II Top. Stud. Oceanogr.* 47, 519–544. https://doi.org/10.1016/S0967-0645(99)00117-4

Rudd, J.W.M., Taylor, C.D., 1980. Methane cycling in aquatic environments. *Adv. Aquat. Microbiol.* 2, 77–150.

Ruggaber, A., Dlugi, R., Bott, A., Forkel, R., Herrmann, H., Jacobi H.-W., 1997, Modelling of radiation quantities and photolysis frequencies in the aqueous phase in the troposphere, *Atmos. Environ.* 31, 3137–3150. https://doi:10.1016/S1352-2310(97)00058-7

Runge, J.A., Simard, Y., 1990. Zooplankton of the St. Lawrence Estuary: the imprint of physical processes on its composition and distribution, in: El-Sabh, M.I., Silverberg, N. (Eds.), Oceanography of a Large-Scale Estuarine System. Springer New York, New York, NY, pp. 296–320. https://doi.org/10.1007/978-1-4615-7534-4_13

Rusanov, I.I., Lein, A.Yu., Pimenov, N.V., Yusupov, S.K., Ivanov, M.V., 2002. The biogeochemical cycle of methane on the northwestern shelf of the Black Sea. *Microbiology* 71, 479–487. https://doi.org/10.1023/A:1019862014508

Sanderson, M.G., 1996. Biomass of termites and their emissions of methane and carbon dioxide: A global database. *Glob. Biogeochem. Cycles* 10, 543–557. https://doi.org/10.1029/96GB01893

Sansone, F.J., Holmes, M.E., Popp, B.N., 1999. Methane stable isotopic ratios and concentrations as indicators of methane dynamics in estuaries. *Glob. Biogeochem. Cycles* 13, 463–474. https://doi.org/10.1029/1999GB900012

Saunois, M., Bousquet, P., Poulter, B., Peregon, A., Ciais, P., Canadell, J.G., Dlugokencky, E.J., Etiope, G., Bastviken, D., Houweling, S., Janssens-Maenhout, G., Tubiello, F.N., Castaldi, S., Jackson, R.B., Alexe, M., Arora, V.K., Beerling, D.J., Bergamaschi, P., Blake, D.R., Brailsford, G., Brovkin, V., Bruhwiler, L., Crevoisier, C., Crill, P., Covey, K., Curry, C., Frankenberg, C., Gedney, N., Höglund-Isaksson, L., Ishizawa, M., Ito, A., Joos, F., Kim, H.-S., Kleinen, T., Krummel, P., Lamarque, J.-F., Langenfelds, R., Locatelli, R., Machida, T., Maksyutov, S., McDonald, K.C., Marshall, J., Melton, J.R., Morino, I., Naik, V., O'Doherty, S., Parmentier, F.-J.W., Patra, P.K., Peng, C., Peng, S., Peters, G.P., Pison, I., Prigent, C., Prinn, R., Ramonet, M., Riley, W.J., Saito, M., Santini, M., Schroeder, R., Simpson, I.J., Spahni, R., Steele, P., Takizawa, A., Thornton, B.F., Tian, H., Tohjima, Y., Viovy, N., Voulgarakis, A., van Weele, M., van der Werf, G.R., Weiss, R., Wiedinmyer, C., Wilton, D.J., Wiltshire, A., Worthy, D., Wunch, D., Xu, X., Yoshida, Y., Zhang, B., Zhang, Z., Zhu, Q., 2016. The global methane budget 2000–2012. Earth Syst Sci Data 8, 697–751. https://doi.org/10.5194/essd-8-697-2016

Saunois, M., Bousquet, P., Poulter, B., Peregon, A., Ciais, P., Canadell, J.G., Dlugokencky, E.J., Etiope, G., Bastviken, D., Houweling, S., Janssens-Maenhout, G., Tubiello, F.N., Castaldi, S., Jackson, R.B., Alexe, M., Arora, V.K., Beerling, D.J., Bergamaschi, P., Blake, D.R., Brailsford, G., Bruhwiler, L., Crevoisier, C., Crill, P., Covey, K., Frankenberg, C., Gedney, N., Höglund-Isaksson, L., Ishizawa, M., Ito, A., Joos, F., Kim, H.-S., Kleinen, T., Krummel, P., Lamarque, J.-F., Langenfelds, R., Locatelli, R., Machida, T., Maksyutov, S., Melton, J.R., Morino, I., Naik, V., O'Doherty, S., Parmentier, F.-J.W., Patra, P.K., Peng, C., Peng, S., Peters, G.P., Pison, I., Prinn, R., Ramonet, M., Riley, W.J., Saito, M., Santini, M., Schroeder, R., Simpson, I.J., Spahni, R., Takizawa, A., Thornton, B.F., Tian, H., Tohjima, Y., Viovy, N., Voulgarakis, A., Weiss, R., Wilton, D.J., Wiltshire, A., Worthy, D., Wunch, D., Xu, X., Yoshida, Y., Zhang, B., Zhang, Z., Zhu, Q., 2017. Variability and quasi-decadal changes in the methane budget over the period 2000–2012. *Atmos. Chem. Phys.* 17, 11135–11161. https://doi.org/10.5194/acp-17-11135-2017

Saunois, M., Stavert, A. R., Poulter, B., Bousquet, P., Canadell, J. G., Jackson, R. B., Raymond, P. A., Dlugokencky, E. J., Houweling, S., Patra, P. K., Ciais, P., Arora, V. K., Bastviken, D., Bergamaschi, P., Blake, D. R., Brailsford, G., Bruhwiler, L., Carlson, K. M., Carrol, M., Castaldi, S., Chandra, N., Crevoisier, C., Crill, P. M., Covey, K., Curry, C. L., Etiope, G., Frankenberg, C., Gedney, N., Hegglin, M. I., Höglund-Isaksson, L., Hugelius, G., Ishizawa, M., Ito, A., Janssens-Maenhout, G., Jensen, K. M., Joos, F., Kleinen, T., Krummel, P. B., Langenfelds, R. L., Laruelle, G. G., Liu, L., Machida, T., Maksyutov, S., McDonald, K. C., McNorton, J., Miller, P. A., Melton, J. R., Morino, I., Müller, J., Murguia-Flores, F., Naik, V., Niwa, Y., Noce, S., O'Doherty, S., Parker, R. J., Peng, C., Peng, S., Peters, G. P., Prigent, C., Prinn, R., Ramonet, M., Regnier, P., Riley, W. J., Rosentreter, J. A., Segers, A., Simpson, I. J., Shi, H., Smith, S. J., Steele, L. P., Thornton, B. F., Tian, H., Tohjima, Y., Tubiello, F. N., Tsuruta, A., Viovy, N., Voulgarakis, A., Weber, T. S., van Weele, M., van der Werf, G. R., Weiss, R. F., Worthy, D., Wunch, D., Yin, Y., Yoshida, Y., Zhang, W., Zhang, Z., Zhao, Y., Zheng, B., Zhu, Q., Zhu, Q., Zhuang, Q., 2020. The global methane budget 2000–2017. *Earth Syst. Sci. Data* 12, 1561–1623. https://doi.org/10.5194/essd-12-1561-2020.

Savard, M.M., Jautzy, J.J., Lavoie, D., Dhillon, R.S., Defliese, W.F., 2021. Clumped and oxygen isotopes reveal differential disequilibrium in the formation of carbonates from marine methane seeps. *Geochim. Cosmochim. Acta* 298, 43–54. https://doi.org/10.1016/j.gca.2021.01.041

Schaefer, H., Fletcher, S.E.M., Veidt, C., Lassey, K.R., Brailsford, G.W., Bromley, T.M., Dlugokencky, E.J., Michel, S.E., Miller, J.B., Levin, I., Lowe, D.C., Martin, R.J., Vaughn, B.H., White, J.W.C., 2016. A 21st-century shift from fossil-fuel to biogenic methane emissions indicated by $^{13}CH_4$. *Science* 352, 80–84. https://doi.org/10.1126/science.aad2705

Schafer, C., Smith, J., Côté, R., 1990. The Saguenay Fiord: A major tributary to the St. Lawrence Estuary. In: El-Sabh, M.I., Silverberg, N. (Eds), Oceanography of a Large-Scale Estuarine System — The St. Lawrence. Coastal and Estuarine Studies, vol 39. Springer, New York, NY, pp. 378–420. https://doi.org/10.1007/978-1-4615-7534-4_17

Schink, B., Zeikus, J.G., 1980. Microbial methanol formation: A major end product of pectin metabolism. *Curr. Microbiol.* 4, 387–389. https://doi.org/10.1007/BF02605383

Schmale, O., Schneider von Deimling, J., Gülzow, W., Nausch, G., Waniek, J.J., Rehder, G., 2010. Distribution of methane in the water column of the Baltic Sea: methane distribution in the Baltic Sea. *Geophys. Res. Lett.* 37, L12604. https://doi.org/10.1029/2010GL043115

Schmale, O., Wäge, J., Morholz, V., Rehder, G., Wasmund, N., Gräwe, U., Labrenz, M., Loick-Wilde, N., 2017. Methane anomalies in the oxygenated upper waters of the central Baltic Sea associated with zooplankton abundance. Presented at the EGU General Assembly Conference Abstracts, p. 7007.

Schmale, O., Wäge, J., Mohrholz, V., Wasmund, N., Gräwe, U., Rehder, G., Labrenz, M., Loick-Wilde, N., 2018. The contribution of zooplankton to methane supersaturation in the oxygenated upper waters of the central Baltic Sea. *Limnol. Oceanogr.* 63, 412–430. https://doi.org/10.1002/lno.10640

Schoell, M., 1980. The hydrogen and carbon isotopic composition of methane from natural gases of various origins. *Geochim. Cosmochim. Acta* 44, 649–661. https://doi.org/10.1016/0016-7037(80)90155-6

Scranton, M.I., Brewer, P.G., 1977. Occurrence of methane in the near-surface waters of the western subtropical North-Atlantic. *Deep Sea Res.* 24, 127–138. https://doi.org/10.1016/0146-6291(77)90548-3

Scranton, M.I., Brewer, P.G., 1978. Consumption of dissolved methane in the deep ocean. *Limnol. Oceanogr.* 23, 1207–1213. https://doi.org/10.4319/lo.1978.23.6.1207

Scranton, M.I., McShane, K., 1991. Methane fluxes in the southern North Sea: the role of European rivers. *Cont. Shelf Res.* 11, 37–52. https://doi.org/10.1016/0278-4343(91)90033-3

Seibert, G.H., Trites, R.W., Reid, S.J., 1979. Deepwater Exchange Processes in the Saguenay Fjord. *J. Fish. Res. Board Can.* 36, 42–53. https://doi.org/10.1139/f79-006

Serodes, J.B., Troude, J.-P., 1984. Sedimentation cycle of a freshwater tidal flat in the St. Lawrence estuary. *Estuaries* 7, 119. https://doi.org/10.2307/1351765

Sharpless, C.M., Blough, N.V., 2014. The importance of charge-transfer interactions in determining chromophoric dissolved organic matter (CDOM) optical and photochemical properties. *Environ. Sci.: Processes & Impacts* 16, 654–671. https://doi.org/10.1039/C3EM00573A

Silverberg, N., Sundby, B., 1990. Sediment-Water Interaction and Early Diagenesis in the Laurentian Trough, in: El-Sabh, M.I., Silverberg, N. (Eds.), Oceanography of a Large-Scale Estuarine System: The St. Lawrence. Springer New York, New York, NY, pp. 202–238. https://doi.org/10.1007/978-1-4615-7534-4_10

Silverberg, N., Sundby, B., 1979. Observations in the turbidity maximum of the St. Lawrence Estuary. *Can. J. Earth Sci.* 16, 939–950. https://doi.org/10.1139/e79-080

Simard, Y., Lavoie, D., 1999. The rich krill aggregation of the Saguenay - St. Lawrence Marine Park: hydroacoustic and geostatistical biomass estimates, structure, variability, and significance for whales. *Can. J. Fish. Aquat. Sci.* 56, 1182–1197. https://doi.org/10.1139/f99-063

Simó, R., 2004. From cells to globe: approaching the dynamics of DMS(P) in the ocean at multiple scales. Can. J. Fish. Aquat. Sci. 61, 673–684. https://doi.org/10.1139/f04-030

Sirdeys, N., 2019. Pockmarks dans le chenal Laurentien, zone d'Old Harry, golfe du Saint-Laurent (est du Canada). Université du Québec à Rimouski, Institut des sciences de la mer de Rimouski (ISMER), Rimouski, Québec.

Sleep, N.H., Meibom, A., Fridriksson, Th., Coleman, R.G., Bird, D.K., 2004. H2-rich fluids from serpentinization: Geochemical and biotic implications. *Proc. Natl. Acad. Sci.* 101, 12818–12823. https://doi.org/10.1073/pnas.0405289101

Smith, J.N., Walton, A., 1980. Sediment accumulation rates and geochronologies measured in the Saguenay Fjord using the Pb-210 dating method. *Geochim. Cosmochim. Acta* 44, 225–240. https://doi.org/10.1016/0016-7037(80)90134-9

Solomon, E.A., Kastner, M., MacDonald, I.R., Leifer, I., 2009. Considerable methane fluxes to the atmosphere from hydrocarbon seeps in the Gulf of Mexico. *Nat. Geosci.* 2, 561–565. https://doi.org/10.1038/ngeo574

Sourisseau, M., Simard, Y., Saucier, F.J., 2006. Krill aggregation in the St. Lawrence system, and supply of krill to the whale feeding grounds in the estuary from the gulf. *Mar. Ecol. Prog. Ser.* 314, 257–270.

Stacey, M.W., Gratton, Y., 2001. The energetics and tidally induced reverse renewal in a two-silled fjord. *J. Phys. Oceanogr.* 31, 1599–1615. https://doi.org/10.1175/1520-0485(2001)031<1599:TEATIR>2.0.CO;2

Stawiarski, B., Otto, S., Thiel, V., Gräwe, U., Loick-Wilde, N., Wittenborn, A.K., Schloemer, S., Wäge, J., Rehder, G., Labrenz, M., Wasmund, N., Schmale, O., 2019. Controls on zooplankton methane production in the central Baltic Sea. *Biogeosciences* 16, 1–16. https://doi.org/10.5194/bg-16-1-2019

St-Onge, G., Hillaire-Marcel, C., 2001. Isotopic constraints of sedimentary inputs and organic carbon burial rates in the Saguenay Fjord, Quebec. *Mar. Geol.* 176, 1–22. https://doi.org/10.1016/S0025-3227(01)00150-5.

Stefels, J., Steinke, M., Turner, S., Malin, G., Belviso, S., 2007. Environmental constraints on the production and removal of the climatically active gas dimethylsulphide (DMS) and implications for ecosystem modelling. *Biogeochemistry* 83, 245–275. https://doi.org/10.1007/s10533-007-9091-5

Stevens, C.M., Rust, F.E., 1982. The carbon isotopic composition of atmospheric methane. *J. Geophys. Res.* 87, 4879. https://doi.org/10.1029/JC087iC07p04879

Strain, P.M., 1988. Chemical oceanography in the Gulf of St. Lawrence. Canadian Government Publishing Centre, Ottawa, ON, Canada.

Strøm, A.R., Olafsen, J.A., Larsen, H., 1979. Trimethylamine Oxide: A terminal electron acceptor in anaerobic respiration of bacteria. *Microbiology* 112, 315–320.

Stubbins, A., Uher, G., Law, C.S., Mopper, K., Robinson, C., Upstill-Goddard, R.C., 2006. Open-ocean carbon monoxide photoproduction. *Deep Sea Res. Part II* 53, 1695–1705. https://doi.org/10.1016/j.dsr2.2006.05.011

Stubbins, A.P., 2001. Aspects of aquatic CO photoproduction from CDOM (Ph.D. thesis). University of Newcastle upon Tyne, United Kingdom.

Syvitski, J., Praeg, D., 1989. Quaternary sedimentation in the St. Lawrence Estuary and adjoining areas, Eastern Canada: An overview based on high-resolution seismo-stratigraphy. *Géographie Phys. Quat.* 43, 291–310. https://doi.org/10.7202/032784ar

Swinnerton, J.W., Linnenbom, V.J., 1967. Gaseous hydrocarbons in sea water: Determination. *Science* 156, 1119–1120. https://doi.org/10.1126/science.156.3778.1119

Swinnerton, J.W., Lamontagne, R.A., 1974. Oceanic distribution of low-molecular-weight hydrocarbons. Baseline measurements. *Environ. Sci. Technol.* 8, 657–663. https://doi.org/10.1021/es60092a006

Thauer, R.K., Jungermann, K., Karl, D., 1977. Energy conservation in chemotrophic anaerobic bacteria. *Bacteriol. Rev.* 41, 100–180. https://doi.org/10.1128/br.41.3.809-809.1977

Thauer, R.K., Kaster, A.-K., Seedorf, H., Buckel, W., Hedderich, R., 2008. Methanogenic archaea: ecologically relevant differences in energy conservation. *Nat. Rev. Microbiol.* 6, 579–591. https://doi.org/10.1038/nrmicro1931

Therriault, J.C., de Ladurantaye, R., Ingram, R.G., 1984. Particulate matter exchange across a fjord sill. *Estuar. Coast. Shelf Sci.* 18, 51–64. https://doi.org/10.1016/0272-7714(84)90006-4

Therriault, J.-C., Levasseur, M., 1986. Freshwater Runoff Control of the Spatio-Temporal Distribution of Phytoplankton in the Lower St. Lawrence Estuary (Canada), in: Skreslet, S. (Ed.), The Role of Freshwater Outflow in Coastal Marine Ecosystems. Springer Berlin Heidelberg, Berlin, Heidelberg, pp. 251–260. https://doi.org/10.1007/978-3-642-70886-2_17

Therriault, J.-C., Legendre, L., Demers, S., 1990. Oceanography and Ecology of Phytoplankton in the St.Lawrence Estuary, in: El-Sabh, M.I., Silverberg, N. (Eds.), Oceanography of a Large-Scale Estuarine System: The St. Lawrence. Springer New York, New York, NY, pp. 269–295. https://doi.org/10.1007/978-1-4615-7534-4_12

Thorneloe, S.A., Barlaz, M.A., Peer, R., Huff, L.C., Davis, L., Mangino, J., 2000. Waste management, in: Khalil, M. (Ed.), Atmospheric Methane: Its Role in the Global Environment. Springer-Verlag, New York, pp. 234–262.

Thornton, B.F., Prytherch, J., Andersson, K., Brooks, I.M., Salisbury, D., Tjernström, M., Crill, P.M., 2020. Shipborne eddy covariance observations of methane fluxes constrain Arctic sea emissions. *Sci. Adv.* 6, eaay7934. https://doi.org/10.1126/sciadv.aay7934

Townsend-Small, A., Botner, E.C., Jimenez, K.L., Schroeder, J.R., Blake, N.J., Meinardi, S., Blake, D.R., Sive, B.C., Bon, D., Crawford, J.H., Pfister, G., Flocke, F.M., 2016. Using stable isotopes of hydrogen to quantify biogenic and thermogenic atmospheric methane sources: A case study from the Colorado Front Range. *Geophys. Res. Lett.* 43, 11,462-11,471. https://doi.org/10.1002/2016GL071438

Tremblay, L., Gagné, J.P., 2009. Organic matter distribution and reactivity in the waters of a large estuarine system. *Mar. Chem.* 116, 1–12. https://doi.org/10.1016/j.marchem.2009.09.006

Tremblay, L., Gagné, J.P., 2007. Distribution and biogeochemistry of sedimentary humic substances in the St. Lawrence Estuary and the Saguenay Fjord, Québec. *Org. Geochem.* 38, 682–699. https://doi.org/10.1016/j.orggeochem.2006.11.003

Tyler, S.C., 1991. The global methane budget, in: Rogers, J.E., Whitman, W.B. (Eds.), Microbial Production and Consumption of Greenhouse Gases: Methane, Nitrogen Oxides, and Halomethanes. American Society for Microbiology, Washington, DC (USA), United States, pp. 7–38.

Upstill-Goddard, R.C., Barnes, J., Frost, T., Punshon, S., Owens, N.J.P., 2000. Methane in the southern North Sea: Low-salinity inputs, estuarine removal, and atmospheric flux. *Glob. Biogeochem. Cycles* 14, 1205–1217. https://doi.org/10.1029/1999GB001236

Upstill-Goddard, R.C., Barnes, J., 2016. Methane emissions from UK estuaries: Re-evaluating the estuarine source of tropospheric methane from Europe. *Mar. Chem.* 180, 14–23. https://doi.org/10.1016/j.marchem.2016.01.010

Valentine, D.L., Blanton, D.C., Reeburgh, W.S., Kastner, M., 2001. Water column methane oxidation adjacent to an area of active hydrate dissociation, Eel River Basin. *Geochim. Cosmochim. Acta* 65, 2633–2640. https://doi.org/10.1016/S0016-7037(01)00625-1

Valentine, D.L., 2002. Biogeochemistry and microbial ecology of methane oxidation in anoxic environments: a review. *Antonie Van Leeuwenhoek* 81, 271–282. https://doi.org/10.1023/A:1020587206351

van der Werf, G.R., Randerson, J.T., Giglio, L., Collatz, G.J., Kasibhatla, P.S., Arellano Jr., A.F., 2006. Interannual variability in global biomass burning emissions from 1997 to 2004. *Atmos. Chem. Phys.* 6, 3423–3441. https://doi.org/10.5194/acp-6-3423-2006

Von Damm, K.L., 1990. Seafloor hydrothermal activity: black smoker chemistry and chimneys. *Annu. Rev. Earth Planet. Sci.* 18, 173–204. https://doi.org/10.1146/annurev.ea.18.050190.001133

Wanninkhof, R., 2014. Relationship between wind speed and gas exchange over the ocean revisited. *Limnol. Oceanogr.: Methods* 12, 351–362. https://doi.org/10.4319/lom.2014.12.351

Ward, B.B., Kilpatrick, K.A., Wopat, A.E., Minnich, E.C., Lidstrom, M.E., 1989. Methane oxidation in Saanich Inlet during summer stratification. *Cont. Shelf Res.* 9, 65–75. https://doi.org/10.1016/0278-4343(89)90083-6

Weber, T., Wiseman, N.A., Kock, A., 2019. Global ocean methane emissions dominated by shallow coastal waters. *Nat. Commun.* 10:4584. https://doi.org/10.1038/s41467-019-12541-7

Weimer, P.J., Zeikus, J.G., 1978. One carbon metabolism in methanogenic bacteria. *Arch. Microbiol.* 119, 49–57. https://doi.org/10.1007/BF00407927

Whiteman, G., Hope, C., Wadhams, P., 2013. Vast costs of Arctic change. *Nature* 499, 401–403. https://doi.org/10.1038/499401a

Whiticar, M.J., Faber, E., 1986. Methane oxidation in sediment and water column environments—Isotope evidence. *Org. Geochem.* 10, 759–768. https://doi.org/10.1016/S0146-6380(86)80013-4

Whiticar, M.J., 1999. Carbon and hydrogen isotope systematics of bacterial formation and oxidation of methane. *Chem. Geol.* 161, 291–314. https://doi.org/10.1016/S0009-2541(99)00092-3

Whiticar, M., Schaefer, H., 2007. Constraining past global tropospheric methane budgets with carbon and hydrogen isotope ratios in ice. *Philos. Trans. R. Soc. Math. Phys. Eng. Sci.* 365, 1793–1828. https://doi.org/10.1098/rsta.2007.2048

Whiticar, M.J., 2020. The biogeochemical methane cycle, in: Wilkes, H. (Ed.), Hydrocarbons, Oils and Lipids: Diversity, Origin, Chemistry and Fate. Springer International Publishing, Cham, pp. 669–746. https://doi.org/10.1007/978-3-319-90569-3_5

Wiesenburg, D.A., Guinasso, N.L., 1979. Equilibrium solubilities of methane, carbon monoxide, and hydrogen in water and sea water. *J. Chem. Eng. Data* 24, 356–360. https://doi.org/10.1021/je60083a006

Wilkniss, P.E., Lamontagne, R.A., Larson, R.E., Swinnerton, J.W., 1978. Atmospheric trace gases and land and sea breezes at the Sepik River coast of Papua New Guinea. *J. Geophys. Res.* 83, 3672. https://doi.org/10.1029/JC083iC07p03672

Woodward, G., Gessner, M.O., Giller, P.S., Gulis, V., Hladyz, S., Lecerf, A., Malmqvist, B., McKie, B.G., Tiegs, S.D., Cariss, H., Dobson, M., Elosegi, A., Ferreira, V., Graça, M.A.S., Fleituch, T., Lacoursière, J.O., Nistorescu, M., Pozo, J., Risnoveanu, G., Schindler, M., Vadineanu, A., Vought, L.B.-M., Chauvet, E., 2012. Continental-scale effects of nutrient pollution on stream ecosystem functioning. *Science* 336, 1438. https://doi.org/10.1126/science.1219534

Worden, J.R., Bloom, A.A., Pandey, S., Jiang, Z., Worden, H.M., Walker, T.W., Houweling, S., Röckmann, T., 2017. Reduced biomass burning emissions reconcile conflicting estimates of the post-2006 atmospheric methane budget. *Nat. Commun.* 8, 2227.

Xie, H., Andrews, S.S., Martin, W.R., Miller, J., Ziolkowski, L., Taylor, C.D., Zafiriou, O.C., 2002. Validated methods for sampling and headspace analysis of carbon monoxide in seawater. *Mar. Chem.* 77, 93–108. https://doi.org/10.1016/S0304-4203(01)00065-2

Xie, H., Zafiriou, O.C., 2009. Evidence for significant photochemical production of carbon monoxide by particles in coastal and oligotrophic marine waters. *Geophys. Res. Lett.* 36. https://doi.org/10.1029/2009GL041158

Xie, H., Aubry, C., Bélanger, S., Song, G., 2012. The dynamics of absorption coefficients of CDOM and particles in the St. Lawrence estuarine system: Biogeochemical and physical implications. *Mar. Chem.* 128–129, 44–56. https://doi.org/10.1016/j.marchem.2011.10.001

Xie, H., Li, Y., Zhang, Y., Geng, L., 2019. CDOM photodegradation: Implications for the oceanic methane paradox. *Geophysical Research Abstracts*, *21*, EGU2019-3396, 2019, EGU General Assembly 2019.

Yamanaka, Y., Tajika, E., 1996. The role of the vertical fluxes of particulate organic matter and calcite in the oceanic carbon cycle: Studies using an ocean biogeochemical general circulation model. *Glob. Biogeochem. Cycles* 10, 361–382. https://doi.org/10.1029/96GB00634

Yamashita, Y., Tanoue, E., 2008. Production of bio-refractory fluorescent dissolved organic matter in the ocean interior. *Nat. Geosci.* 1, 579–582. https://doi.org/10.1038/ngeo279

Yang, F., Song, G., Massicotte, P., Wei, H., Xie, H., 2020. Depth-resolved photochemical lability of dissolved organic matter in the western tropical Pacific Ocean. *J. Geophys. Res. Biogeosciences* 125, e2019. https://doi.org/10.1029/2019JG005425

Ye, W., Wang, X.L., Zhang, X.H., Zhang, G.L., 2020. Methane production in oxic seawater of the western North Pacific and its marginal seas. *Limnol. Oceanogr*. https://doi.org/10.1002/lno.11457

Ye, W., Zhang, G., Zheng, W., Zhang, H., Wu, Y., 2019. Methane distributions and sea-to-air fluxes in the Pearl River Estuary and the northern South China sea. *Deep Sea Res*. Part II 167, 34-45. https://doi.org/10.1016/j.dsr2.2019.06.016

Ye, W., Zhang, G., Zhu, Z., Huang, D., Han, Y., Wang, L., Sun, M., 2016. Methane distribution and sea-to-air flux in the East China Sea during the summer of 2013: Impact of hypoxia. *Deep Sea Res. Part II* 124, 74-83. https://doi.org/10.1016/j.dsr2.2015.01.008

Ye, W., Zhang, G., Zheng, W., Zhang, H., Wu, Y., 2019. Methane distributions and sea-to-air fluxes in the Pearl River Estuary and the northern South China sea. *Living-Resour. Ecosyst. Dyn. Slope South China Sea LEDS* 167, 34–45. https://doi.org/10.1016/j.dsr2.2019.06.016

Yeats, P.A., 1990. Reactivity and transport of nutrients and metals in the St. Lawrence Estuary, in: El-Sabh, M.I., Silverberg, N. (Eds.), Oceanography of a Large-Scale Estuarine System: The St. Lawrence. Springer New York, New York, NY, pp. 155–169. https://doi.org/10.1007/978-1-4615-7534-4_8

Yoch, D.C., 2002. Dimethylsulfoniopropionate: Its sources, role in the marine food web, and biological degradation to dimethylsulfide. *Appl. Environ. Microbiol.* 68, 5804–5815. https://doi.org/10.1128/AEM.68.12.5804-5815.2002

Zafiriou, O.C., Andrews, S.S., Wang, W., 2003. Concordant estimates of oceanic carbon monoxide source and sink processes in the Pacific yield a balanced global "blue-water" CO budget. *Global Biogeochem. Cycles* 17. https://doi.org/10.1029/2001GB001638

Zavala-Araiza, D., Omara, M., Gautam, R., Smith, M.L., Pandey, S., Aben, I., Almanza-Veloz, V., Conley, S., Houweling, S., Kort, E.A., Maasakkers, J.D., Molina, L.T., Pusuluri, A., Scarpelli, T., Schwietzke, S., Shen, L., Zavala, M., Hamburg, S.P., 2021. A tale of two regions: methane emissions from oil and gas production in offshore/onshore Mexico. *Environ. Res. Lett.* 16, 024019. https://doi.org/10.1088/1748-9326/abceeb

Zhang, B., Tian, H., Ren, W., Tao, B., Lu, C., Yang, J., Banger, K., Pan, S., 2016. Methane emissions from global rice fields: Magnitude, spatiotemporal patterns, and environmental controls. *Glob. Biogeochem. Cycles* 30, 1246–1263. https://doi.org/10.1002/2016GB005381

Zhang, G., Zhang, J., Liu, S., Ren, J., Xu, J., Zhang, F., 2008. Methane in the Changjiang (Yangtze River) Estuary and its adjacent marine area: riverine input, sediment release and atmospheric fluxes. *Biogeochemistry* 91, 71–84. https://doi.org/10.1007/s10533-008-9259-7

Zhang, Y., Xie, H., Chen, G., 2006. Factors affecting the efficiency of carbon monoxide photoproduction in the St. Lawrence estuarine system (Canada). *Environm. Sci. Technol.* 40, 7771–7777.

Zhang, Y., Xie, H., 2015. Photomineralization and photomethanification of dissolved organic matter in Saguenay River surface water. *Biogeosciences* 12, 6823–6836. https://doi.org/10.5194/bg-12-6823-2015

Zhang, Y., Chen, B., Zhai, W., 2020. Exploring sources and biogeochemical dynamics of dissolved methane in the central Bohai Sea in summer. *Front. Mar. Sci.* 7, 79. https://doi.org/10.3389/fmars.2020.00079

Zhu, Y., Kieber, D.J., 2018. Wavelength-and temperature-dependent apparent quantum yields for photochemical production of carbonyl compounds in the North Pacific Ocean. *Environm. Sci. Technol.* 52, 1929–1939.

Zhu, Y., Kieber, D.J., 2020. Global model for depth-dependent carbonyl photochemical production rates in seawater. *Glob. Biogeochem. Cycles* 34. https://doi.org/10.1029/2019GB006431

Zindler, C., Peeken, I., Marandino, C.A., Bange, H.W., 2012. Environmental control on the variability of DMS and DMSP in the Mauritanian upwelling region. *Biogeosciences* 9, 1041–1051. https://doi.org/10.5194/bg-9-1041-2012